Dissecting Tumor Heterogeneity in Lung Cancer

by

Aparna Padhye, MBBS

APPROVED

_____
Don L. Gibbons, M.D., Ph.D.
Advisory Professor

_____
Andrew Gladden, Ph.D.

_____
Jichao Chen, Ph.D.

_____
Lauren Byers, M.D.

_____
Walter Hilttelman, Ph.D.

_____
Varsha Gandhi, Ph.D.

APPROVED

_____
Dean, The University of Texas
MD Anderson Cancer Center UTHealth Graduate School of Biomedical Sciences

Dissecting Tumor Heterogeneity in Lung Cancer

A

DISSERTATION

Presented to the Faculty of

The University of Texas

MD Anderson Cancer Center UTHealth

Graduate School of Biomedical Sciences

in Partial Fulfillment

of the Requirements

for the Degree of

DOCTOR OF PHILOSOPHY

by

Aparna Padhye, MBBS
Houston, Texas

August, 2021

Dedication

To my parents and brother, for their unwavering and unconditional love and support, even from a thousand miles away.

Acknowledgement

This work would not have been complete without the support and guidance of many people. First of all my academic advisor, Dr. Don L. Gibbons, who gave me the opportunity to work in his research group. From the beginning, he encouraged me to think through the scientific problems, to reason and to overcome hurdles in a systematic way. His enthusiasm for science kept me motivated even when I was brought down by negative data or failed hypotheses. He patiently worked with me to improve in my areas of weakness, including presentations and scientific writing, which have truly made me a better scientist. Even with all the ups and downs that came along the way, I knew I could count on him for his advice and support. I also want to thank my advisory committee members Drs. Varsha Gandhi, Andrew Gladden, Walter Hittelman, Jichao Chen and Lauren Byers for taking the time and providing valuable feedback that helped me bring this work to fruition.

I also want to thank all the Gibbons lab members, current and former. The atmosphere in the lab has always been one of teamwork, support and encouragement which made lab work a little more fun. I want to thank Dr. Christin Ungewiss and Dr. Jonathon Roybal, who were there when I first joined the lab and who have remained very close friends even after leaving the lab. They always looked out for me and gave me unique tips for research that made my life much easier. I want to thank Dr. Letty Rodriguez and Dr. Jessica Konen who were there to brainstorm ideas with, and sometimes just as a sounding board when things did not go as planned, Laura Gibson for being an amazing lab manager and Jared Fradette for all the help with mouse experiments.

I also want to thank all my friends in graduate school and outside, who shared these experiences with me and kept me sane. Exploring different restaurants in Houston with them was definitely something I looked forward to after a long week in lab.

Dissecting Tumor Heterogeneity in Lung Cancer

Aparna Padhye, M.B.B.S.

Advisory Professor: Don L. Gibbons, M.D., Ph.D.

Lung cancer is a heterogeneous disease composed of genetically and phenotypically distinct tumor cells as well as a heterogeneous microenvironment consisting of non-cancer cells and extracellular matrix. Constant interactions among these components ultimately leads to a complex tumor tissue that is ever evolving and poses a therapeutic challenge for sustained benefit. Strategies for targeting lung cancers are largely guided by the genetic alterations identified in the tumor specimens. However, in order to gain a better understanding of lung cancer progression and develop effective treatment modalities, studying tumor in context of its microenvironment is crucial. The first aim of this project was to establish an experimental model to capture tumor heterogeneity. We developed an *Ex Vivo* Tumor system that preserved tumor composition and allowed the introduction of specific modifications in the tumor microenvironment to investigate their role in tumor progression. We utilized this system to demonstrate the role of extrinsic as well as intrinsic alterations that modify tumor cell behavior. Next, we explored the biological phenomenon epithelial-to-mesenchymal transition as a source of tumor cell heterogeneity and therapeutic resistance. Genetically identical KRAS mutant lung cancer cells displayed different phenotypic states that were associated with distinct survival pathways that allowed cancer cells to escape therapeutic targeting. With the use of extensive *in vitro, ex vivo* and *in vivo* models, we identified that a combinatorial approach of utilizing CDK4 and MEK inhibitors to effectively control tumor growth by targeting distinct tumor subpopulations within lung cancer and prevented emergent resistance to either single agent.

Table of Contents

List of Illustrations

List of Tables

Chapter 1: Introduction

1.1 Lung cancer

Lung cancer continues to account for the highest cancer-related mortality in the US[1]. Two-thirds of the patients present in the clinic at an advanced stage with metastatic disease progression that results in a dismal 5-year survival rate (Figure 1). The morbidity is also exacerbated in patients with early-stage disease, who may have initial an response to treatments but demonstrate a recurrence rate of approximately 50 percent due to the development of resistance to therapeutic agents.

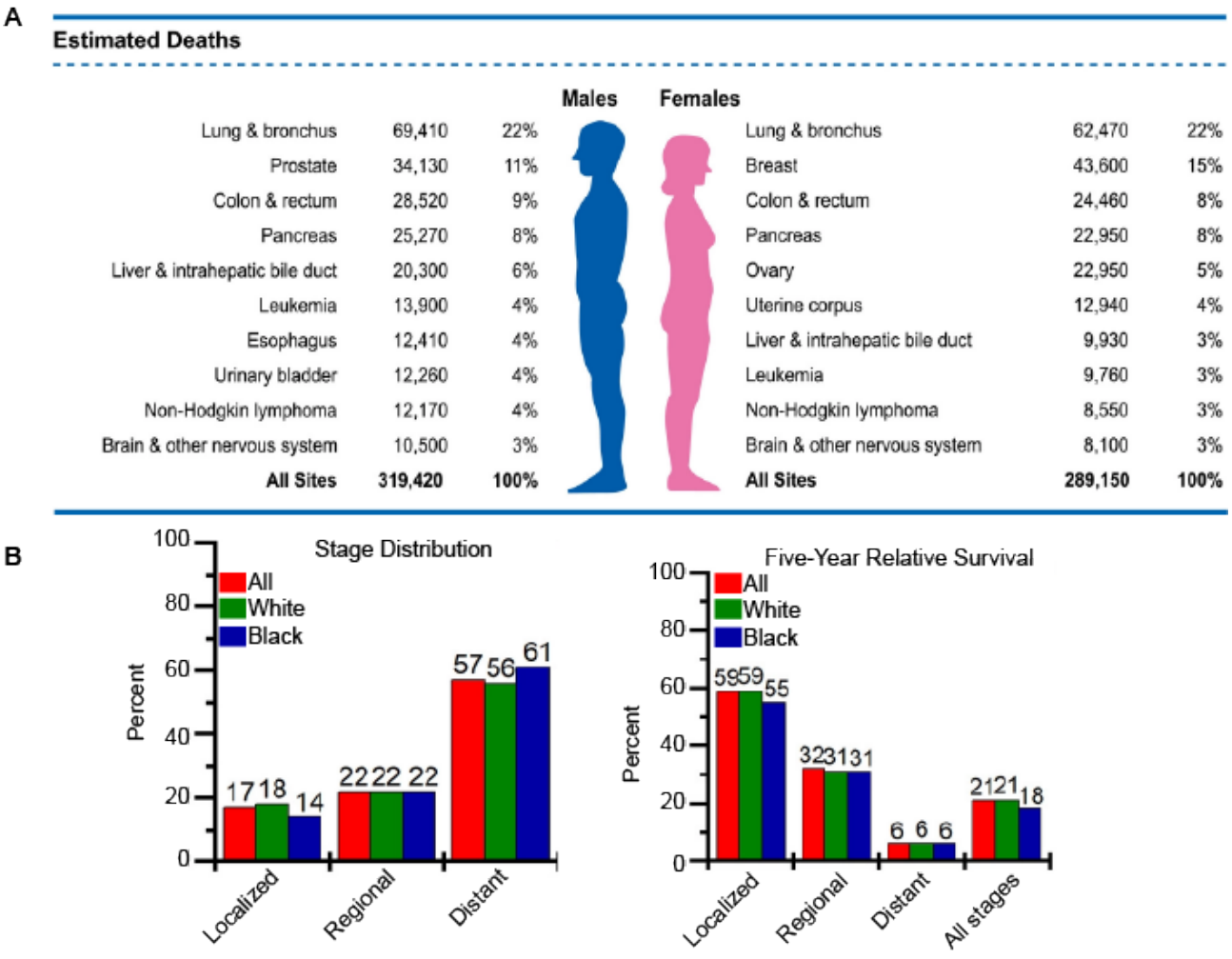

Figure 1. Lung cancer statistics.
(A) Leading cancer types for the estimated new cancer deaths, US, 2021. (B) Top: Stage distribution for lung cancer, US, 2010 to 2016. Bottom: Five-year relative survival for lung cancer by stage at diagnosis, US, 2010 to 2016. Obtained with permission from John Wiley and Sons.

Conventionally, lung cancer is broadly classified into small cell (SCLC) and non-small cell lung cancer (NSCLC) based on histopathological characteristics (Figure 2). SCLC occurs in about 20% of the patients while the majority of the burden comes from NSCLC (80%), which is further classified as adenocarcinoma (ADC, ~50%), squamous cell carcinoma (SCC, ~40%) and large cell carcinoma (LCC, by exclusion of ADC and SCC). SCLC and LCC are distinct set of neuroendocrine malignancies and have an independent route of clinical management[2,3]. ADCs arise in more distal airways whereas SCCs arise in more proximal airways with a stronger associated with smoking. There are distinct biomarkers determining the origin of lung tumors which dictates the treatment decisions.

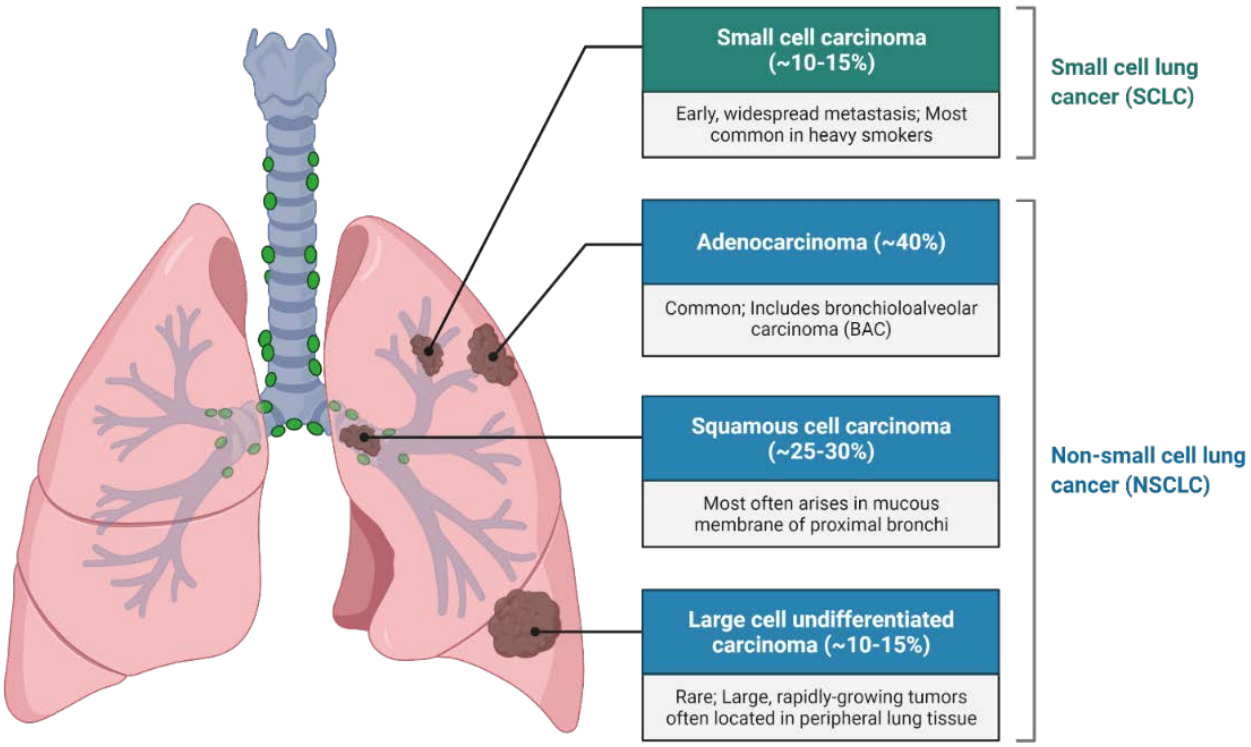

Figure 2. Histological subtypes in Lung Cancer.
Clincil subclassificaton of lung cancer based on histopathological characteristics and location of the tumor origins. Image was created with BioRender.com

1.2 Lung cancer heterogeneity

Lung cancer patients presenting in the clinic at an advanced stage have a very high mutational burden[4]. The most commonly identified mutations in lung cancer patients are *KRAS, EGFR, EML4-ALK, c-MET, AKT/PI3K* and their associated signaling pathways[5]. The diagnosis and treatment strategies for lung cancer are based on the genetic defects detected from a small biopsy specimen and are used to classify patients for appropriate treatment approach. It is important to note that this approach has significantly improved patient outcome relative to the conventional cytotoxic chemotherapies like cisplatin and carboplatin[6]. The identification of driver mutations in patients allowed the combination of chemotherapy with targeted agents which significantly improved the response rate and progression-free survival in lung cancer patients. However, these therapies are designed to target only a specific subset of mutations and eventually become ineffective[7] resulting in the recurrence of the disease[8]. This is the one of the greatest challenge faced by lung cancer patients and oncologists.

While precision medicine largely focuses on genetic and molecular profiling of tumor cells, identification of various biomarkers to predict disease progression does not necessarily translate into successful clinical outcomes. The complexity of tumors and the heterogeneity within is now a well-established concept. The term tumor heterogeneity broadly encompasses tumor cell heterogeneity (intratumoral heterogeneity ITH), tumor microenvironment heterogeneity (TME), and inter patient heterogeneity. Lung cancer is not just a composition of epithelial cancer cells with different mutations but an ecosystem consisting of phenotypically distinct tumor cells, surrounded by cellular and non-cellular components that are dynamically interacting and causing tumor evolution. One of the most outstanding examples of clinical application of this concept has been utilization of immunotherapy. The development and success of immune checkpoint inhibitors in many susceptible tumors has led to the approval of anti-PD1 drugs either as single agent or combination with chemotherapy

for first-line treatment for many lung cancer patients. However, only a small percentage of lung cancer patients respond upfront and eventually develop resistance[9-11]. To overcome the therapeutic plateau in lung cancer patients, an extensive understanding of the complexities of lung cancer heterogeneity is needed. In the following sections, we discuss the different sources of intratumor heterogeneity in lung cancer and the current clinical approaches in lung cancer. We also discuss the importance of studying lung cancer microenvironment as a source of heterogeneity and its implications for improving patient outcome.

1.2.1 Genetic Heterogeneity

Molecular characterization of lung cancer is primarily based on mutations in *EGFR, KRAS, p53, c-MET, EML4-ALK* and their associated signaling pathways[7] (Figure 3). However, lung cancer cells within a single tumor carry multiple mutations which contributes to genetic heterogeneity. For a long time, the single oncogene paradigm which identified the founder events, such as *KRAS* or *EGFR* mutations, determined the treatment strategy. However, ADC and SCCs are characterized by high mutational burden and co-occurrence of multiple genomic alterations may have important biological implications on tumor evolution. The significance of co-mutations mediating phenotypic diversity has recently challenged the single oncogene paradigm but the biological effects remain largely uncaptured[12].

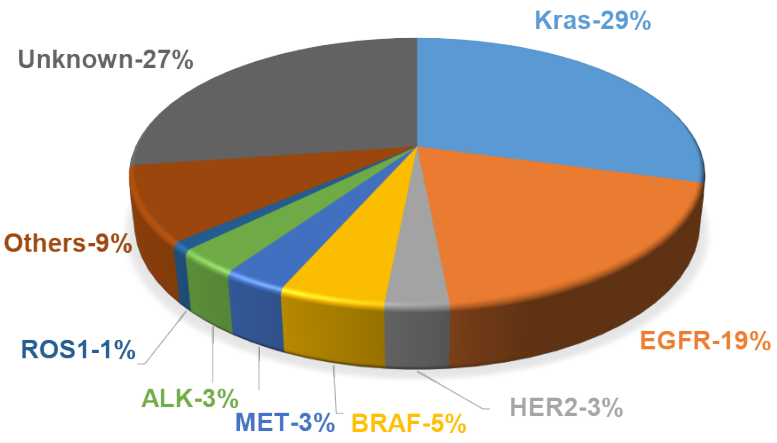

Figure 3. Oncogenic drivers in lung adenocarcinoma.
Mutations in different oncogenes contribute to genetic heterogeneity in lung cancer.

One of the models that attempts to explain ITH is the clonal evolution (CE) model which is primarily gene centric[13]. In the classical view of CE, a single initiating cell gains mutational hits which divides to form other tumor cells. As the tumor progresses, different groups of cells acquire different genetic aberrations. The different tumor subpopulations undergo Darwinian evolution through natural selection and the subpopulations with greatest cellular fitness, attributed to acquisition of genomic alterations, dominate over the others providing a growth advantage to the tumor. As more and more mutations accumulate in the cancer cells, the tumor adopts to a more aggressive form. Thus, the tumor is composed of heterogeneous populations of cancer cells with different genetic backgrounds with variable invasive and metastatic potential, and responses to therapy. In order to support the CE model and trace the of evolution of clones in cancer, advanced techniques like multiregional sequencing and genome wide exome sequencing have been applied to patient derived samples from different cancers, including lung cancer[14-16]. Multi-region whole exome sequencing of patient derived lung cancer samples suggested that lung cancer follows a branching evolution. A study led by deBruin et al. identified regionally separated driver mutations showing branched evolution with driver mutations arising before and after sub clonal diversification[15]. Another study by Zhang et al. suggested that single region sequencing may be sufficient to identify the gene mutations associated with lung cancers[16]. However, limitations with these studies were the small sample size [25 and 11 patients respectively]. As the sample size gets larger, the chances of detecting more molecular defects in the genome increase. Therefore, these studies do not represent the entire population of NSCLC patients or the entire tumor within a single patient. Although these studies have limitations, identification of oncogenes and tumor suppressors remained a focus of research and management of patients guiding personalized medicine[4]. It has beyond doubt improved patient outcomes when compared to generalized chemotherapy based treatments. The progress, however, has been limited to specific groups of patients like those carrying *EGFR, ALK, KRAS* mutations[17]. Availability of easier, cheaper

and faster genome sequencing for detection of mutations is one of the reason for focusing on genetic aspect of lung cancer for designing therapies.

The concept of co-mutations should also be kept in mind while understanding lung cancer progression, a noteworthy example is the co-occurrence of *KRAS* and *TP53* mutations in lung cancer[12]. The functional impact of such co-mutational burden on downstream signaling within lung cancer cells needs to be evaluated during therapeutic stratification of patients. Despite the presence of a large number of genetic alterations in a lung tumor, it is important to define which aberrations are functionally cooperative and biologically relevant. Many of the defects identified maybe presented as therapeutic challenges but may not always be translationally relevant. In addition, studies should account for the possible interactions that these genetic defects may cause between the different tumor subpopulations and the components of the tumor microenvironment (TME)[18]. It is challenging to incorporate for TME components at the time of diagnosis, but understanding tumor as a whole will provide better insight to its progression. Targeting only mutations identified in cancer cells eventually leads to failure of therapy because the tumor continues to evolve spatially and temporally under selective pressures.

1.2.2 Epigenetic Heterogeneity

Although epithelial cells in lung cancer acquire multiple genetic hits which largely influence the functional characteristics, there is still marked phenotypic plasticity between genetically identical cancer cells. It has been suggested that cells can exist in different phenotypic states which are regulated by intrinsic and extrinsic factors. Intrinsic factors include the fluctuations in gene expressions and other cellular processes, pre-existing differentiation states, genetic interactions between different mutations and epigenetic modifications. If these fluctuations cross a specific threshold, cells can cross over to a different phenotypic state[19]. Extrinsic factors include the dynamic interactions with the TME

which actively modulate the tumor progression. These alterations can be transient or permanent and can change cellular, molecular and epigenetic characteristics of cancer cells.

Epigenetic regulation of gene expression is well recognized for maintaining the normal cellular functions and homeostasis in the tissues. These are heritable changes in gene expression without any genetic changes in the DNA[20]. The epigenetic mechanisms include DNA methylation, histone modifications and non-coding RNAs like microRNAs. Alterations in these epigenetic mechanisms can lead to a dysregulation in the homeostasis of the normal cellular state which leads to variations in the phenotype of the cancer cell while maintaining the same genetic background. Accumulation of epigenetic alterations overtime has been associated with progression from pre-neoplastic to neoplastic stage[21].

Alterations in DNA methylation status have been identified in lung cancer. Promoter regions of the tumor suppressor genes are more frequently hypermethylated in lung cancer, and these genes are involved in some crucial cellular functions like proliferation, apoptosis, adhesion, motility, cell cycle and DNA repair. Genes most commonly found hypermethylated in lung cancer are: *p16INK4a, RASSF1A, APC, RARβ, CDH1, CDH13, DAPK, FHIT* and *MGMT*[22] which correlates with poor patient outcome. Analysis of patient samples in clinical studies represents a snapshot of the methylation status in the tumor and in a specific region of the tumor. Genome wide hypomethylation also occurs in lung cancers which leads to an oncogenic activation. This generally occurs in later stages in tumor progression. However, gene specific hypomethylation is found in *MAGEA, TKTL1, BORIS, DDR1, TMSB10, TP73, ZNF711, G6PD AMD 14-3-3σ*[22]. Histone modifications occur in concert with DNA methylation and are responsible for regulation of chromatin conformation and gene expression. Modifications occur at the histone tails which include acetylation, deacetylation, methylation, phosphorylation and ubiquitylation. There are different enzymes catalyzing these reactions (readers, writers and erasers) and the most common are Histone acetyl transferases (HATs) and Histone deacetylases (HDACs). Generally, HDACs are overexpressed in lung cancers and thus cause transcriptional silencing of tumor suppressor genes. Lower cellular levels of

histone modifications are associated with poorer clinical outcomes[23]. MicroRNAs are small non coding RNAs (~22 nucleotides) that bind to the 3' untranslated regions of messenger RNA (mRNA), causing degradation of the mRNA or inhibition of protein translation resulting in decreased gene expression. Numerous microRNAs are frequently dysregulated in lung cancer at different stages of the disease[24] A single microRNA can have multiple target genes and a single gene can be targeted by many microRNAs. This can lead to heterogeneity in the tissue as the regulation depends on the temporal and spatial characteristics of the tumor.

Epigenetic studies have mainly focused on identifying the dysregulations associated with lung cancer in the clinic primarily for biomarker development. However, similar to the large scale studies for identifying new mutations in lung cancer, only correlative studies for epigenetic alterations may not be the best approach. Firstly, these epigenetic alterations occur commonly in many cancers and it is difficult to establish exclusivity. Secondly, there is limited data on epigenetics from normal lung for comparison. Thirdly, no single alteration will capture all the tumors on account of heterogeneity in lung cancers and since epigenetic marks are dynamic in nature, they are context dependent.

Epigenetic alterations are also believed to maintain a small subpopulation of cells known as cancer stem cells (CSCs)[25]. The cancer stem cell model posits that cancers are maintained by a small subpopulation of cells that have stem cell like properties similar to stem cells that populate the normal tissues. These CSCs have almost unlimited proliferative capacity and differentiate into cells of different lineages giving rise to a hierarchical organization in the tumor[26,27]. The descendant cells have limited proliferative capacity and form the bulk of the tumor. Since they are of different lineages, they contribute to the heterogeneity in the tumor. These cancer stem cells are believed to promote tumor progression and metastasis and have inherent resistance to therapies. CSCs have been reported to exist in lung cancer and associated markers include CD133, CD44, expression and/or activity of the cytoplasmic enzyme aldehyde dehydrogenase ALDH and presence of cells known as side populations. Embryonic stem cell pathways such as Hedgehog, Notch

and WNT have also been reported to be altered in lung cancer[28]. However, lack of sensitivity and specificity of these markers and substantial experimental evidence stems the controversy of significance of CSCs.

The impact of selection forces on different phenotypes within heterogeneous tumors is reflected in terms of drug resistance as well as metastatic potential of cancer cells. It is challenging to account for these non-genetic traits in clinical practice, especially because the phenotypes can be highly plastic. Stochastic nature of biochemical processes within cancer cells can also affect the phenotype, for example variable gene expression in response to external modifications. However, greater efforts are being made to incorporate tumor cell heterogeneity in clinical decision making and understanding lung cancer biology at a fundamental level.

1.2.3 Microenvironmental heterogeneity

Tumors are complex ecosystems surrounded by a microenvironment consisting of immune cells, fibroblasts, endothelial cells, extracellular matrix, chemokines and cytokines. They are continuously evolving which results in a heterogeneous mix of phenotypically different cells. Spatial and temporal variability of the tumor microenvironment (TME) with respect to the tumor also plays a role in heterogeneity. At a given time, each part of a tumor is exposed to different components of the TME. Thus, there may be additional stable phenotypic states of cancer cells which may not have been present in the normal tissue contributing to intra tumor heterogeneity. The bidirectional interaction between the cancer cells and TME can either promote or inhibit tumorigenesis[18]. The abnormal stroma surrounding the cancer cells can induce stress responses and genomic instability[29], epithelial to mesenchymal transition[30], cause vascular mimicry[31] and promote tumorigenesis through tissue reorganization[32]. Some correlative clinical studies, in vitro and animal studies have demonstrated the significance of studying stroma and its association with lung cancer prognosis. However, most of these studies have limitations like studying a single component

or a unidirectional effect. Here, we briefly iterate what is known about the tumor microenvironment in lung cancer.

Extracellular matrix (ECM) was considered just a supportive framework for tumors for a long time. However, it plays a more dynamic role in modulating the process of tumor progression[33]. ECM is composed of large variety of proteins, glycoproteins, proteoglycans, and polysaccharides[34]. It maintains tissue architecture and function through dynamic bidirectional interactions[35] and disruption in this interaction can cause tumor formation and progression. On the other hand, it has also been demonstrated that altering the matrix components in a manner that mimics non-malignant tissue can revert the malignant phenotype in cancer cells[36]. Normal lung tissue is characterized by limited ECM components as well as low stiffness. Laminin and collagen IV are the predominant ECM proteins in non-malignant lung tissue alongwith lower amounts of other collagens, elastin and glycosaminoglycans[37]. However, progression from non-malignant to premalignant and malignant lesions is characterized by dysplastic reaction which is associated with accumulation of and alteration in the ECM proteins[38]. One such example is an increased deposition of collagen I in the extracellular matrix that is highly cross-linked leading to greater linearity and organization which aids in invasion and metastasis of cancer cells[39]. In SCLC, ECM proteins have been shown to protect against apoptosis, enhance tumorigenesis, and confer chemoresistance through beta-1 integrin mediated tyrosine kinases activation[40]. Thomas et al. showed that there was a positive correlation between the expression of metalloproteinases and metastasis in NSCLC[41]. SPARC/osteonectin synthesized by tumor stroma showed a strong association with intratumor hypoxia and acidity indicating a link between cellular metabolism and induction of supportive stroma that favors cancer cell migrations and invasion, leading to poor prognosis[42]. Integrin mediated adhesive interactions with ECM have been implicated in cancer progression and invasion[43]. ECM protein interactions with intergrins on cell surface can also modulate the phenotypic characteristics of the tumor cells by activating outside-in signaling and modulating the levels of microRNA-

200. In turn, microRNA-200 family members can modulate the inside-out signaling that alters ECM components in lung cancer. These signaling pathways allow the dynamic switch of cellular phenotype between metastasis-prone and metastasis-incompetent[39,44,45].

Fibroblasts are one of the principal cellular component of the TME and have a significant role in deposition of ECM[46]. Activated fibroblasts are found in cancers and are known as cancer associated fibroblasts (CAFs). Responses of fibroblasts to activation include proliferation, fibrinogenesis, and release of cytokine and proteolytic enzymes. Activated fibroblasts in CAFs are characterized as alpha-smooth muscle actin-positive myofibroblasts and actin-negative fibroblasts, both of which are competent to support tumor growth and progression[47]. Role of CAFs have been studied in lung cancers only recently[48,49,50,51,52]. Although CAFs are mostly considered pro-tumorigenic, there is some evidence indicating their anti-tumor effects. CAFs were shown to impart resistance to EGFR tyrosine kinase inhibitors through HGF production[49], but a recent study suggested that there is an increased autophagy in lung cancer cells in response to erlotinib treatment when co-cultured with CAFs through an increased production of IL-6 an IL-8 [48]. Other groups suggest the supportive role of CAFs by demonstrating enhanced motility of NSCLC cells[51], increased expression of MMP-2 on CAFs with a cross-talk between CAFs and ECM, correlation of poor prognosis with increased CAFs[50] and increased plasticity of cancer cells in presence of CAFs[52]. A recent study in lung cancer demonstrated CAFs can also exhibit phenotypic heterogeneity that is determined by tumor cell interactions[53], further underscoring the bi-directional heterotypic interactions.

The microenvironment in lung cancer is rich in resident and circulating immune cells. Clinical correlative studies have shown that infiltrating immune cells can determine the prognosis of lung cancer. Using human lung tumor xenografts, it has been shown that inflammatory cells, tumor infiltrating lymphocytes (TILs), within the stroma are functional and can suppress tumor growth through exogenous cytokines like IL-12[54]. Increased infiltration and invasion of macrophage and mast cells[55], dendritic cells[56] and lymphocytes[57,58] within the

tumor have been shown to correlate with better clinical outcome suggesting that stromal immune component may have an anti-tumor effect in NSCLC. Additionally, using mouse models of lung cancer, a specific gene expression signature was identified in the tumor associated macrophages suggesting that tumor cells affect the immune cells as much as the other way around and could be potentially used as surrogate tissue for patient stratification and predicting clinical outcome[59]. Recent data suggests that there is a heterogeneity in immune cell infiltrates between primary and metastatic sites in lung cancer[60]. CD4+ and CD8+ T cells were compared within tumor cell islets and stromal compartment by immunohistochemistry which showed that there were fewer immune cells in the tumor cell clusters. Majority of the immune cells were found in the stromal compartment of the tumor tissue. This was also true for metastatic lesions of the corresponding primary tumor. In addition, the metastatic lesions generally had significantly lower CD8+ T cells compared to the primary tumors. The differential pattern of immune cell infiltration in primary and metastatic tumor suggests a weakened immune response at the distant metastatic sites.

In response to the structural changes, many metabolic alterations also occur during lung cancer progression such as release of cytokines, chemokines, growth factors, differential alterations in vasculature and hypoxia. The cross talk between stromal and cancer cells potentially occurs through soluble factors like cytokines and chemokines secreted by them. Many such factors have been identified in lung cancer. One of the earliest chemokines identified in lung cancer was SDF-1/CXCL12-CXC4 axis, which appeared to regulate metastasis[61]. Many others have shown that multiple paracrine signaling occurs in lung cancer, in order to create a more suitable microenvironment for tumor progression. CXCR4 and CCR7 have been implicated in metastasis, IL-7R provides signals to lymphocytes and is associated with shorter survival in lung cancer patients[62]. Hepatocyte derived growth factor (HGF) from fibroblasts induces chemotherapeutic resistance to EGFR receptor tyrosine kinase inhibitors[49]. Tumor sub-clones in SCLC communicate via fibroblast derived growth factor (Fgf-2) in order to promote metastasis[63]. Secreted factors from stromal component affect

tumorigenesis and alter tumor cell secretome[64]. This suggests that there is an active exchange between cancer cells and stromal components which modify one another contributing to ITH.

Rapidly dividing tumor cells and the recruitment of heterotypic cells supporting tumor growth can cause a strain on the oxygen supply in the tumor microenvironment. Hypoxia-driven gene and protein changes can further enhance tumorigenesis by regulating other aspects of the stroma like ECM remodeling, EMT, promoting angiogenesis and imparting resistance to therapy[65]. However, evidence from another study suggests that hypoxic TME could also be anti-tumorigenic[66]. In an attempt to map the heterogeneity in the hypoxic TME, Cui et al. injected nude mice with lung cancer cell subcutaneously and injected 18F-fluoromisonidazole and hypoxia marker pimonidazole hydrochloride intravenously. Series of PET scans, autoradiography and microscopy helped in the visualization of heterogeneity in hypoxic microenvironment. The study also suggested that cancer cells had shorter life span in a hypoxic in vivo environment, which is in contradiction to what is observed in vitro. Nevertheless, this study suggested that the cancer cells are spatially and temporally exposed to differential levels of oxygen which could alter their phenotypic characteristics thus contributing to ITH. Figure 4 summarizes the different sources of tumor heterogeneity within lung cancer.

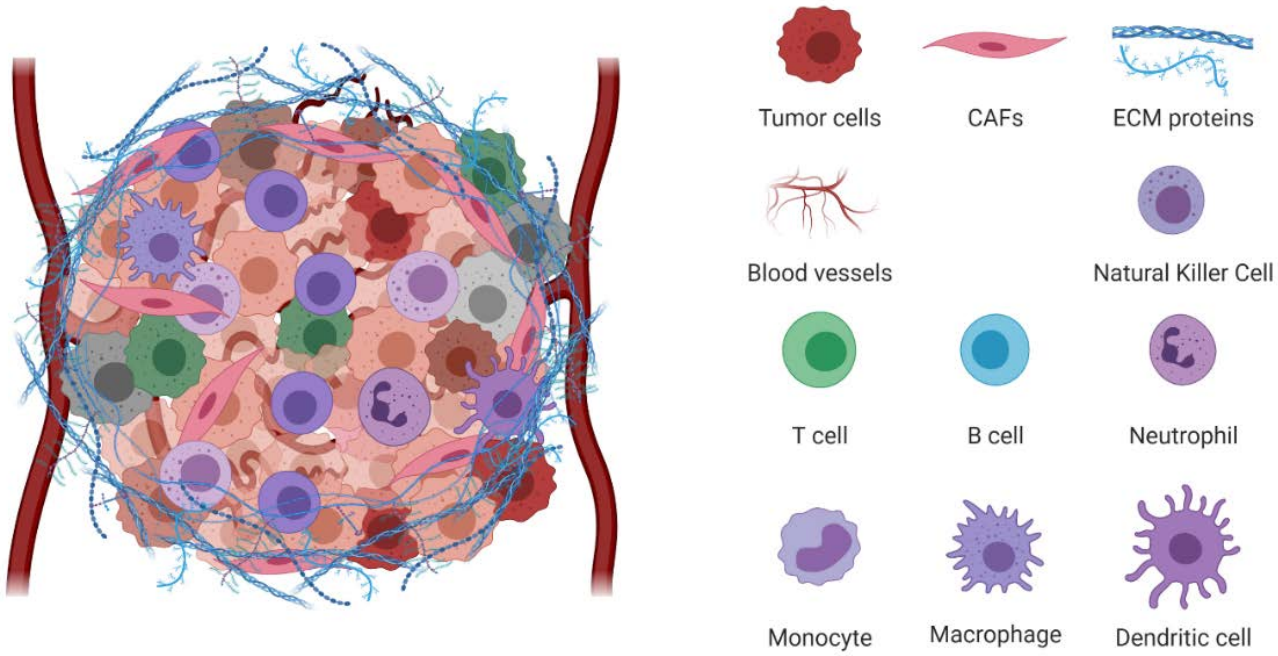

Figure 4. Origins of heterogeneity within lung cancer.
Cell-intrinsic and cell-extrinsic factors contribute to tumor heterogeneity in lung cancer. Cell-to-cell variability in genetic and phenotypic characterisitcs cause tumor cell heterogeneity. Stromal components including extracellular matrix (ECM), immune cells, cancer associated fibroblasts (CAFs) and vascular supply are extrinsic factors that affect tumour cell heterogeneity and function. Multiple sources of heterogeneity within a tumor may co-exist and interact with each other overtime to shape up the heterogeneous cancer. Figure created with BioRender.com

1.2.4 Clinical significance of tumor heterogeneity

With technological advances in personalized medicine, great strides have been achieved in the outcome of lung cancer patients. Personalized medicine targeting specific mutations is a main treatment strategy adopted in the clinic. However, lung cancer heterogeneity plays an important role in the development of drug resistance. Thus, understanding the biology of lung cancer progression in context of heterogeneity due to both genetic and non-genetic factors is essential to improve therapeutic strategies. This knowledge would help revisit the approach of lung cancer diagnosis and classification with a treatment strategy that would take into account the complexity of tumors.

Resistance to small molecule inhibitors is frequently attributed to accumulation of additional mutations or activation of a bypass pathway. One of the most successful targeted therapies in lung cancer is the use of EGFR tyrosine kinase inhibitors which include gefitinib and erlotinib. However, about 50% of the patients treated with EGFR inhibitors acquire T790M mutations[67] [68]. These patients are responsive to osimertinib, and as a first-line therapy the drug is able to prevent emergence of resistance due to T790M mutation[69]. MET and ERBB2 amplification have been reported to cause primary resistance to third-generation EGFR inhibitors, including osimertinib[70]. This is a key example of presence of co-mutations driving genetic heterogeneity in tumors ultimately leading to therapeutic resistance. It is vital to determine whether such co-mutations present are secondary drivers or merely passenger mutations. Molecular subtype of lung cancer is driven by ALK fusion accounts for a small percentage of patients, of which ~60% respond to targeted inhibitors such as crizotinib, ceritinib, alectinib, and brigatinib. These tumors also demonstrate abundant genomic heterogeneity which may account for differences in treatment response with targeted ALK inhibitors[71]. Many clinical trials have explored novel drugs for different driver mutations by restricting to specific molecular subtypes[72]. Large scale screening studies are also being conducted to identify novel drivers of lung cancer progression, metastasis and therapeutic

resistance[4]. This approach certainly provides a detailed insight into the molecular mechanisms in lung cancer. Nevertheless, both cell-intrinsic and cell-extrinsic factors should be evaluate in the consideration for improvement of clinical outcome.

Targeting phenotypically distinct subpopulations by identifying therapeutic vulnerabilities allows for a robust control of tumor growth and this concept has been extensively applied in KRAS mutation driven lung cancers. Due to undruggable nature of KRAS oncoproteins, downstream effector pathways are targeted, which include MAPK pathway members[73]. Despite the availability of specific drugs targeting these pathways, clinical efficacy has remained poor as single agent or in combination with chemotherapy [74,75]. The underlying explanation is due to the presence of profound tumor heterogeneity. Cancer subpopulations with pre-existing resistance or emergence of acquired resistance to drugs eventually leads to the failure of therapy in the clinic[76].

Components of TME, especially CAFs and immune cells, also impart resistance to therapy by modulating cancer cell characteristics[77]. Cancer cells escape detection by the host immune system and in order to elicit a response, cancer drugs are usually designed to eradicate the cancer cells. In recent years, the importance of engaging the host immune system in cancer treatment has been recognized. Lung cancer cells escape immune detection many mechanisms. There can be decreased tumor antigen presentation, recruitment of tumor suppressor cells, and engagement of checkpoint pathway inhibiting antitumor immunity[78]. The checkpoint pathways include cytotoxic T-lymphocytes antigen-4 (CTLA-4) and programmed death receptor-1 (PD-1). Efforts are directed to block these pathways in order to elicit an immune response against the tumor cells. Anti-CTLA-4 include ipilimumab which has shown efficacy in melanoma[79] [Phan 2003], is currently in clinical trials for lung cancer[80]. Anti-PD-1 agent nivolumab improved the overall survival in lung cancer patients after platinum based chemotherapy when compared to docetaxel[81]. Adoptive cell therapy is also being investigated where immune cells are isolated from peripheral blood

followed by ex vivo expansion of tumor suppressor cells and autologous administration in the host[82]. Significance of immunotherapy lies in the fact that it is effective regardless of any heterogeneity between the tumor cells. In addition, combining chemotherapy (paclitaxel) with immunotherapy (ipilimumab), targeted therapy (EGFR inhibitors) with immunotherapy (ipilimumab) and different checkpoint inhibitors (anti CTLA-4 and anti PD-1) has proven extremely effective and in fact are standard of care in NSCLC[83]. Although CAFs and ECM seem attractive targets for therapy to prevent tumor progression, due to limited preclinical, effective targeting has not been achieved. Therapies targeting vascular endothelial growth factor (VEGF) like bevacizumab, in combination with chemotherapy have been shown to have some benefit over chemotherapy alone[84]. However, due to heterogeneity in vasculature around the tumor tissue, the response to these agents is limited and not very consistent. Instead, the idea of reverting blood supply to normal conditions is being explored which can improve drug delivery and reduce TME heterogeneity[85].

These examples underscore the importance of understanding and targeting tumor heterogeneity for sustained benefit. Many unanswered questions that are worth exploring include: whether genetically different subsets of lung cancer have their own unique microenvironment and regulation, how does the targeted therapy affect the microenvironment and how does it influence the progression of the disease, how is the microenvironment different between primary, metastatic and recurrent tumor. To effectively understand these roles in context of all compartments of the TME, better modelling of the human disease is important. It can be achieved by using existing *in vitro* (primary cell cultures, co-cultures, 3-D systems) techniques and animal models (genetically engineered mouse models (GEMMs), syngeneic, xenografts, patient derived xenografts) in combination with clinical studies to boost the translation of experimental findings to the clinic. Efforts in the clinic must also be directed towards improving non-invasive imaging and diagnostic techniques to represent the heterogeneity in stroma for targeting the stroma in addition to the cancer cells. There are

limitations in all the models, but effectively combining these can closely recapitulate the human disease for understanding the biology and improving patient outcome.

1.3 Models to study heterogeneity

Despite extensive research efforts and advancements in the understanding of lung cancer progression, tumor growth control is only short-term and achieving complete/long-lasting cures from current therapies seems unattainable. Strategies to prevent metastatic disease and therapeutically target mutant KRAS-driven cancers have been limited by many factors, including the significant heterogeneity of tumors. Many unanswered questions that are worth exploring include: whether genetically different subsets of lung cancer have their own unique microenvironment and regulation, how does the targeted therapy affect the microenvironment and how does it influence the progression of the disease, how is the microenvironment different between primary, metastatic and recurrent tumor. The modest translation of the extensive experimental research into clinical outcome begs the question if current decision-making approaches are accounting for all aspects contributing to tumor progression. Due to the paucity of suitable experimental models that reproduce ITH observed in human tumors, there has been a disparity between efficacy observed in pre-clinical models and the actual translatability into patient response. An untapped therapeutic potential of the other components of lung tumors needs to be exploited. Nuanced observations and evolving understanding of the effect of tumor subpopulations adopting distinct cellular states, extracellular matrix modulating the response to therapy, cancer-associated fibroblasts aiding in metastatic process and vascular compartment affecting drug delivery are moving to the forefront and have drastic implications on the sensitivity to therapies. To effectively understand these roles in the context of all compartments of the TME, better modelling of the human disease is important. It can be achieved by using existing *in vitro* (primary cell cultures, co-cultures, 3D systems) techniques and animal models (genetically engineered mouse models (GEMMs), syngeneic, xenografts, patient derived xenografts) in combination with clinical studies to boost the translation of experimental findings to the clinic. Efforts in the

clinic must also be directed towards improving non-invasive imaging and diagnostic techniques to represent the heterogeneity in stroma for targeting the stroma in addition to the cancer cells. There are limitations in all the models, but effectively combining these can closely recapitulate the human disease for understanding the biology and improving patient outcome.

1.3.1 Three dimensional models

Artificially-created environment in which cancer cells are permitted to grow and interact with their surroundings in all three dimensions serve to bridge the gap between the uses of whole animals at one end of the spectrum, with cellular monolayers at the other. 3D spheroids more closely resemble *in vivo* tissue in terms of cellular communications and the development of extracellular matrices[86,87]. When normal human bronchial epithelial cells are grown in 2D cultures, they proliferate until they form a confluent monolayer, but in 3D Matrigel cultures, they differentiate into a characteristic lumen-containing glandular structure, termed an acinus representing *in vivo* characteristics[88]. 3D cultures can therefore be used to study tumor morphology and understand the differences between cell lines from tumors of similar and dissimilar organs and tissues. However, a limitation of monocellular 3D cultures derived from cancer cells cultured in petri dishes is that long term exposure to 2D culture causes alterations in the response of cancer cells to any external stimuli. Primary tumors that are isolated and cultured without prior adaption to 2D growth could provide better insights into the interactions occurring in a 3D space that can have effects on gene expression and cell behavior. With the ability to mimic *in vivo* phenotype, early steps in tumorigenesis can be captured and studied with tumors that harvested and grown in appropriate 3D environment.

Microenvironment components play a significant role in cancer progression and 3D cultures provide an advantage to introduce heterotypic cells and different matrices which captures microenvironment heterogeneity. Selection pressure from TME components on cancer cells can affect the cellular phenotype and gene expression which can be studied in

a high throughput manner and in real-time which is difficult in animal models. Additionally, introduction of controlled modifications in the microenvironment components can allow the study of response of cancer cells to specific alterations in those components. For example, ECM-tumor cell interactions and matrix-dependent signaling that occurs in early tumor progression are not completely understood. Understanding the signaling pathways activated in response to ECM and disrupting these interactions early-on in tumor evolution will prevent the emergence of metastatic subpopulations and aggressive disease.

3D cancer models are gaining increased traction in the field of drug discovery and development as well. Although 2D cultures continue to be the *de facto* platform used for pharmaceutical studies, the cells often adopt physiologically irrelevant phenotype and signaling patterns due to the lack of appropriate external cues. While cell lines provide us with excellent homogenous study material that have significantly contributed to drug discovery, 3D models allow for more accurate representation of both the phenotype of cells as well as provide more realistic drug response by preserving tumor heterogeneity and thereby are more suitable for predicting outcomes to therapeutic agents[89].

1.3.2 Mouse models

Genetically engineered mouse models (GEMMs) have enabled numerous studies that would not be possible solely with patients' samples or cancer cell lines, especially testing of targeted therapies in immunocompetent models. KRAS driven lung cancer mouse models have given great insights into progression from early to late tumorigenesis as well as combining with different oncogenes or tumor suppressors to elucidate biological relevance of specific oncogenes and tumor suppressors in tumor development. Limitation of these models arises due to lack of genetic complexity as they are driven by limited number of mutations, unlike human cancers. Due to the exposure to environmental carcinogens as well as other physiological factors in patients, tumors express high mutational burden which has impact on tumor evolution. Although mouse models do not necessarily provide this information, they are

highly reproducible and allow for more extensive analysis of tumor tissues over a period of time which is very difficult in patients[90]. Next generation GEMMs represent conditional mouse models that are genetically engineered to accurately mimic sporadic human cancer are now being utilized to more accurately mimic human cancers, including heterogeneity[91,92].

About 30% of lung adenocarcinoma patients present with KRAS mutations usually with accompanying co-mutations like p53 which confers metastatic ability to cancer cells. Over a decade ago, our group generated a mouse model driven by *Kras*^{G12D}/*p53*^{R172H} mutation which develops spontaneous lung cancer and closely recapitulates the features of patients with metastasis prone lung adenocarcinoma[93]. This model has served greatly in understanding key aspects of Kras mutant lung cancer biology, including metastasis and tumor heterogeneity. Using this model, a panel of lung adenocarcinoma cell lines was derived from primary and metastatic sties. Cell lines were named according to the mouse number and site of derivation. Extensive characterization of these cell lines, both *in vitro* and *in vivo*, broadly classified them into 2 groups, metastasis competent, mesenchymal cancer cells and metastasis incompetent epithelial cancer cells. The genetic abnormalities that were detected in these cells were reminiscent of those seen in human lung adenocarcinoma. Thus, this model serves as an excellent starting point to study tumor heterogeneity in lung cancer that is relevant to the human disease. In addition to the spontaneous *Kras*^{G12D}/*p53*^{R172H} cancer model, we also utilize autochthonous models that are generated by administration of adenovirus expressing Cre recombinase. *Kras*^{G12D} mutation is coupled with either p53 homozygous deletion, homozygous mutation or heterozygous deletion and mutation. These models have many advantages as mentioned above. They are genetically more complex, demonstrate heterogeneity and can be controlled temporally. The models are described in further detail in Chapter 5 (5.2.7)

1.4 EMT in lung cancer and therapeutic resistance

The epithelial-to-mesenchymal transition (EMT) contributes to the progression of cancer by promoting loss of cell–cell adhesion, leading to a shift in cytoskeletal dynamics.

Hallmarks of EMT include the loss of stable cell junctions, apico-basal polarity and E-cadherin expression and concomitant increase of mesenchymal characteristics such as increased migratory ability, matrix degradation, and upregulation of markers such as N-cadherin and ZEB1[94] (Figure 5). Tumors with a mesenchymal phenotype are associated with aggressive disease and poor prognosis[95]. In addition to metastatic disease, EMT has also been implicated for development of resistance to chemotherapy, radiation and targeted therapies[96-101]. Transcription factor ZEB1 is central to promoting a mesenchymal phenotype in cancer cells. ZEB1 represses the transcription of key epithelial genes, including E-cadherin and miR-200. ZEB1 expression in patient samples is also associated with poor patient prognosis[99]. More details can be found in Chapter 4.

It is now widely accepted that tumor cells are not locked in one or the other EMT states, rather are fluctuating between these cellular phenotypes. Within a heterogeneous tumor, at any given time, there are distinct tumor subpopulations that display characteristics on the EMT spectrum. As such, when a single drug is administered, a pre-existing resistant subpopulation emerges as well as previously sensitive cancer cells acquire resistant to the targeted therapy. To achieve robust response, all the subsets of cancer cells need to be efficiently targeted to prevent outgrowth. In order to do that, we need to understand the survival dependencies of the epithelial and mesenchymal tumor subpopulations and mechanistic pathways that drive intrinsic and acquired resistance.

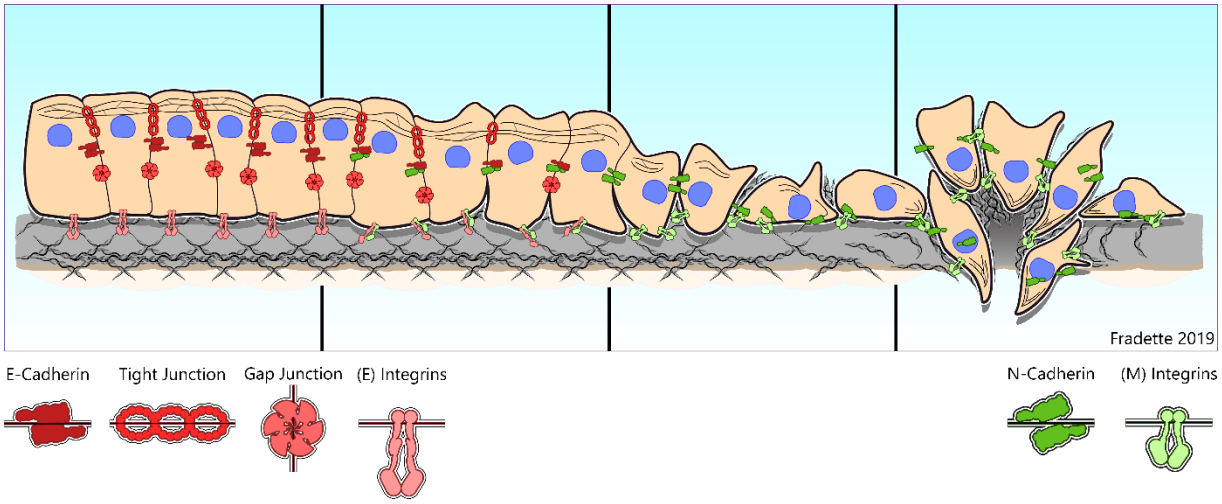

Figure 5. Epithelial to Mesenchymal Transition (EMT).
Schematic illustration of cancer cells undergoing shift in phenotypic states from epitheilal on one end of the spectrum to mesenchymal on the other end with partial or hybrid states in the middle. Epithelial cancer cells are characterized by tight junctions and apico-basal polarity. Mesenchymal cancer cells are characterized by increased matrix degradation and ability to invade and metastasize.
Illustration used with permission from Jared Fradette.

1.5 Dissertation objectives

The objectives of the project were two-fold: developing cancer models to effectively recapitulate tumor heterogeneity in lung cancer and leverage multiple strategies to identify therapeutic vulnerabilities of distinct tumor cell subpopulations for enhanced control of lung cancer progression. Chapter 3 and 4 describe the establishment and characterization of an *Ex Vivo* Tumor model with incorporation of sensor cells that detect dynamic changes in EMT status of cancer cells. We demonstrate the significance of utilizing these models for identifying novel biological process in lung cancer and as a high throughput screening tool.

Chapter 5 identifies CDK4 as a major survival dependency in Kras mutant mesenchymal lung cancer cells. Targeting CDK4 and MAPK pathways with clinically approved pharmacological inhibitors showed a robust tumor growth control as well as prevented emergence of resistance to either single agent. We also describe the mechanistic basis of the increased dependency on CDK4 which occurs through dysregulated ZEB1-p21-CDK4 axis. Correlation of ZEB1 and p21 in murine and human lung cancer tissue provides evidence for incorporating these as biomarkers to determine sensitivity to CDK4 inhibitors.

Chapter 2: Materials and Methods

2.1 Murine lung cancer cell lines and syngeneic mouse model.

All animal experiments were reviewed and approved by the Institutional Animal Care and Use Committee at The University of Texas M.D. Anderson Cancer Center performed in accordance to their guidelines. All mice used in the studies were immunocompetent and assessed for health daily by the Department of Veterinary Medicine and Surgery (DVMS). All mice were genotyped to determine the mutational status by tail snips 2 weeks after birth. Primary and metastatic murine lung cancer cell lines previously derived from spontaneous Kras/p53 GEMMs[93] were cultured in RPMI 1640 with 10% FBS. 344SQ cell lines are metastatic *in vivo* upon subcutaneous implantation. Wild-type 129/SV mice from our colony (males and females) of at least 8 week of age were used for the syngeneic tumor experiments. Subcutaneous injections of 1 million cells in single-cell suspension were placed in the posterior flank in 100 µL of media. Animals were monitored regularly and euthanized when they exhibited signs of morbidity or when size of the subcutaneous tumor required sacrifice (5–6 weeks). For intratracheal implantation of tumor cells, mice were anesthetized via intra-peritoneal injection of room temperature 20 mg/ml avertin and intubated as previously described[102]. $2.5x10^4$ cells in single-cell suspension of 50 µL of media were delivered through trachea and were allowed to grow for three weeks before harvesting. The animals received intraperitoneal injections 5 days/week with DMSO or dasatinib (purchased from Selleckchem) at a dose of 10 or 20 mg/kg in 50µl. Mice were examined for metastasis and tissues for the subcutaneous tumor, lungs and any organs with visible metastasis were collected. The results are represented as mean ± standard deviation and student's t-test was performed for statistical significance.

For *in vivo* tumor growth assays with transplantation of mouse lung cancer cell lines, male and female wild-type 129/Sv mice ages 3 months and up were used. Cells were implanted subcutaneously into the right flanks of 129/Sv mice and allowed to form tumors for

2 to 3 weeks, at which point tumor volumes were approximately 150 to 200 mm^3 measured using digital calipers. For conditional mouse models of lung adenocarcinoma (*Kras*$^{LSL/+}$, *Kras*$^{LSL/+}$*p53*$^{flox/flox}$ and *Kras*$^{LSL/+}$*miR-200c*$^{-/-}$) (previously describes in ref.[103]), adenovirus-expressing Cre recombinase was administered into mouse lungs at 3 months of age by intratracheal intubation at a viral titer of $2.5x10^7$ viruses per mouse. Mice were housed specifically in suites designated for biohazard handling as approved under the IACUC protocol. Two weeks post-infection, mice were returned to the regular housing suite. At 3 months post-induction, mouse lungs were visualized by micro-CT scans to confirm tumor formation and measure tumor areas. For drug treatment experiments, mice were randomized to either treatment or vehicle control groups AZD6244 (Selleckchem) and palbociclib (MedChemExpress) were administered daily by oral gavage at a dosage of 25 mg/kg mouse weight and 50 mg/kg mouse weight, respectively. Tumor sizes were measured weekly after treatment began. AZD6244 was dissolved at 5 mg/mL in solvent (4% DMSO, 30% PEG 300, 5% Tween 80), and palbociclib was dissolved at 10 mg/mL in solvent (Lactic acid buffer (50 mM, pH 4.0)). Control mice received solvent at a volume equal to the drug dosage at the indicated drug concentrations. Mouse weights were measured weekly to adjust total dosage and assess the effects of drug combinations on mouse health. After euthanasia by CO_2 exposure at 3 L/min, syngeneic primary tumors and/or mouse lungs were formalin-fixed, paraffin-embedded, and sectioned for histological analysis.

In vivo combination synergy analysis was done using the method of Bliss Independence as previously described [104]. A primary analysis day was specified for each study, usually at or near the last day of treatment. On that day, the expected additive response (EAR) tumor volume for the combination group was defined, per the Bliss method, as $EAR=(V_1*V_2)/V_C$, where V_1 and V_2 are the mean tumor volumes in the single-agent groups, and V_C is the mean volume in the control group. Next, the control group tumor volume change from baseline was defined as $\Delta V=V_C-V_0$. Then an additive range around the EAR was defined, via upper and lower limits, as EAR_U = min(2*EAR, EAR + 0.15*dV) and

EAR_L=max(*EAR*/2,*EAR*-0.15*dV). If the observed mean combination volume on that day was larger than the mean volume of either single agent, the combination was called antagonistic. If it was smaller than that but larger than EAR_U, the combination was called less than additive. If it was between EAR_U and EAR_L, then the combination was called additive; otherwise, the combination was called synergistic.

2.2 *Ex Vivo* Tumors: isolation, processing and 3D assays

Primary subcutaneous and orthotopic lung tumors were isolated and collected in PBS-10% FBS solution at 6 weeks after implantation. Tumor tissues were initially subjected to mechanical breakdown by mincing the tumors with scalpel followed by chemical digestion in 10 ml of 0.2% Collagenase A (Sigma Aldrich 10103578001), 0.2% trypsin (Gibco 27250018), 0.5% FBS in RPMI for one hour at 37^0C. Tissue suspension was further broken down in a gentleMACS™ dissociator using the lowest setting to yield multicellular tumor aggregates. The solution was centrifuged at 1500 rpm for 10 min to remove Collagenase/trypsin from the solution and incubated with DNAase (2U/µL) for 5 minutes at room temperature. Three rounds of differential centrifugation were performed to remove any single cell from the EVTs. EVTs were cryopreserved in 90% FBS-10% DMSO solution for future use.

The processed EVTs were cultured for one day in poly(dimethylsiloxane) (PDMS) microwell inserts designed for standard tissue culture plates[105,6]. The microwells within each insert are ~100 µm in diameter allowing exclusion of aggregates greater than 100 µm and yielding EVTs of uniform size. EVTs harvested from microwells were embedded in 100 µL of Matrigel (BD 356231), plated on 8-well chamber slides pre-coated with 25 µL of Matrigel and incubated at 37^0C for 30 minutes. The cultures were supplemented with media containing RPMI 1640, 10% FBS, 2% Matrigel and 1% Penicillin-Streptomycin. Invasive potential of EVTs was tested in response to Transforming Growth Factor β (TGFβ) (CST # 8915LC) in the media and rat tail Collagen I (BD 354249) in the matrix. TGFβ at 5ng/ml was added to the

media and replenished every 48 hrs. EVTs were scored as invasion-positive in response to TGFβ if one or more protrusive structures were present. EVTs were embedded in Matrigel/Collagen mixture, plated on 8-well chamber slides pre-coated with 25 µL of Collagen mix at the indicated concentration, incubated at 37^0C for 45 minutes to allow polymerization of Collagen and then supplemented with RPMI 1640 containing 10% FBS, 2% Matrigel and 1% Penicillin-Streptomycin. The structure sizes and invasion were scored at the end of the experiment, with structures counted invasion-positive in Matrigel/Collagen mixture if one or more protrusions were present. Cell viability of EVTs was measured using Cell Titer-Glo (Promega) following manufacturer recommendations. Luminescence intensity was measured with a Synergy HT microplate reader (BioTek) and normalized to intensities of controls. Spheres were imaged using an inverted microscope. Adobe Photoshop software (RRID:SCR_014199) was used for RFP and GFP pixel analysis by histogram analysis of green and red pixels as a percentage of total colored pixels per field of view (FOV). Minimum number of independent FOVs counted was 4. Spheres were also imaged using an Olympus IX73 microscope.

2.3 Flow cytometry on EVTs for TME components

For isolation of single cells from EVTs, media was removed from the wells and washed with PBS. EVTs were collected in 50 mL falcon tubes with 10 mL of cold PBS-EDTA and shaken at 4ºC for 30 minutes. The solution was centrifuged, supernatant removed and resuspended in Collagenase-trypsin mix. This was shaken at 37ºC for 30 minutes followed by neutralization with complete media. Supernatant was removed after centrifugation and cells were resuspended in 100 µL of FACS buffer (PBS+ 5% FBS). Samples were stained with conjugated flow cytometry antibodies for TME components. Zombie Aqua (Biolegend 423101) was used as a marker to detect live cells. CAFs were detected with CD90.1 antibody (PerCP Mouse Anti-Rat CD90/Mouse Catalog No. 557266), endothelial cells were detected with CD31 antibody (PE anti-mouse Catalog No. 102407) and immune cells were detected

with CD45 antibody (FITC anti-mouse Catalog No. 103108). To further identify immune cells, we used CD3 antibody (PE/Dazzle™ 594 anti-mouse Catalog No. 100246) for T-cells and F-480 antibody (APC/Cy7 anti-mouse Catalog o. 123117) for macrophages. All antibodies were used at 1:100 dilution and samples were stained for 30 mins. Analysis was done using FlowJo software (version 10). All subpopulations were analyzed independently under total live cells unless otherwise noted.

2.4 Migration and invasion assays

Cells were seeded at $5x10^4$ per well in serum-free media in a 24-well Transwell or Matrigel plate (BD Biosciences, pore size 8 µm). RPMI with 10 % FBS was placed in the lower chamber as chemoattractant and cells were allowed to migrate for 6 (H157 cells) or 16 hrs (murine cells) at 37 °C, 5 % CO2. The migrated/invaded cells were stained with 0.1 % crystal violet, captured in five microscopic fields at 4x magnification per well and counted. The results are represented as mean ± SD and student's t-test was performed for statistical significance. The graphs in each figure represent one experiment. Each assay was performed in triplicate.

2.5 Cell culture

Human and murine lung cancer cell lines were cultured in RPMI1640 (Gibco, Thermo Fisher Scientific) supplemented with 10% fetal bovine serum (FBS, Gibco). 293T cells were cultured in DMEM (Gibco) supplemented with 10% FBS. All human cell lines were obtained through ATCC. Murine lung cancer cells were created from *Kras*$^{LA1/+}$/*p53*^{R172H} genetically engineered mice as previously described[93]. Manipulated human and murine cells cell lines with ZEB1 and miR-200 expression were derived as previously described[103]. All cells were cultured at 37^{O}C in a humidified incubator at 5% CO_2. Cell lines with inducible ZEB1, miR-200, sh-CDK4 and sh-p21 expression were treated with a final concentration of 2 µg/mL doxycycline (dox) from Sigma-Aldrich.

2.6 Transfections, and lentivirus generation and transduction

Transfections of si-RNAs were performed using the Lipofectamine 2000 Transfection Reagent (Thermo Fisher Scientific). For lentiviral transductions, viruses were first generated by co-transfecting packaging vector psPAX2, envelope vector pMD2.G, and the pLenti-puro expression vector into 293T cells using Lipofectamine 2000. Transfection medium was removed and 293T cells were cultured in RPMI 1640 supplemented with FBS for 48 hours. Viruses were then syringe-filtered through a 0.45 µm nylon filter and polybrene (Santa Cruz) was added to a final concentration of 8 µg/mL. Medium containing lentiviruses was then added to cells, left to allow infection of the cells for 48 hours, and replaced with fresh medium for further experiments.

Generation of 344SQ_Z-cad cell lines: Reporter constructs d2GFP-Zeb1 3' UTR and E-cadherin promoter-RFP were obtained[106]. 344SQ cell lines were transduced with lentiviral fluorescent sensors. Viruses were generated as described above. The 344SQ cells were sorted for GFP positive cells followed by RFP positive cells to confirm both plasmids were expressed in all cells using FACS Aria III (BD). After confirmation of GFP/RFP expression, the cells were referred to as 344SQ_Z-cad.

Constitutive Cdkn1a overexpression cell lines were generated by using Cdkn1a mouse Tagged ORF Clone (Origene (NM_007669)). Cdkn1a ORF was also subcloned into dox-inducible pTRIPZ-GFP vector to generate doxycycline inducible cell lines using EcoRI and AgeI restriction cut sites. Constitutive Cdkn1a shRNAs were purchased from Milipore sigma. The sequences used in the experiments are listed in table S11. Dox-inducible shRNAs were expressed in Tet-pLKO-puro vector with a scramble sequence as the non-targeting control. Tet-pLKO-puro was a gift from Dmitri Wiederschain (Addgene plasmid # 21915; http://n2t.net/addgene:21915; RRID: Addgene_21915)[107]. CDK4 and Cdkn1a shRNA oligo sequences that were used in the studies are listed in Table 9.

2.7 RNA Isolation and RT-PCR

Cultured cells were washed with PBS, and total RNA was isolated using TRIzol Reagent (Thermo Fisher Scientific). EVTs were isolated from the gels using cold PBS-EDTA. For dissolving the Matrigel/Collagen layer, Collagenase treatment was performed after the initial wash. Each well was incubated with Collagenase Type I (1,000 U/ml, Calbiochem #234153) for 30 min at 37 °C. Total RNA was isolated using TRIzol Reagent. For qPCR analysis of mRNA expression, cDNA was generated from purified mRNA using qSCRIPT reverse transcriptase mix (Quanta Biosciences). QPCR assays were performed using SYBR Green PCR Master Mix (Thermo Fisher Scientific) along with primers in Table 6 and normalized to the *L32* gene. All qPCR reactions were performed using the 7500 Fast Real-Time PCR System (Applied Biosystems).

2.8 Protein isolation and western blotting

Cultured cells were washed with PBS, and proteins were extracted from cell lysates using 1xRIPA buffer (Cell Signaling) with protease inhibitors and phosphatase. Samples were loaded onto a 10% SDS polyacrylamide gel, separated by SDS-PAGE, and transferred to a nitrocellulose membrane. Membranes containing the transferred proteins were blocked with 5% w/v fat free dry milk (Bio-Rad) dissolved in TBST. Membranes were probed with the primary antibodies listed in Table 2 diluted in 1% w/v bovine serum albumin (BSA) and dissolved in TBST overnight at 4^{O}C. Next, horseradish peroxidase (HRP)-conjugated secondary antibodies diluted in blocking solution were added to the membranes and incubated at room temperature for 1 hour. HRP-induced chemiluminescence signal was produced using Pierce ECL Western Blotting Substrate (Thermo Fisher Scientific). ECL signal from antibody-probed protein was detected using autoradiography film (BioExpress) and developer. Subcellular fractionation assay was performed using Cell Fractionation Kit #9038 according to manufacturer instructions.

2.9 Reverse Phase Protein Array (RPPA) preparation and analysis

Cultured cells described above were washed with PBS, and proteins were extracted by the addition of lysis buffer (1% Triton X-100, 50 mM HEPES [pH 7.4], 150 mM NaCl, 1.5 mM MgCl2, 1 mM EGTA, 100 mM NaF, 10 mM NaPPi, 10% glycerol, 1 mM phenylmethylsulfonyl fluoride, 1 mM Na3VO4, and protease and phosphoprotease inhibitors from Roche), incubated on ice for 20 minutes, centrifuged at 14,000 rpm for 10 minutes, and collected for supernatant. Protein concentration was measured using the Pierce BCA Protein Assay Kit (Thermo Fisher Scientific), and protein samples were prepared to a final concentration of 1 µg/µl after mixing with 4x SDS sample buffer (40% glycerol, 8% SDS, 0.25M Tris-HCl pH 6.8, 10% 2-mercaptoethanol) to produce a 1x SDS sample buffer solution. Protein samples were then boiled at 100^{O}C for 5 minutes and stored at -80^{O}C for RPPA processing described here (https://www.mdanderson.org/research/research-resources/core-facilities/functional-proteomicsrppa-core/rppa-process.html).

2.10 *In vitro* Drug Response and Cell Growth Assays

Cells were seeded in 96-well plates at 1,000 cells per well, and each row was treated with the indicated concentrations of drugs (the first row was the solvent control without any drug). After 48 hours of drug treatments, MTT reagent (Sigma-Aldrich) was added to each well at a final concentration of 0.5 mg/mL and incubated at 37^{O}C for 1 hour. Color intensity measured at 570 nm, with 630 nm reading subtracted for background. Percent surviving fraction of cells was normalized against cells treated with solvent control only.

2.11 Synergy determination

The Chou-Talalay method was used to determine possible synergistic effects between inhibitors[108]. Compusyn software (ComboSyn Inc.) was used to determine synergy between drug combinations. A fixed ratio of 1:1 µM was utilized over the concentration series

of 0.03, 0.06, 0.125, 0.25, 0.5, 1, 2 µM. Drug-drug interactions were analyzed based on combination index whereby interactions can be additive (CI=1), antagonistic (CI>1), or synergistic (CI<1). Drug concentrations in the combination were compared to the amount of drug alone required to reach same effects. This is expressed as the dose reduction index, DRI.

2.12 Apoptosis detection

Annexin and PI staining: Cells were harvested by trypsinization followed by PBS wash and twice with cold BioLegend's Cell Staining Buffer. 5 µL of FITC Annexin V and 10 µL of Propidium Iodide Solution were added to 100 µL of cell suspension followed by gentle vortexing and incubation for 15 min at room temperature in the dark. 400 µL of Annexin V Binding Buffer was added to sample. Analysis was done by flow cytometry using FlowJo software (v10).

NucView 405 Caspase-3 Substrate assay: For detecting apoptosis in live Z-cad fluorescent cells, a blue fluorescent caspase-3/7 substrate was used at 2 µM concentration. Images were acquired using 405 nm laser excitation using an Eclipse Ti inverted microscope with A1+ confocal scanner (Nikon). Flow cytometry was also performed on cells incubated with NucView reagent. Briefly, cells were detached from culture substrate using trypsin. Cells were resuspended in media and NucView substrate at final concentration of 2 µM was added to the cells. Cells were incubated at room temperature for 30 minutes, protected from light followed by analysis by flow cytometry.

2.13 Cell cycle analysis

Cells were harvested by trypsinization followed by PBS washes. Cold 70% ethanol added to cells dropwise while vortexing was used for fixation for 30 min at 4^{O}C. Cells were washed with PBS, centrifuged to collect cell pellet. Cells were treated with RNAase and then

stained with propidium iodide for 30 min at room temperature. Cell cycle was analyzed by flow cytometry using FlowJo software (version 10).

2.14 Immunofluorescence

Cells were plated on poly-L-lysine coated cover slips. Cells were fixed with 100% methanol, permeabilized with 0.3% Triton-X, and blocked with 5% normal goat serum. Primary antibodies listed in Table 5 were incubated overnight. Alexa-Fluor conjugated secondary antibodies were used for protein visualization (anti-mouse 546, anti-rabbit 488) and coverslips were mounted with ProLong Gold with DAPI for nuclear stain. Images were taken on the Olympus IX73 using a 40x objective.

2.15 Immunohistochemistry

Paraffin-embedded tissue sections were rehydrated, and heat-mediated antigen retrieval was performed using citrate buffer, pH 6.0 (Dako Agilent Technologies). Endogenous peroxidases were blocked with 3% H_2O_2 in TBS, and slides were further blocked with 5% goat serum in TBST. Tissues were probed with primary antibodies listed in Table 4, diluted in goat serum overnight at 4^{o}C. Slides were then washed three times with TBST and incubated with streptavidin-conjugated secondary antibodies targeting rabbit IgG diluted in goat serum for 1 hour at room temperature. Slides were washed again and incubated with biotinylated HRP in goat serum for 30 minutes at room temperature. After washing, signal was attained by developing with DAB reagent (Dako) for 5 minutes at room temperature. Slides were washed with ddH_2O to stop the reaction and then stained with Harris Hematoxylin (Thermo Fisher Scientific) for 1 minute and rinsed with warm tap water for 5 minutes. Slides were dipped eight times in 0.25% HCl in 70% ethanol and rinsed with tap water again for 5 minutes. Slides were dehydrated and mounted for further analysis by bright field microscopy.

2.16 Short hairpin RNA (shRNA) screens

Murine lung cancer cell lines (393P and 344P) were infected at a multiplicity-of-infection (MOI) of 0.3 with a pooled shRNA lentiviral library targeting genes associated with known kinase activity (10 shRNA/gene, for target list see Table 12 and Table 14). Parallel *in vivo* and *in vitro* screens were performed, and the shRNA-coupled barcodes were detected by high-throughput sequencing technology [for detailed procedures and primer sequences see[109]]. *In vivo* and *in vitro* screens were carried out in triplicate and duplicate, respectively. Raw counts for the screen endpoints and a reference population, isolated after transduction, were normalized using the variance stabilizing transformation with the DESeq2 in R. The normalized counts were divided by the reference cells that were isolated immediately following transduction to estimate a fold change in barcode abundance. Four independent shRNAs targeting essential genes (*RPL30, PSMA1*) or luciferase (LUC) were cloned with 5 unique barcodes each and incorporated in the library as positive and negative controls (20 reagents/control, see Table 11 and Table 13). One *LUC* hairpin showed apparent off-target effect, which has been observed over a wide-spectrum of *in vitro* and *in vivo* screens. One hairpin for *PSMA1* did not show robust drop out, and this pattern was consistent across the 5 barcodes, indicating that this result was not reflective of poor screen performance. The separation of positive and negative controls was evaluated by the robust strictly standardized mean (SSM, Table 11**Table 10** and Table 13), excluding the hairpins mentioned above. Fold change distribution was converted to percentiles, and biological replicates were collapsed for RSA analysis. The RSA logP-values and ranks are provided in Table 12 and Table 14.

2.17 Immunoprecipitation assay

Cells were washed twice with PBS on ice, scraped and pelleted. Supernatant was removed and the pellet was lysed in 500 µl lysis buffer [150 mM NaCl, 50 mM Tris-HCl (pH 7.5), 0.5% NP-40, 50 mM NaF, 1 mM Na orthovanate, 1 mM β-glycerophosphate, 10%

glycerol, PMSF and protease inhibitor] and incubated on ice for 30 min. Samples were sonicated for 1 min and centrifuged at 13,000 rpm for 10 min. The supernatant was collected and precleared for 1 hour at 4^{O}C with non-specific IgG and protein A/G agarose beads. Dynabeads were incubated for 1h with 2µg of antibody at 4°C on a rotating platform. 500 µg of pre-cleared lysate was subjected to immunoprecipitation overnight at 4°C. Antibody-antigen complexes were washed with lysis buffer and then eluted with 2x SDS sample Buffer at 100^{O}C and analyzed by western blot. Reagents used for IP are listed in Table 3.

2.18 Chromatin Immunoprecipitation (ChIP)

Cells were cross-linked with 1% formaldehyde at room temperature for 10 min. Glycine was added to a final concentration of 0.125 M for 5 min at room temperature. Cells were then washed with PBS with protease inhibitor, scraped and centrifuged (12,000 rpm, 4^{O}C for 2 min). The supernatant was removed and the pellet was resuspended in 1 ml of lysis buffer [50mM Tris-HCl (pH 8.1), 10mM EDTA, 1% SDS, protease inhibitor] incubated on ice for 10 min. Samples were sonicated on ice for 30 cycles at 50% amplitude with 5 seconds pulse intervals and 10 seconds rest intervals. Supernatants were recovered by centrifugation at 12,000 rpm for 5 min. Lysates are diluted 1:10 in ChIP dilution buffer [16.7 mM Tris-HCl (pH 8.1), 16.7 mM NaCl, 1.2 mM EDTA, 0.01% SDS, 1.1% Triton X-100, protease inhibitor]. Sheared DNA was precleared with 2 µg sheared salmon sperm DNA and 30 µL protein A/G beads (sc-2003) at 4^{O}C for 1 hour with rotation. Beads were pelleted, the supernatant was collected and an aliquot (1/20th) of the chromatin preparation was set aside and designated as the Input Fraction. The rest of the sample was divided into parts for incubation with 2 µg rabbit IgG (sc-2027) and ZEB1 (santacruz) antibodies overnight at 4^{O}C with rotation. The immune complexes were captured the next day by incubation with 30 µL of pre-cleared beads and 2 µg sheared salmon sperm DNA for 2 h at 4^{O}C. Beads were pelleted by centrifugation for 1 min at 4^{O}C at 100 g and washed sequentially for 10 min at 4^{o}C with rotation with 1 ml of the following buffers: low salt wash buffer [20 mM Tris-HCl (pH 8.1), 150 mM NaCl, 2 mM

EDTA, 1% Triton X-100, 0.1% SDS]; high salt wash buffer [20 mM Tris-HCl (pH 8.1), 500 mM NaCl, 2 mM EDTA, 1% Triton X-100, 0.1% SDS]; LiCl wash buffer [10 mM Tris-HCl (pH 8.1), 1 mM EDTA, 1% sodium deoxycholate, 1% NP-40, 0.25 mM LiCl]. Finally, the beads were washed twice with 1 ml TE buffer [1 mM EDTA, 10 mM Tris–HCl (pH 8.0)] for 5 min at 4^{O}C. The immuno-complexes were then eluted in 120 µl elution buffer [1% SDS, 100 mM NaHCO3] for 15 min with rotation at room temperature. Reverse cross-linking was done by adding NaCl to the final concentration of 200 mM to ChIP and input samples and incubating at 65^{O}C for 6 hrs. This followed by treatment with RNAase and proteinase K (40 µg/ml) incubating for 1 hour at 45^{O}C. DNA was purified using QIAquick PCR Purification Kit (Qiagen), and 50 ng of eluted DNA was used for each qPCR reaction with primers listed in Table 7 to quantify relative ChIP signal. Other reagents used for ChIP assay are listed in Table 8.

2.19 Luciferase Reporter Assay

pGL2-p21 promoter-Luc was purchased from Addgene. Human cells (H441, H358 and H1299) expressing ZEB1 and miR-200 were co-transfected with 500 ng of the reporter construct and 50 ng of the pRL-TK renilla luciferase vector (Promega) using Lipofectamine 2000 (Thermo Fisher Scientific). Assays were carried out using Dual-Luciferase Reporter Assay System (Promega), where renilla signal was used as an internal control. Relative luciferin signal was normalized to signal from the empty pGL2 promoter vector control.

2.20 Statistical analysis

Unpaired students two-tailed *t*- test were performed for all statistical analysis with two comparisons, and one-way ANOVA for comparisons with 3 or more groups. Tukey's correction was used to correct for multiple comparisons. A p-value of <0.05 was considered statistically significant. Error bars represent standard deviation unless otherwise noted. All analyses were performed in GraphPad Prism (v.8.0.0; RRID: SCR_002798) unless otherwise noted.

Table 1. Pharmacological agents

Reagent	Manufacturer
Dasatinib	Selleckchem
AZD0530	Selleckchem
TGF-β	Cell Signaling
Itgb1	BD Pharmingen
Y-15	Selleckchem
BGB324	Selleckchem
Milciclib	Selleckchem
Palbociclib (*in vitro)*	Selleckchem
Palbociclib (*in vivo)*	MedChem Express
Abemaciclib	Selleckchem
AZD6244	Selleckchem
Mocetinostat	Selleckchem

Table 2. Western blot antibodies

Antibody	Company	Catalog
Cortactin	MilliPore	05-180
Cttn pY421	Invitrogen	47768
FAK	Invitrogen	AHO0502
FAK pY397	Invitrogen	44624G
FAK pY576/577	Cell Signaling	3281
FAK pY861	Invitrogen	44-626G
Integrin β1	Cell Signaling	4706
N-cadherin	BD Pharmingen	610921
p130Cas	Upstate	06-500
p130Cas pY410	Cell Signaling	4011
p-Paxillin Y118	Abcam	4833
Paxillin	Abcam	2264
Src	Cell Signaling	2108s
Src pY416	Cell Signaling	2101L
Vimentin	Cell Signaling	3932S
Zeb1	GeneTex	GTX105278
E-cadherin	BD Biosciences	610181
N-cadherin	BD Biosciences	610921
pCDK4	Abclonal	AP0593
CDK4	Abcam	ab137675
p21	Santa cruz	sc-6246
pErk	Cell signaling	9101
Erk	Cell signaling	4695
pRB S780	Cell signaling	8180
pRB S807/811	Cell signaling	8516
RB	abcam	ab218526

pFOXM1	abcam	ab180710
FOXM1	abcam	ab207298
Actin	ProteinTech	66009-1-Ig
Cleaved caspase-3	Cell signaling	9661
Lamin A/C	Cell signaling	2032
Tubulin	Cell signaling	2148

Table 3. IP reagents

Reagent	Company	Catalog
CDK4 antibody	Santa cruz	sc-56277
p21 antibody	invitrogen	PA1-30399
Clean blot IP reagent	thermofisher	21230
normal mouse IgG	santa cruz	2025
normal rabbit IgG	cell signaling	2729
dynabeads protein a	thermofisher	10001D
Dynabeads protein g	thermofisher	10003D

Table 4. IHC antibodies

Antibody	Company	Catalog
p-Src Y418		MP569373
Zeb1	Bethyl	IHC-00419
pRB	Cell signaling	8516
pCDK4	Invitrogen	PA5-64482
p21	Novus	NB100-1941
pErk	Cell signaling	9101
Ki67	Abcam	ab15580

Table 5. IF antibodies

Antibody	Company	Catalog
pRB	Cell signaling	8516
CDK4	Abcam	ab137675
pCDK4	Invitrogen	PA5-64482
p21	Santa cruz	sc-6246

Table 6. RT-PCR primers

Gene name	Primer sequence
ms-L32-F	GGAGAAGGTTCAAGGGCCAG
ms-L32-R	TGCTCCCATAACCGATGTTG

ms-CDK4-F	CATACCTGGACAAAGCACCTCC
ms-CDK4-R	GAATGTTCTCTGGCTTCAGGTCC
ms-Ecad-F	CCATCTCAAGCTCGCGGATA
ms-Ecad-R	TCCAACGTGGTCACCTGGT
ms-Zeb1-F	ATGCTCTGAACGCGCAGC
ms-Zeb1-R	AATCGGCGATCTTTGAGAGCT
ms-Vimentin-F	CGGAAAGTGGAATCCTTGCAGG
ms-Vimentin-R	AGCAGTGAGGTCAGGCTTGGAA
ms-Ncad-F	CCTCCAGAGTTTACTGCCATGAC
ms-Ncad-R	CCACCACTGATTCTGTATGCCG
ms-p21-F	GTGGCCTTGTCGCTGTCTT
ms-p21-R	GCGCTTGGAGTGATAGAAATCTG
ms-p27-F	AGCAGTGTCCAGGGATGAGGAA
ms-p27-R	TTCTTGGGCGTCTGCTCCACAG
hs L32-F	CCTTGTGAAGCCCAAGATCG
hs L32-R	TGCCGGATGAACTTCTTGGT
hs-p21-F	CAGCAGAGGAAGACCATGTG
hs-p21-R	GGCGTTTGGAGTGGTAGAAA
hs-Zeb1-F	GGCATACACCTACTCAACTACGG
hs-Zeb1-R	TGGGCGGTGTAGAATCAGAGTC

Table 7. ChIP Primers

Gene name	Primer sequence
GAPDH-F	AGTGCCAGCCTCGTCCCGTAGACAAAATG
GAPDH-R	AAGTGGGCCCCGGCCTTCTCCAT
mir-200c-F	AGGGCTCACCAGGAAGTGT
mir-200c-R	AGATCCCTGGCTCCCATC
CDKN1A-cp-F	TATTAGCTGGGCATGGTGGT
CDKN1A-cp-R	GCAGCCCTGGCTTTTTGTTT

Table 8. ChIP reagents

Reagent	Company	Catalog
ZEB1 antibody	santa cruz	H-102X
normal rabbit IgG	cell signaling	2729
dynabeads protein a	thermofisher	10001D

Table 9. List of shRNA oligonucleotides

Gene name	Primer sequence

sh-p21-oligo_1.1	CCGGGCCCGAGAACGGTGGAACTTTCTCGAGAAAGTTCCACCGTTCTCGGGCTTTTTG
sh-p21-oligo_1.2	AATTCAAAAAGCCCGAGAACGGTGGAACTTTCTCGAGAAAGTTCCACCGTTCTCGGGC
shCdk4-oligo_1.1	CCGGGCCCTCAAGAGTGTGAGAGTTCTCGAGAACTCTCACACTCTTGAGGGCTTTTT
shCdk4-oligo_1.2	AATTAAAAAGCCCTCAAGAGTGTGAGAGTTCTCGAGAACTCTCACACTCTTGAGGGC
shCdk4-oligo_2.1	CCGGCTGCCGGTTGAGACCATTAAGCTCGAGCTTAATGGTCTCAACCGGCAGTTTTTG
shCdk4-oligo_2.2	AATTCAAAAACTGCCGGTTGAGACCATTAAGCTCGAGCTTAATGGTCTCAACCGGCAG

Chapter 3: A novel *ex vivo* tumor system identifies Src-mediated invasion and metastasis in mesenchymal tumor cells in non-small cell lung cancer

Contents of this chapter are derived from the publication Padhye, A. et al. A novel *ex vivo* tumor system identifies Src-mediated invasion and metastasis in mesenchymal tumor cells in non-small cell lung cancer. Sci Rep 9, 4819 (2019) with approval from Nature Publishing Group.

3.1 Introduction

Lung tumors display pronounced heterogeneity, including genetically and epigenetically distinct tumor cells surrounded by heterotypic cell types and extracellular matrix that dynamically interact with each of the cell types[3,110,111]. Experimental cancer research is often restricted to two dimensional *in vitro* cell cultures of immortalized cancer cell lines which largely fail to capture the cellular or microenvironmental heterogeneity of a tumor. For a fundamental understanding of cancer progression and therapeutic vulnerabilities, lung cancer should be studied in a context as close to an *in vivo* setting as possible. However, animal models can be limited by the degree to which conditions can be tested, with added time and expense.

In order to address these deficiencies in current lung cancer models, we established an *Ex Vivo* Tumor (EVT) platform to culture lung tumors in 3D matrices. This system has specific advantages over the more commonly used *in vitro* and *in vivo* systems. First, it retains tumor cell heterogeneity contributed by genetically identical but phenotypically distinct subpopulations arising due to *in vivo* selection pressure and environmental influences[3]. Since the tumors are cultured in a 3D space, the responses of tumor cells to external manipulations like drug treatments are more realistic and can be studied in real time[77,89,112]. It affords an ability to rapidly test therapeutic sensitivity of tumors in a high throughput manner. Finally, the influences of the tumor microenvironment components can be effectively studied because controlled modifications can be introduced and the system can be tuned to test these

interactions[113]. EVTs are intended to bridge the gap between *in vitro* and *in vivo* models for mechanistic and therapeutic study of lung cancer.

Our group and others have previously modeled lung adenocarcinoma using genetically-engineered murine (GEM) systems with mutant KRAS and p53[93]. These GEM models develop lung adenocarcinoma that recapitulates the aggressive and metastatic features observed in patients. Metastasis in this model occurs in a manner that is dependent on an epithelial-mesenchymal transition (EMT) regulated by a double-negative feedback loop between the microRNA-200 family and the ZEB1 transcription repressor[114]. Using syngeneic models, we have previously demonstrated that upon loss of the microRNA-200 family, the mesenchymal tumor cells are dependent on the interaction of the cell adhesion molecule integrin β1 and the extracellular matrix component collagen type I. This interaction drives the formation of the focal adhesion complex through recruitment of the adaptor molecule CRKL, which is a direct miR-200 target[115]. Herein, we use the EVT system to investigate the Src signaling pathway downstream of CRKL and demonstrate that lung cancer cells are highly dependent on Src activation for invasion and metastasis. Src is an oncogene that is overexpressed in many cancer types and known to be involved in multiple cellular processes, such as proliferation, cell morphology, migration, invasion and adhesion[116]. The tyrosine kinase acts as a signal transducer from cell surface receptors (e.g. integrins) through phosphorylation of tyrosine residues on substrates as FAK, Cas and paxillin[117].

To establish the EVT model we used KP syngeneic murine lung adenocarcinoma tumors[93], which were isolated, processed and cultured in 3D matrices. We characterized the behavior of EVTs in different matrices and demonstrate the proof-of-principal for this system to tease out signaling pathways driving metastasis *in vivo*. Our findings demonstrate that matrix-dependent invasion of mesenchymal cells is mediated through activated Src signaling, which was validated by experiments using the *in vivo* models wherein Src inhibition suppresses metastases. Our study also establishes EVTs as a valuable model representative

of *in vivo* tumor response. The system presented here can be extended to identify and understand other novel signaling pathways that regulate malignant progression or define therapeutic sensitivities in lung cancer.

3.2 Results

3.2.1 EVTs are representative of the cellular composition in primary tumors.

To study the underlying mechanisms driving lung cancer progression, we wanted to develop a model that bridges the gap between conventional 2D cell culture systems and *in vivo* models. We utilized murine KP lung adenocarcinoma cell line models (e.g. 344SQ) implanted in immunocompetent syngeneic mice, which form primary tumors that grow over 4-6 weeks and metastasize to the lungs and distant organs[93]. Primary tumors were harvested and processed by mechanical and enzymatic digestion to yield multicellular aggregates, referred to as *Ex Vivo* Tumors (EVTs) (Figure 6). Prior to embedding in 3D matrices, EVTs were cultured in laser ablated poly(dimethylsiloxane) (PDMS) microwell inserts designed for standard tissue culture plates, which we have previously described for single-cell suspensions[105]. The microwells within each insert are ~100 µm in diameter, allowing exclusion of tumor aggregates greater than 100 µm and thereby enhancing the uniformity of the starting size for EVTs. EVTs harvested from microwells were then embedded in different matrices for further downstream investigations.

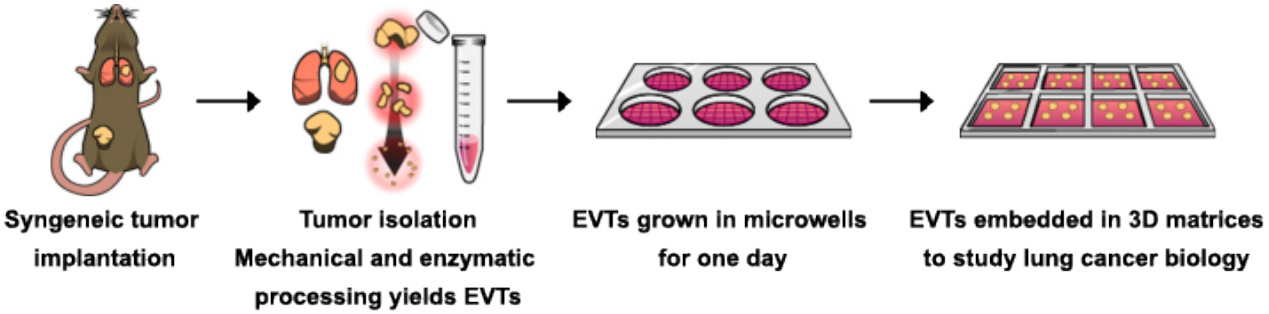

Figure 6. Schematic description of isolation and 3D culture of EVTs.
Syngeneic murine subcutaneous tumors were harvested 4 weeks after implantation. After isolation and processing of tumors, EVTs are cultured in microwells for one day to yield structures of uniform size. *(Padhye et al, Sci Rep 9, 4819, 2019).*

Tumor cells dynamically interact with the components of the tumor microenvironment (TME) like extracellular matrix (ECM), cancer associated fibroblasts (CAFs), immune cells and endothelial cells[77,111,118]. While establishing this system, we wanted to characterize the cellular TME components present in EVTs that may afford an advantage over conventional 3D cell culture systems. We compared the cellular composition of primary syngeneic tumors and EVTs derived from them by flow cytometry. Figure 7 demonstrates the gating scheme for different TME cells within primary tumor and EVTs. The CD45 cell surface marker was used to identify immune cells within the live cell population, which were further classified as $CD3^+$ T-cells or $F4/80^+$ macrophages. The two immune cell subpopulations were primarily studied as they have been shown to actively modulate tumor cell behavior. The percentage of T-cells within primary tumors and EVTs was consistent (10-15%) and macrophages followed similar patterns (10-15%). CAFs were identified by the CD90 (Thy1) cell surface marker[53,119] and were about 5-7% of the cells in tumors and EVTs. $CD31^+$ endothelial cells made up about 20% of the total live cell population in EVTs and primary tumors.

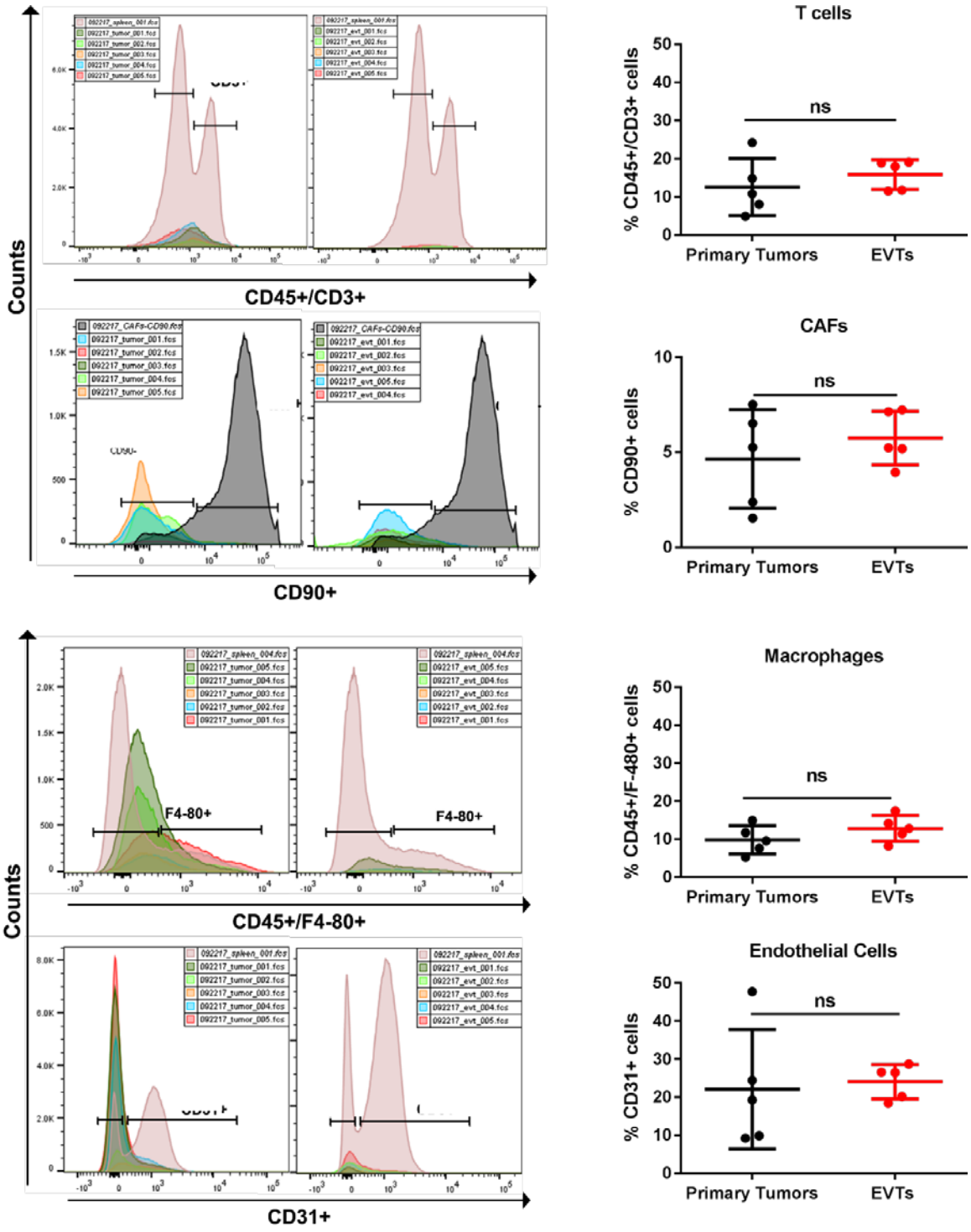

Figure 7. EVTs are representative of the cellular composition of syngeneic murine tumors. (Left) Gating scheme to show different TME cells within primary tumors and EVTs (Right) Flow cytometry analysis to compare the cellular composition of EVTs to the primary syngeneic tumors. No significant difference observed in percentage of T-cells, macrophages, CAFs and endothelial cells between the two groups. *(Padhye et al, Sci Rep 9, 4819, 2019).*

We further analyzed T cell subpopulations in terms of CD4+ and CD8+ cells Figure 8. EVTs have a higher percentage of CD8+ T cells and lower percentage of CD4+ T cells when compared to primary tumors. On further sub-classification into exhausted T cells (PD1+/Lag3+) and regulatory T cells (CD25+/FoxP3+), we did not observe any differences between tumors and EVTs.

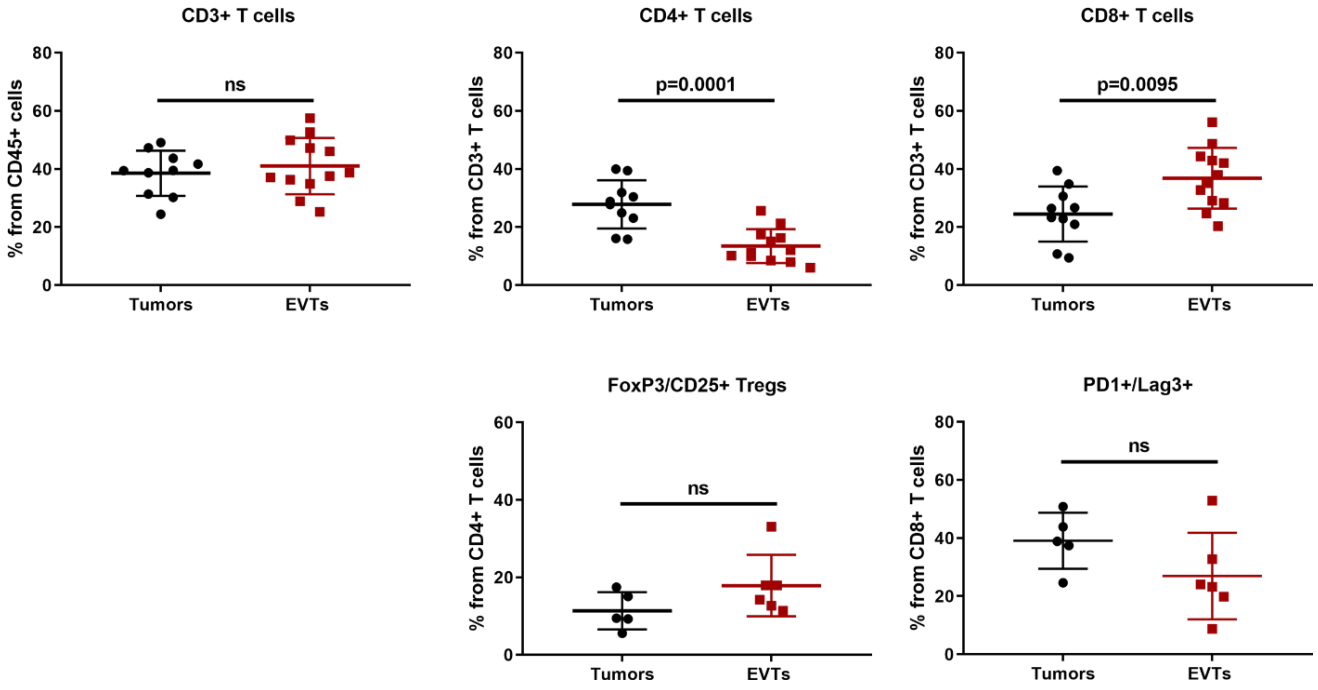

Figure 8. Flow cytometry analysis of T cell subpopulations.
CD8+ and CD4+ T cells within EVTs and primary syngeneic tumor were analyzed. No significant difference observed in percentage of CD3+T-cells but EVTs had higher percentage of CD8+ and lower percentage of CD4+ T cells compared to primary tumors. Further classification into exhausted CD8 T cells and regulatory CD4 T cells did not show significant differences between EVTs and primary tumors.*(Padhye et al, Sci Rep 9, 4819, 2019).*

To determine if TME cells were still present in 3D cultured EVTs after a few days without any external stimulation, EVTs were grown in Matrigel for 5 days and the percentage of different cell types was compared over time (Figure 9). Although there was a decline in the percentage of TME cells in cultured EVTs without any external stimulation, we were successfully able to detect TME components in EVTs at the time of seeding into matrices and after 5 days of culture, allowing us to mimic an *in vivo* environment. The presence of TME cells within EVTs can be further exploited to investigate the heterotypic interactions within tumors by utilizing appropriate stimulatory factors.

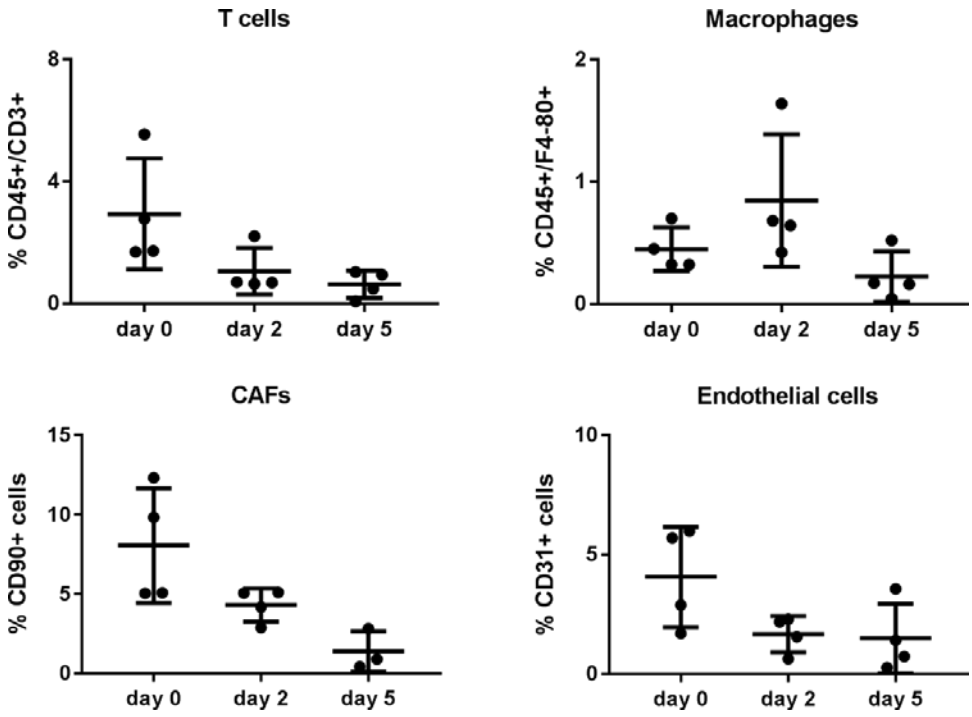

Figure 9. Flow cytometry analysis of cellular composition of EVTs after 5 days in Matrigel. *(Padhye et al, Sci Rep 9, 4819, 2019).*

3.2.2 Immunofluorescence on tumor microenvironment components.

Next, we optimized immunofluorescence staining of EVTs before and after culture in matrices in order to determine spatial distribution of TME components as well as presence of phenotypically different tumor cells. EVTs harvested from microwells stained for CD8+ T cells within the micro-tumors (Figure 10A). Further studies to examine the impact of immune cells on cancer cells can be designed with appropriate stimulatory factors. Additionally, the EVT platform can serve as a platform to interrogate the effect of immunotherapeutic agents.

We also detected collagen I around the EVTs that were harvested from microwells with an increase in collagen I staining after being cultured in Matrigel for 5 days (Figure 10B) indicating that EVTs produce collagen production overtime. This underscores that EVTs indeed are capable of recapitulating *in vivo* like behavior. We also noted that EVTs were more organized in Matrigel as compared to microwells (Figure 10B), due to the presence of laminin in the matrix which is responsible for promoting epithelial like phenotype. Since EVTs are derived from tumors, there is marked tumor cell heterogeneity as well. Using the markers that are normally used to determine the EMT status of cancer cells, we observed that within EVTs derived from same tumors, there were cells expressing different EMT markers such as E-cadherin, β-catenin, α-smooth muscle actin and vimentin (Figure 10B). EVTs from primarily epithelial cancer cells (393P) also retained cellular heterogeneity with the presence of cells with different EMT status (Figure 10C). Laminin production was also noted in EVTs isolated from microwells (Figure 10C). Orthotopic lung EVTs also behaved in a similar manner as EVTs derived from primary subcutaneous tumors. EVTs were more organized and epithelial-like in Matrigel as seen by E-cadherin and β-catenin staining, but still retained some mesenchymal like features demonstrated by α-smooth muscle actin and collagen staining. Laminin production in EVTs cultured in microwells was also detected (Figure 10D). Findings from immunofluorescence staining are important as they highlight that EVTs are capable of modeling tumor microenvironment as well as tumor cell heterogeneity.

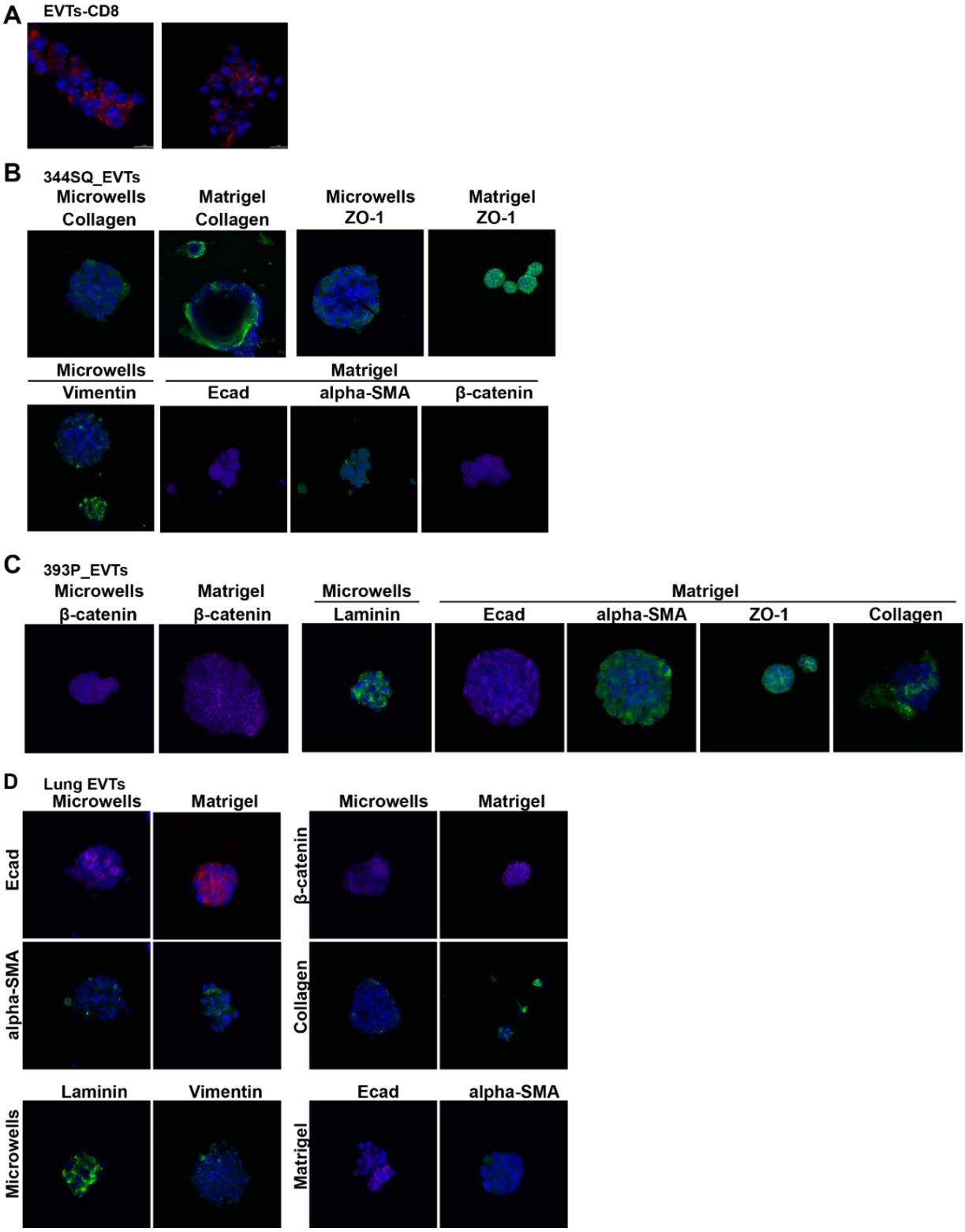

Figure 10. Immunofluroscent staining on EVTs for indicated markers.
(A) EVTs were harvested from microwells after one day and stained for CD8 cells. (B-D) EVTs cultured in microwells and Matrigel were isolated and stained for indicated markers for tumor cells and matrix components.

3.2.3 Establishing EVT platform for different tumor types.

We have previously demonstrated that tumor cell phenotype can be altered by modulating intrinsic factors such as ZEB1/miR-200 axis[93]. The different phenotypic states of cancer cells are capable of interacting with tumor microenvironment in unique manner, which eventually contributes to a heterogeneity within tumors and leads to cancer progression. In order to model more complexities within lung cancer, we utilized 344SQ tumors with doxycycline inducible GFP-ZEB1 overexpression. Mice bearing 344SQ_ZEB1 tumors were divided into 2 groups: with and without doxycycline feed. Tumors were harvested from each group and processed to yield EVTs. EVTs from both groups were cultured in Matrigel with or without doxycycline. Based on the ZEB1 induction *in vivo* and *ex vivo* each condition was designated as - -, + -, - + and + +. EVTs without any ZEB1 overexpression (- -) were completely non-invasive whereas the same EVTs when treated with doxycycline *ex vivo* (- +) became significantly more invasive. Conversely, when EVTs that were induced *in vivo* were cultured without doxycycline in Matrigel, the invasive phenotype was shut down (+ -). EVTs that were under constant doxycycline exposure (+ +) had a much more significant invasive phenotype as well as larger structures (Figure 11A-C). These findings demonstrate the plastic nature of cancer cells and the ability to undergo phenotypic shift depending on intrinsic and extrinsic factors and are not locked in one constant cellular state. It is accompanied by transcriptional reprograming and activation of different signal transduction pathways for survival and escape from therapeutic targeting. Since these are important biological questions that need to be explored, EVTs with modifiable tumor cell phenotypes can serve as high throughput platform to incorporate a variety of complexities such as ECM alterations, heterotypic cells and response to pharmacological agents.

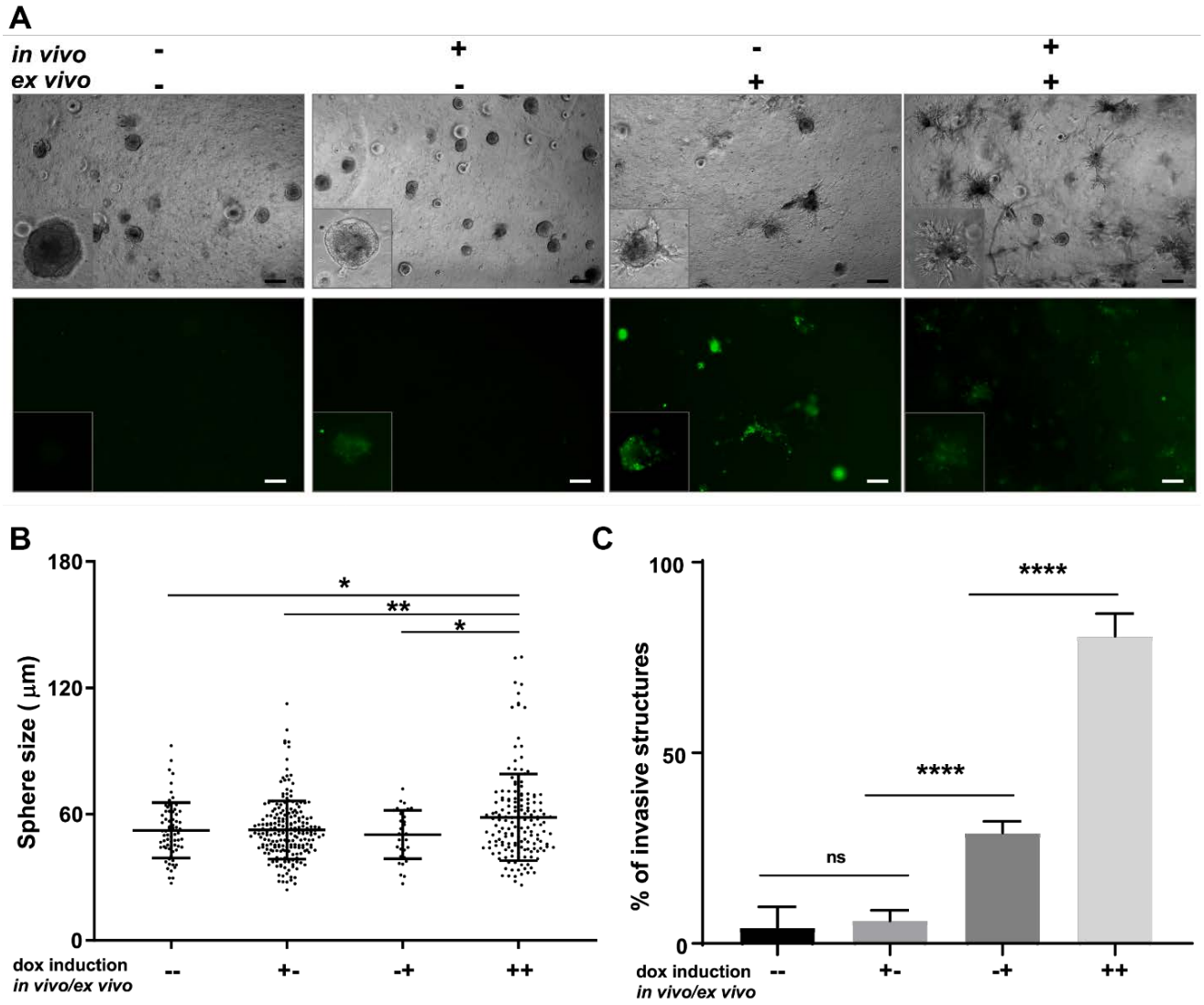

Figure 11. EVTs derived from ZEB1 overexpressing tumors.
(A) EVTs cultured in Matrigel for 5 days with or without doxycyclline (2µg/ml) treatment. Images taken at day 5. Scale bar:100 µm. (B) Sphere size of EVTs measured on day 5. (C) Percentage of invasive structures were quantified on day 5.

Autochthonous lung tumor models represent human lung cancer more accurately. Our group utilizes *Kras$^{G12D/+}$ and Kras$^{G12D/+}$; p53$^{flox/flox}$* driven lung tumor models to investigate cancer progression. Mutant Kras and Kras/p53 GEMMs tumors were cultured as EVTs in microwells, Matrigel or Matrigel/collagen I matrices to study tumor evolution of early-stage tumors. Immunofluroscent staining of Kras mutant EVTs revealed the presence of phenotypically distinct tumor cell subtypes with production of both laminin and collagen I (Figure 12A). Kras mutant lung cancers fail to generate cell lines when cultured in petri dishes. However, when cultured as EVTs in different matrices, tumors can be propagated overtime (Figure 12B). When cultured in Matrigel/collagen I, Kras and Kras/p53 mutant EVTs demonstrate an invasive phenotype that not observed in Matrigel alone (Figure 12C), recapitulating the phenotype observed in metastatic lung cancer with high collagen levels. Establishing the baseline morphological characteristics sets up EVTs for understanding tumor cell interactions with TME components, especially with ECM components. EVTs can allow us to drive the phenotype of the tumor cells towards a specific lineage and help us monitor the selection process over time. The effect of ECM and other TME components on the tumor heterogeneity within lung cancer as well as the emergence of more aggressive cellular phenotypes during cancer progression can be studied.

When normal human bronchial epithelial cells are grown in 2D cultures they proliferate until they form a confluent monolayer, but in 3D Matrigel cultures, they differentiate into a characteristic lumen-containing glandular structure, termed an acinus representing *in vivo* characteristics. Similarly, autochthons lung tumor EVTs can be used to study tumor morphology and interactions occurring in a 3D space that can have effects on gene expression and cell behavior. Due to the ability to mimic *in vivo* microenvironment, early changes in tumor progression and evolution can be studied with EVTs. Selection pressure on cancer cells can affect the phenotype and gene expression which can be studied in a high throughput manner and in real-time which is more difficult in animal models. Additionally, controlled TME modification can help study the response of cancer cells to specific alterations

in those components. We have established a wide variety of EVT platforms which provides unique tools to assay different biological questions.

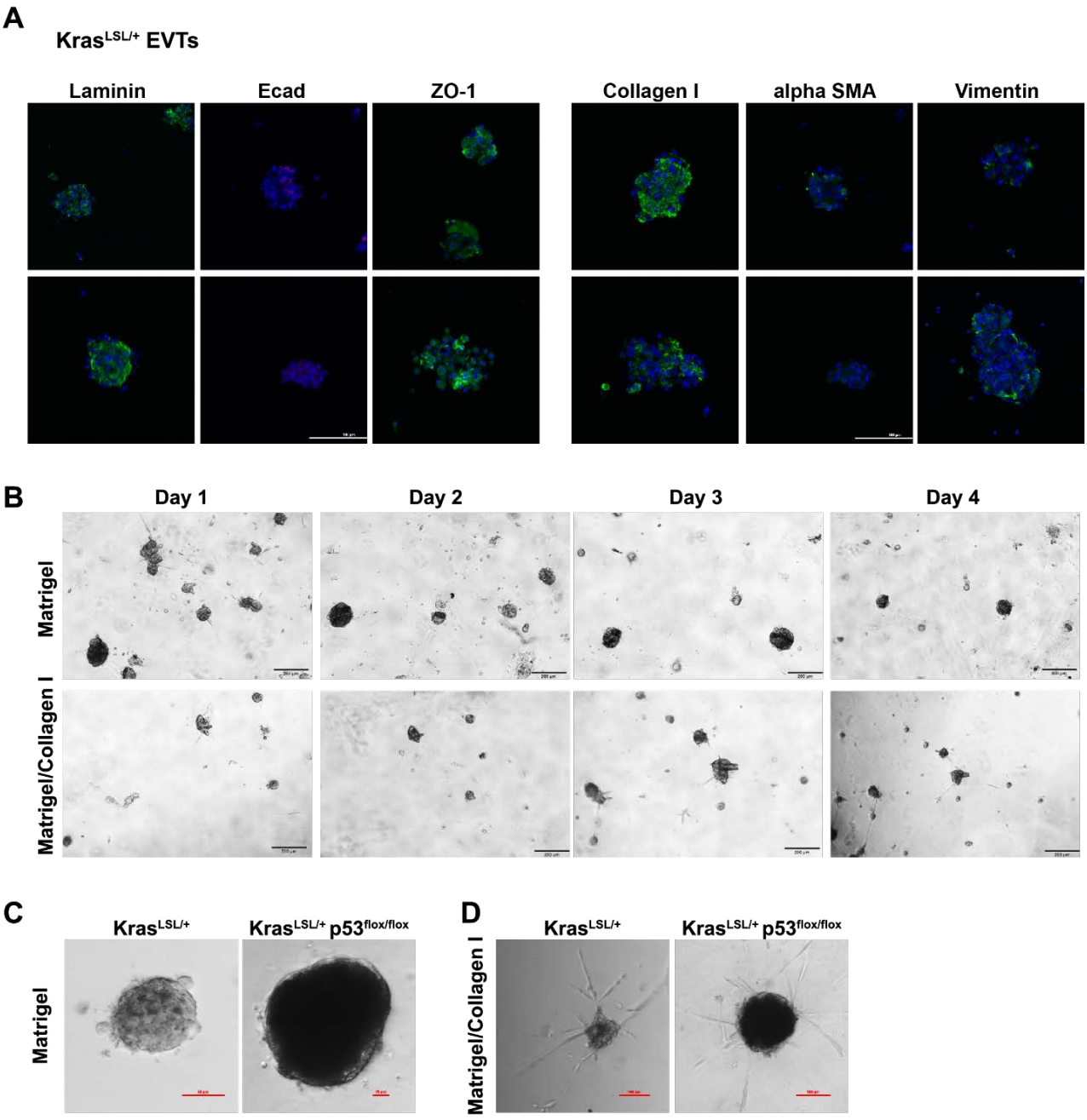

Figure 12. EVTs derived from primary autochthnous lung tumors.
(A) Immunofluroscent staining of Kras mutant EVTs from microwells for indicated markers. (B) Kras mutant EVTs cultured in Matrigel and Matrigel/collagen I for 4 days. (C) Images of Kras and Kras/p53 mutant EVTs cultured in Matrigel and Matrigel/collagen I for 4 days.

3.2.4 EVTs are responsive to the external stimulus TGFβ and undergo EMT.

Tumors are surrounded by extracellular matrix, which provides physical support as well as biochemical signals to tumor cells, and is frequently altered over the course of tumor progression. We initially utilized Matrigel, which is a solubilized basement membrane preparation rich in primarily laminin and collagen IV, to model the ECM-EVT interactions found in tumors. 344SQ_EVTs were cultured in Matrigel for 7 days and treated with TGFβ starting on the third day after seeding. TGFβ is frequently present at high levels in tumors and is known to induce an EMT by suppression of miR-200 expression[93], thereby promoting invasion and metastasis. EVTs grown in Matrigel alone increase from ~75 µm to ~100 µm in size over 7 days, but upon treatment with TGFβ, they hyper-proliferate and are ~200 µm by day 7 (Figure 13A,B). TGFβ treated EVTs developed invasive protrusions suggesting a shift to a mesenchymal phenotype (Figure 13A, C). To confirm that EMT is occurring at a molecular level, we collected RNA and protein from EVTs at day 7. Quantitative RT-PCR analysis for canonical EMT markers E-cadherin, N-cadherin, vimentin and Zeb1 revealed that EVTs undergo EMT upon TGFβ treatment (Figure 13D, E). Consistent with our previous work using murine lung cancer cells alone[93], with EVTs we observed an increase in Zeb1 in response to TGFβ, with subsequent transcriptional repression of the miR-200 family members miR-200 a, b, c (Figure 13E). Additionally, we observed an increased expression of mesenchymal markers at the protein level by western blot analysis (Figure 13F).

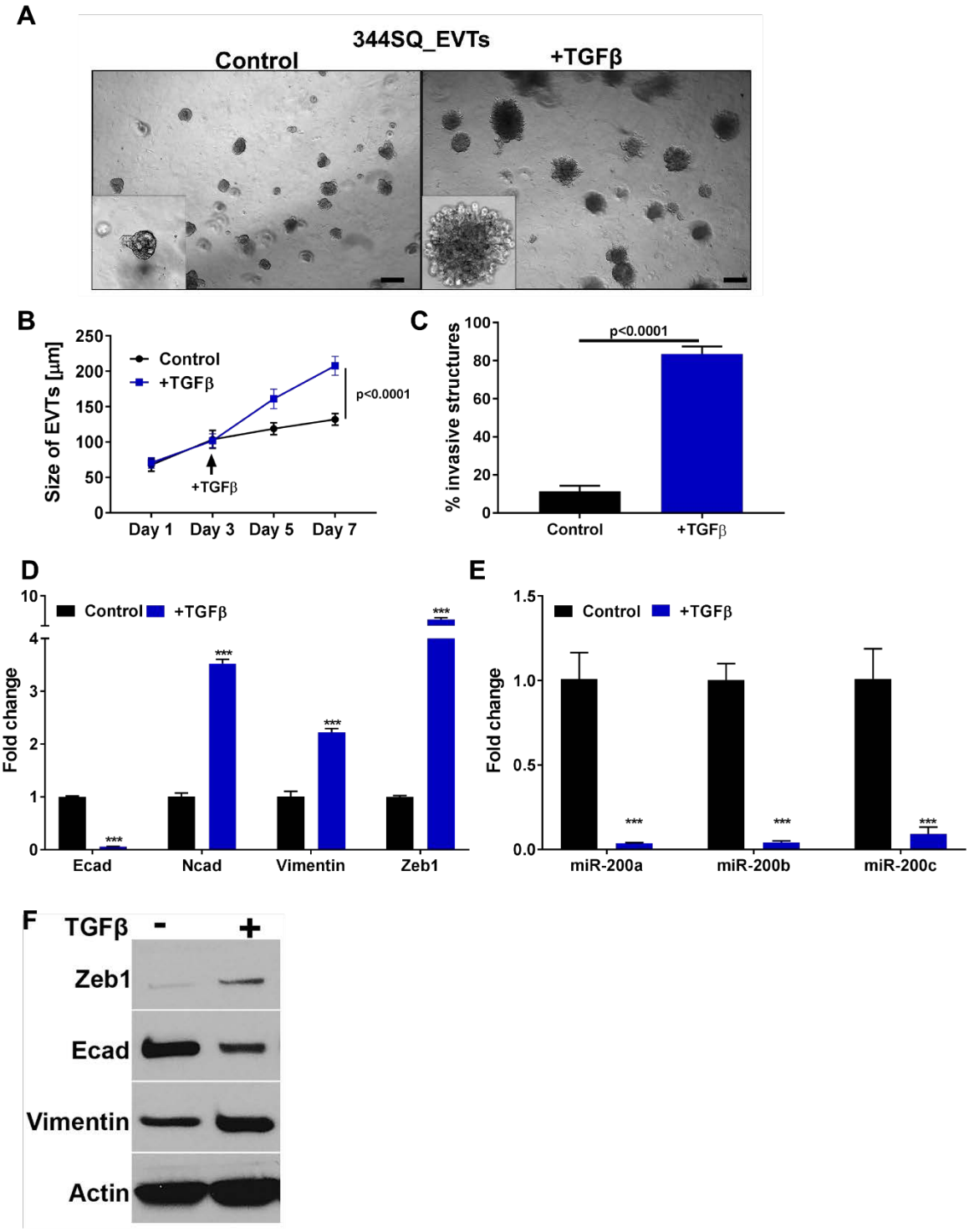

Figure 13. EVTs are responsive to external stimulus TGFβ and undergo EMT.
(A) 344SQ_EVTs are cultured in Matrigel for 7 days and treated with TGFβ (5 ng/ml) on day 3 (scale bar is 200 µM). In response to TGFβ, EVTs (B) hyper proliferate and (C) are more invasive. For each condition, 1000 structures were measured in size and scored for invasiveness. (D) Quantitative RT–PCR of indicated markers, shown as fold change upon TGFβ treatment. (E) Taqman RT–PCR assay of individual miR-200 members for EVTs in Matrigel and following TGFβ treatment. ***$p < 0.0001$. (F) Western blot analysis for EMT markers in Matrigel with or without TGFβ treatment.
(Padhye et al, Sci Rep 9, 4819, 2019).

To demonstrate the broader utility of the system, we intratracheally implanted RFP expressing 344SQ tumor cells into the lungs and harvested orthotopic lung tumors after three weeks of growth. H&E staining of lungs reveal presence of tumors formed from implantation of tumor cells. Lung-EVTs were cultured in Matrigel over 7 days and demonstrated similar morphological and molecular characteristics as EVTs derived from subcutaneous tumors (Figure 14A). In response to TGFβ, they developed an invasive morphology corresponding to the changes in EMT markers at the molecular level (Figure 14B).

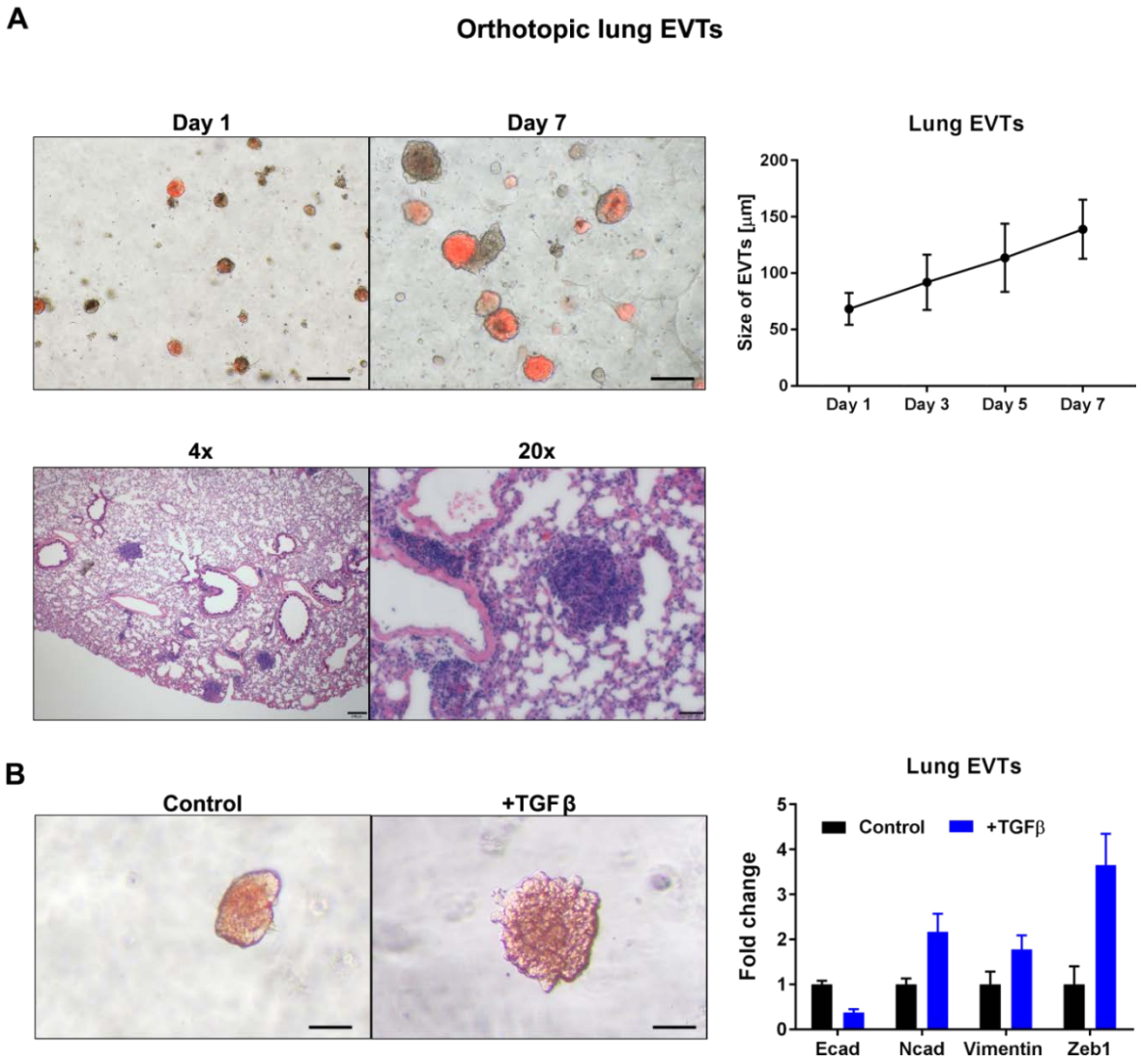

Figure 14. EVTs derived fron orthotopic lung tumors.
(A) EVTs derived from orthotopic lung tumors are cultured in Matrigel for 7 days and sphere size is quantified during that time. H&E staining of the lungs to show tumors. (B) Lung EVTs are treated with TGFβ (5ng/ml) and demonstrate an increase in size and invasiveness Scale bar µM. Quantitative RT–PCR of indicated markers, shown as fold change upon TGFβ treatment**.**
(Padhye et al, Sci Rep 9, 4819, 2019).

3.2.5 Extracellular matrix manipulations induce phenotypic alterations in EVTs.

One of the factors contributing to intratumor heterogeneity is the plasticity of tumor cells to transition between different phenotypic states. Tumor cell intrinsic genetic or epigenetic alterations are usually considered drivers of cancer progression. However, modification of the extracellular matrix can independently modulate the phenotype of tumor cells with or without affecting the epigenetic state of the tumor cells. To test the effects of matrix composition on tumor behavior, we cultured 344SQ_EVTs in Matrigel or mixed in increasing concentrations of collagen I. The presence of higher amounts of collagen I has been shown to promote an invasive and more aggressive tumor phenotype. We observed that with each higher collagen I concentration the percentage of invasive EVTs significantly increased up to ~80% (Figure 15 A, B). These data demonstrate that ECM components are capable of driving the phenotypic behavior of the tumor cells. To determine if interaction with collagen I is altering the tumor cells by inducing an EMT, we collected RNA and protein from the structures. Quantitative RT-PCR (Figure 15 C) and western blot analysis (Figure 15 D) did not reveal an EMT occurring in EVTs, demonstrating that ECM is driving the invasive phenotype of the tumor cells without inducing epigenetic changes that result in a mesenchymal state.

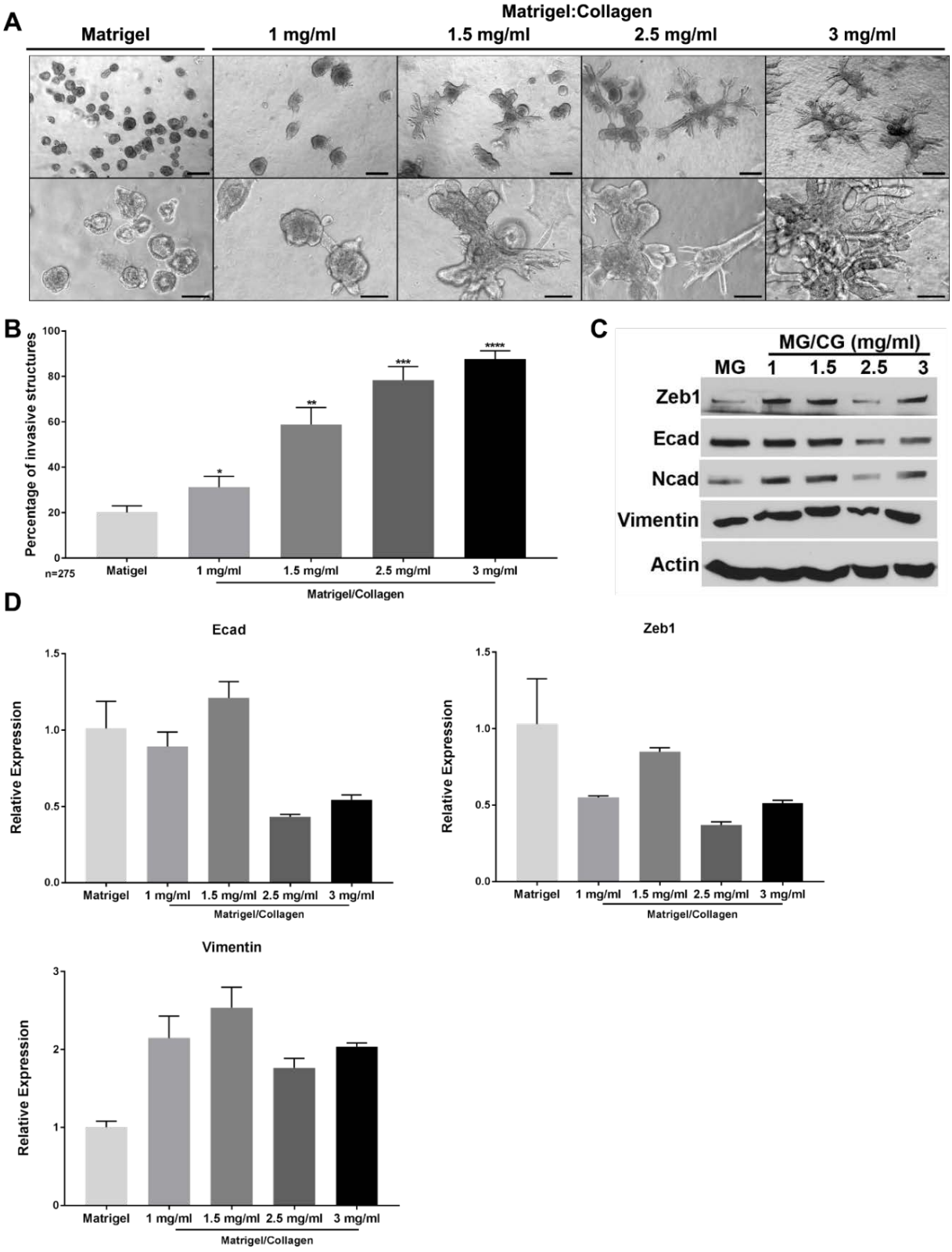

Figure 15. Extracellular matrix manipulations induce phenotypic alterations in EVTs.
(A) EVTs cultured in MG or MG/CG I with different concentrations of Collagen I for 5 days. (B) Quantification of invasive structures in response to alterations of the matrix. For each condition, 250 structures were scored for invasiveness. (C) Western blot analysis of EMT markers. (D) Quantitative RT–PCR of indicated EMT markers show no change in response to Collagen I in the matrix.
(Padhye et al, Sci Rep 9, 4819, 2019).

To test the utility of this platform across different tumor cell types, we harvested EVTs from non-metastatic, epithelial 393P tumors. 393P_EVTs cultured in Matrigel grew as aggregates which were significantly invasive in response to TGFβ treatment or inclusion of collagen I in the matrix (Figure 16 A). An invasive phenotype was also observed with EVTs from orthotopic lung tumors cultured in Matrigel/Collagen I (Figure 16 B). Our previous work has revealed that Zeb1 expression drives a mesenchymal phenotype in non-metastatic, epithelial cell line 393P[115]. EVTs derived from genetically manipulated 393P cells with constitutive Zeb1 expression were cultured in Matrigel or Matrigel/Collagen I and displayed significant invasion in MG/CG I as compared to the 393P-Vector_EVTs (Figure 16 C). Overall, testing of multiple different tumor cell models demonstrates the utility of the EVT platform to study the dynamic interactions of cell intrinsic factors with the extracellular conditions.

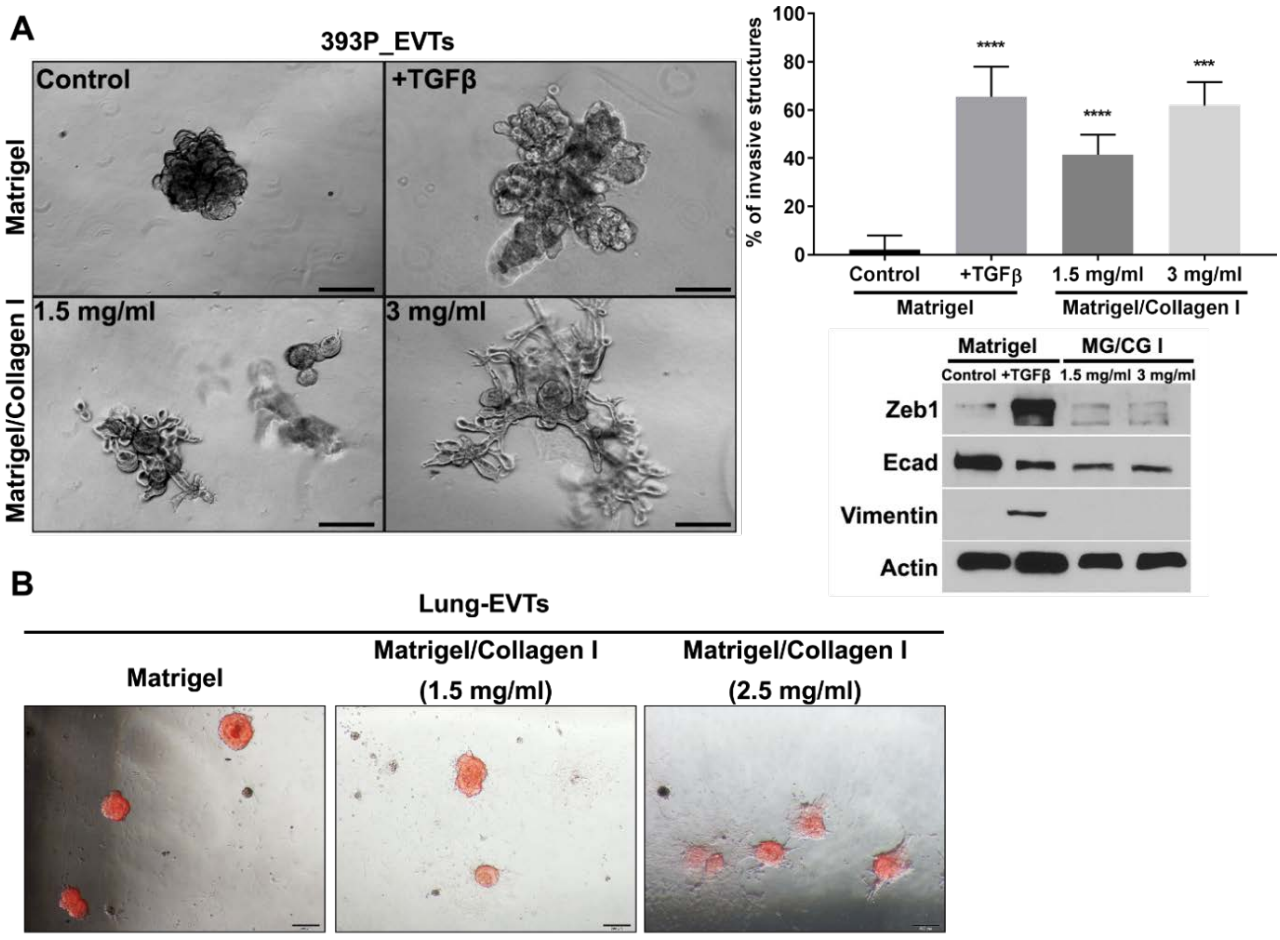

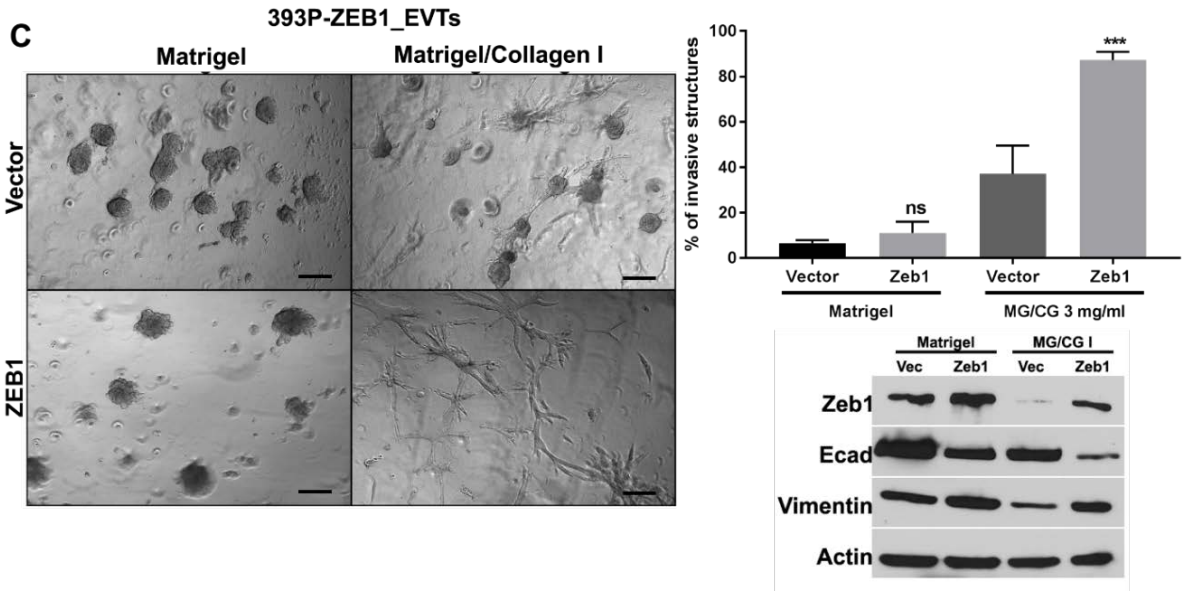

Figure 16. 393P-ZEB1 EVTs retain responses to external stimuli.
(A) Non-metastatic, epithelial 393P_EVTs cultured in Matrigel as control and treated with TGFβ or cultured in varying Collagen I mixtures. Quantification shows percentage of structures invasive in response to alterations. Western blot analysis on EMT markers. (B) Lung-EVTs are cultured in Matrigel or Matrigel/Collagen I with different concentrations of Collagen I for 5 days. (C) 393P vector and 393P Zeb1 EVTs are cultured in Matrigel and Matrigel/Collagen I (3 mg/ml) for 5 days (scale bar: 200 µM). Invasiveness of EVTs in response to intrinsic (Zeb1) or extrinsic (Collagen I) manipulation. Western blot analysis to show an EMT induction.
(Padhye et al, Sci Rep 9, 4819, 2019).

To further study the mechanism by which collagen I promotes an invasive phenotype, we cultured 344SQ_EVTs in Matrigel/Collagen I at 3 mg/ml concentration and treated with an integrin β1 blocking antibody. The antibody decreased the invasive ability of EVTs by two-thirds (Figure 17A, B). Western blot analysis also demonstrated that FAK/Src signaling is activated in the presence of collagen I and is suppressed by addition of integrin β1 blocking antibody (Figure 17C). We tested the effect of integrin β1 blocking antibody on 393P_EVTs in Matrigel alone (Figure 17D). In the absence or presence of the blocking antibody, we did not observe any invasion of EVTs in Matrigel, further demonstrating that integrin β1 receptors on tumor cells require interaction with collagen I in the matrix to produce invasion.

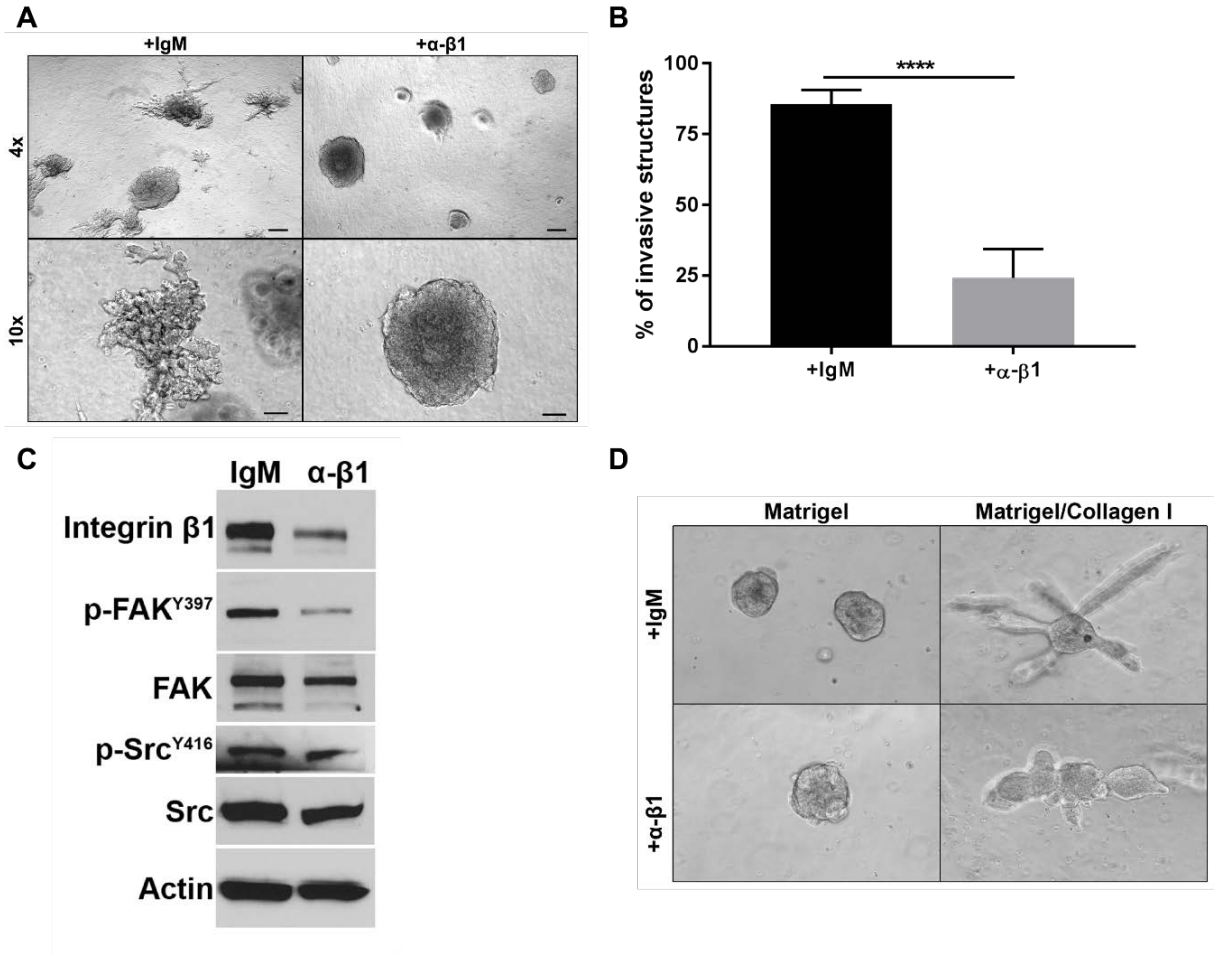

Figure 17. Collagen I-integrin β1 interaction is necessary for invasive phenotype in EVTs.
(A) 344SQ_EVTs cultured in Matrigel and Matrigel/Collagen I (3 mg/ml) and treated with an ITGβ1-blocking antibody or IgM control for 5 days. (B) For each condition, 500 structures were scored for invasiveness. (C) Western blot analysis of FAK/Src signaling in EVTs treated with ITGβ1-blocking antibody. (D) 393P_EVTs cultured in Matrigel and Matrigel/Collagen I (3 mg/ml) and treated with an ITGβ1-blocking antibody or IgM control for 5 days.
(Padhye et al, Sci Rep 9, 4819, 2019).

To further test that invasion in EVTs is occurring through an integrin β1-collagen I interaction, we cultured EVTs of 344SQ with integrin β1 knockdown (344SQ_ITGB1 KD) in Matrigel and Matrigel/collagen I (Figure 18A). There was a significant decrease in the percentage of invasive EVTs in Matrigel/Collagen I upon integrin β1 knockdown as compared to EVTs from scramble control cells (Figure 18B). Western blot analysis showed a decrease in p-FAK and p-Src in integrin β1 knockdown EVTs (Figure 18C). These results demonstrate the utility of EVTs for interrogating the role of TME components like ECM in cancer

progression and highlight the collagen I-integrin β1 interactions as critical to downstream signaling and tumor cell invasion.

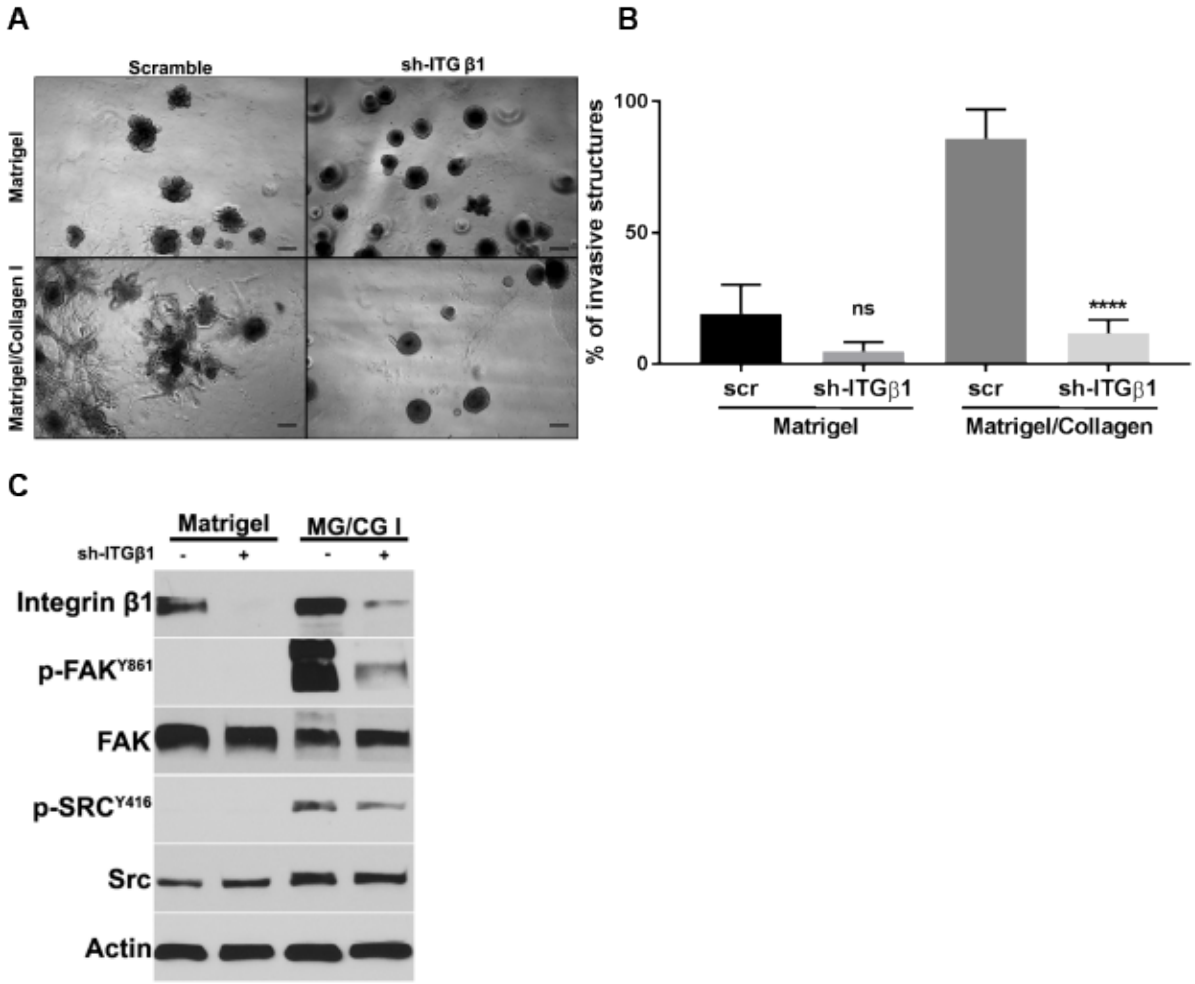

Figure 18. Integrin β1 knockdown overcomes invasive phenotype in EVTs.
(A) 344SQ_scr and 344SQ_shITGβ1 EVTs cultured in Matrigel and Matrigel/Collagen I (3 mg/ml). (B) Percentage of invasive structures calculated at day 5. (C) Western blot to show integrin β1 knockdown and FAK/Src signaling.
(Padhye et al, Sci Rep 9, 4819, 2019).

3.2.6 Src pathway is required for initiation and maintenance of invasion in EVTs.

We previously demonstrated that the EMT status of tumor cells modulates collagen I-dependent activation by regulating integrin β1-mediated FAK activation[115]. We sought to further investigate the signaling downstream of integrin β1 that accounts for the invasive phenotype. Focal adhesion kinase (FAK) is a non-receptor tyrosine kinase that mediates extracellular signals to the intracellular machinery to regulate cell migration and invasion. Cancer cells harness this pathway for increased and efficient invasion leading to metastatic disease (Figure 19A). The interaction of collagen I and integrin receptors recruit FAK to the sites which are known as focal adhesions and initiate a multistep process starting with auto-phosphorylation of FAK at tyrosine 397 (Y397). This activates a cascade of signaling which also lead to activation of Src pathway. We utilized a pharmacological inhibitor Y-15 specific inhibitor of FAK that inhibits its autophosphorylation activity. When 344SQ cells cultured in 2D were treated with Y-15 with dose escalation, there was a suppression of phospho-FAK (Figure 19B). Cells grown in 3D culture with Matrigel/collagen I matrix, the invasive structures formed were disintegrated when treated with FAK inhibitor (Figure 19C). EVTs, however, failed to show similar response to FAK inhibitor. There was a slight decrease in the length of the invasive protrusions without any disintegration (Figure 19C). Interestingly, when mice bearing subcutaneous tumors were treated with the same inhibitor, there was no significant impact on tumor weight or lung metastases (Figure 19D). Many preclinical models have demonstrated the benefits of FAK inhibitors in controlling tumor growth which do not always translate into an effective response in the clinic[120]. Our results are of importance because we demonstrate that EVTs are predictive of response of tumors, even when other 2D and 3D assays may demonstrate otherwise. Therefore, EVTs are a useful to perform an initial large scale screen of therapeutic agents in a cost effective manner, without using expensive animal models.

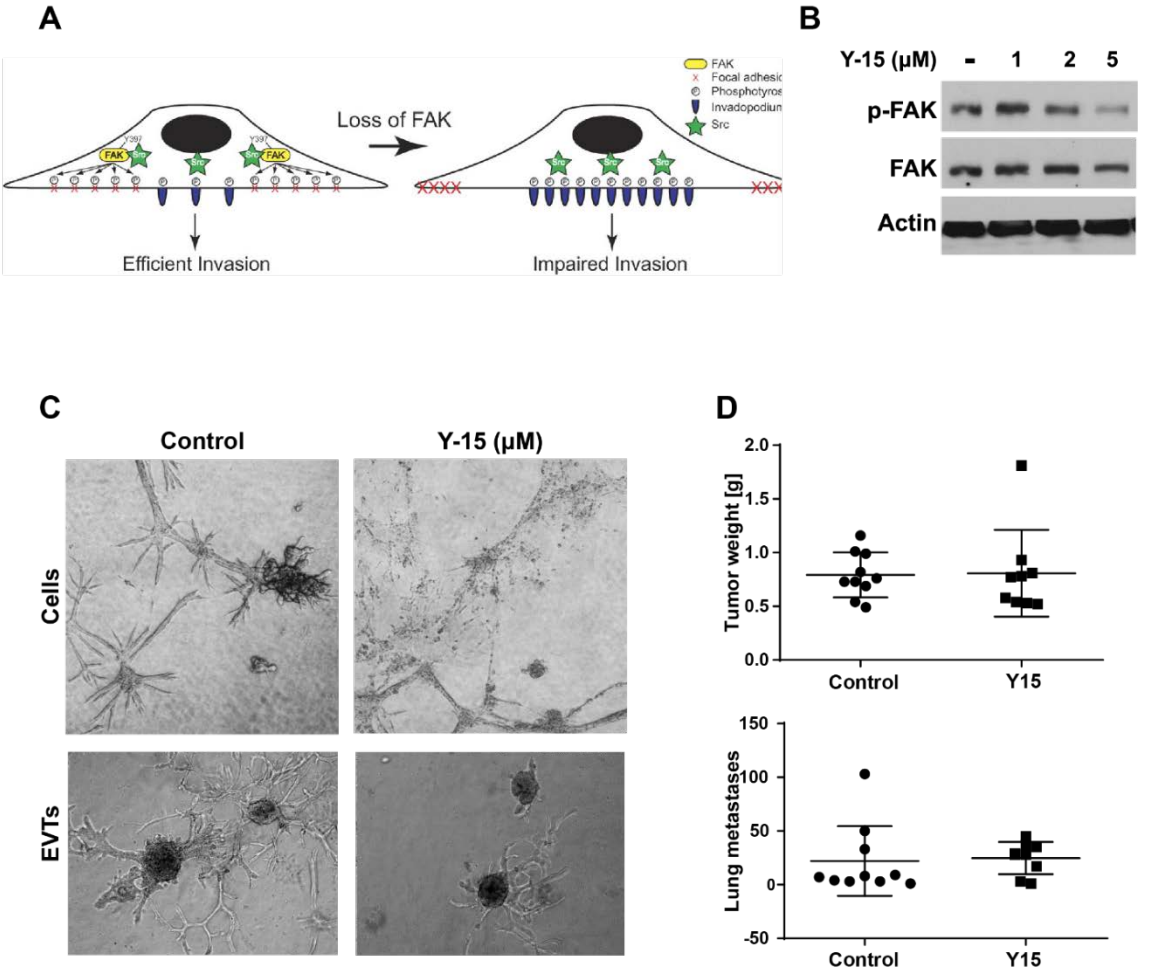

Figure 19. Response of EVTs to FAK inhibitor Y-15.
(A) Role of FAKs in invasion (B) 344SQ cells treated with FAK inhibitor Y-15 for 72 hrs. (C) 344SQ cells and EVTs cultured in MG/CG I (3 mg/ml) for 5 days and treated 5 μM of Y-15. Images from day 5. (D) 344SQ cells implanted subcutaneously in syngeneic wild type mice that were treated with Y-15 at 30 mg/kg daily for 6 weeks. Top: tumor weight at necropsy, bottom: number of lung metastases at necropsy.

Stratification of murine KP cell lines derived from spontaneous Kras/p53 tumors by their epithelial or mesenchymal status revealed a significant activation of the downstream Src/cortactin pathway in the mesenchymal cells compared to the epithelial cells (Figure 20A, B). Furthermore, in the genetically manipulated 393P cells, we observed a direct correlation between the activation of this pathway and the Zeb1 levels (Figure 20C). To further study the importance of the Src pathway in regulating invasion, we assayed the effect of the Src tyrosine kinase inhibitor, dasatinib. Dasatinib treatment for 7 hours blocked FAK and Src activation (Figure 20C). Dasatinib treatment in 3D assays inhibited the collagen I-dependent invasion of the mesenchymal 393P_ZEB1 cells but had no effect on the control cells (Figure 20D-E). To further elucidate the utility of EVTs for investigating signaling pathways responsible for lung cancer invasion and metastasis, we cultured EVTs derived from 344SQ tumors in Matrigel. This is one of the KP models that is mesenchymal and metastatic, owing to its ability to undergo epigenetic changes and readily respond to the external microenvironment, including ECM changes. 344SQ_ EVTs grown in Matrigel/Collagen I were tested for their dependency on Src signaling for invasion. Three groups were setup, with one serving as control without dasatinib, another received dasatinib at the time of seeding and the third group was allowed to invade in collagen I for 3 days before dasatinib was added to the culture. Dasatinib was able to significantly suppress invasion in both early and late conditions, emphasizing that Src is necessary for initiation and maintenance of invasion (Figure 20F, G).

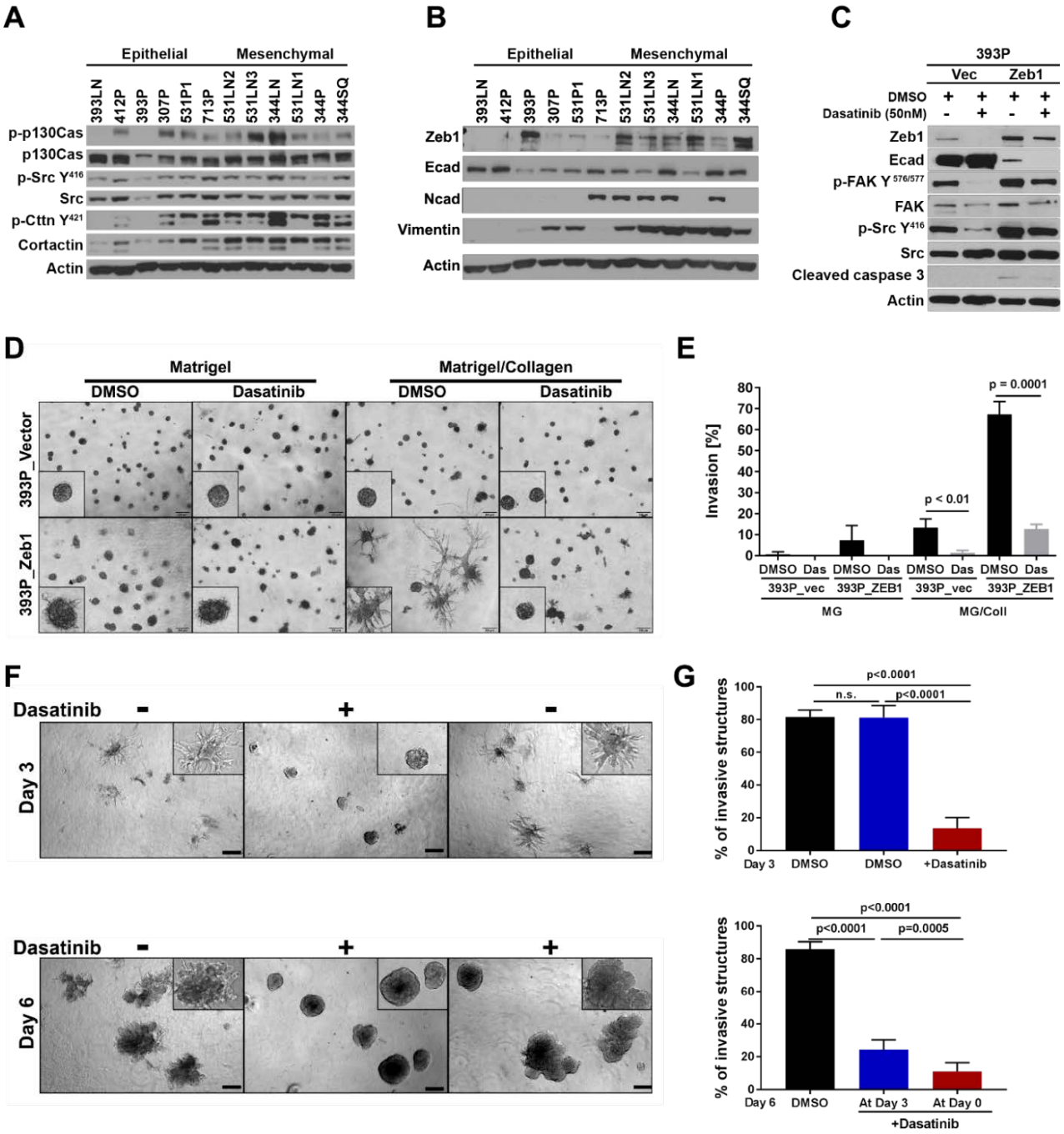

Figure 20. Src pathway is required for initiation and maintenance of invasion.
(A) Western Blot analysis shows increased Src pathway activation in the mesenchymal cells lines. (B) Western blot analysis to show the EMT markers in the murine KP cell line panel. (C) Western Blot analysis shows increased Src pathway activation in cell lines stably expressing Zeb1 which is inhibited upon treatment with dasatinib (50 nM). (D) 393P_Zeb1 and control cells grown in 3D cultures. Invasion of 393P_Zeb1 cells in a mixture of Matrigel/Collagen I (1.75 mg/ml) is inhibited upon dasatinib treatment (50 nM). Images were taken at day 7 after a 3 day treatment. (E) Quantification invasiveness of cells in 3D cultures from (D). Represented is the average of 3 wells, each measuring 30 structures in size and scoring 50 structures for invasiveness. (F) Dasatinib treatment of EVTs cultured in Matrigel/Collagen I (3 mg/ml) before (at day 0) and after initiation of invasion (day 4). Images were taken at day 3 and day 6. (I) Quantification of invasive structures before and after dasatinib treatment. For each condition, 500 structures were scored for invasiveness.
(Padhye et al, Sci Rep 9, 4819, 2019).

3.2.7 Dasatinib overcomes TGFβ mediated invasion and decrease in vivo metastases.

TGFβ is a well-known EMT inducer to which we have previously shown the metastasis-prone KP cells are quite sensitive. We next tested if Src inhibition would block the TGFβ-induced EMT. We utilized dasatinib and a second Src inhibitor, AZD0530 (saracatinib).We previously showed that inhibition of integrin β1 or the adaptor molecule CRKL significantly decreased the ability of the cells in 3D cultures to become invasive upon TGFβ treatment[115]. A similar result was seen in the combined treatment of TGFβ with the Src inhibitors, leading to a significant reduction in sphere size and invasion, which was more pronounced with AZD0530 treatment. 344SQ_EVTs cultured in Matrigel were treated with Src inhibitors alone or in combination with TGFβ. EVTs hyper-proliferated and developed invasive protrusions in response to TGFβ. This phenotype was suppressed in EVTs pre-treated with dasatinib (Figure 21A-C) or AZD0530 (Figure 21D-F). TGFβ caused an increase of canonical mesenchymal markers like Zeb1 and Vimentin and suppressed E-cadherin levels. There was also an upregulation of p-FAK and p-Src in response to TGFβ. However, Src inhibition was able to overcome TGFβ mediated FAK/Src pathway activation and the subsequent invasive phenotype, despite the TGFβ-induced EMT in EVTs observed by western blot (Figure 21C, F). These results illustrate that the Src pathway is activated through integrin β1 in an ECM-dependent manner and cell invasion can be inhibited by targeting the cell-ECM interactions or signal transduction pathways *in vitro* and *ex vivo*. We were able to demonstrate the strength of EVTs to facilitate the interrogation of tumor phenotype at multiple levels, in a high throughput manner that would not be otherwise easily attainable *in vivo*. The 344SQ cells are paradigmatic of the highly metastatic KP cells in our syngeneic murine model. To assess whether the EVT results were predictive of the *in vivo* activity of dasatinib to block the Src signaling pathway and suppress metastases, we injected syngeneic mice with 344SQ cells and dosed them with 10 or 20 mg/kg Dasatinib 5 days/week. Treatment at either concentration significantly reduced the number of lung metastases (Figure 21G, H).

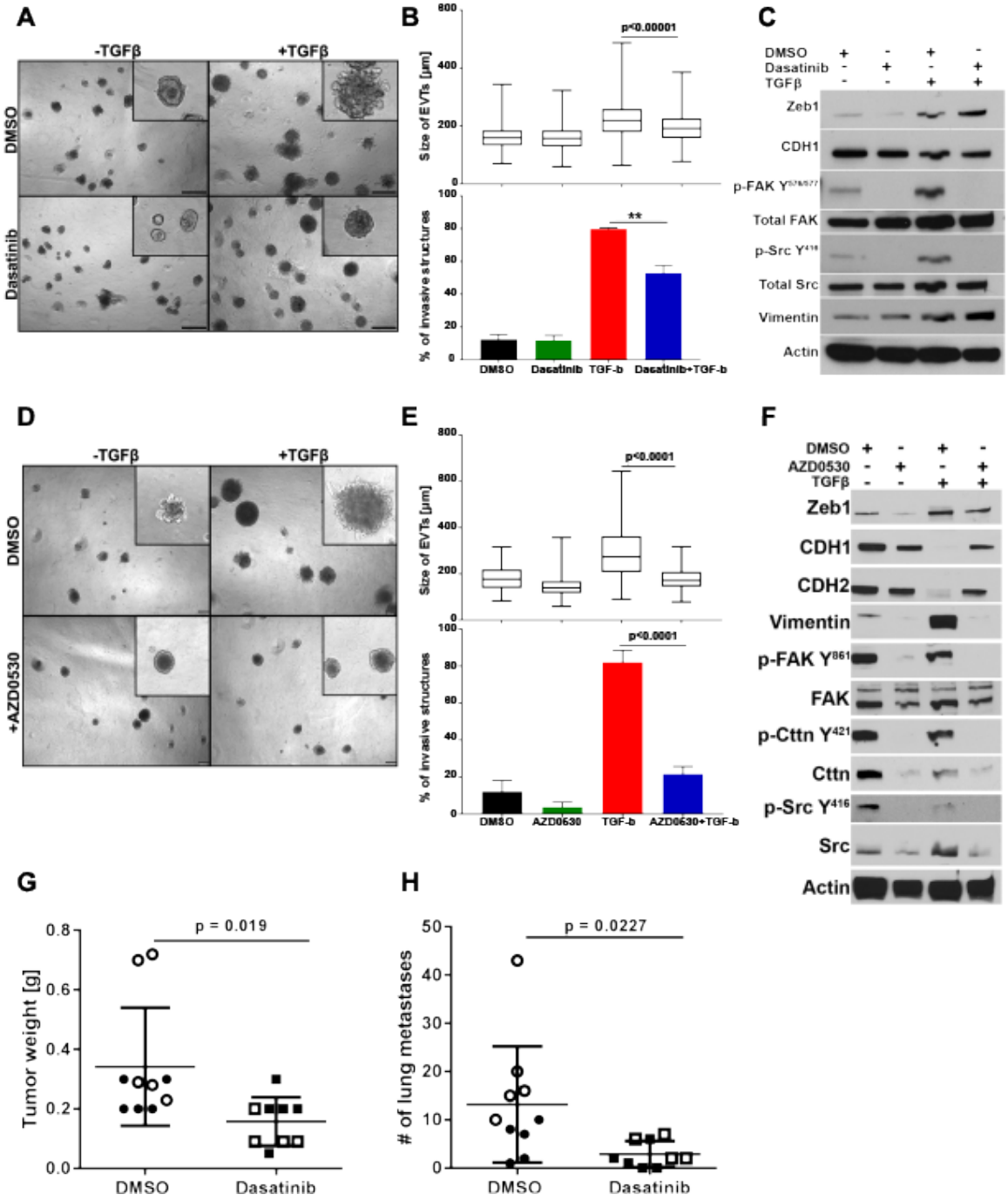

Figure 21. Dasatinib overcomes TGFβ mediated invasion and decrease *in vivo* metastases.
(A) EVTs culture in Matrigel for 8 days. Images were taken at day 8. Dasatinib (50 nM) was added at the time of seeding and TGFβ (5 ng/ml) at day 4. (B) Size of EVTs and invasiveness of EVTs on TGFβ and dasatinib treatments. (C) Western blot analysis of EVTs treated with Dasatinib and TGFβ at indicate concentrations. (D) 344SQ_EVTs culture in Matrigel for 8 days. Images were taken at day 8. AZD0530 (3 µM) was added at the time of seeding and TGFβ (5 ng/ml) at day 4. (E) Size of EVTs and invasiveness of EVTs on TGFβ and AZD0530 treatments. (F) Western blot analysis of EVTs treated with AZD0530 and TGFβ at indicate concentrations. (G) Primary tumor weight and (H) number of lung metastases in syngeneic mice treated with Dasatinib, n = 9 (10 mg/kg: solid shapes, 20 mg/kg: empty shapes) or vehicle, n = 10.
(Padhye et al, Sci Rep 9, 4819, 2019).

3.3 Discussion

The role of intra- and inter-tumor heterogeneity in driving tumor metastasis and therapy resistance has been greatly emphasized in recent years[77,91,121]. Tumors are not just a mass of cancer cells, but instead are composed of a heterogeneous tumor microenvironment, including changes in the ECM and heterotypic cell types, that dynamically interacts with tumor cells. The diverse selection pressures from the microenvironment profoundly affect the behavior and phenotype of cancer cells and must be taken into account while studying mechanisms that drive cancer progression. The goals of this study were to establish a unique system to better model *in vivo* conditions, identify mechanisms driving invasion of mesenchymal lung cancer cells and demonstrate the ability to identify therapeutic sensitivities of tumor cell subsets dependent upon the microenvironmental interactions.

The *Ex Vivo* Tumors (EVTs) utilized in this study are micro-tumors derived from immunocompetent murine syngeneic tumors and cultured in 3D matrices. We determined that EVTs faithfully represent the cellular composition of tumors and retain the heterotypic heterogeneity within tumors. A decline of heterotypic cell types was observed in culture over time in the absence of additional stimulatory factors. However, such factors can be included in subsequent studies in order to study specific interactions of tumor cells with heterotypic cell types. These features demonstrate that the EVT platform can be used to study micro-tumors and investigate influences of non-tumor cells in a high throughput manner which cannot be achieved with conventional 2D or 3D cell cultures.

EVTs were functionally characterized by investigating their responses to external manipulations like growth factors and matrix alterations. Using a laminin rich matrix we recapitulated a basement membrane-like microenvironment and EVTs were non-invasive even though primary tumors are highly metastatic[93]. This underlines the importance of architecture and contextual cues in growth of tumor cells which are lost in monolayer cell

cultures. TGFβ induced a central EMT and invasive phenotype in tumor cells. ECM modification promoted an invasive phenotype in EVTs without altering the EMT state of the tumor cells. This finding is in contrast to previously observed collagen I-mediated EMT in tumor cells through autocrine TGFβ signaling[122]. However, it is known that ECM components actively interact with tumor cells for malignant progression through a variety of signaling cues modulating cellular behavior, ranging from tumor cell survival to invasion and metastasis[123,124] and TGFβ-mediated signaling may be independent of collagen I influence. It also indicates that EVTs are more amenable to dynamic phenotypic alterations, which may be attributable to the presence of distinct tumor cell subpopulations. This emphasizes the importance of investigating TME-tumor cell interactions in the context of tumor cell heterogeneity. Monolayer cell cultures of tumor cells are unable to capture this heterogeneity and hence have limited biological relevance.

Based on the effect of ECM composition on tumor cell phenotype observed in our system, we investigated the signaling downstream of collagen I-integrin β1 interactions as responsible for driving invasion and metastasis. An increased activation of Src signaling pathway molecules in mesenchymal cells suggested a dependency on p-Src for their invasive phenotype. Src inhibition has been shown to decrease migration *in vitro*, tumor growth and invasion *in vivo* in NSCLC using murine xenograft models[125,126]. Dasatinib has also shown to improve antitumor activity if anti-PD-1 by inhibiting T-regs cell population within tumors[127]. Furthermore, inhibition of Src using the ATP binding competitive inhibitor dasatinib decreased the development of liver metastases in a murine model of pancreatic carcinoma and caused a decrease in cell adhesion, migration and invasion in colon cancer cell lines. In thyroid cancer cell lines, dasatinib was shown to have a cytostatic activity both *in vitro* and *in vivo* causing cell cycle arrest and an increase in senescence[128]. Tumor cells in our 3D matrix experiments demonstrated that Src-mediated invasion was substrate dependent. Type I collagen in the matrix enhanced p-Src expression in tumor cells, which was abrogated upon treatment with Src inhibitors. Pharmacological inhibition of Src was sufficient to prevent

initiation and maintenance of invasive structures in 3D cultures with collagen I, further demonstrating the importance of Src signaling in lung cancer cells. TGFβ is a well-known inducer of EMT and subsequent invasive phenotype. TGFβ has also been shown to mediate cell adhesion to ECM and increased collagen I synthesis in a Src-dependent manner[129]. We wanted to test the hypothesis if Src inhibition is sufficient to overcome TGFβ-mediated invasion. A combination treatment with TGFβ and pharmacological Src inhibitors prevented invasion, despite EMT, emphasizing the high dependency of tumor cells on Src signaling. These findings were in concert with another study which demonstrated Src inhibition could overcome TGFβ induced myofibroblast differentiation[130]. Furthermore, *in vivo* studies showed a significant decrease in metastases with Src inhibition. We identified collagen I-integrin β1 activated Src signaling as a major driver of invasion and metastasis in lung cancer. Combined with our previous findings, ITGβ1 and Src are interesting targets for a combinatorial treatment approach in lung cancer. Invasion mediated through the Src signaling pathway demonstrates the utility and applicability of EVTs as a potent tool for mechanistic interrogation of invasion and metastasis in lung cancer. The tumor model presented here incorporates tumor cell and tumor microenvironment heterogeneity arising *in vivo* in response to different selection pressures. It also retains the ability of tumor cells to respond to the intrinsic (Zeb1 expression in cells) and extrinsic manipulations (matrix and soluble factors). This suggests that phenotypic differences between tumor cells arise due to their differing ability to interact with the stromal components around them as much as due to genetic differences.

Our next step is to expand the EVT system by introducing cellular complexities and accounting for the effect of tumor cell and tumor microenvironment heterogeneity. Early work led by Bissell and colleagues in the field was landmark to establish the significance of three-dimensional models in normal breast epithelial differentiation and tumor cell morphogenesis[131-134]. The role of cell-cell and cell-matrix interaction has been widely emphasized for recapitulating tissue architecture, tissue morphogenesis, and epithelial organization and these aspects become significantly more important when investigating

biological phenomenon in cancer cells. Following the pioneering work in normal and malignant breast tissue, the field rapidly expanded to simulate 3D growth of different organs such as skin[135,136], bone[137,138], brain[139,140], pancreas[141,142] , colorectal[143] and prostrate[144,145]. The most commonly used three dimensional systems to recapitulate tumor growth are usually monocultures of cancer cells[112 146] or co-cultures to study heterotypic interactions between tumor cells and other cell types like CAFs or immune cells[113,147] where multicellular spheroids are cultured in artificially created environments. A common objective for many of these studies is to serve as an intermediate between the use of whole animals at one end of the spectrum and cellular monolayers at the other, but are limited to studying a single TME component or a unidirectional effect. However, these models have been limited to interactions between one component of the TME with the tumor cells[148]. EVTs have a distinct advantage of recruiting TME cellular components and retaining the integrity of a tumor which confers the ability to investigate specific roles of TME components in the tumor progression[118,149]. In addition to heterotypic heterogeneity, we are able to account for tumor cell heterogeneity in the system. We have a large panel of murine NSCLC cell lines isolated from Kras/p53 GEM model from the primary and metastatic tumor sites, which demonstrate phenotypic differences. When re-implanted subcutaneously or orthotopically in syngeneic animals, the cell lines demonstrate varying metastatic potential and differential interactions with the TME components *in vitro*[39,44,150,151]. Therefore, EVTs derived from different cell types can allow us to tease out the tumor cell heterogeneity modulated by cell intrinsic and extrinsic manipulations, creating a robust tool for investigating lung cancer progression.

Multiple groups have also demonstrated that in addition to recapitulating tissue morphology, the intracellular signaling characteristics are more accurately represented in 3D cultures[152-155]. Birgersdotter et al[156], Li et al[157] and Luca et al[158] demonstrate considerable differences in gene expression and mRNA splicing patterns when cells are cultured under 2D versus 3D conditions. Other studies have utilized 3D tumor spheroid-based functional assays for target validation and drug evaluation and have demonstrated that sensitivity and response

of cancer cells to different compounds can vary between 2D and 3D cell cultures[159]. Organization of tumor cells in polarized structures in an integrin β4-dependent manner imparted resistance to apoptosis in mammary epithelium suggesting signaling pathways determining sensitivity to drugs can vary based on the tissue architecture[160].

It is now widely accepted that the response of tumor cells to drug treatments is not dependent on oncogenic drivers alone. The TME plays a very significant role in modulating the outcome of therapeutic interventions[77,161-165]. Multiple groups have attempted to capture the complexity of the microenvironment and test therapeutic sensitivity to drug treatments. For example, tumor cells have been cultured in different matrices to identify ECM combinations driving lung cancer[163,166]. Ex vivo systems to test the efficacy of immune checkpoint blockade are also currently being employed for facilitating efforts in precision immune-oncology[167,168]. Work done by such groups has given great insights into individual heterotypic interactions, however, these studies have been conducted using cell lines in an artificially created environment. Our tumor model incorporates cells from a tumor's microenvironment allowing us to maintain the complexity of the tumors in a physiologically relevant context. Building on the groundwork in the present study, this approach can be utilized in a high throughput manner to investigate tumor cell and microenvironment heterogeneity in lung cancer metastasis and resistance to drug treatments.

Chapter 4: Tumor cell heterogeneity: EMT and tools to study

Contents of this chapter are derived from the publication Jessica M. Konen, B. Leticia Rodriguez, Aparna Padhye, Joshua K. Ochieng, Laura Gibson, Lixia Diao, Natalie W. Fowlkes, Jared J. Fradette, David H. Peng, Robert J. Cardnell, Jeffrey J. Kovacs, Jing Wang, Lauren A. Byers and Don L. Gibbons. Cancer Res March 1 2021 (81) (5) 1398-1412; DOI: 10.1158/0008-5472.CAN-20-1895 with approval from American Association for Cancer Research.

4.1 Introduction

The epithelial-to-mesenchymal transition (EMT) is an epigenetic event that is required by cells to maintain normal biological processes such as organogenesis, tissue healing and embryonic development and is evolutionarily conserved[169 170]. It is a dynamic process which allows cells to acquire distinct phenotypic states in a bi-directional manner, across a spectrum. At one of the spectrum is an epithelial state characterized by tight cell junctions and apico-basal polarity and at the other end of the spectrum is a stem-like mesenchymal state with increased ability to self-renew and migrate[171]. Cancer cells are capable of activating this process to acquire more aggressive phenotype, including an increased metastatic potential and acquisition of therapeutic resistance. The ability of cancer cells to slide on the spectrum of different epigenetic states allows cancer cells to handle diverse environmental stressors which contributes to phenotypic heterogeneity. Accompanying alterations at the molecular level have been extensively studied, including transcriptional reprograming in cancer cells and have been correlated with tumorigenicity and metastatic propensity across several tumor types[172-176], highlighting the importance of this complex process in driving tumor progression. In non–small cell lung cancer (NSCLC), the ZEB1/miR-200 double negative feedback loop is a tightly regulated axis that can lead to EMT via upregulation of ZEB1 and concurrent downregulation of epithelial features, including the miR-200 family, E-cadherin, and other epithelial differentiation genes[93,177-179]. Moreover, tumor microenvironment components such as extracellular matrix (ECM)[39] and cancer associated fibroblasts (CAFs)[53] drive a mesenchymal phenotype in cancer cells. Upon EMT, cancer cells are more motile and

invasive, and this process can initiate the metastatic cascade. Besides an increase in invasiveness and metastatic propensity, mesenchymal tumor cells also gain characteristics that promote aggressiveness, including stem cell–like features and drug resistance. Enrichment of EMT markers at the RNA, protein and phenotypic levels has been described after exposure to a broad spectrum of therapeutic modalities, including hormonal therapies, chemotherapies, radiotherapy and many targeted therapies[180]. Thus, to improve prevention and treatment strategies, it is critical to better understand the survival dependencies of cells along the epithelial-to-mesenchymal spectrum.

Methodologies that are generally utilized to study cancer cells undergoing EMT include cell lines *in vitro* and pathological specimens from tumors. These assays are either bulk assays like western blot analysis, or endpoint assay such as immunohistochemistry. These techniques preclude the assessment of the real-time, dynamic shifts in the phenotype of cancer cells within a heterogeneous population. In order to address these deficiencies, we utilized a dual fluorescent reporter system that functions as a sensor for dynamic monitoring of EMT states[106]. In a highly metastatic KP-mutant murine cell line, we expressed the Z-cad reporter and analyzed the impact of alterations in the matrix and drug treatments on epithelial and mesenchymal subpopulations over time in two- and three-dimensional (2D and 3D) culture model systems. We demonstrate that Z-cad cells are capable of demonstrating distinct EMT states in response to external manipulations in real time by fluorescent imaging. When combined with the EVTs platform, Z-cad EVTs served as heterogeneous micro-tumors which were very useful for screening for therapeutic agents targeting distinct cancer cell subpopulations.

4.2 Results

4.2.1 Z-cad sensor cells detect the EMT status of tumors cells in real-time.

In order to understand the role phenotypically distinct tumor cells in cancer progression, we utilized fluorescence protein tagged epithelial 393P and mesenchymal 344SQ cells. Multi-cellular aggregates (MCAs) were generated by culturing cells either alone or in together 1:1 ratio in microwells as described in Chapter 3. MCAs were cultured in Matrigel for 8 days (Figure 22A). Over a course of 5 days, there was a significant increase in the size of the MCAs. Dual MCAs demonstrated the presence of both cell types but appeared smaller in size. Despite modeling tumor cell heterogeneity, the challenge was to determine whether there was dynamic shift in phenotypic status of tumor cells along the EMT spectrum within mosaics. Therefore, we utilized the dual fluorescence reporter system stably transfected in 344SQ cancer cells to detect EMT status of cancer cells in real-time. Briefly, this two-plasmid sensor system, termed the Z-cad sensor, uses one construct with a destabilized GFP linked to the 3′ UTR of Zeb1 and a separate plasmid with RFP expressed downstream of the E-cadherin promoter (Figure 22B). When cells are in a mesenchymal state, the endogenous ZEB1 protein levels are high, leading to suppression of its targets including miR-200 and E-cadherin, and thus RFP expression. In an epithelial state, high miR-200 levels downregulate ZEB1 levels post transcriptionally via its 3′UTR, decreasing the GFP signal. The suppression of ZEB1 leads to the derepression of the E-cadherin promotor and increased RFP expression. We co-expressed the Z-cad sensor plasmids in the mesenchymal 344SQ murine cell line (344SQ_Z-cad). We utilized the 344SQ because they display greater plasticity and readily undergo MET under different conditions[44,93]; thus, they were an ideal cell line to test the dynamic readout of the Z-cad reporter.

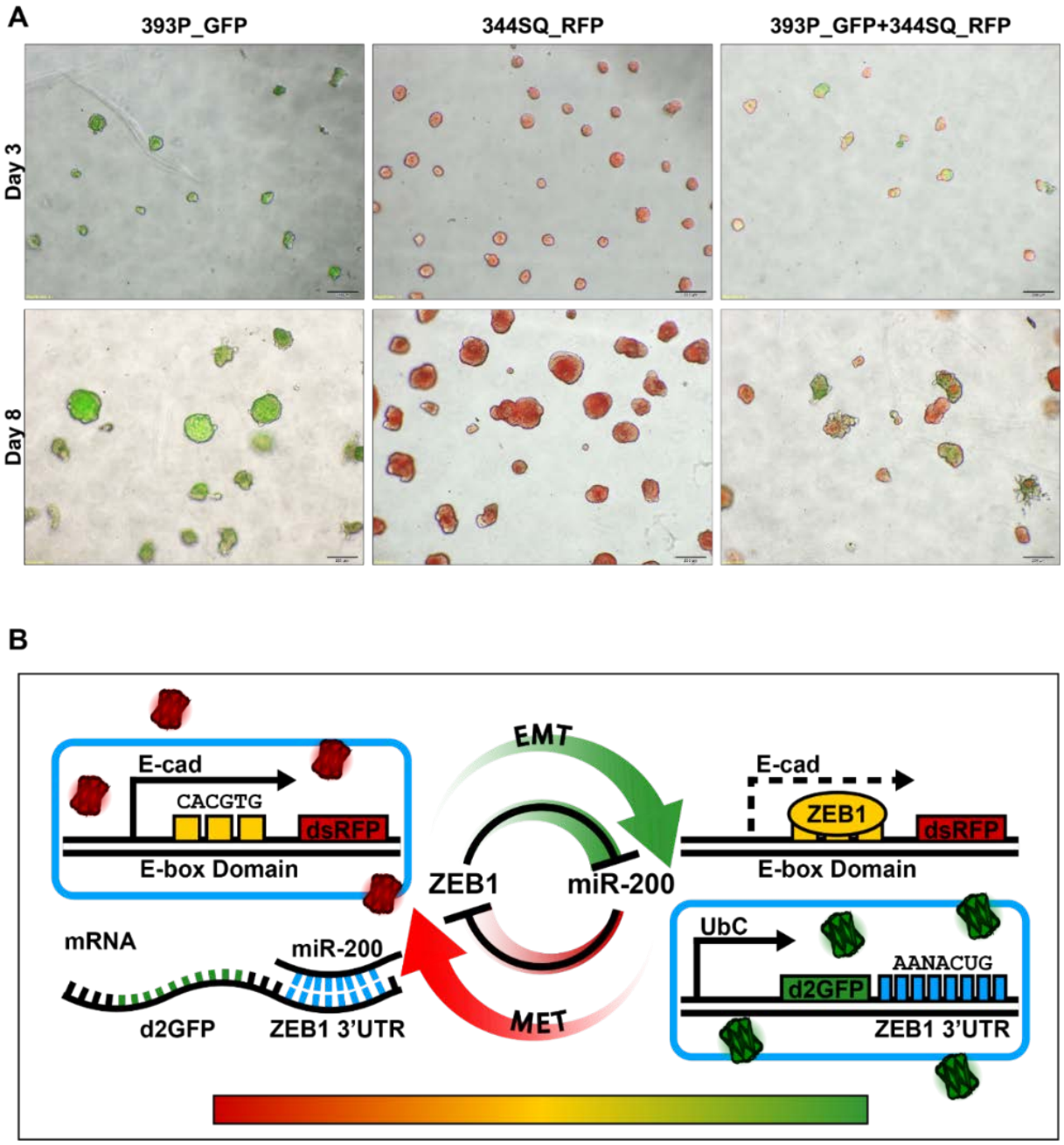

Figure 22. Tools to study EMT mediated tumor cell heterogeneity.
(A) Mosaics derived from epithelial 393P_GFP and mesenchymal 344SQ_RFP cells were cultured in Matrigel to study tumor cell heterogeneity. (B) Schematic diagram illustrating the Z-cad dual sensor constructs. The d2GFP-Zeb1 3′UTR construct constitutively expresses destabilized GFP under the control of a ubiquitin promoter. The Zeb1 3′ UTR, which contains eight miR-200–binding sites, is expressed downstream of d2GFP. The E-cad-RFP construct contains the E-cadherin promoter, with 3 E-box domains. This promoter regulates the expression of RFP.

We confirmed the functionality of the sensor in detecting each phenotypic state. In 2D culture, the 344SQ_Z-cad cell line is approximately 58% GFP+ at baseline by fluorescent imaging, whereas only approximately 4% of the population is RFP+ (Figure 23A)[181]. To determine that the sensor responds in a dynamic manner to EMT-promoting conditions, the 344SQ_Z-cad cells were stimulated with TGFβ1 to further induce a mesenchymal state. As expected, the addition of TGFβ1 significantly increased the percentage of GFP+ cells within 24 hours, with a significant decrease in the RFP+ epithelial cells occurring within 2 days and continuing throughout the experiment (Figure 23A). We also performed scratch assay to determine which cell subtype had a greater migratory capacity. After 2 days, GFP+ cells were detected at the leading edge which was expected as mesenchymal cancer cells have greater migratory, invasive and metastatic potential (Figure 23 B). The phenotypically plastic 344SQ cells can shift their EMT status based on external stimuli. When cultured in a 3D laminin-rich Matrigel matrix, the cells form polarized epithelial spheres[93]. Thus, we tested whether these epithelial structures were also RFP+ by plating the 344SQ_Z-cad cells in a Matrigel matrix. Fluorescent imaging and flow cytometry confirmed that while 50% GFP+ after initial plating, each day in Matrigel caused a reduction in the GFP+ subpopulation with a steady increase in the RFP+ population (Figure 23 C, D). After 9 days in culture, the 3D structures were roughly 40% RFP+ and <10% of cells maintained GFP expression. Again, addition of TGFβ1 at day 5 of 3D culture stimulated EMT and produced GFP+ expression within 24 hours (Figure 23 C, D) overcoming the influence of the Matrigel matrix. Additional characterization of the 344SQ_Z-cad cells were published by our group (Konen et al[181]).

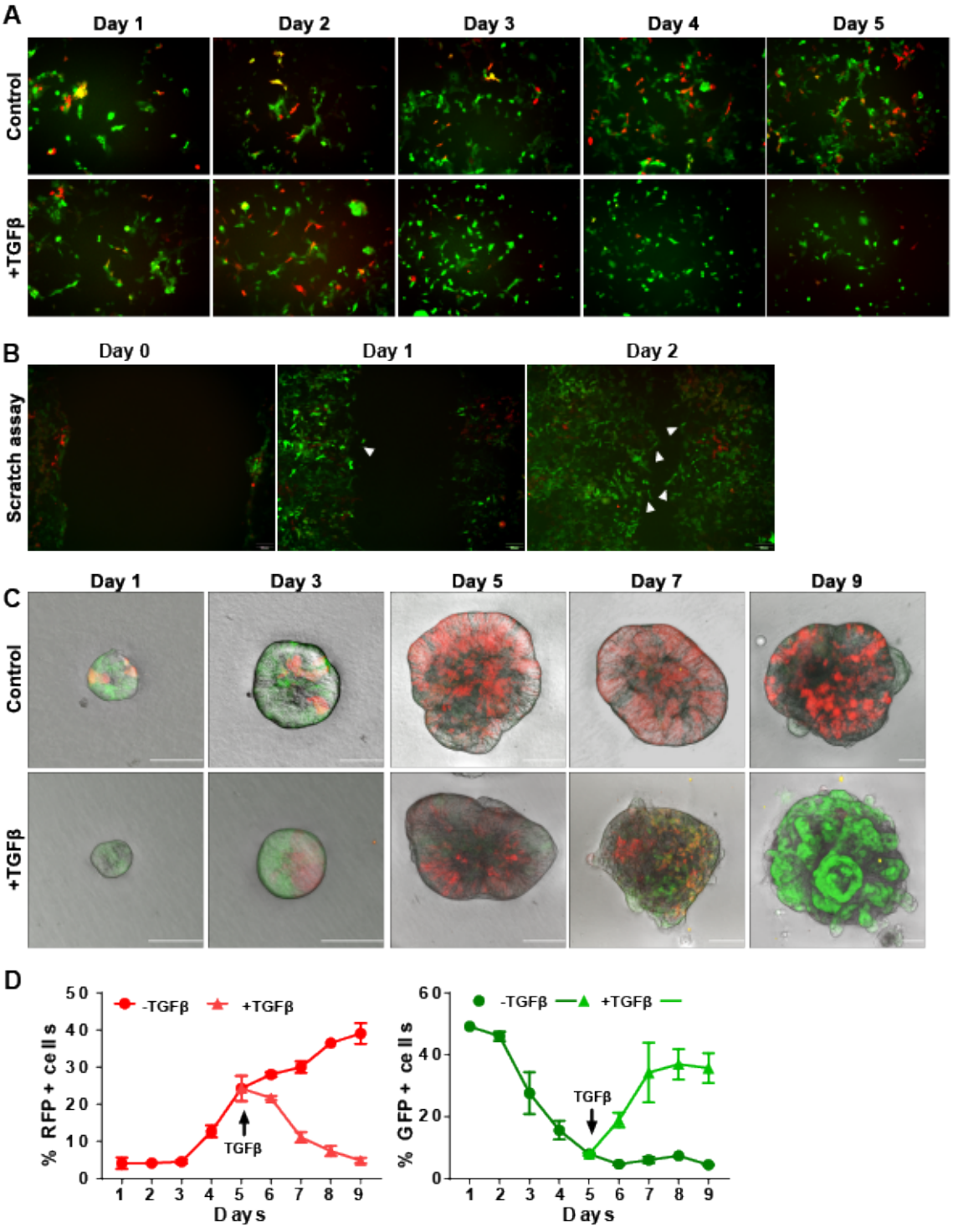

Figure 23. Z-cad sensor cells detect the EMT status of tumors cells in real-time.
(A) The 344SQ_Z-cad cells were grown over 4 days with and without TGFβ (5 ng/mL), and fluorescent microscopy was performed. Representative images are shown. (B) Scratch assay performed on Z-cad cells and observed for 48 hours to determine migratory subpopulations. (C) Fluorescent confocal images were acquired of 344SQ_Z-cad cells plated on a Matrigel matrix. On day 5, TGFβ (5 ng/mL) was added. Confocal images acquired over 9 days, and representative images are shown on each day. (D) Flow cytometry of the percentage of GFP+ and RFP+ cells was performed on the 344SQ_Z-cad 3D spheres grown over 9 days as described in E.
(Konen et al, Cancer Res March 1 2021 (81) (5) 1398).

As demonstrated in Chapter 3, our EVT setup is capable of modeling tumor microenvironment and therefore capture the heterogeneity within murine tumors. Since we had two strong experimental models for tumor heterogeneity, we decided to combine them to increase the complexity of EVTs. We implanted 344SQ_Z-cad cells in syngeneic wild type mice and allowed the tumors to develop for 4 weeks. At the time of necropsy, we collected tumors and processed them to yield EVTs (as mentioned before) as well as collected a representative sample for analysis of subpopulations within the tumors. We detected presence of both GFP+ and RFP+ cells in the tumors (Figure 24 A-D). We also generated MCAs from 344SQ_Z-cad cells taken from 2D culture and grown in microwells for a day. These were used as a comparison for the Z-cad_EVTs which clearly demonstrated more tumor cell heterogeneity than the pure MCAs (Figure 24 C, D).

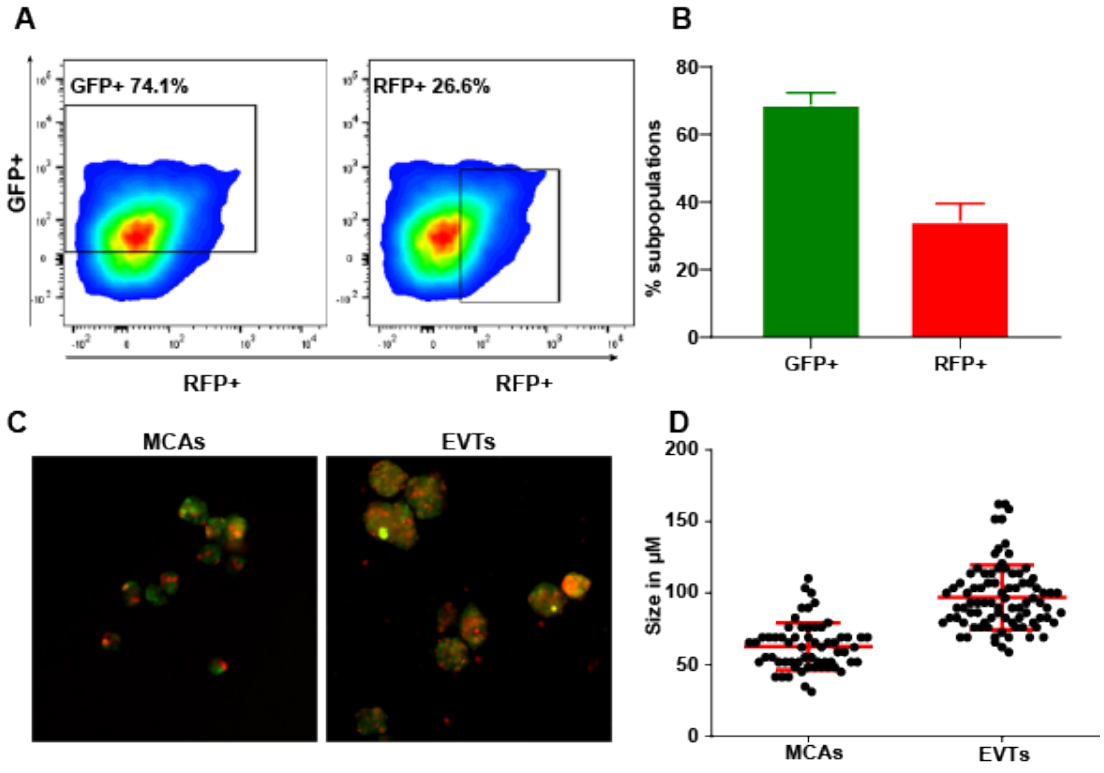

Figure 24. Z-cad cells cultured as MCAs and EVTs.
(A) Representative dot plot of the percentage of GFP+ and RFP+ cells from a single 344SQ_Z-cad tumor. (B) Quantification of subpopulations in 344SQ-Zcad tumors. (C) 344SQ-Z-cad MCAs and EVTs after one day in culture in microwells. (D) Size of spheres derived from (C).

4.2.2 Z-cad EVTs alter phenotype in response to matrix manipulation.

After characterizing Z-cad cells and EVTs in terms of subpopulations, we wanted to confirm that Z-cad_EVTs retained their biological behaviors to external manipulations. For each assay, the Zcad_EVTs were cultured in microwells (MW) for one day before transferring to respective matrices. First we cultured the EVTs in laminin rich Matrigel. At the beginning of the assay, we observed a mixture of both RFP+ and GFP+ cells. However, continuous signals from Matrigel lead to an enrichment of RFP+ epithelial cells over 5 days as we have previously noted in our studies (Figure 25 A, B). Treatment with TGFβ drove the phenotype in the opposite direction, making the EVTs increasingly GFP+ as well as highly invasive (Figure 25 A, B, D). We confirmed that there was induction of EMT at the molecular level by collecting the EVTs from Matrigel and analyzing by qPCR for EMT markers ZEB1 and E-cadherin (Figure 25 C).

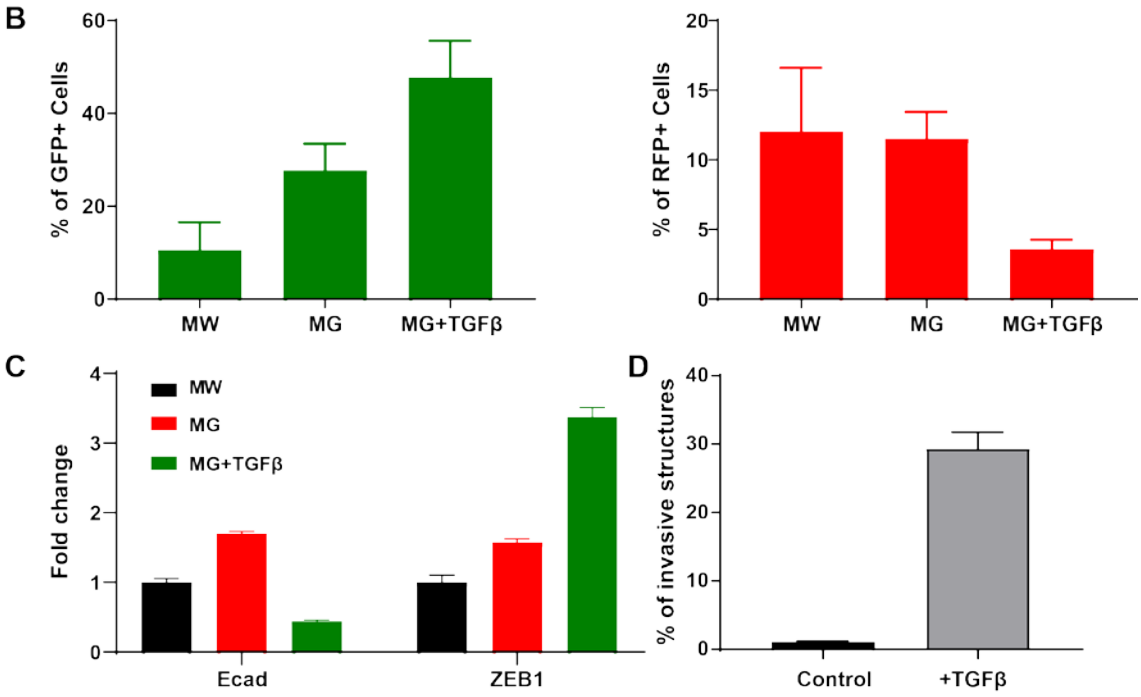

Figure 25. Z-cad EVTs alter phenotype in response to external stimulants.
(A) Fluorescent confocal images of 344SQ_Z-cad EVTs cultured in Matrigel matrix for 5 days. EVTs were treated with TGFβ (5 ng/mL) one day after seeding. (B) Flow cytometry of the percentage of GFP+ and RFP+ cells was performed on EVTs in (A). (C) Real-time PCR (qPCR) analysis for relative expression of ZEB1 and E-cadherin of EVTs treated with TGFβ. (D) EVTs are highly invasive in response to TGFβ with enrichment of GFP+ cells.

When Z-cad_EVTs were cultured in Matrigel/Collagen I for 5 days, a depletion of RFP+, an enrichment of GFP+ cells as well as very invasive phenotype was observed (Figure 26A,B,D). Cells in the center of the sphere retained epithelial phenotype and were largely non-invasive. Treatment with dasatinib prevented the emergence of invasive phenotype (Figure 26A,D), however, did not necessarily promote an epithelial phenotype. This was in contrast with our previous observations where treatment with dasatinib induced an MET in wild type EVTs after about 8 days of treatment. With a long term treatment, we would expect to see similar results and this effect of Src-inhibitor on mesenchymal subpopulations needs further exploration. There was a moderate suppression of E-cadherin in Matrigel/Collagen, whereas ZEB1 levels remain unchanged (Figure 26C). The lack of significant changes in EMT markers can be due to one of 2 reasons: the signal is muted or missed because qPCR is a bulk assay or that ECM is driving the invasive phenotype of the tumor cells without inducing

epigenetic changes that result in a mesenchymal state. The complex interplay between epigenetic state and influence of the ECM on tumor cell phenotype warrant further investigations.

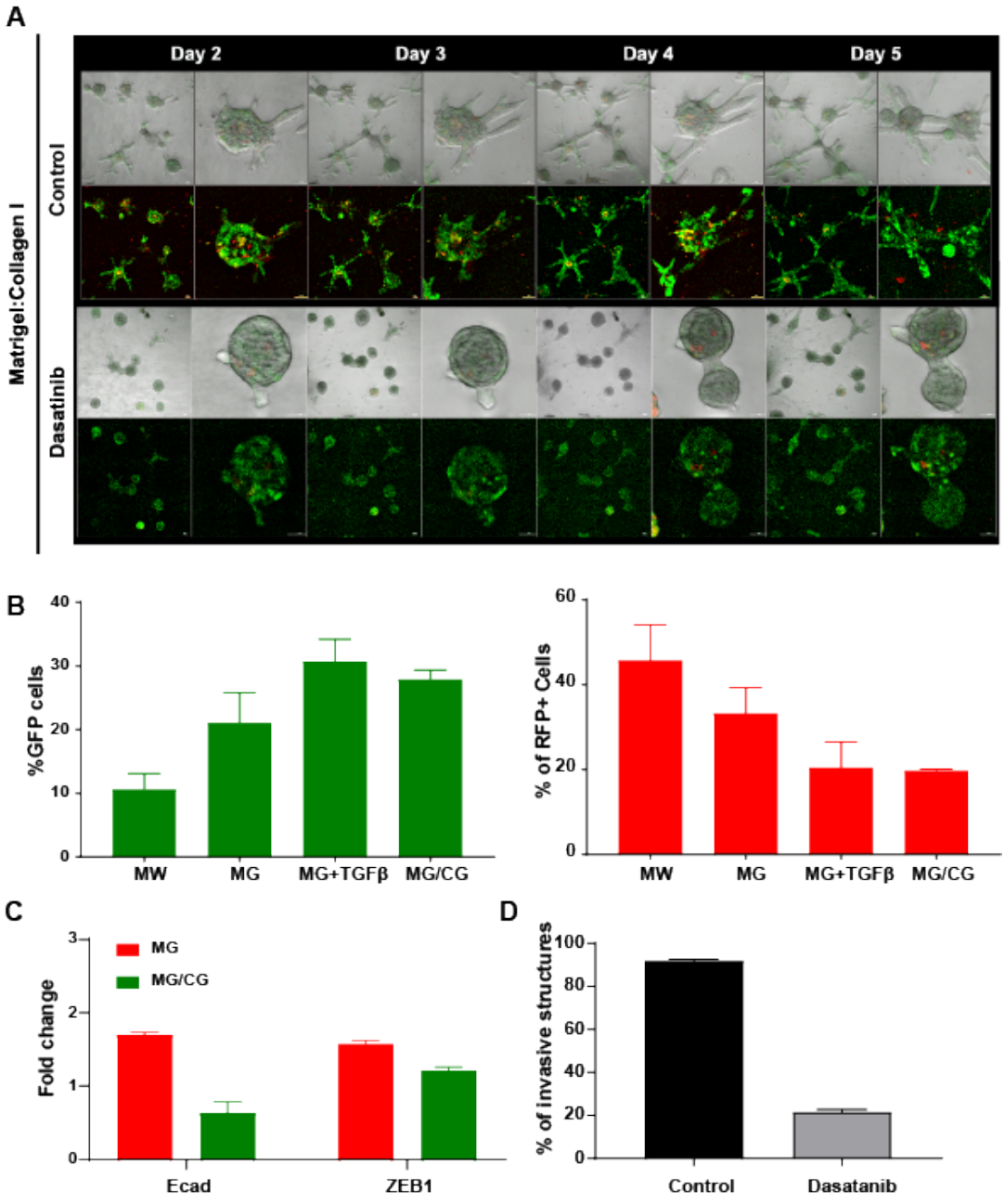

Figure 26. Z-cad EVTs alter phenotype in response to matrix manipulation.
(A) Fluorescent confocal images were acquired of 344SQ_Z-cad EVTs cultured in Matrigel/Collagen I (3 mg/ml) matrix for 5 days. EVTs were treated with dasatinib (50 nM) one day after seeding. (B) Flow cytometry of the percentage of GFP+ and RFP+ cells was performed on EVTs in (E). (C) Real-time PCR (qPCR) analysis for relative expression of ZEB1 and E-cadherin of EVTs in Matrigel and Matrigel/Collagen I. (D) EVTs are highly invasive Matrigel/Collagen I. Invasion is overcome with treatment of dasatinib.

4.2.3 Screening of pharmacological agents to target EMT using Z-cad sensor cells.

We next utilized the Z-cad sensors for testing the selective sensitivity of cancer cell subpopulations to different therapeutic agents. Mocetinostat, an HDAC-1 inhibitor, is a known to induce MET by upregulation of miR200[182]. We used it mocetinostat as a positive control to demonstrate the shift in EMT states. When 344SQ_Z-cad cells in 2D and Z-cad_EVTs in Matrigel were treated with mocetinostat, there was significant enrichment of RFP+ epithelial cells with a depletion of GFP+ cells (Figure 27A, B). On the other hand, as previously noted, MEK inhibitors are very effective in targeting Kras-mutant epithelial cells whereas mesenchymal cells remain largely resistant. These findings were confirmed when Z-cad cells and EVTs were treated with the MEK inhibitor AZD6244 (selumetinib), as significant decrease in viable RFP+ cells showed that MEKi preferentially targeted epithelial cells (Figure 27A, B). In fact, published work from our lab has shown that treatment with mocetinostat can sensitize murine tumors to selumetinib by inducing MET in mesenchymal subpopulations and therefore aid in overcoming therapeutic resistance[103].

We wanted to further expand our findings to identify effective combination strategies for targeting both epithelial and mesenchymal tumor cells. We integrated the information from published shRNA screens and RPPA datasets to narrow down potential targets, which can be found published by our group (Konen et al[181]). Two top hits, CDK4 and AXL, were significantly and differentially depleted in mesenchymal cancer cells. 344SQ_Z-cad cells and EVTs were treated with selective inhibitors for each, palbociclib and bemcentinib (BGB324), respectively. Flow cytometry analysis from 344SQ_Z-cad cells treated with single agents found that palbociclib and bemcentinib treatment significantly decreased the GFP+ viable population (Figure 27A, B). The information from preliminary drug screen provided sufficient evidence to further follow-up 2 combinations: MEKi + CDK4i and MEKi + AXLi, for targeting tumor heterogeneity mediated by EMT. MEKi + CDK4i combination was extensively evaluated and details can be found in Chapter 4. Part of the findings from MEKi + AXLi

combination are shown in Figure 27C-E. We embedded the 344SQ_Z-cad cell lines within a 3D matrix and treated with single agent or combination of selumetinib and bemcentinib. To quantify, we calculated the percentage of the colored pixels that are either GFP or RFP per field of view (Figure 27C, D). Selumetinib treatment caused an enrichment in GFP+ structures whereas bemcentinib had little effect, likely due to the lower percentage of GFP+ cells at baseline. Therefore, we also utilized a collagen type I and Matrigel (Coll/MG) matrix, which promotes a mesenchymal phenotype as shown in Figure 27E. In a Coll/MG matrix, 344SQ_Z-cad structures were 68% GFP+ at baseline (Figure 27C, D). Treatment with selumetinib had little impact in this matrix; however, bemcentinib significantly enriched the epithelial RFP+ population. In both matrices, the combination of selumetinib and bemcentinib returned the RFP and GFP percentages to about 50:50, suggesting that both tumor cell subpopulations are being targeted equally. We also analyzed the viability of these 3D structures in single-agent and combination treatments. In MG, selumetinib significantly decreased cell viability, whereas bemcentinib had no significant effect. Combining selumetinib and bemcentinib significantly decreased viability compared with single-agent MEK inhibition. In Coll/MG, both single agents decreased viability to about 50%, whereas the combination had a greater impact than either single agent (Figure 27E). Further *in vitro* and *in vivo* validation of this combination can be found in the study by Konen et al[181]. Together, the data provides rational drug combination that co-targets MEK and AXL signaling pathways. This combination works effectively to target cells in an epithelial or mesenchymal phenotypic state, leading to significant repression of tumor growth and prevention of resistant outgrowth by targeting EMT-related tumor heterogeneity.

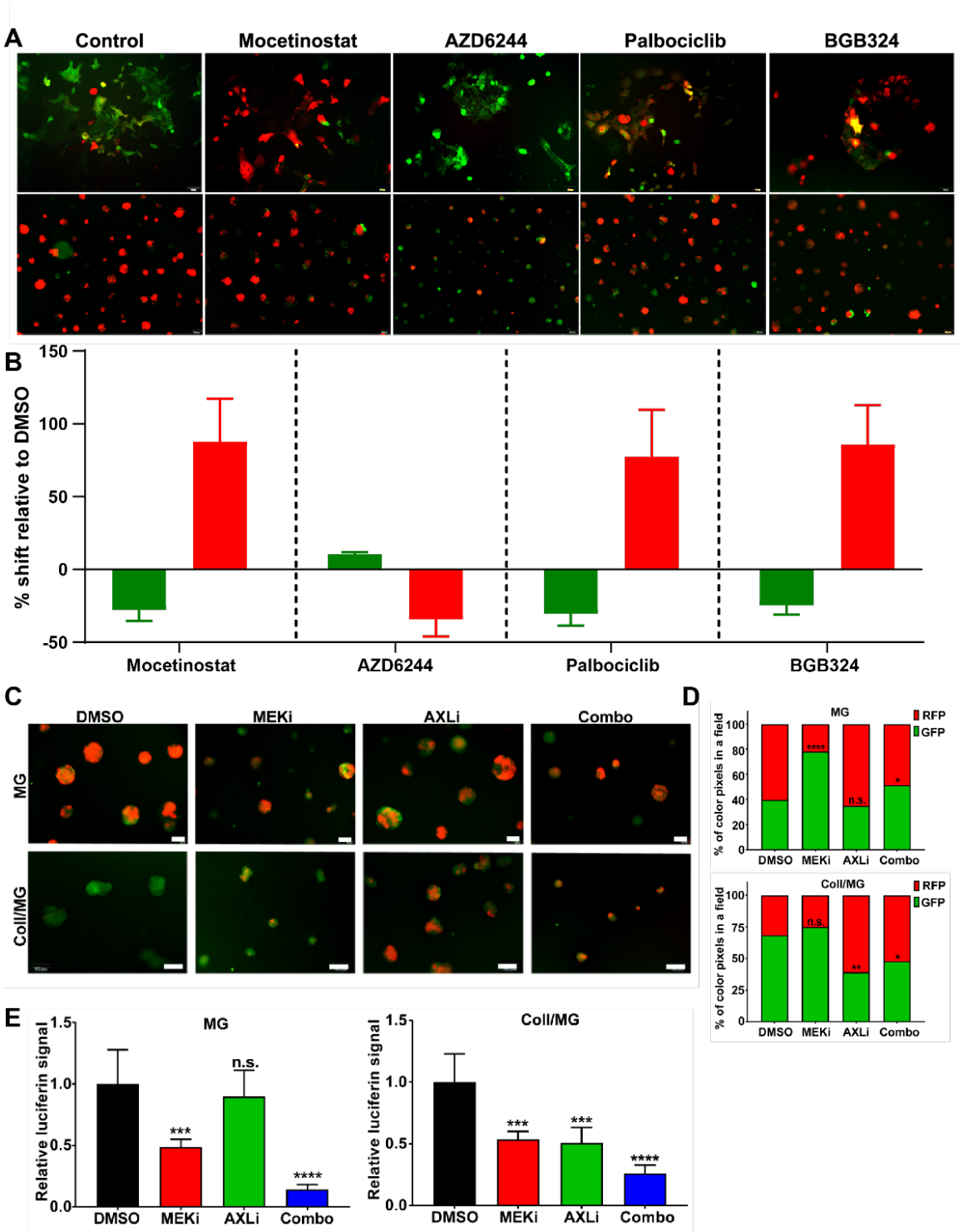

Figure 27. Z-cad cells can detect differential drug sensitivities of cancer subpopulations. (A) 344SQ_Z-cad cells and EVTs were treated with DMSO, mocetinostat (1 μM), AZD6344 (5 μM), palbociclib (5 μM) and BGB324 (5 μM) in 2D culture (top) and Matrigel matrix (bottom). (B) Flow cytometry quantification of the shift in GFP and RFP subpopulations in response to each treatment in 2D culture. (C) 344SQ_Z-cad cells were plated on a Matrigel (MG) or a Collagen I/Matrigel (Coll/MG) matrix. Two days after seeding, DMSO, AZD6244 (MEKi) (5 μM), BGB324 (AXLi) (2 μM), or the combination (combo) were added. Fluorescence microscopy was then performed, and representative images are shown on day 7 (MG) or day 5 (Coll/MG). Scale bar = 100 μM. (C) Images obtained from (B) were quantified for the percentage of RFP or GFP pixels (D) 344SQ_Z-cad cells were plated in Matrigel (MG) or Collagen/Matrigel (Coll/MG) matrix. After 24 hours, structures were treated with DMSO, MEKi (5 μM), AXLi (2 μM), or the combination. After 4 days of treatment, Cell Titer-Glo reagent was added and luminescence measured. *(Konen et al, Cancer Res March 1 2021 (81) (5) 1398)*

4.3 Discussion

EMT is a well-studied but complex and dynamic epigenetic reprogramming event that promotes tumor progression, metastasis, and drug resistance, facilitating cancer cell adaption to conditions within the TME to ensure survival and thereby producing considerable cellular heterogeneity. With a selective drug screen combined with models capturing tumor heterogeneity, we identified distinct therapeutic sensitivities in heterogeneous tumor subpopulations to prevent EMT-mediated escape. As the miR-200/Zeb1 axis is critical for EMT, this was an ideal model to evaluate EMT shifts in the face of ECM changes and targeted agent treatments. By expressing the Z-cad sensor in the murine 344SQ cells, we determined that collagen I promoted a mesenchymal phenotype, MEKi selumetinib and AXLi bemcentinib specifically target RFP+ epithelial and GFP+ mesenchymal populations, respectively, and when combined, significantly inhibit tumor cell growth in 2D and 3D *in vitro* systems.

In addition to the identification of the therapeutic sensitivities, there a many more uses of Z-cad dual fluorescent sensors that need to be further explored. One such example is exploration of epithelial to mesenchymal plasticity (EMP) which is a broader, and more recently used, term encompassing the dynamic and directional transitory states, EMT and MET[180]. According to this description, only a small population within tumors exhibit the plasticity and transition between the 2 polar states. The spatial and temporal presence of these subpopulations determines their role in metastasis and therapeutic resistance. Another concept that is gaining more traction is the phenotype of cancer cells exhibiting partial/hybrid EMT where cells retain characteristics associated with the conventional epithelial and mesenchymal states. These cell are also know to be present in a metastable state and evidence from the past few years has shown that, among hybrid subpopulations, those that retain more epithelial features with less mesenchymal conversion have the greatest malignant and metastatic potential[183,184]. Based on mathematical modeling, it is predicted that a hybrid state occurs with medium levels of both miR200 and ZEB1[185]. The Z-cad cells appear

to have certain of these subpopulations as characterized by expressing both RFP and GFP or expressing neither. These double positive and double negative subpopulations could represent these hybrid states undergoing transition. It is possible that this subpopulation is maintained in a heterogeneous cell population as an equilibrium. Also, since these cells have both epithelial and mesenchymal characteristics, they are potentially more aggressive (collective migration, but also might not be targetable by either epithelial or mesenchymal targeting drugs) and can even be enriched in tumors following therapeutic targeting[186]. Open ended questions include what cell intrinsic and extrinsic factors promote the appearance and stability of these hybrid phenotypes and if those molecular mechanisms could be therapeutically targeted for translation relevance. Further exploration and characterizing of these cell types would allow us to explain the biological phenomenon of EMP.

Chapter 5: Targeting CDK4 overcomes EMT-mediated tumor heterogeneity and therapeutic resistance in KRAS mutant lung cancer CDK4

5.1 Introduction

Activating *KRAS* mutation is one of the most frequent oncogenic events in lung cancer, occurring in about 30% of lung adenocarcinoma patients[187-189]. Despite the identification of the oncogene over 20 years ago and efforts to effectively treat this subset of patients, 5-year survival rates remain dismal[1]. Unlike *EGFR* mutant lung cancer, K-Ras oncoproteins are largely undruggable, with the very recent exception of the $KRAS^{G12C}$ allele[190,191]. Pharmacological inhibitors of the MAPK pathway (e.g., MEK), such as selumetinib and trametinib are available, but preclinical and clinical trials have demonstrated poor responses to MEK inhibitors[192]. Combination of MEK inhibitors with conventional chemotherapy did not demonstrate any added benefit to progression free survival[74]. Resistance to MEK inhibitors may be intrinsic (*de novo*) due to tumor cell heterogeneity or acquired due to tumor evolution as an adaptive response to pharmacological agents. In either case, the presence of phenotypically distinct tumor cell subpopulations with reprogrammed cellular machinery makes it difficult to effectively eliminate the broader tumor cell population. To address this, we need to understand the differences in the tumor cell subpopulations within a heterogeneous tumor.

Genetically identical tumor cells possess the ability to undergo transcriptional reprogramming to activate alternate survival pathways and evade therapeutic targeting. Research from our group and others has extensively demonstrated that epithelial-to-mesenchymal transition (EMT) is a central phenomenon occurring in K-Ras mutant lung cancer, which contributes to intracellular tumor heterogeneity, increased metastatic potential, therapeutic resistance to pharmacological agents and poor patient outcomes[93,103,193]. Murine lung cancer models driven by *Kras* and *p53* mutations recapitulate EMT-mediated tumor cell heterogeneity with the ZEB1/miR-200 double negative feedback loop playing a central role in dynamically altering the cellular phenotype[93]. Our previous research highlighted the reliance

of K-ras mutant epithelial lung cancer cells on activated MAPK signaling pathway and increased susceptibility to MEK inhibitors. On the other hand, tumors demonstrating a mesenchymal phenotype remained largely unresponsive to MEK inhibitors. Moreover, after an initial response to MEK inhibition, epithelial tumors acquired therapeutic resistance by undergoing EMT[103,194]. The study identified an unmet need to develop therapeutic approaches to target distinct tumor subpopulations within heterogeneous K-ras mutant lung tumor to achieve a robust therapeutic response. Utilizing multiple loss-of-function shRNA screens, we analyzed the transcriptome of the phenotypically different tumor subpopulations and identified CDK4-RB as a major survival pathway in mesenchymal tumor cells. We validated our finding using multiple *in vitro*, *ex vivo* and *in vivo* models well suited for studying EMT-mediated tumor cell heterogeneity.

CDK4 acts as a master integrator of mitogenic/oncogenic signaling cascades by initiating the inactivation of the central tumor suppressor RB and cell cycle commitment at the restriction point allowing cells to transition to S phase[195]. The CDK4 axis is altered in many cancers, with clinically approved pharmacologic inhibitors showing promising antitumor activity[196]. Some studies have shown that CDK4 and cyclin D1 expression is correlated with the presence of *KRAS* mutation in lung tumors[197] and a synthetic lethal interaction occurs between K-ras and CDK4 in lung cancer tumor progression[198,199]. We found that the differential activation of the CDK4 pathway in epithelial and mesenchymal cells was determined by ZEB1-mediated p21 regulation. As an intrinsic regulator of CDK4, p21 levels in cells determine the downstream CDK4 pathway activity. p21 is transcriptionally regulated by ZEB1 by direct binding to the promoter region. Our study demonstrates in preclinical models that intrinsic and acquired MEK inhibitor resistance is associated with a rewired kinome in tumors by which the mesenchymal phenotype activates the CDK4 pathway as a common occurrence across models. This CDK4 signaling dependence resulted in a potential therapeutic approach to combine MEK and CDK4 inhibitors to target different tumor

subpopulations for a more robust tumor response and combat resistant outgrowth of epigenetic subsets in a heterogeneous tumor.

5.2 Results

5.2.1 Mesenchymal lung cancer cells exhibit increased dependency on CDK4

In order to effectively target the mesenchymal tumor subpopulations within heterogeneous tumors, we sought to identify the survival dependencies of these tumor cells. A loss of function screen with a barcoded, pooled small hairpin RNA (shRNA) library targeting about 500 genes with known kinase activity (Kinome) was conducted. Each gene was targeted with 10 unique shRNA sequences to limit false hits due to off-target effects. This library of shRNAs was transduced into representative non-metastatic, epithelial (393P) and metastatic, mesenchymal (344P) murine lung cancer cell lines derived from a previously described KP genetically engineered mouse model (GEMM)[93]. The cell lines stably expressing the shRNAs from the Kinome library were either cultured *in vitro* or implanted subcutaneously in nude mice (Figure 28 A). Tumors were harvested, shRNA barcodes were quantified by deep sequencing and referenced with the respective *in vitro* cell population and quality control measures were completed to ensure sufficient barcode coverage across the library was maintained *in vivo* (Figure 28 B, Table 11). The phenotypic impact of gene knockdown was inferred by the redundant shRNA activity (RSA) algorithm, where a lower rank of the shRNA barcodes signified dropout from the population and greater dependency on the gene for tumorigenesis (Table 12). Although both cell line models have activating $Kras^{G12D}$ and $p53^{R172H}$ mutations, comparison of the results of the Kinome screen revealed that the mesenchymal cell line (344P) and the matched syngeneic tumors were more reliant on *Cdk4* for *in vitro* and *in vivo* growth (Figure 28 C). Other top hits identified in the screen as more significant in mesenchymal than epithelial cells were *Aurka, Atr, Pik3Ca, Plk1, and Adrbk2* (Figure 28 C), consistent with recent publications about the role of the spindle assembly checkpoint in mesenchymal cells[200]. We also compared these results to our

previously published FDAome shRNA[103] screen performed in a similar manner and identified *Cdk4* as the most consistent hit across *in vitro* and *in vivo* conditions in both screens (Figure 28 C, Table 14 and Table 15).

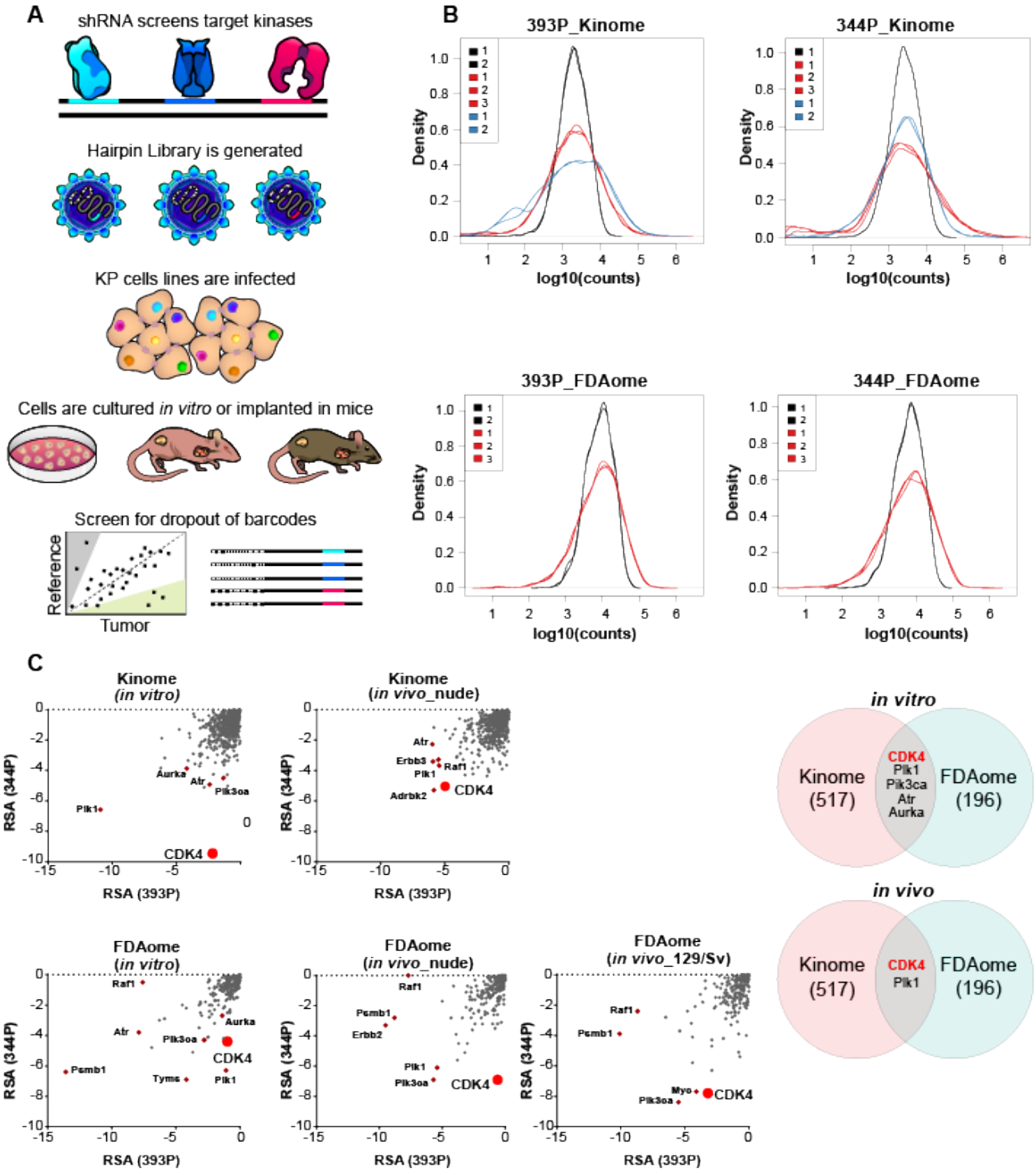

Figure 28. shRNA screens identify survival dependencies in lung cancer cells.
(A) Schematic illustration of the workflow of the shRNA dropout screens. A library of lentiviral particles expressing 10 different barcoded shRNAs was transduced into murine KP mutant lung cancer cells.

The cells were cultured *in vitro* or implanted in nude or syngeneic 129/Sv mice and later sequenced for barcoded shRNAs and compared to reference cells. (B) Viral integration distribution of reference population, cell lines and tumors determined through barcode sequencing (counts per million). Black = reference, red = in vivo samples, blue = in vitro samples. (C) Results from Kinome and FDAome shRNA dropout screens in 393P (epithelial) and 344P (mesenchymal) cell lines and tumors compared based on the redundant shRNA activity (RSA). Top differential hits are labeled on the graphs, most important being CDK4 (red). Venn diagram shows comparisons across different conditions and top hits identified. *(Padhye et al JCI insight, 2021, in press).*

CDK4 mRNA expression in a panel of 118 human NSCLC cell lines showed a positive correlation with our previously reported 76-gene EMT signature[201] (Figure 29 A). When sub-classified based on mutational status, 41 KRAS-mutant NSCLC cell lines also showed positive correlation of *CDK4* mRNA with the EMT signature (Figure 29 B). A panel of epithelial and mesenchymal murine lung cancer cells were tested by quantitative polymerase chain reaction (qPCR), which demonstrated higher CDK4 mRNA levels in the mesenchymal cells (Figure 29 C). TCGA dataset analysis of lung adenocarcinoma patients revealed alterations in the CDK4-RB core pathway in about 30-40% of the cases (Figure 29 D), which represents over 40,000 new patients annually. These analyses demonstrate the importance of CDK4 pathway members in patients with lung adenocarcinoma.

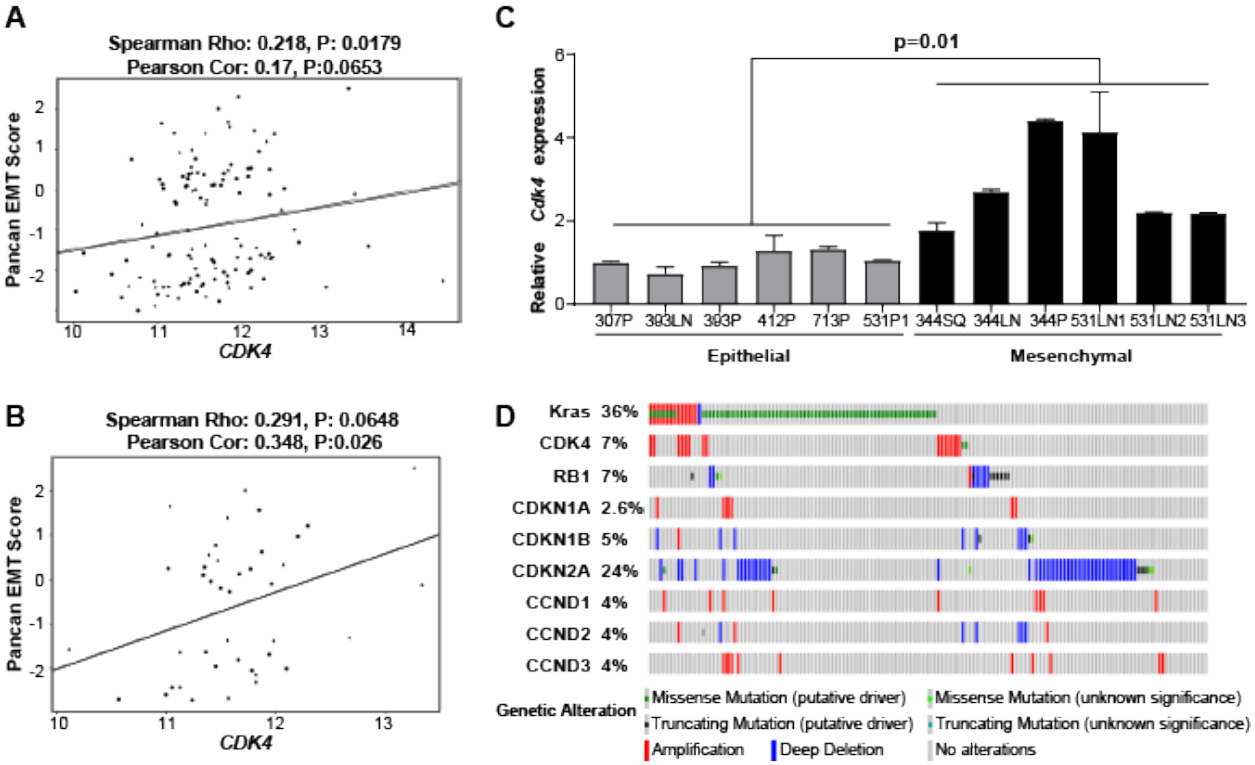

Figure 29. CDK4 levels positively correlate with EMT score in lung cancer.
(A) Cluster plot analysis of Spearman's rank correlation between EMT score and CDK4 mRNA expression of 118 human NSCLC cell lines. (B) Cluster plot analysis of Spearman's rank correlation between EMT score and CDK4 mRNA expression of 41 KRAS mutant human NSCLC cell lines. (C) Relative mRNA expression of CDK4 in a panel of murine KP epithelial and mesenchymal cells. (D) CDK4 pathway components and their corresponding mutation frequencies in the provisional lung adenocarcinoma TCGA dataset (Firehose legacy) (n=586).
(Padhye et al JCI insight, 2021, in press).

To functionally validate the shRNA screen and determine whether response to CDK4 inhibitors is dependent on the EMT status of tumor cells, we treated a panel of human and murine KRAS mutant NSCLC cell lines, stratified as either epithelial or mesenchymal based on previous profiling[93,201], with CDK4 inhibitors. Both human and murine mesenchymal NSCLC cells were more sensitive to the CDK4 inhibitors palbociclib, abemaciclib and ribociclib (Figure 30 A, B). As previously noted[93], EMT status is tightly regulated by the ZEB1/miR-200 double negative feedback loop and manipulation of this axis can induce an epithelial or mesenchymal shift in tumor cells. We therefore utilized isogenic pairs of human (H441) and murine (393P) epithelial cell lines with ZEB1 expression to produce a mesenchymal phenotype[39] and isogenic pairs of human (H1299) and murine (344SQ) mesenchymal cells with miR-200 expression to push the cells to an epithelial state[115]. Comparisons across the different cell line pairs revealed that sensitivity to all CDK4 inhibitors was determined by the EMT status of lung cancer cells (Table 10).

Table 10. IC50 of epithelial and mesenchymal cell lines for CDK4 inhibitors.

CDK4 inhibitor	Epithelial cells	IC50	Mesenchymal cells	IC50
Palbociclib	393P	10.8	344SQ	2.2
	393P_Vector	5.2	393P_ZEB1	0.6
	344SQ_miR-200	5.2	344SQ_Vector	0.8
	344SQ_sh_ZEB1#1	1.5	344SQ_Scramble	0.6
	344SQ_sh_ZEB1#3	2		
	H358	9.6	A549	1.1
	H441	10	H1299	0.5
	H441_Vector	16	H441_ZEB1	2.6
	H1299_miR-200	3	H1299_Vector	0.6
Abemaciclib	393P	15	344SQ	2.2
	H358	1	H1299	0.2
Ribociclib	393P	19.2	344SQ	3.8
	H358	29	H1299	3.3

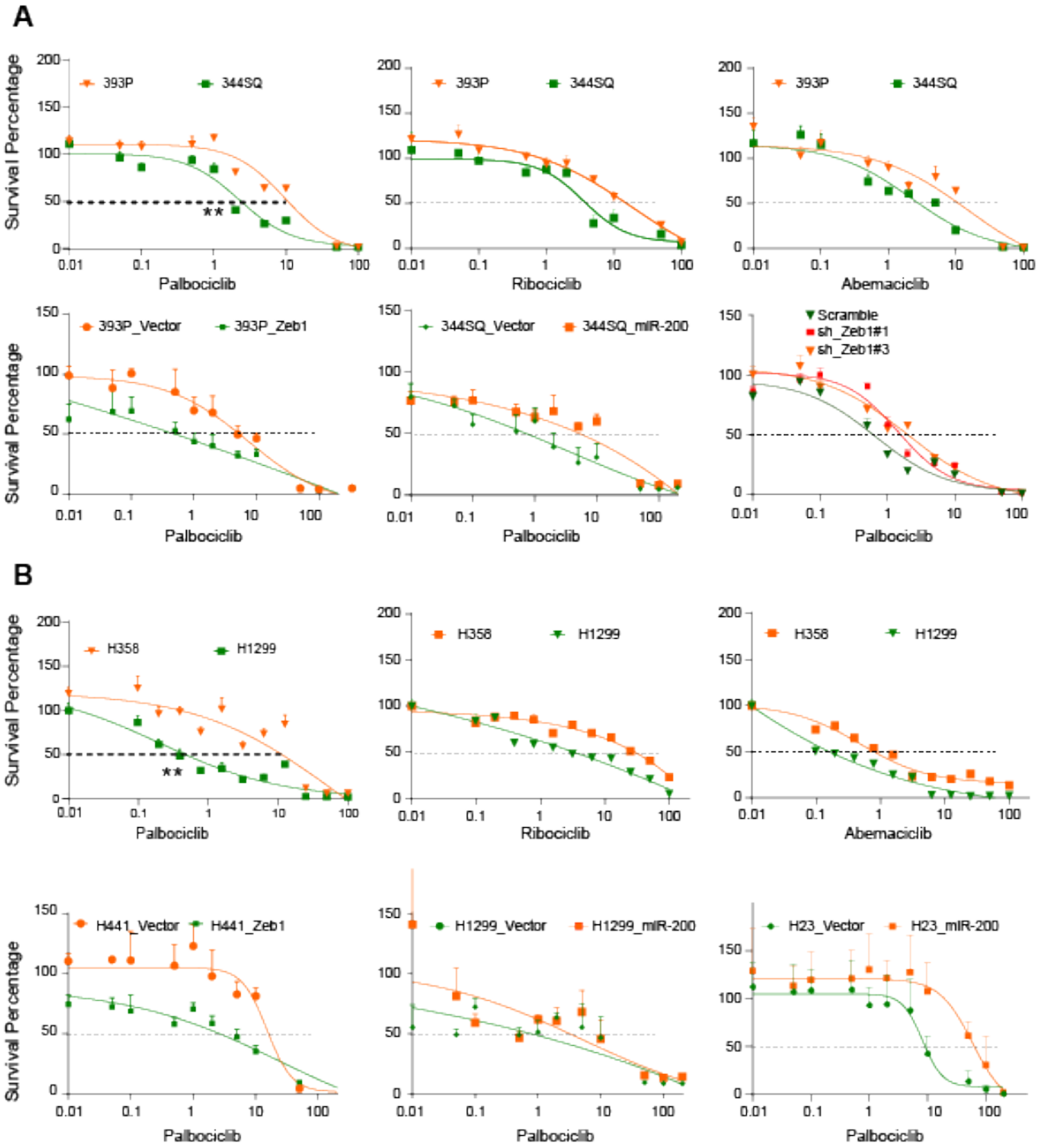

Figure 30. Cell viability assay in a panel of epithelial and mesenchymal cells after 48 hours. n=8 per drug concentration. The curve was generated using a nonlinear regression fit model. *(Padhye et al JCI insight, 2021, in press).*

The downstream targets of CDK4, RB and FoxM1, are important readouts for CDK4 kinase activity, whereas phospho-CDK4 may continue to be present for another 24 hours post inhibitor treatment. Suppression of the RB and FoxM1 was observed in mesenchymal cells upon treatment with abemaciclib and ribociclib for 24 and 48 hours (Figure 31 A). Epithelial tumor cells showed an initial suppression of CDK4 targets, but it was not a sustained response. The mesenchymal 344SQ cells showed a more robust response to the inhibitor palbociclib over a range of concentrations and at shorter treatment times compared to epithelial cells (393P) in terms of suppression of downstream signaling and induction of apoptosis (Figure 31 B).

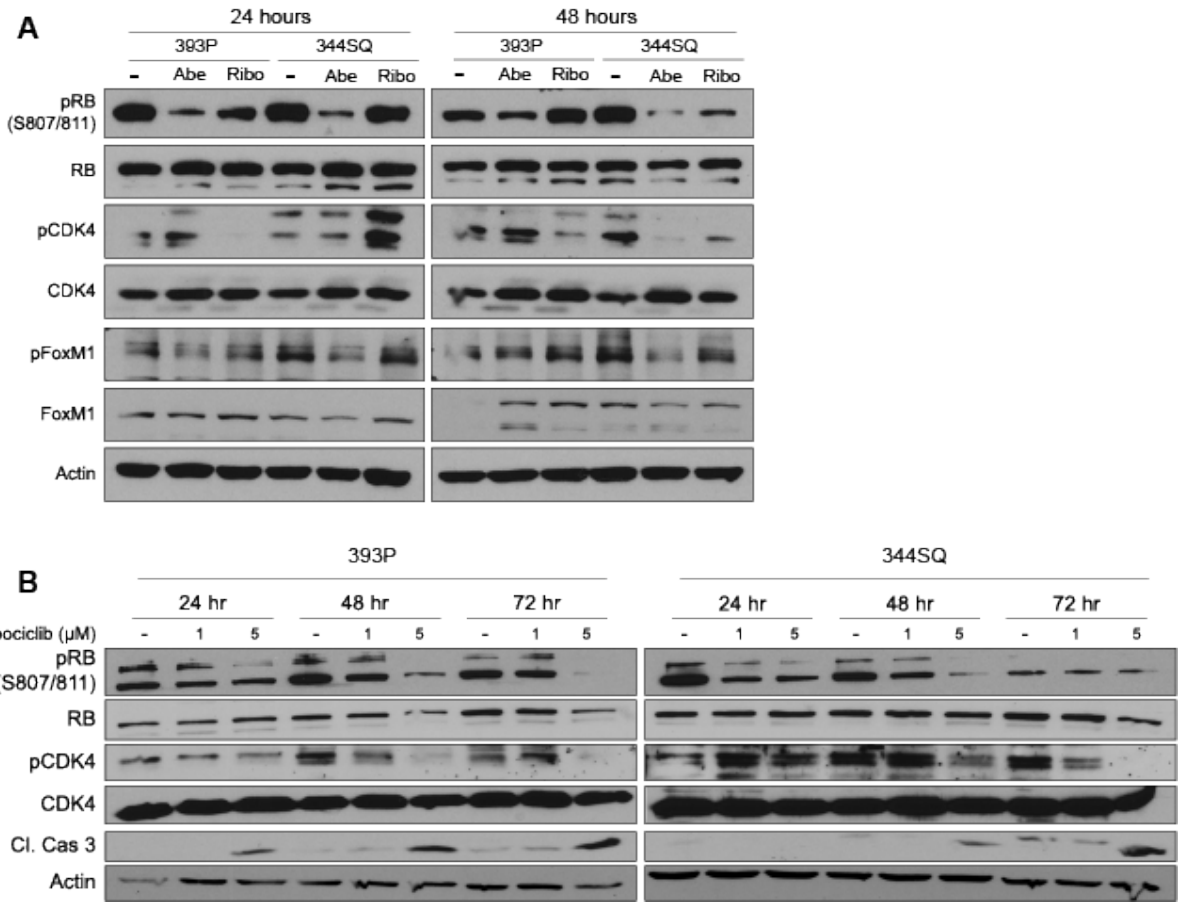

Figure 31. Effect on CDK4 pathway with pharmacological inhibitors of CDK4
(A) Western blot showing the effect on signaling in 393P and 344SQ tumor cells upon treatment with abemaciclib (A: 2 μM) and ribociclib (R: 2 μM) for 24 and 48 hours. (B) 344SQ and 393P cells were treated for 24, 48 and 72 hours with 1 and 5 μM palbociclib, and western blot analysis was utilized to demonstrate drug efficacy over a dose range. Cleaved caspase-3 was used as an apoptotic marker. *(Padhye et al JCI insight, 2021, in press).*

In addition to pharmacologic inhibition, we also employed a genetic approach to confirm the dependency of mesenchymal tumor cells on CDK4 for survival. Mesenchymal cell lines with an inducible shRNA targeting CDK4 showed a greater reduction in tumor cell growth (Figure 32 A), with suppression of phospho-RB (Figure 32 B) compared to epithelial cells. In fact, epithelial 393P tumor cells appeared to have slightly greater growth rate with CDK4 knockdown than the control cells (Figure 32 B) and continued RB phosphorylation.

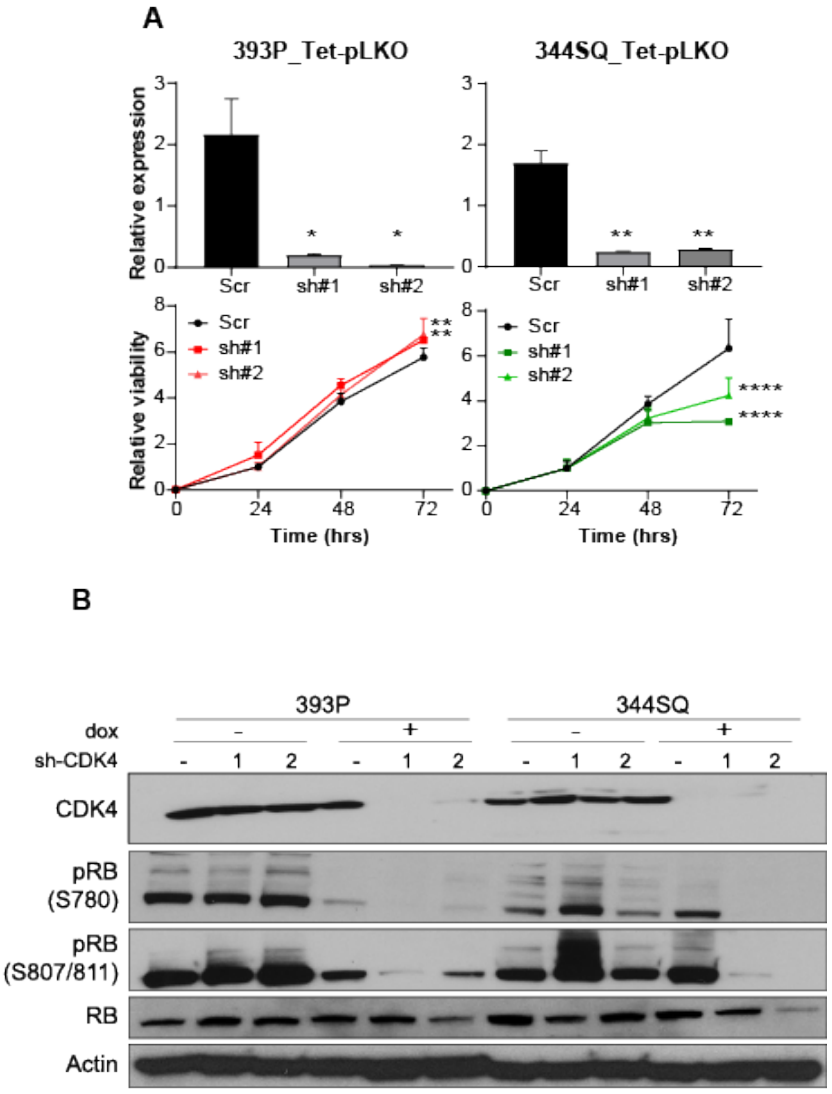

Figure 32. Effect on CDK4 pathway with doxycycline inducible shRNA targeting CDK4.
(A) Top: Relative mRNA expression of CDK4 upon doxycycline mediated induction of shRNAs targeting CDK4 at 72 hours. Bottom: Growth rates of 393P and 344SO cells with or without CDK4 knockdown over 72 hours measured by MTT assay. One and two-way ANOVA test was used for statistical analysis, respectively. (B) Western blot analysis of CDK4 pathway after 72 hours of CDK4 knockdown. **** p<0.0001; ** p<0.001.
(Padhye et al JCI insight, 2021, in press).

5.2.2 CDK4 pathway is dynamically regulated by the EMT status of tumor cells

Because the primary role of CDK4 is cell cycle regulation at the G1-S transition, we next tested if there are phenotypic differences in the manner which epithelial and mesenchymal NSCLC cell lines undergo cell cycle progression. Upon serum starvation for up to 48 hours, epithelial 393P cells almost completely (~90% of the cells) arrested in the G0-G1 phase of the cell cycle with a complete suppression of the CDK4 pathway (Figure 33 A). In contrast, the mesenchymal cells resisted cell cycle arrest in serum free conditions, with ~80% of the cells in G0-G1 state but 20% of cells continuing to cycle through S or G2/M (Figure 33 A). This observation corresponded to higher levels of CDK4, Cyclin D1 and phospho-RB in the cells when assayed by subcellular fractionation (Figure 33 B), suggesting that CDK4 activity in mesenchymal tumor cells could be uncoupled from extrinsic mitogenic signals. After release of cells from the arrested state by addition of serum containing media, the mesenchymal cells transitioned into S phase more readily (within 20 hours) than the epithelial cells, which remained arrested in G1 phase up to 36 hours before returning to the baseline cycling state (Figure 33 A). Although cell cycle arrest in G1 phase with palbociclib was similar between 393P and 344SQ cells, a significant increase in the percentage of 344SQ cells in G0 state (apoptotic cells) was detected (Figure 33 C, D), corresponding to increased cleaved caspase-3 as observed in Figure 31 B.

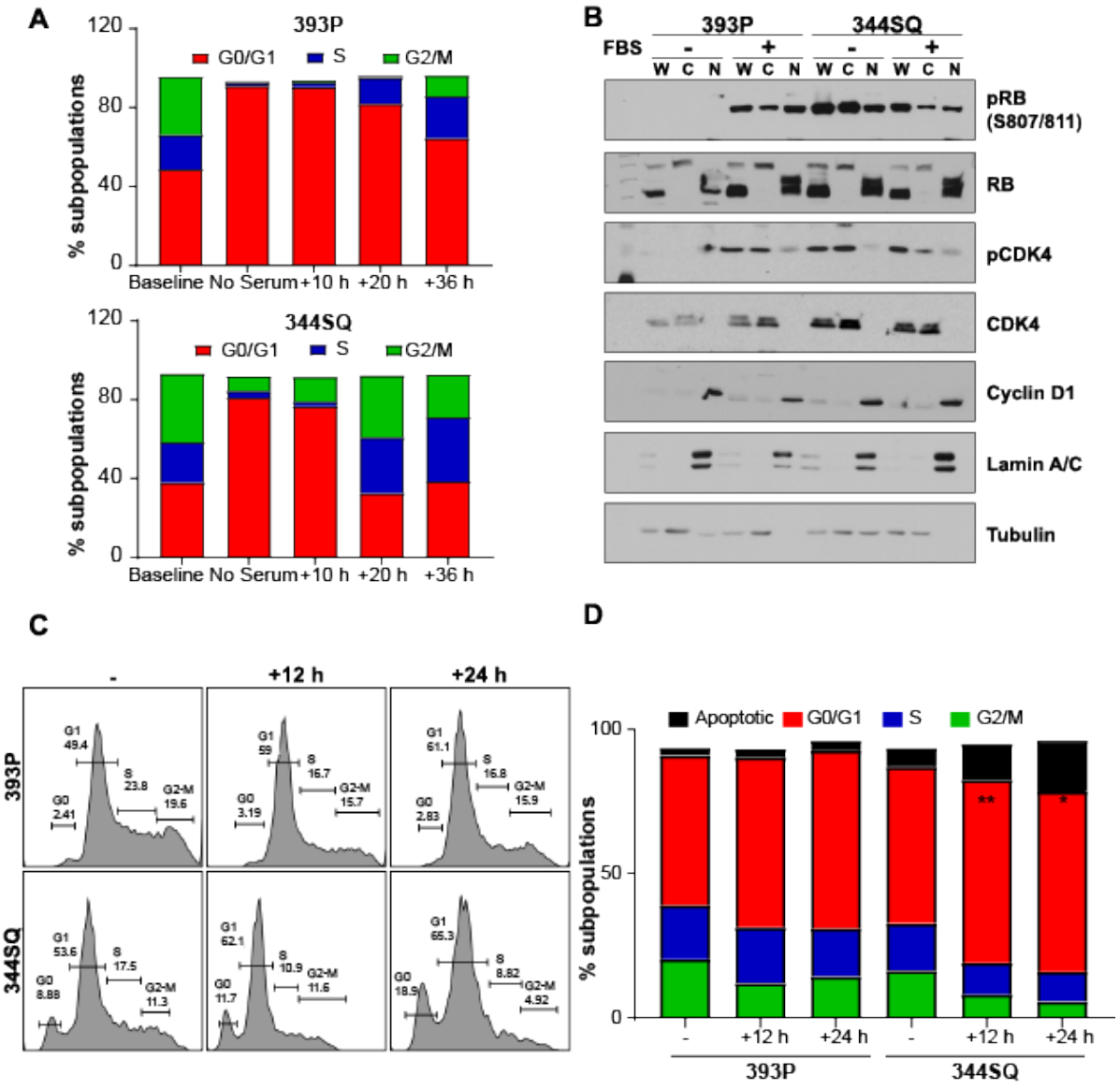

Figure 33. Cell cycle analysis in epithelial and mesenchymal cells.
(A) Cell cycle analysis 393P and 344SQ cells using propidium iodide (PI). Baseline cell cycle was determined by staining cells in culture with PI. Cell cycle arrest was induced by serum starvation of cells for 24 hours followed by release into cell cycle by addition of FBS containing media and analyzed after 10, 20 and 36 hours. (B) Subcellular fractionation followed by western blot analysis of indicated cell cycle markers. (C) Cell cycle analysis 393P and 344SQ cells treated with palbociclib (5μM) for 12 and 24 hours using (PI). (D) Quantification of subpopulations in different cell cycle phase. Data are presented as mean and statistical analysis was done using one-way ANOVA test.* p< 0.05, **p< 0.01. *(Padhye et al JCI insight, 2021, in press).*

Using reverse phase protein arrays (RPPA) to analyze changes in cell signaling proteins in a high-throughput manner, we screened a panel of previously characterized isogenic murine epithelial and mesenchymal lung cancer cell lines and observed an increase in CDK4 axis related molecules, phospho-RB and Cyclin D1 (as downstream markers for CDK4 signaling pathway activation), in cells with a mesenchymal phenotype (Figure 34 a). A subcellular fractionation assay also showed higher levels of phospho-RB, Cyclin D1 and CDK4 in mesenchymal cells (Figure 34 B). Immunofluroscent staining of tumor cells also demonstrated an activated CDK4/RB axis with a higher percentage of 344SQ tumor cells with positive nuclear staining for phospho-CDK4 and phospho-RB and a stronger staining for total CDK4 (Figure 34 C,D).

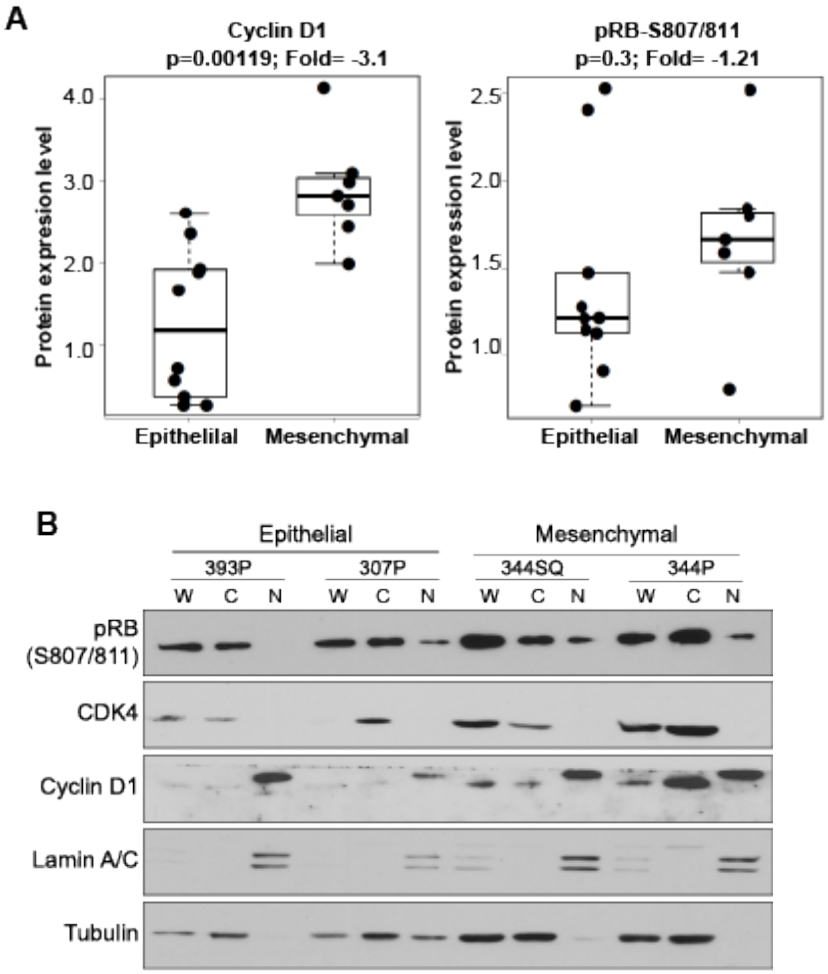

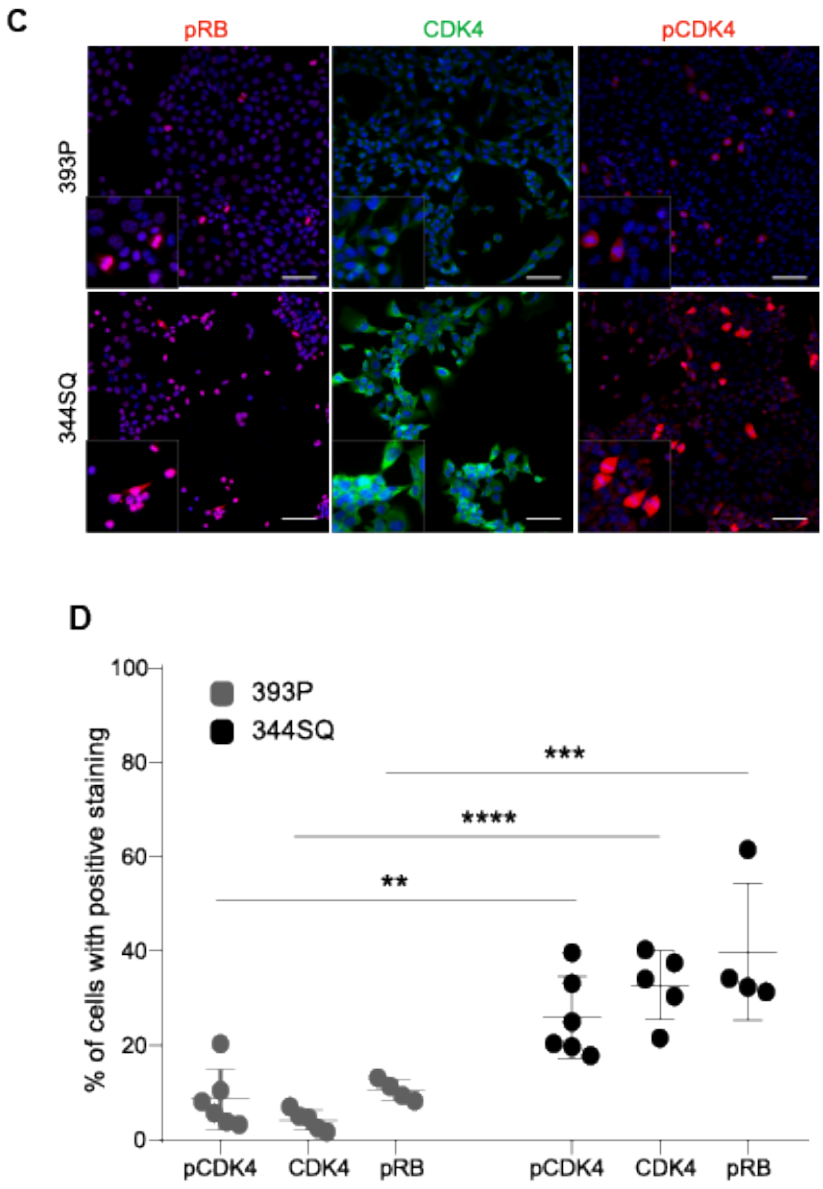

Figure 34. CDK4 pathway is upregulated in mesenchymal cells.
(A) Dot plots of Cyclin D1 and RB phosphorylation (S807/811) from RPPA dataset in a panel of epithelial and mesenchymal murine lung cancer cell lines. (B) Subcellular fractionation of 393P, 307P (epithelial) and 344SQ, 344P (mesenchymal) cells for indicated markers. (C) Representative images of immunofluorescence on 393P and 344SQ wild type cells for indicated markers. Scale bar: 50 µM. (D) 4-6 biological replicates were analyzed for quantification of the fluorescent signal. One-way ANOVA was used for statistical analysis.
(Padhye et al JCI insight, 2021, in press).

We next tested the effects of altering the EMT status of tumor cells on the CDK4 signaling pathway using the previously described isogenic cell line pairs. ZEB1 overexpression in murine (393P) and human (H441) epithelial cells produced higher levels of CDK4 and phospho-RB (Figure 35 A). Conversely, miR-200 expression in murine (344SQ) and human (H1299) cells caused a suppression of the CDK4 axis (Figure 35 B).

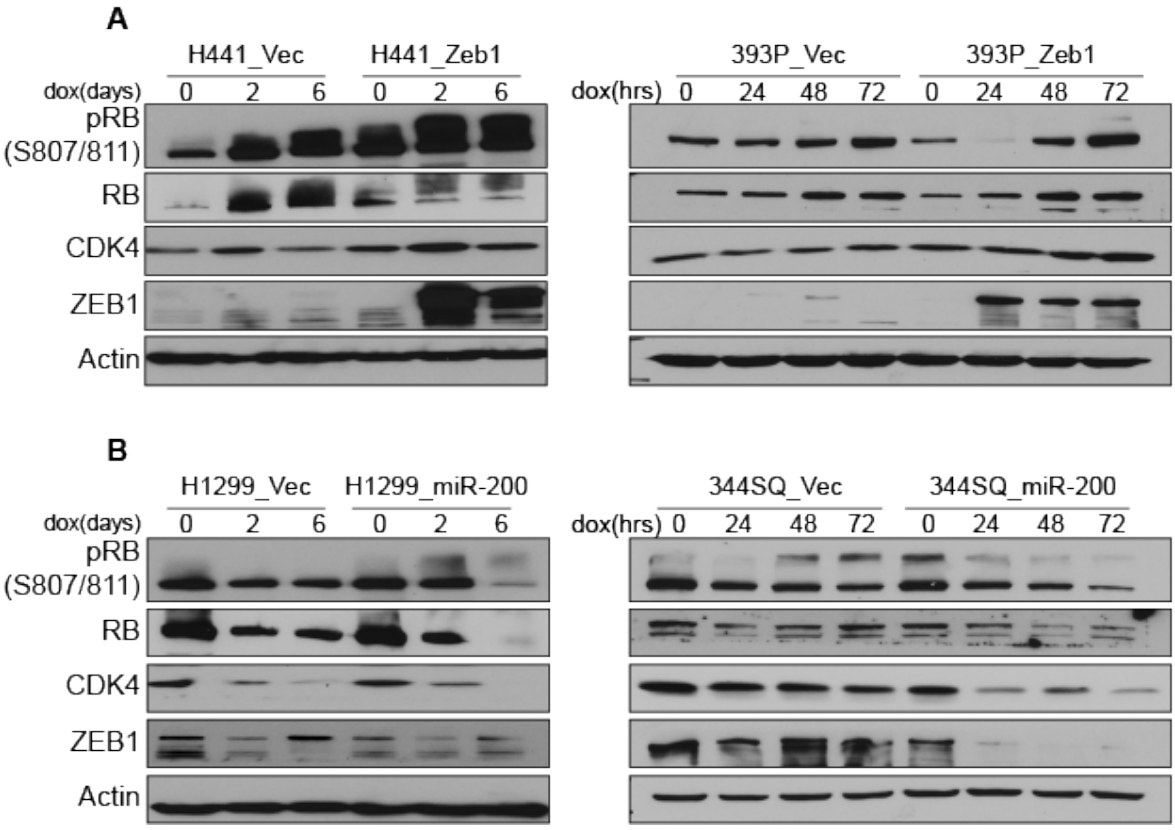

Figure 35. CDK4 pathway is dynamically regulated by the EMT status of tumor cells.
Western blot analysis of murine and human cells with ZEB1 and miR-200 expression. Cells were induced with 2 µg/ml of doxycycline for times indicated.
(Padhye et al JCI insight, 2021, in press).

Immunohistochemistry on mesenchymal 344SQ syngeneic tumors revealed higher phospho-CDK4 and phospho-RB staining with absent phospho-Erk, and the reverse was observed in the epithelial 393P syngeneic tumors (Figure 36 A). The dynamic nature of tumor evolution and adaptation contributes to intratumoral cellular heterogeneity and allows for escape from therapeutic targeting. We have previously observed that epithelial 393P tumors initially respond to MEK inhibitors (e.g. AZD6244), however, long-term exposure leads to acquired resistance with the acquisition of a mesenchymal phenotype (393P-AZD^{R})[103]. We investigated whether tumors that have acquired resistance to MEK inhibitors have an activated CDK4 pathway. 393P-AZD^{R} tumors showed higher phospho-CDK4 and phospho-RB staining, with suppressed phospho-Erk, an observation similar to the *de novo* 344SQ mesenchymal tumors (Figure 36 A). Cell lines derived from 393P-AZD^{R} tumors showed higher phospho-CDK4 and ZEB1 expression, with generally lower levels of phospho-Erk (Figure 36 B). Resistant cells were no longer sensitive to AZD6244, and instead became sensitive to palbociclib with an IC50 similar to 344SQ cells (Figure 36 C), and greater suppression of phospho-RB and phospho-CDK4 in 393P-AZD^{R} than in 393P-vehicle cell lines. In contrast there was an accumulation of phospho-CDK4 in 393P-vehicle cells (Figure 36 D). We conclude from the above findings that tumor cells that demonstrate a mesenchymal-like phenotype, either due to intrinsic factors or arising from epithelial cells undergoing EMT as an adaptive resistance mechanism, have rewired survival pathways to activate CDK4 signaling.

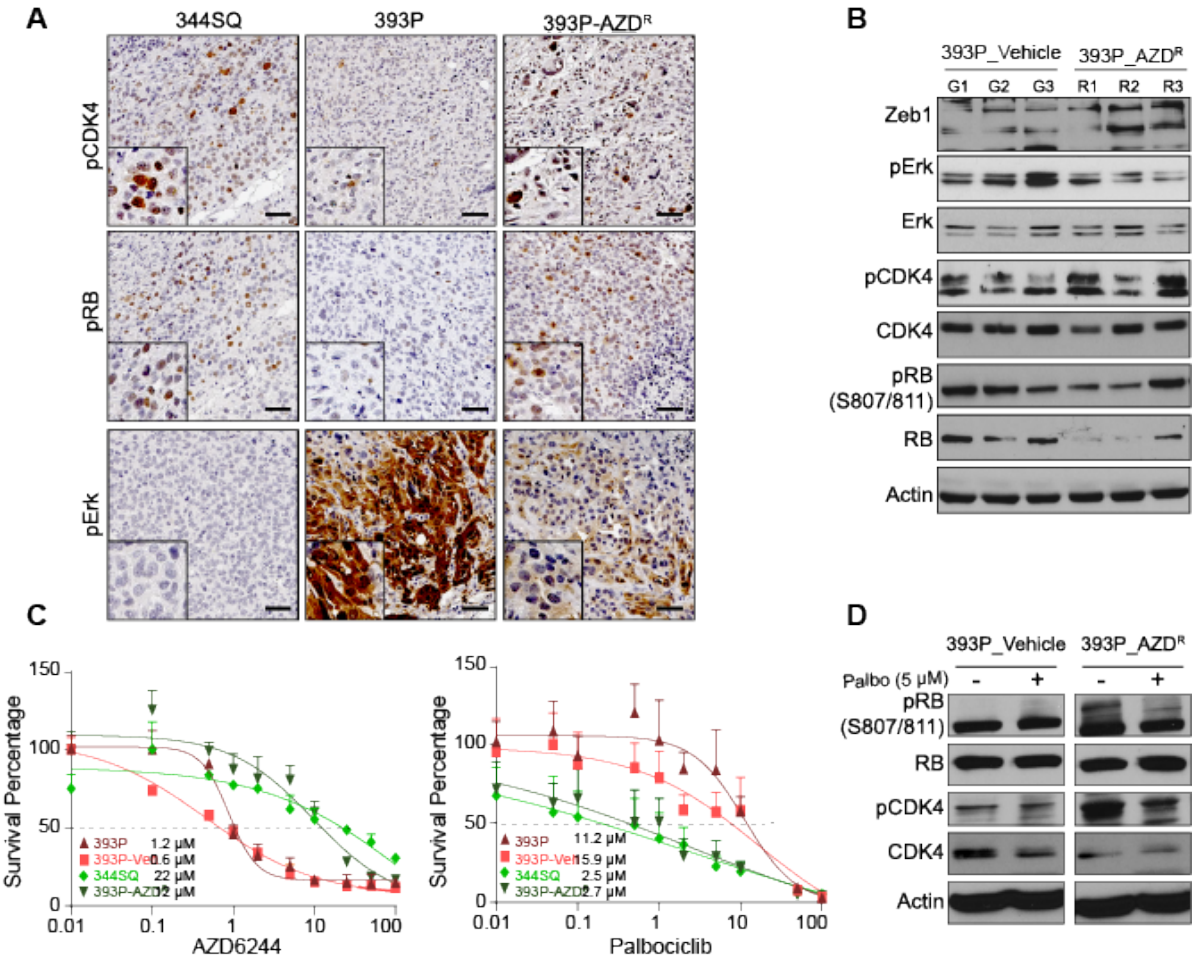

Figure 36. CDK4 pathway is upregulated in 393P-AZD^R tumors and cells.
(A) Immunohistochemistry on tumors derived from 393P, 344SQ and 393P-AZD^R tumors for indicated markers. Scale bar: 50 µM. (B) Western blot analysis on cell lines derived from 393P tumors treated with vehicle or AZD6244 for indicated markers. (C) In vitro cell viability assay on 393P, 344SQ, 393P-vehicle and 393P-AZD^R after 48 hours of AZD6244 and palbociclib treatment. n=8 per drug concentration. The curve was generated using a nonlinear regression fit model. **** p<0.0001; *** p<0.005; ** p<0.001. (D) Western blot analysis of 393P-vehicle and 393P-AZD^R cells after treatment with palbociclib (5µM) for 48 hours for indicated markers.
(Padhye et al JCI insight, 2021, in press).

5.2.3 ZEB1 regulates p21 expression and causes differential CDK4 pathway activity

To identify the mechanistic basis of the differential dependency on the CDK4 pathway between the phenotypic epithelial and mesenchymal cancer cells we investigated the canonical upstream survival pathways but did not observe their differential regulation between epithelial and mesenchymal cells. We then focused on the intrinsic regulators of CDK4 activity, p21 (WAF1/CIP1) and p27 (KIP1), and used si-RNAs for transient knockdown of each in epithelial and mesenchymal cells to determine the downstream effects on the CDK4 pathway (Figure 37 A). Knockdown of p21 had a more significant impact on the phosphorylation of CDK4 and RB compared to p27 (Figure 37 B), which indicated that p21 was more important in the differential regulation of the CDK4 pathway between epithelial and mesenchymal tumor cells. The much higher phosphorylation of RB in 393P cells with p21 knockdown indicated that p21 maintains a check on the CDK4-RB pathway in the epithelial cells and when disrupted increases activation of the pathway. Loss of p21 in mesenchymal cells only modestly increased phosphorylation of RB compared to the control cells, suggesting that an intrinsic deficiency of p21 protein in the mesenchymal cells could lead to a dysregulated CDK4 pathway.

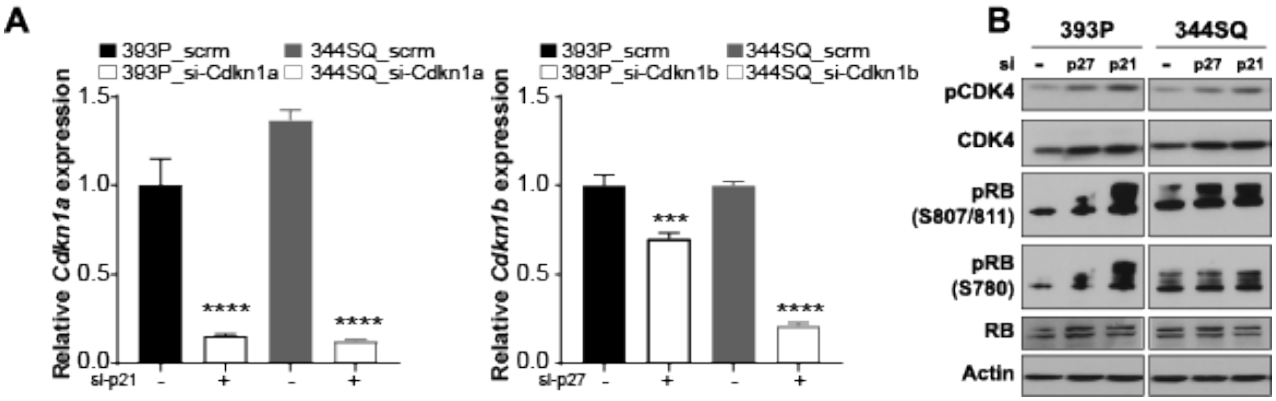

Figure 37. Transient knockdown of p21 and p27.
(A) Relative mRNA expression after 48 hours of knockdown of p21 and p27 in 393P and 344SQ cells.
(B) Western blot analysis of CDK4 pathway with p21 and p27 knockdown.
(Padhye et al JCI insight, 2021, in press).

Since alterations in the tumor suppressor *TP53* is one of the most commonly occurring co-mutation events in KRAS driven lung cancer and because p21 is a direct target of p53, we wanted to determine the effect of p53 and whether any differences might account for CDK4 pathway regulation in the epithelial and mesenchymal tumor cells. With transient knockdown of p53, we did not observe any significant difference in downstream pathway signaling (Figure 38 A, B). Additionally, we also utilized previously published *Kras*^{G12D} mutant (K1) and *Kras*^{G12D}/*p21*$^{-/-}$ (KC3 and KC4) murine tumor cells[202] to determine if p21 could regulate the sensitivity of tumor cells to CDK4 inhibitors. Absence of p21 in tumor cells sensitized KC cell lines to palbociclib with an increase in CDK4 signaling (Figure 38 C, D). This further emphasized that p21-mediated CDK4 dysregulation was independent of p53 control.

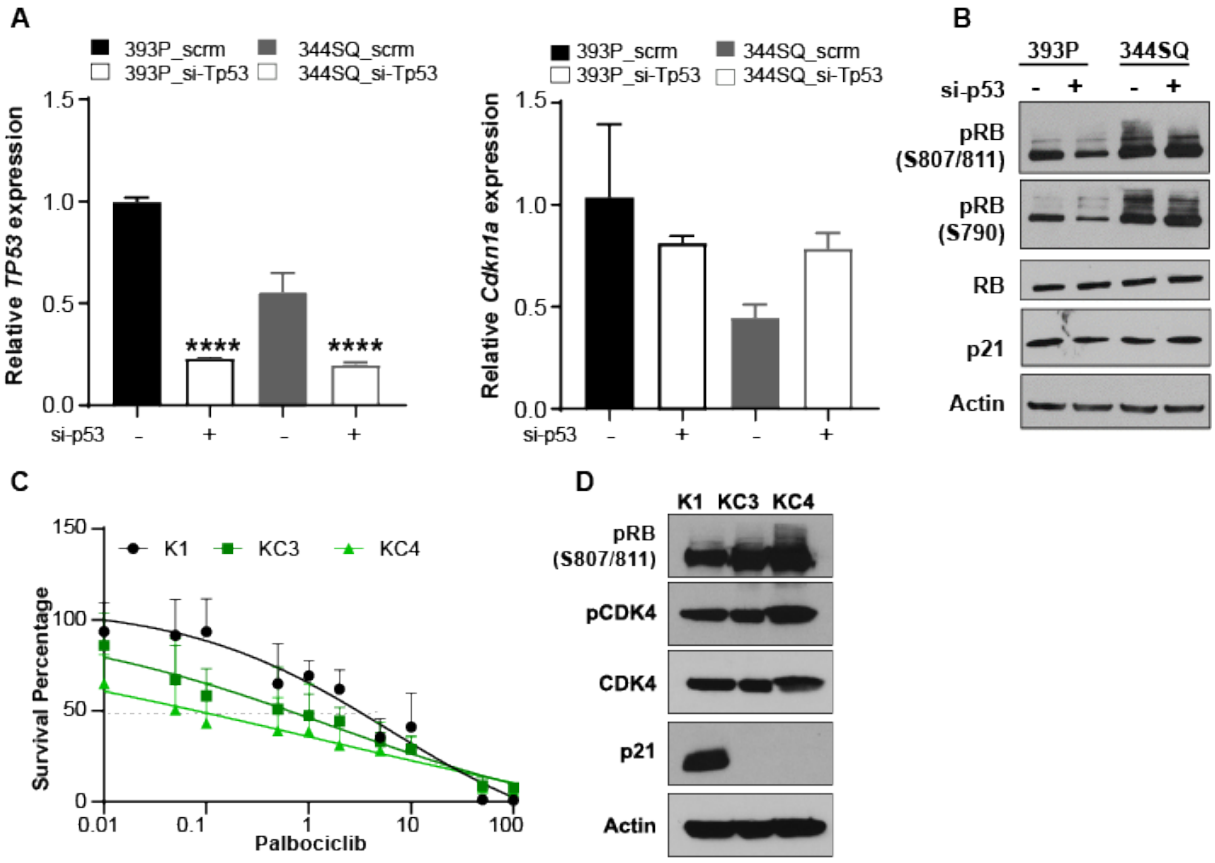

Figure 38. Effect of p53 on p21-CDK4 pathway.
(A) Relative mRNA expression of Tp53 (left) and Cdkn1a (right) with transient knockdown of Tp53. (B) Western blot analysis of indicated markers upon transient knockdown of Tp53 for 48 hours. (C) *In vitro* cell viability after 48 hour palbociclib treatment of K1, KC3 and KC4 cells. (D) Western blot analysis of indicated markers in K1, KC3 and KC4 cells.
(Padhye et al JCI insight, 2021, in press).

We next sought to ascertain whether EMT status of tumor cells could directly regulate the expression of p21. Our previously published[93] microarray datasets that interrogate differential gene expressions in epithelial and mesenchymal tumor cells demonstrated that epithelial cells have a higher expression of *Cdkn1a* (gene encoding for p21), including comparisons of 344SQ vs 393P cells (fold change 0.57, p=0.003) and 393P-ZEB1 vs 393P-vector (fold change 0.27, p<0.0001). We confirmed and extended this observation with a panel of murine cell lines by qPCR and found that p21 levels inversely correlated with ZEB1 levels across the panel (Figure 39 A, B). Analysis of *CDKN1A* mRNA expression in 29 KRAS mutant human lung adenocarcinoma cell lines revealed an inverse correlation with a previously published EMT gene signature[201] (Figure 39 C).

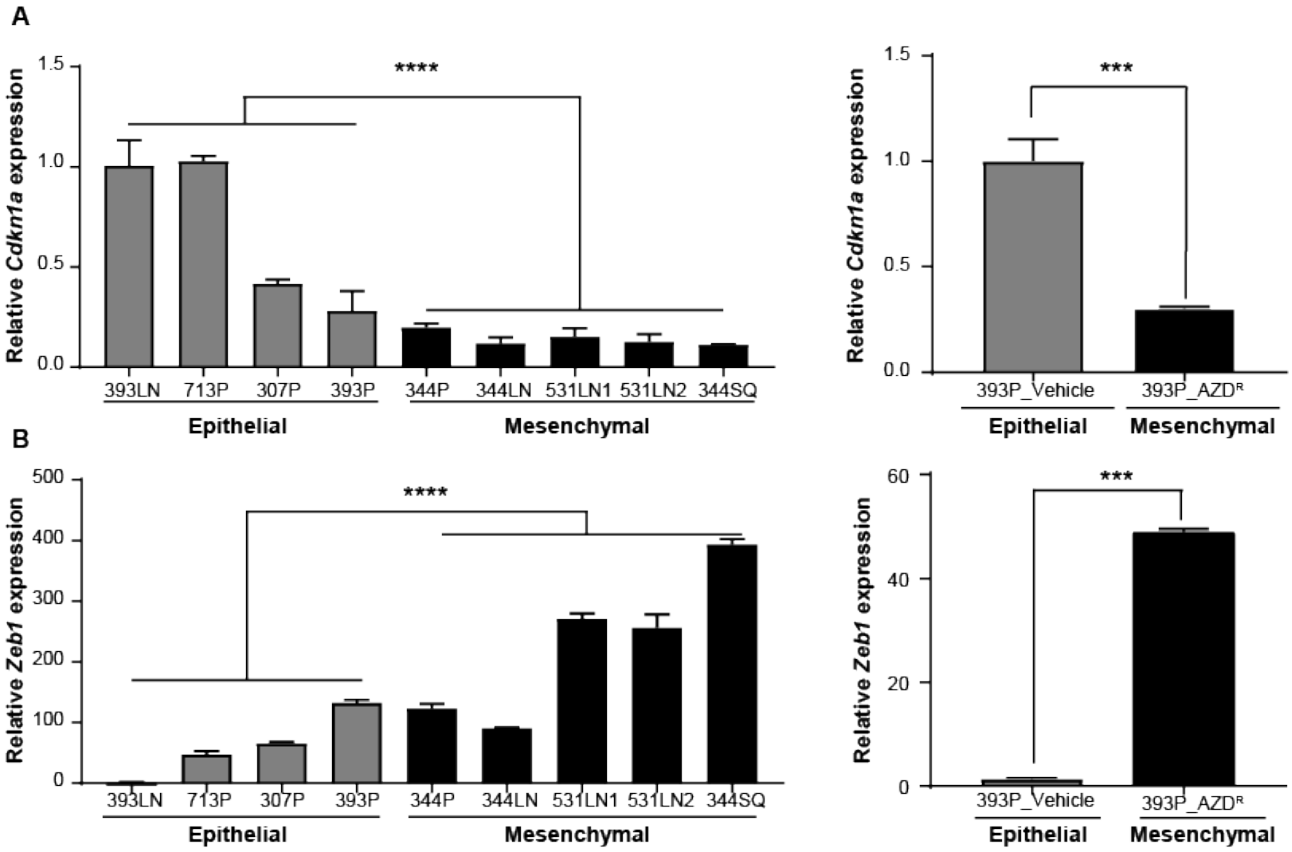

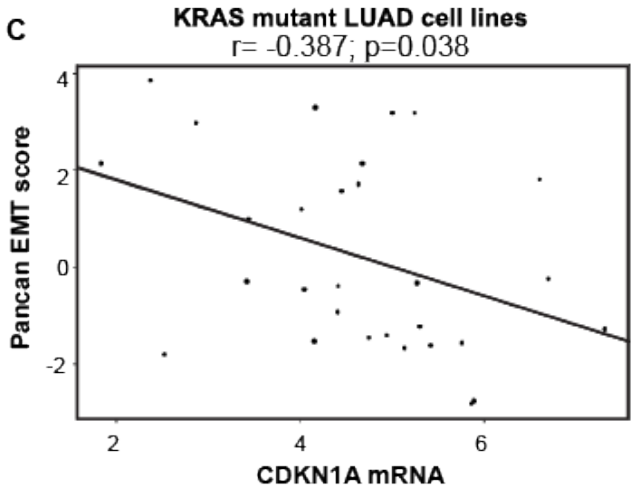

Figure 39. EMT status of cancer cells determines p21 levels.
(A) Relative expression of Cdkn1a mRNA in a panel of epithelial and mesenchymal murine lung cancer cells (left) and 393P vehicle and AZD^R cell lines (right). (B) Relative expression of Zeb1 mRNA in a panel of epithelial and mesenchymal murine lung cancer cells (left) and 393P vehicle and AZD^R cell lines (right). (C) Cluster plot analysis of Pearson's correlation between CDKN1A mRNA and EMT score in 29 KRAS mutant human lung adenocarcinoma cell lines.
(Padhye et al JCI insight, 2021, in press).

Immunofluorescence assay on 393P, 393P-AZD^R and 344SQ cells revealed that a higher percentage of epithelial cells had nuclear p21 than mesenchymal cells, along with higher co-localization of CDK4 and p21 in epithelial tumor cells (Figure 25 B). Immunohistochemistry analysis of epithelial (393P) and mesenchymal (344SQ) and 393P-AZD^R tumors also showed an inverse correlation between p21 and ZEB1 levels (Figure 25E). Pathologic analysis of human NSCLC samples for ZEB1 and p21 by IHC staining revealed an inverse correlation between nuclear ZEB1 and p21 H-scores (Figure 25F). We also grouped the samples based on low ZEB1 (<4 H-Score) or high ZEB1 (>4 H-score) staining and found a significant difference in p21 H-score (Figure 25G). Combined together the data support the regulation of p21 by EMT status and more specifically by ZEB1.

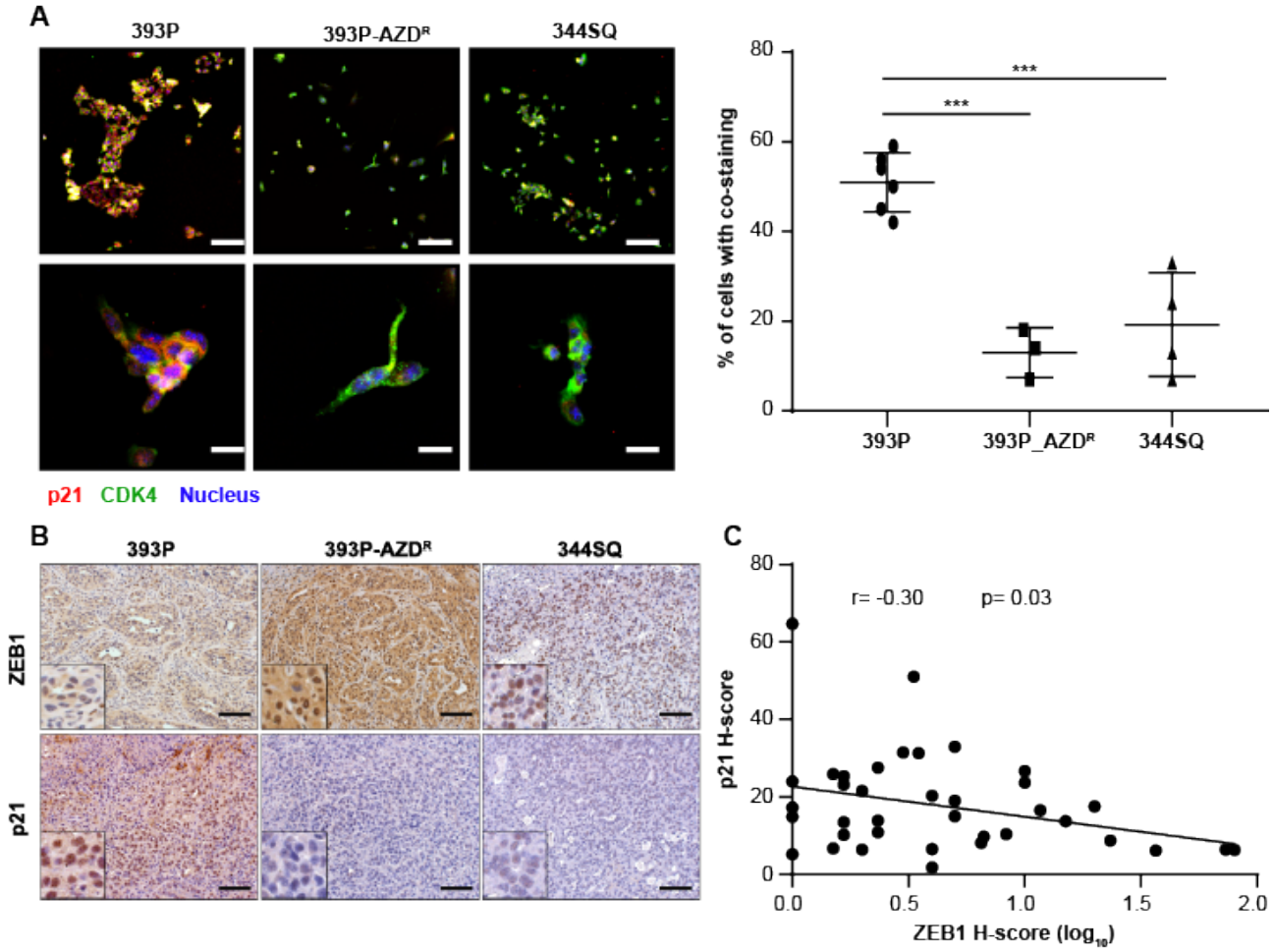

Figure 40. ZEB1 levels inversely correlate with p21 levels.
(A) (Left) Immunofluroscent staining of 393P, 393P_AZD^R and 344SQ cells. Scale bar top: 100 µM, bottom: 10 µM. (Right) Quantification of cells co-staining positive for CDK4 and p21 in each cell lines. 4-6 biological replicates were analyzed for quantification of the fluorescent signal. (B) immunohistochemistry on tumors derived from 393P, 344SQ and 393P-AZDR cells Scale bar: 50 µM. (C) Cluster plot analysis of Pearson's correlation between ZEB1 and p21 H scores in NSCLC specimens.
(Padhye et al JCI insight, 2021, in press).

We further tested this observation by inducing EMT or MET by overexpression of ZEB1 or miR-200 in human and murine isogenic cell line pairs. We observed p21 transcriptional and translational repression with ZEB1 expression. Conversely, with miR-200 expression, there was an upregulation of p21 (Figure 41 A, B).

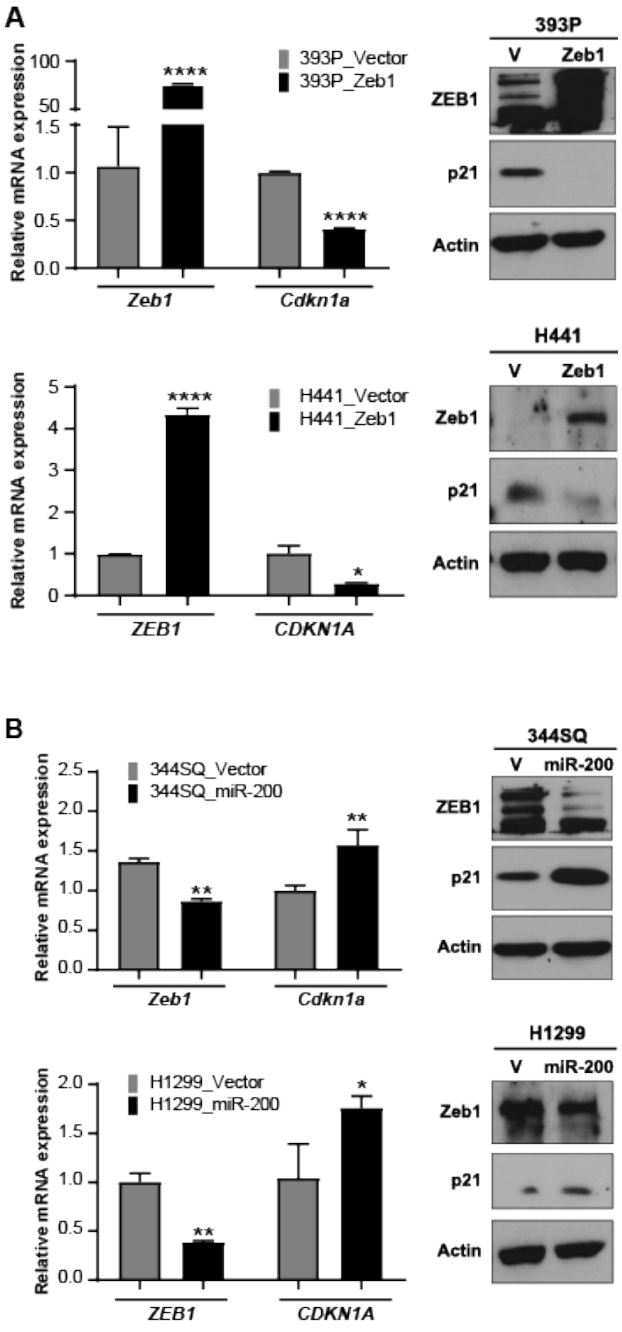

Figure 41. ZEB1 mediated EMT regulates p21 expression.
(A) ZEB1 induction for 48 hours with 2 µg/ml of doxycycline in murine and human epithelial lung cancer cell lines. (B) miR-200 induction for 48 hours with 2 µg/ml of doxycycline in murine and human mesenchymal lung cancer cell lines. *(Padhye et al JCI insight, 2021, in press).*

Transient and stable knockdown of ZEB1 in human and murine cells, respectively, caused p21 expression (Figure 42 A-C). Cells treated with the HDAC inhibitor mocetinostat undergo an MET by upregulation of the miR-200 family and ZEB1 suppression[103,182]. Treatment also produced increased expression of p21 (Figure 42 D-F). Induction of miR-200 in tumor cells by different means pushes the cells to a more epithelial state, which is generally considered a less aggressive phenotype for tumor cells and more akin to a "normal" cell state. Expression of p21 in an epithelial like state restores the cell cycle checkpoint that is lost or blunted in mesenchymal tumor cells with high ZEB1 activity and a more aggressive phenotype.

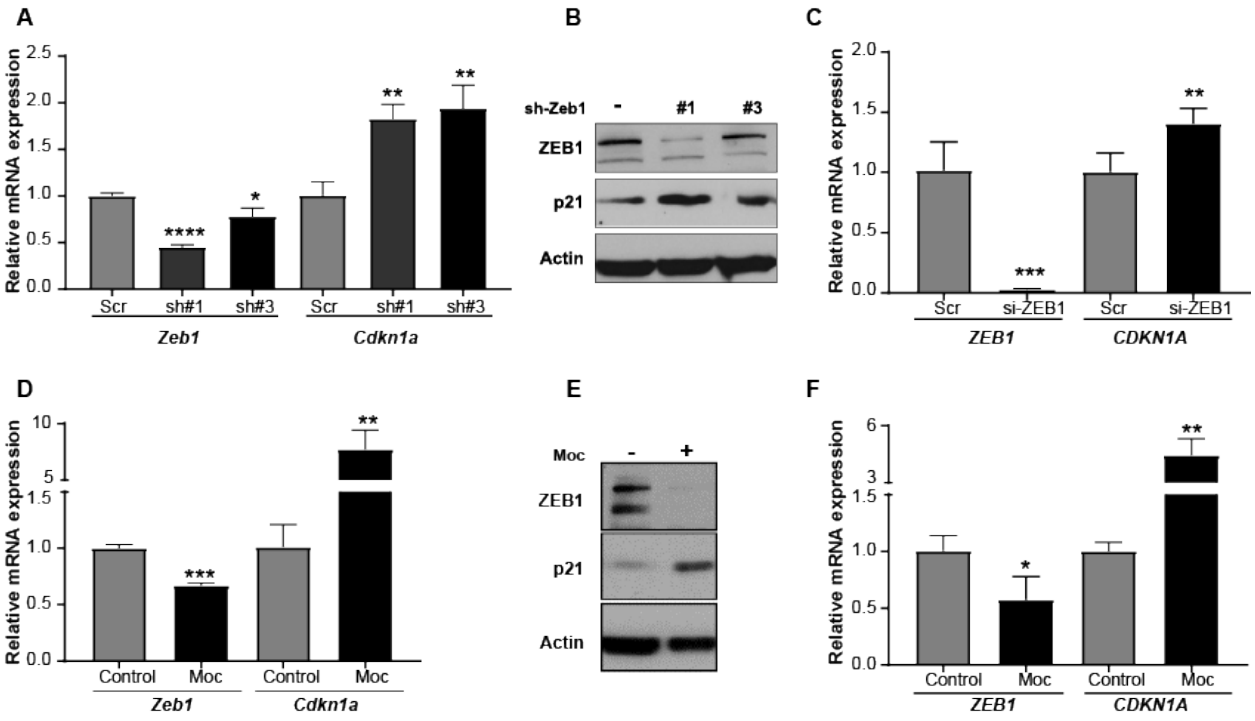

Figure 42. Genetic and pharmacological suppression of ZEB1 alters p21 expression.
(A) Relative mRNA expression in 344SQ cells with stable ZEB1 knockdown. (B) Western blot analysis of indicated markers in 344SQ cells with stable ZEB1 knockdown. (C) Relative mRNA expression of indicated markers in H1299 cells with transient ZEB1 knockdown. (D) Relative mRNA expression of indicated markers in 344SQ cells upon treatment with mocetinostat (1μM) for 48 hours. (E) Western blot analysis of 344SQ cells upon treatment with mocetinostat (1μM) for 48 hours. (F) Relative mRNA expression in H1299 cells upon treatment with mocetinostat (1μM) for 48 hours. Statistical analysis for A, E and G: Unpaired t-test and for F, H, J, K and M: One-way ANOVA test. **** p<0.0001; *** p<0.005; ** p<0.001; * p< 0.05.
(Padhye et al JCI insight, 2021, in press).

Luciferase reporter assays were utilized to investigate ZEB1 mediated transcriptional regulation of p21. The promoter region of p21 was cloned upstream of a luciferase reporter and transfected into human lung cancer cells with either ZEB1 or miR-200 expression. H358 and H441 cells expressing ZEB1 led to a decrease in relative luciferin signal confirming transcriptional repression of the p21 promoter in the presence of high ZEB1. Conversely, an increase in luciferin signal was detected in H1299 cells with miR-200 induction, which suppresses the endogenous cellular ZEB1 expression and relieves transcriptional repression of the p21 promoter (Figure 43 A). Binding of ZEB1 to the endogenous p21 promoter was confirmed by ChIP qPCR assays in cells with inducible ZEB1 or miR-200 expression, using previously published primer pairs [203] (Figure 43 B). Using GAPDH as the negative control and miR-200c as a positive control, we confirmed direct binding of ZEB1 to the p21 promoter.

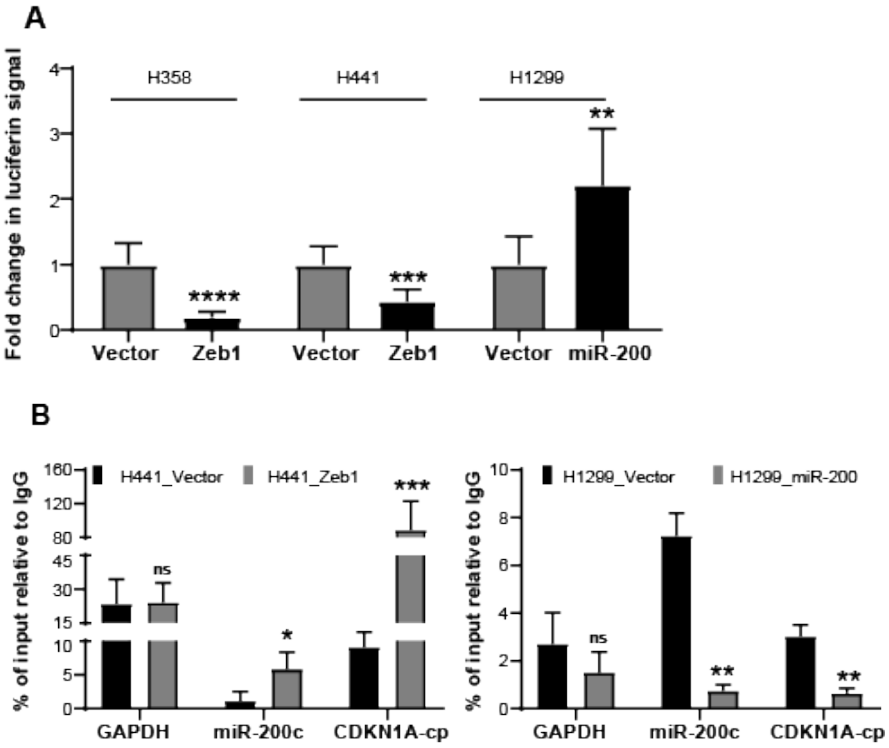

Figure 43. Transcriptional repression of p21 occurs by direct binding of ZEB1 to promoter.
(A) Relative luciferase activity of CDKN1A promoter reporter construct transfected into epithelial H358 and H441 cells with induced ZEB1 expression or mesenchymal H1299 with induced miR-200 expression. Relative luciferin signal was normalized to promoter-less vector control signal. (B) Fold enrichment by qPCR analysis of CDKN1A promoter containing ZEB1 binding site after endogenous ZEB1 ChIP in H441 cells with inducible ZEB1 expression or H1299 cells with inducible miR-200 expression, using ZEB1 antibody or immunoglobulin G (IgG) control antibody.
(Padhye et al JCI insight, 2021, in press).

5.2.4 Suppression of p21 in mesenchymal cells regulates CDK4 pathway

We next explored the effect of p21 on CDK4 activity in epithelial and mesenchymal lung cancer cells. With transient knockdown of CDK4, phosphorylation of RB was continuously suppressed in mesenchymal cells for 48 hours (Figure 44 A,B). On the contrary, CDK4 knockdown in epithelial tumor cells appeared to have only slightly muted downstream signaling (phosphorylation of RB), which coincided with a rather surprising accumulation of phosphorylated CDK4, even with very low levels of total CDK4 protein. The CDK4 accumulation corresponded to a continued presence of p21 protein in the epithelial cells (Figure 44 B). The intriguing findings observed here recapitulated the data in a previous report by Bisteau et al.[204], which showed that a sustained presence of p21 protein in cells was able to maintain the phosphorylation status of CDK4 (hence the stability of the complex), but still inhibit kinase activity. A similar observation was made in our epithelial, but not mesenchymal, model where the presence of p21 maintains the CDK4 in the phosphorylated state. A similar outcome was observed with pharmacological inhibition of CDK4, including a partial suppression of phospho-RB, an accumulation of phospho-CDK4 with the presence of p21 in epithelial cells, versus a lack of p21 with a near complete suppression of phospho-RB in the mesenchymal cells by 48 hours (Figure 44 C).

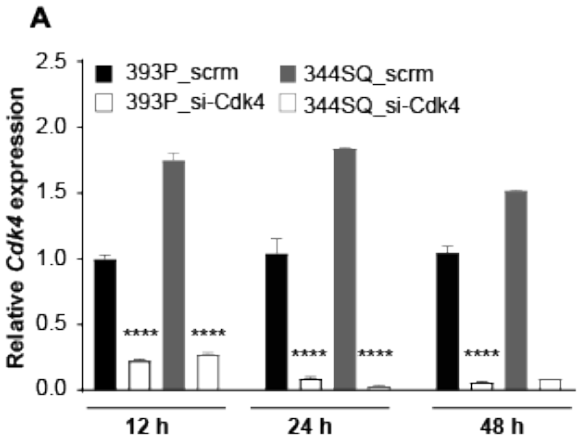

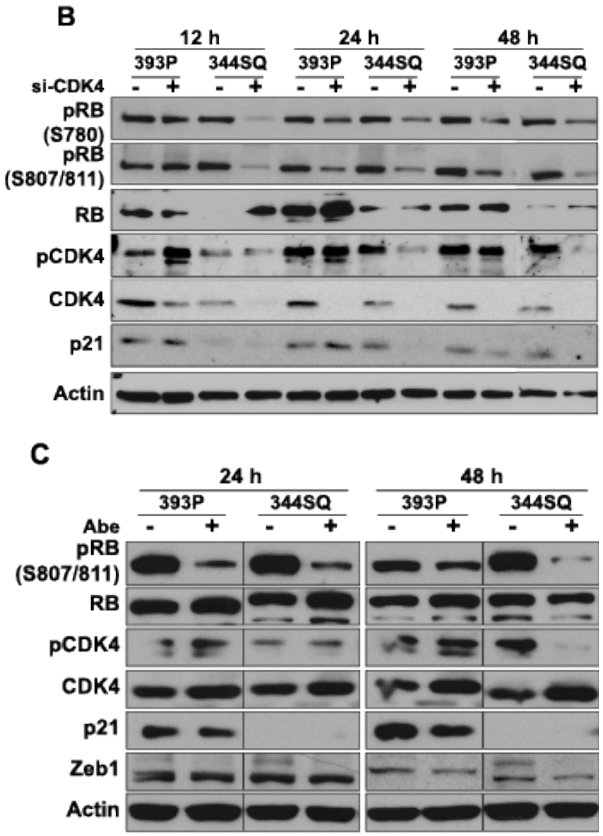

Figure 44. p21 maintains CDK4 phosphorylation despite CDK4 loss.
(A) Relative CDK4 mRNA expression after transient knockdown using 20 nM si-RNA. (B) Western blot analysis after transient knockdown of CDK4 for 12, 24 and 48 hours in epithelial and mesenchymal cancer cells. (C) Western blot of CDK4 signaling pathway after treatment with 2 μM of abemaciclib at indicated times.
(Padhye et al JCI insight, 2021, in press).

To further demonstrate this point, we co-immunoprecipitated CDK4 and p21 in mesenchymal and epithelial cancer cells (Figure 45 A). In mesenchymal 344SQ and 344SQ_vector cells, lower amounts of CDK4-p21 complex co-immunoprecipitated together compared to epithelial 393P and 344SQ_miR-200 cells where an increased binding of CDK4 and p21 was detected. We also observed the seemingly contradictory presence of phospho-RB in epithelial cells alongside p21 expression. An explanation for this observation is the sequestration of p21 into the CDK4 complex, alleviating the repression from the CDK2-Cyclin E complex, which can then phosphorylate RB to maintain cell cycle progression. In fact, we observed that epithelial cells are more sensitive to the CDK2 inhibitor (miciclib) than mesenchymal cells (Figure 45 B), indicating that CDK2 may be the primary regulator of cell cycle in epithelial cells. Lower binding of p21 to CDK4 in mesenchymal cancer cells is only sufficient to maintain the activity of the CDK4 complex but not in abundant enough to exert an inhibitory effect on the downstream pathway.

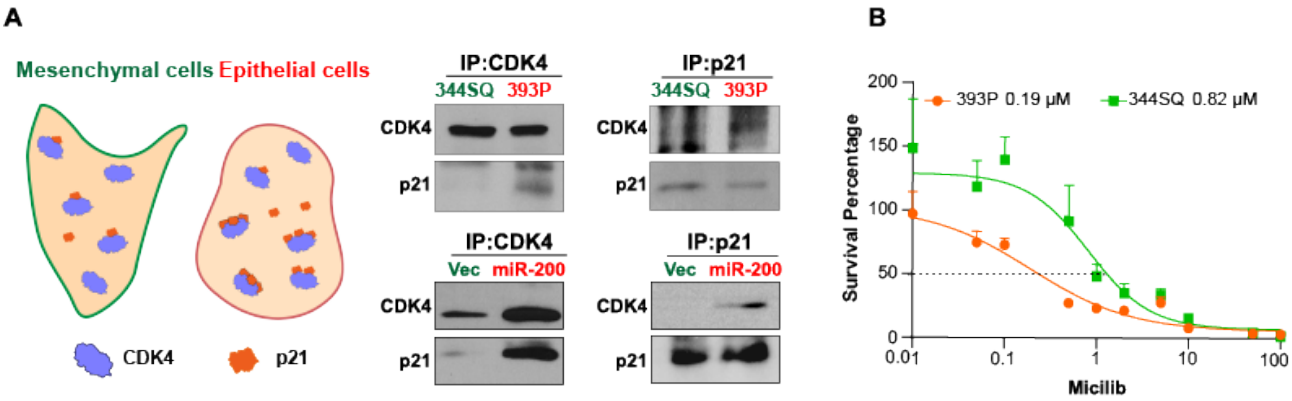

Figure 45. Co-immunoprecipitation of CDK4-p21 in epithelial and mesenchymal cells.
(A) (Left) Graphical representation of the differences in CDK4-p21 complex formation in epithelial and mesenchymal cancer cells. (Right) Co-IP of endogenous CDK4 and p21 in epithelial (393P and 344SQ_miR-200) and mesenchymal (344SQ and 344SQ_vec) cell lines and analyzed by western blot with anti-CDK4 and anti-p21 antibodies. (B) In vitro cell viability assay after 48 hour miciclib treatment in 393P and 344P cells.
(Padhye et al JCI insight, 2021, in press).

Constitutive (344SQ_pCMV6) or doxycycline-inducible (344SQ_pTripZ) expression of p21 in the mesenchymal 344SQ cells was used to determine the direct effect of p21 on CDK4 activity. Upon p21 expression, there was suppression of phospho-RB and phospho-CDK4, which correlated with detection of higher amounts of the CDK4-p21 complex (Figure 46 A, C). These cells also demonstrated slower *in vitro* growth compared to the vector only cells (Figure 46 B, D) and a decreased sensitivity to palbociclib (Figure 47 A, C). When the cells were subcutaneously implanted in syngeneic wildtype mice, the p21 overexpressing tumors grew significantly slower (Figure 47 B, D), with about one-third of tumors undergoing complete regression.

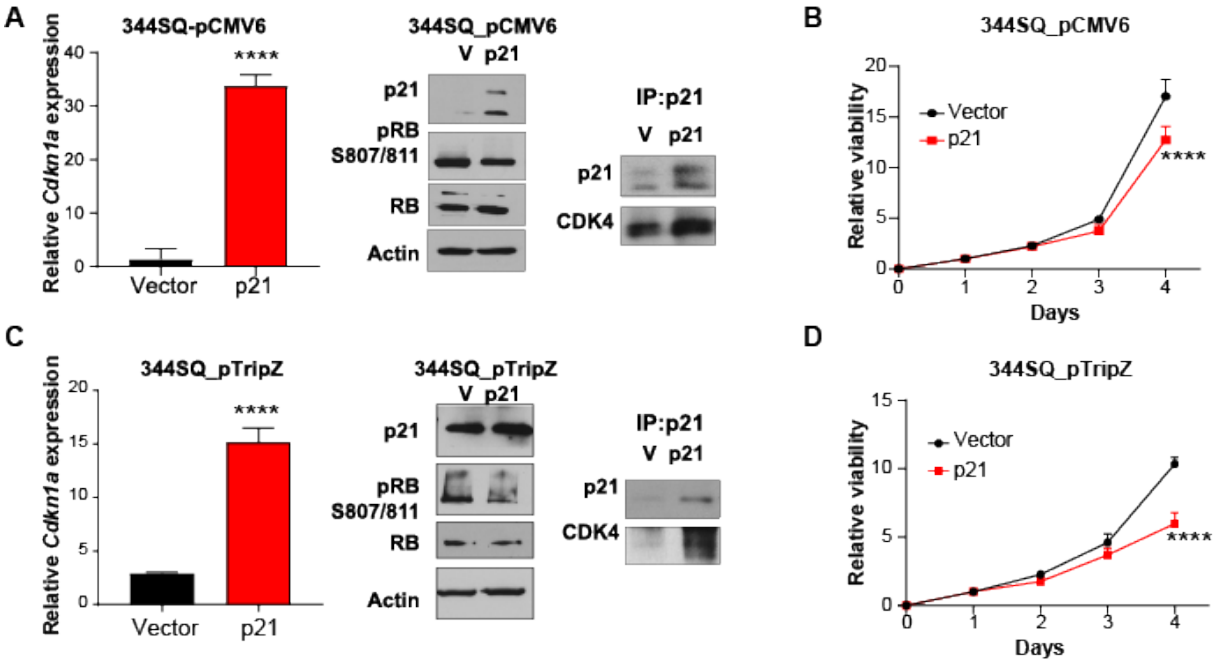

Figure 46. Overexpression of p21 in mesenchymal cells regulates CDK4 pathway.
(A) Constitutive overexpression of Cdkn1a in 344SQ cells. Relative expression of Cdkn1a (left), western blot of CDK4 pathway (middle) and co-IP of CDK4 and p21 in 344SQ cells (right). (B) Growth rates of 344SQ cells ± p21 OE over 4 days measured by WST-1 assay. (C) Inducible overexpression of Cdkn1a in 344SQ cells. Relative mRNA expression of Cdkn1a (left), western blot of CDK4 pathway (middle) and co-IP of CDK4 and p21 in 344SQ cells (right). (D) Growth rates of 344SQ cells ± p21 OE (dox induced) over 4 days measured by WST-1 assay.
(Padhye et al JCI insight, 2021, in press).

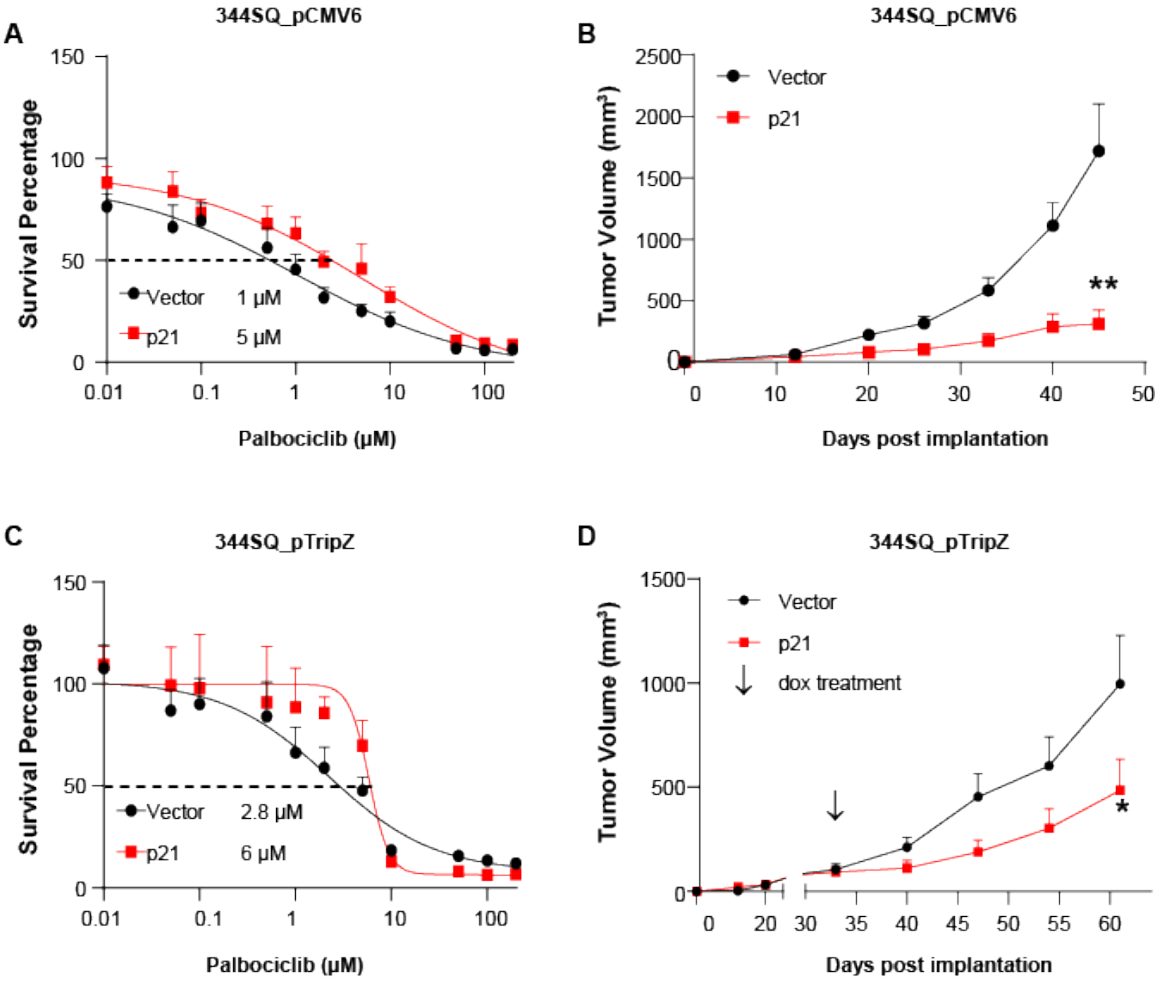

Figure 47. Overexpression of p21 in mesenchymal cells regulates tumor growth.
(A) In vitro cell viability assay after 48 hours of palbociclib treatment in 344SQ cells ± p21. (B) Tumor volume measurements at indicated time points of 344SQ tumors ± p21 (n= 5 per group). (C) In vitro cell viability assay after 48 hour palbociclib treatment in 344SQ cells ± p21 with doxycycline induction. (D) Tumor volume measurements of 344SQ tumors ± p21 expression with dox feed (n=9-10/group). Dox feed was started after tumors reached a size of 100-150 mm3 (indicated by arrow). Doxycycline feed was started after tumors reached a size of 100-150 mm^3 (indicated by arrow). Data are presented as mean ± SEM.
(Padhye et al JCI insight, 2021, in press).

We also generated 393P cells with stable or doxycycline-inducible knockdown of p21 (Figure 48 A-D). A modest increase in phospho-RB was detected with p21 knockdown (Figure 48 A,C), alongwith slightly higher growth rates and enhanced sensitivity of the epithelial 393P cells to palbociclib (Figure 48 B, C).

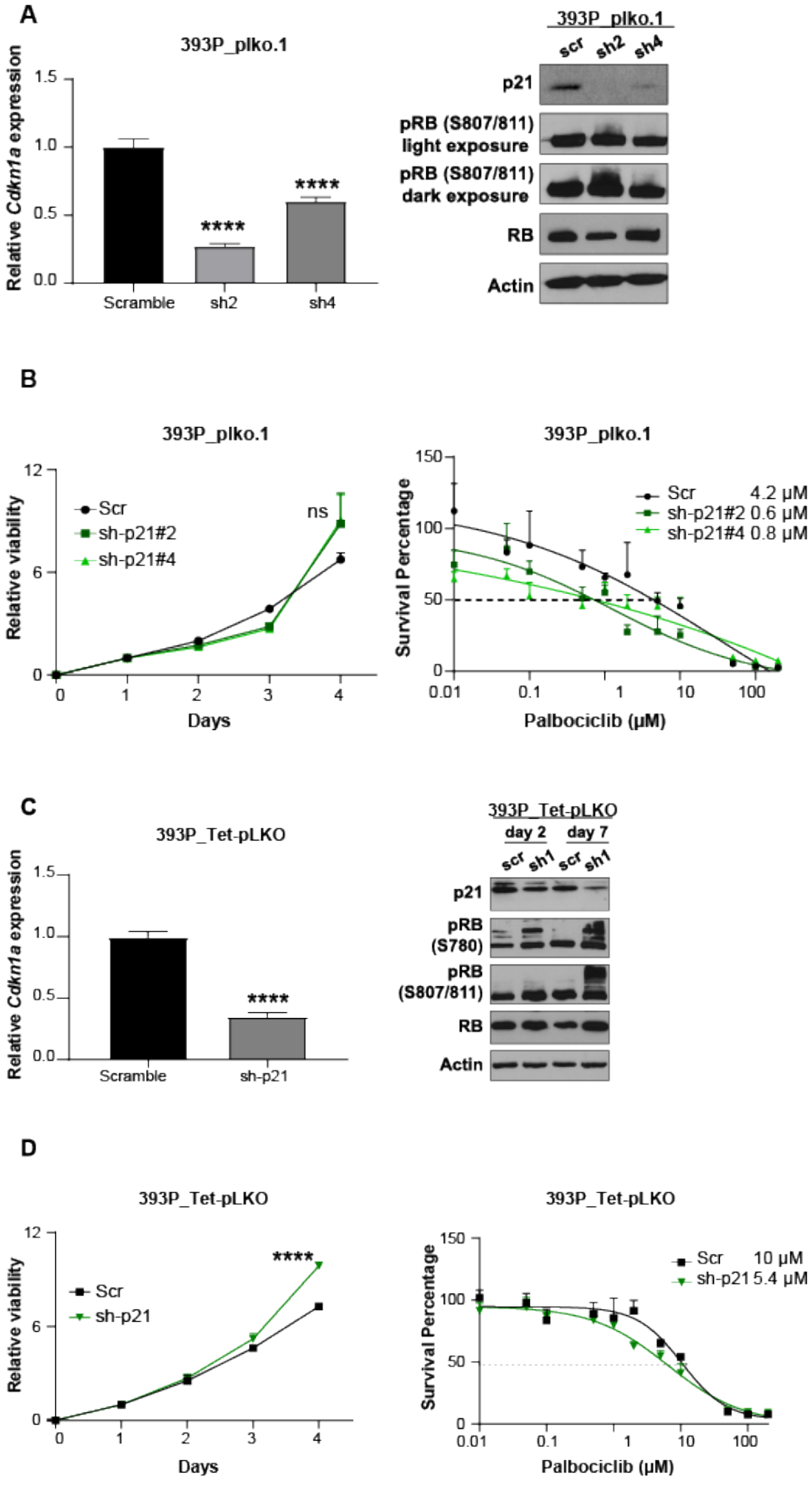
A
393P_plko.1
Relative Cdkn1a expression
1.5
1.0
0.5
0.0
****
****
Scramble
sh2
sh4
393P_plko.1
scr
sh2
sh4
p21
pRB (S807/811) light exposure
pRB (S807/811) dark exposure
RB
Actin
B
393P_plko.1
Relative viability
12
6
0
Scr
sh-p21#2
sh-p21#4
ns
0
1
2
3
4
Days
393P_plko.1
Survival Percentage
150
100
50
0
Scr 4.2 µM
sh-p21#2 0.6 µM
sh-p21#4 0.8 µM
0.01
0.1
1
10
100
Palbociclib (µM)
C
393P_Tet-pLKO
Relative Cdkn1a expression
1.5
1.0
0.5
0.0
****
Scramble
sh-p21
393P_Tet-pLKO
day 2
day 7
scr
sh1
scr
sh1
p21
pRB (S780)
pRB (S807/811)
RB
Actin
D
393P_Tet-pLKO
Relative viability
12
6
0
****
Scr
sh-p21
0
1
2
3
4
Days
393P_Tet-pLKO
Survival Percentage
150
100
50
0
Scr 10 µM
sh-p21 5.4 µM
0.01
0.1
1
10
100
Palbociclib (µM)

Figure 48. Suppression of p21 in mesenchymal cells regulates CDK4 pathway.
(A) (Left) Relative mRNA expression of Cdkn1a in 393P cells with stable knockdown using shRNA for Cdkn1a. (Right) Western blot for CDK4 pathway in response to Cdkn1a knockdown. (B) (Left) Growth rates of 393P cells ± p21 knockdown over 4 days measured by WST-1 assay. (Right) In vitro viability assay after 48 hours of palbociclib treatment in 393P cells with Cdkn1a knockdown. (C) (Left) Relative mRNA expression of Cdkn1a in 393P cells with knockdown using doxycycline inducible shRNA for Cdkn1a for 48 hours. (Right) Western blot for CDK4 pathway in 393P in response to Cdkn1a knockdown using doxycycline inducible shRNA for Cdkn1a for 2 and 7 days. (D) (Left) Growth rates of 393P cells ± p21 knockdown with doxycycline induction of shRNA over 4 days measured by WST-1 assay. (Right) In vitro viability assay after 48 hours of palbociclib treatment in 393P cells with Cdkn1a knockdown with doxycycline induced shRNA. Statistical analysis for A, H and L: One-way ANOVA, E and G: Unpaired t-test and J and N: Two-way ANOVA. **** $p<0.0001$; *** $p<0.005$; ** $p<0.001$; * $p< 0.05$; ns: not significant. *(Padhye et al JCI insight, 2021, in press).*

We next tested the long-term effect of inhibiting CDK4 on the EMT status of tumor cells. With doxycycline-mediated induction of CDK4 shRNA for 7 days, we observed a shift towards an epithelial phenotype indicated by decreased ZEB1 and vimentin levels and an accumulation of phospho-Erk (Figure 49 A). We also generated palbociclib-resistant cells with treatment of 344SQ cells for ~4 weeks (Figure 49 B). An epithelial phenotype was observed with an increase in E-cadherin and decrease in ZEB1 and vimentin levels (Figure 49 C, D). Therefore, targeting CDK4 allows the tumor population to shift to a more epithelial state, which would prime the tumor cells for MEK inhibitor treatment.

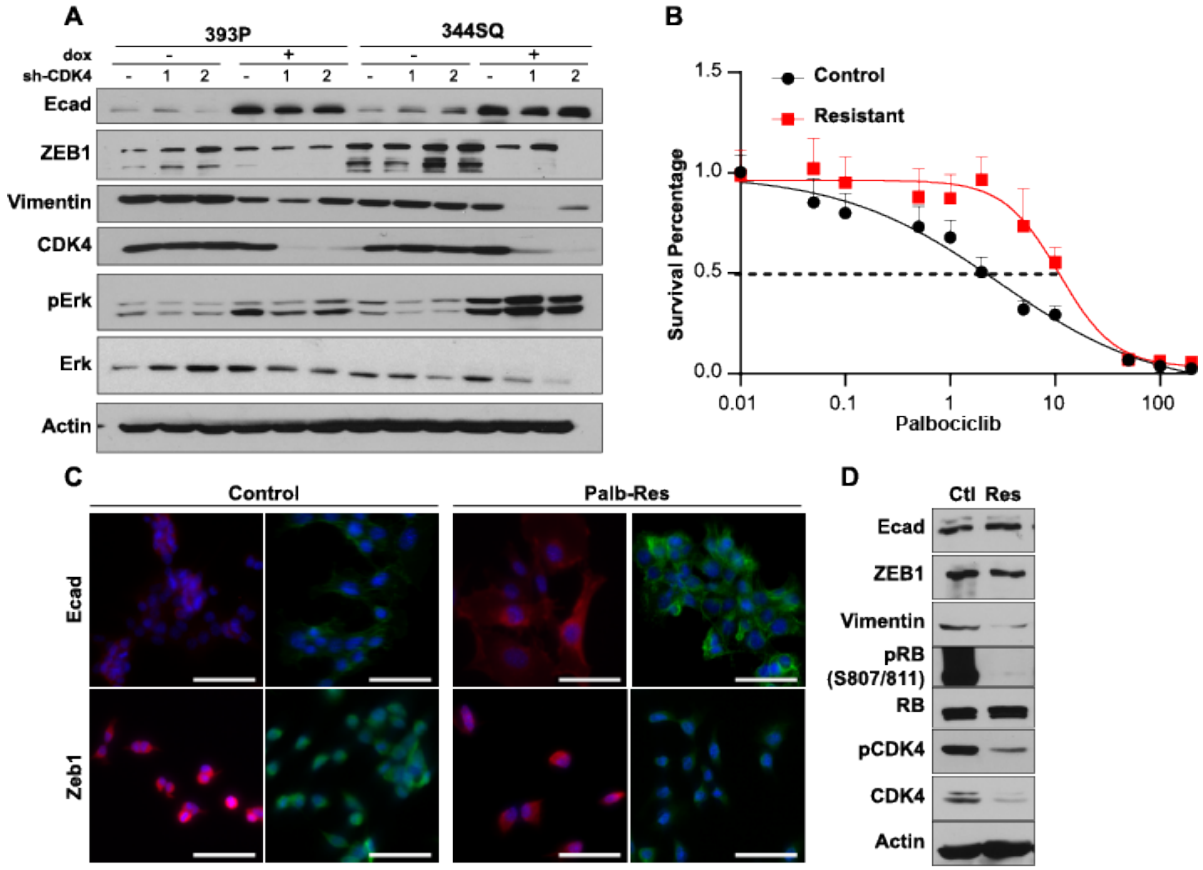

Figure 49. CDK4 inhibition induces MET in lung cancer cells.
(A) Western blot analysis of 393P and 344SQ cells with CDK4 knockdown for 7 days. (B) Cell viability after 48 hours of palbociclib treatment in 344SQ control and palbociclib resistant cells. Cell viability curves were generated using a nonlinear regression fit model. Data are presented as mean ± SD. n=8 per each drug concentration. (C) Immunofluroscent staining in 344SQ control and palbociclib resistant cells for indicated markers. Blue: DAPI. Scale bar: 50 µm (D) Western blot analysis of indicated markers in 344SQ control and palbociclib resistant cells.
(Padhye et al JCI insight, 2021, in press).

When tumor cells were treated with single-agent MEK or CDK4 inhibitor, there was a reciprocal activation of the CDK4 or MEK signaling pathways, respectively (Figure 50 A), showing a dynamic switching of signaling pathway activation and survival dependencies in the face of pharmacological treatments. Transient knocked down of CDK4 in mesenchymal cells followed by treatment with AZD6244 sensitized the previously unresponsive mesenchymal-like 344SQ and 344P cells to MEK inhibition (Figure 50 B). We then tested the effect of combination palbociclib and AZD6244 treatment using a series of fixed concentrations at 1:1 ratio and calculated the fraction affected (Fa) values after exposure to the drugs. The Chou-Talalay method [108] was used to determine the combination index (CI)

and drug reduction index (DRI). The favorable DRI, shown in yellow (Figure 50), was used to confirm the CI data. The drug combinations showed favorable DRI (DRI>1) and evidence of synergism (CI<1) at Fa>0.5 for palbociclib and AZD6244 (Figure 50 C). These data provided basis for further exploring the combination of CDK4 and MEK inhibitors.

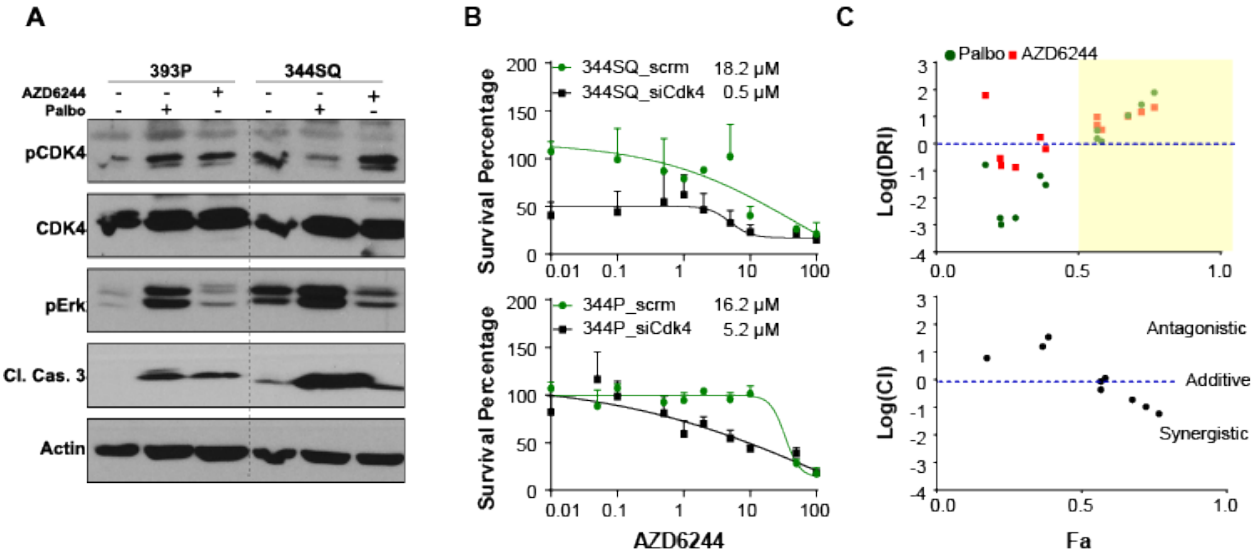

Figure 50. CDK4 and MEK inhibition is synergistic.
(A) Western blot on cells treated with AZD6244 (5μM) and palbociclib (5μM) for 48 hours. (B) *In vitro* cell viability assay on 344SQ (top) and 344P (bottom) lung cancer cell lines with or without transient knockdown of CDK4 and treatment with AZD6244 for 48 hours. (C) Drug Reduction Index (DRI) and Combination Index (CI) using Chou-Talalay method on 344SQ cells. Statistical analysis for C, E, F and H: Unpaired t-test and for D and G: Two-way ANOVA test. **** p<0.0001; *** p<0.005; ** p<0.001; * p< 0.05. *(Padhye et al JCI insight, 2021, in press).*

5.2.5 Co-targeting CDK4 and MAPK pathways targets different tumor cell subsets

We have previously described that MEK inhibitors preferentially target epithelial K-ras mutant tumor cells[103,194] and with the evidence presented here that CDK4 inhibitors have a greater impact on mesenchymal tumor cells, we set out to test the effects of combination treatment on the tumor cell subpopulations. We treated human (H1299 and H358) and murine (393P and 344SQ) tumor cells with AZD6244 and palbociclib and stained the cells with annexin V and propidium iodide. Both human (H1299) and murine (344SQ) mesenchymal tumor cells underwent greater apoptosis in response to CDK4 inhibitors and epithelial tumor cells (H358 and 393P) were highly sensitive to MEK inhibition (Figure 51).

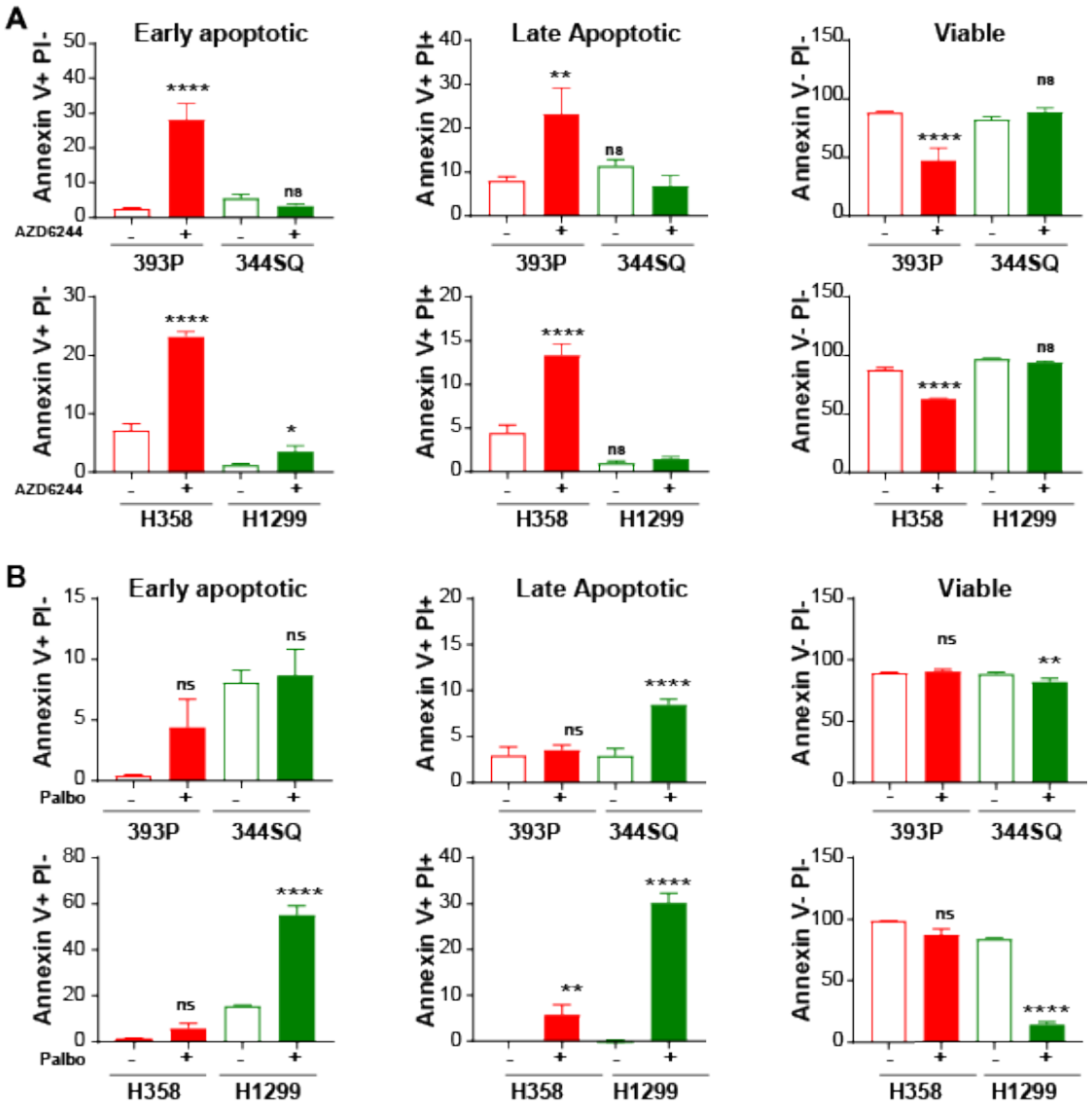

Figure 51. CDK4 and MEK inhibitors induce differential apoptosis in tumor subpopulations. (A-B) Apoptosis was determined by annexin V and propidium iodide staining after treatment with AZD6244 (5 μM) or palbociclib (5 μM) for 48 hours. Data are presented as the mean ± SD. *(Padhye et al JCI insight, 2021, in press).*

Given that tumors are heterogeneous and consist of cell subsets with distinct phenotypes, we utilized the previously described sensor model, which can detect the epithelial or mesenchymal state of individual tumor cells in real time[106,194]. As seen in Figure 52 A, the majority of the cells in 2D culture were mesenchymal and GFP^+. With treatment of mocetinostat, there was an enrichment of RFP^+ epithelial cells. We utilized this system to test if CDK4 and MEK inhibitors differentially target epithelial and mesenchymal subpopulations. We observed a reduction of epithelial RFP cells with MEK inhibitor (AZD6244) treatment and mesenchymal GFP cells with CDK4 inhibitor (palbociclib) treatment (Figure 52 A, B). With dose escalation of single agent treatment, reciprocal pathway activation occurred, while combination treatment with both drugs suppressed MAPK and CDK4 pathways (Figure 52 C) and enhanced tumor cell killing.

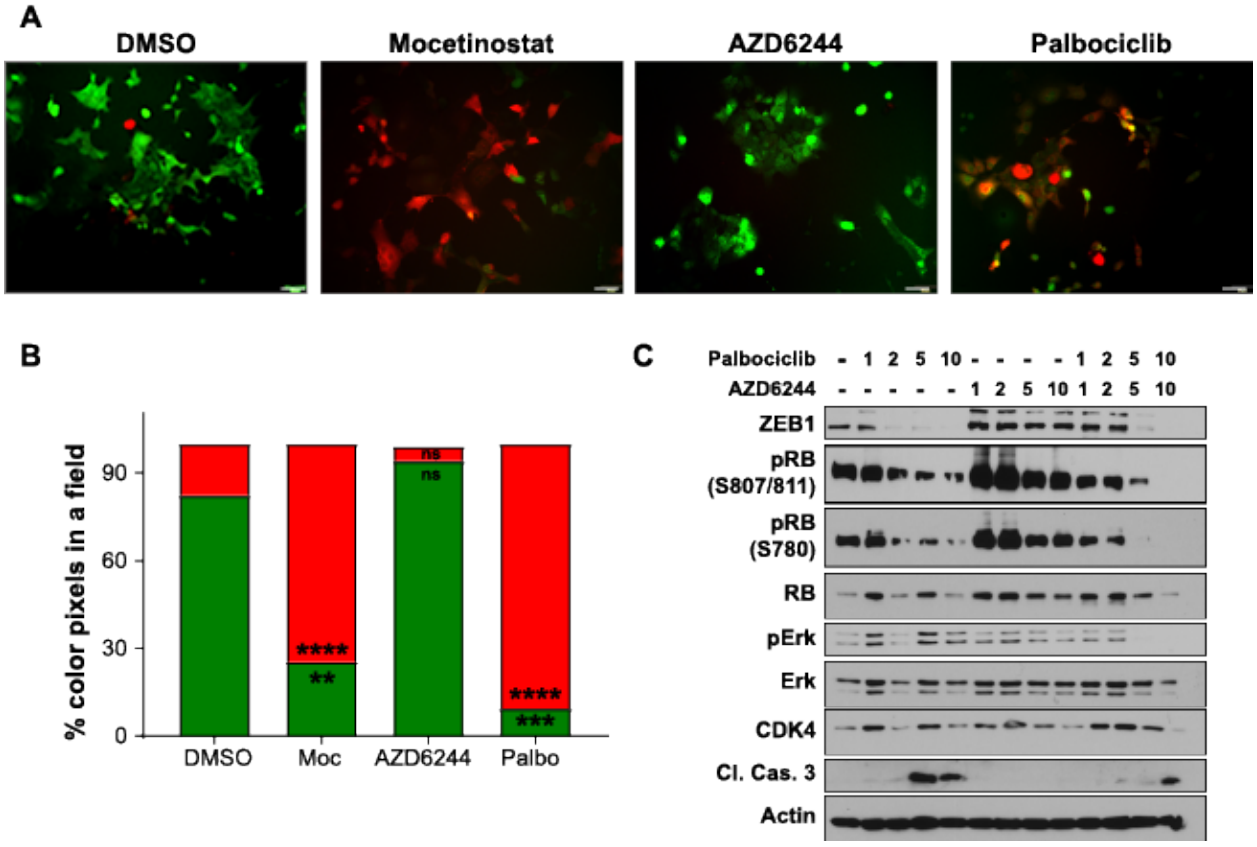

Figure 52. Distinct subpopulations within Z-cad sensor cells have differential sensitivities. (A) 344SQ_Z-cad cells were treated with mocetinostat (1 μM), AZD6244 (5 μM), or palbociclib (5 μM) for 48 hours followed by fluorescent imaging. Scale bar: 50 μM. (B) Images from (A) were quantified for the percentage of RFP or GFP color pixels calculated per field of view (FOV). n=4-6 FOVs. (C) Western blot analysis of 344SQ_Z-cad cells treated with increasing concentrations of palbociclib, AZD6244 or both. *Padhye et al JCI insight, 2021, in press).*

Since western blots are bulk assays, we wanted to assess which specific populations undergo apoptosis within this heterogeneous dynamic system. We utilized a DNA binding dye that is cleaved by caspases present in the cells undergoing apoptosis to produce blue fluorescence, which can be detected by microscopy and flow cytometry. Co-localization of blue/green fluorescence with palbociclib treatment and blue/red fluorescence with AZD6244 treatment demonstrated the specificity of each individual drug to target specific cell types, whereas the combination of both drugs targeted both subpopulations (Figure 53).

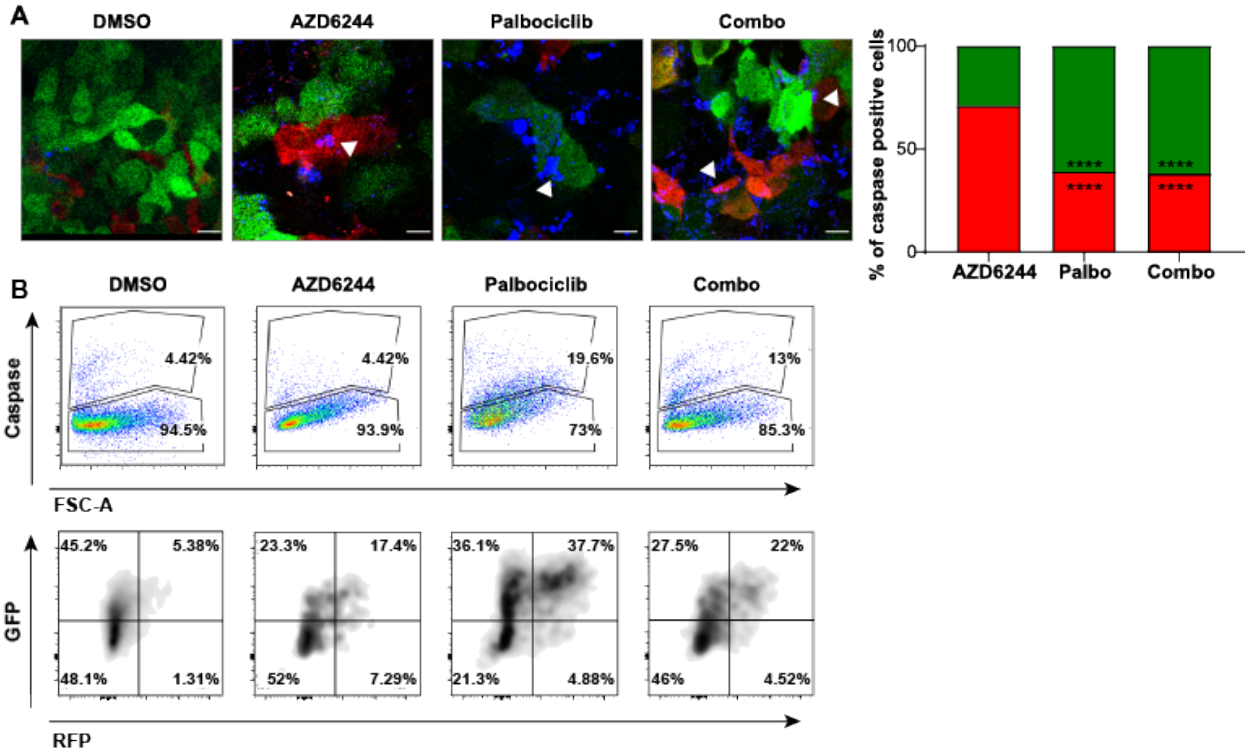

Figure 53. Co-targeting CDK4 and MAPK pathways targets different tumor cell subsets. (A) 344SQ_Z-cad cells were treated with DMSO, AZD6244 (5 μM), palbociclib (5 μM) or the combination. NucView® 405 Caspase 3 substrate was used as a readout for apoptosis. Representative fluorescent images were acquired 48 hours after addition of drugs (left). Scale bar = 25 μM. Arrows indicate apoptotic cells. Images were quantified for total caspase-3+ cells as a percentage of total cells in 4-6 FOVs (right). (B) 344SQ_Z-cad cells treated with indicated drugs were stained with NucView® 405 Caspase 3 substrate and analyzed by flow cytometry. Representative plots are shown. *(Padhye et al JCI insight, 2021, in press).*

In vitro three dimensional assays very closely recapitulate the tumor growth *in vivo*. An established *ex vivo* tumor (EVT) model to culture lung tumors that retains tumor cell heterogeneity[205] was utilized to test the therapeutic sensitivity of distinct tumor cell subpopulations. Similar to the observations in 2D cultures, we found different subpopulations being targeted by individual drugs when EVTs were cultured in laminin-rich Matrigel (MG). Since MG is known to promote an epithelial phenotype[93,133,205], MEK inhibition effectively eliminated this cell subtype and resulted in an enrichment of the GFP^+ cells. CDK4 inhibitor, conversely, caused a depletion of mesenchymal tumor cells within the heterogeneous EVTs and enrichment of the RFP^+ cells (Figure 54 A-C). We also noted a change in phenotype of EVTs treated with palbociclib, producing more structures with a central lumen as compared to other groups (Figure 54 d). Lumen formation and organization in a 3D matrix is characteristic of epithelial cells. Clearly, treatment with CDK4 inhibitor not only targets mesenchymal cells but also promotes an epithelial phenotype, which makes it ideal to be combined with MEK inhibition. In combination treatment, both populations were targeted, which produced a net decrease in size and viability of EVTs (Figure 54 B, D).

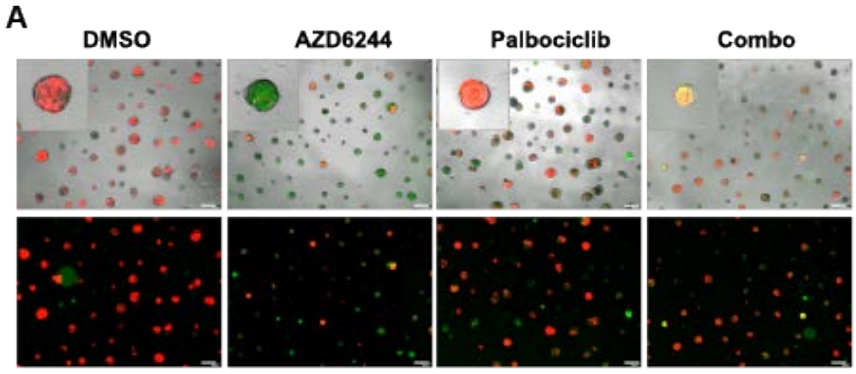

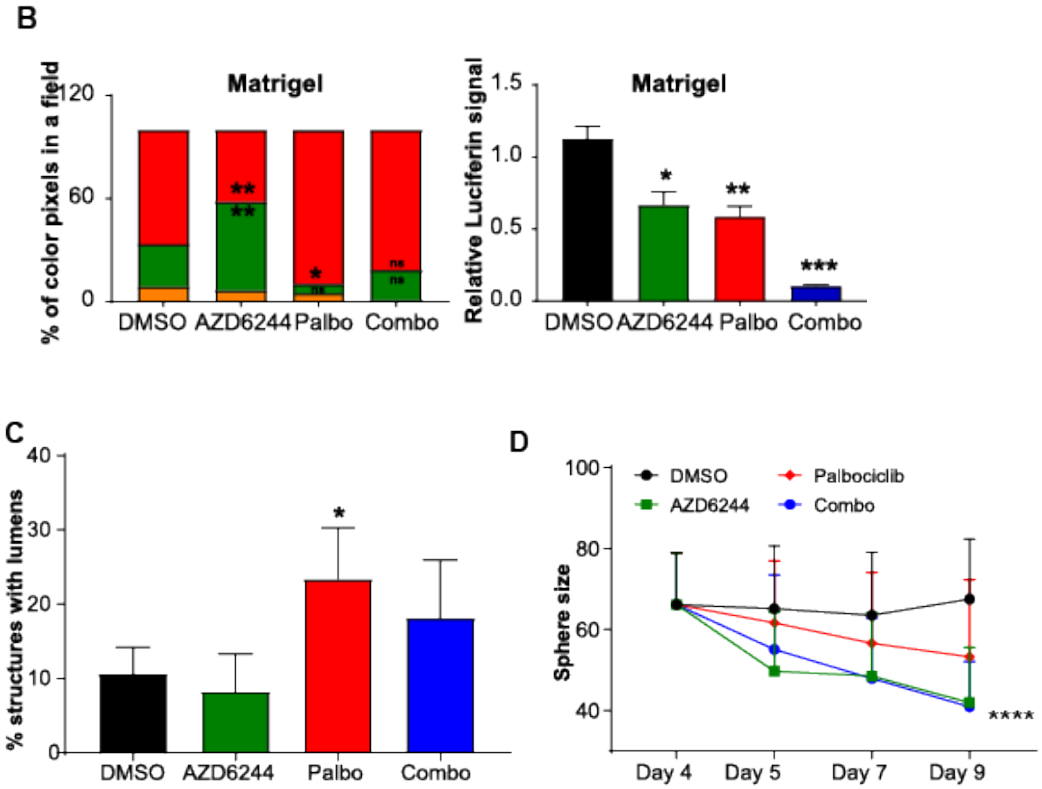

Figure 54. Co-targeting CDK4 and MAPK pathways in Z-cad EVTs in Matrigel.
(A) EVTs were plated in a Matrigel. After 24 hours, EVTs were treated with AZD6244 (5 μM), palbociclib (5 μM) or the combination for 9 days with representative images from last day of the culture shown (scale bar: 200 μM). (B) % of RFP and GFP color pixels in 4-6 FOVs (left panel). Cell Titer-Glo reagent was added and relative luciferin signal was measured (right panel). Treatment groups were compared to DMSO using one-way ANOVA in all the panels. **** p<0.0001; *** p<0.005; ** p<0.001; * p< 0.05; ns: not significant. (C) EVTs cultured in MG and treated with drugs indicated were scored for percentage of structures with central lumens. n=5 FOVs. Treatment groups were compared to DMSO using one-way ANOVA. (D) Quantification of size of EVTs from (A) at indicated times after plating in MG and treatment with indicated drugs. One-way ANOVA was used for statistical significance. **** p<0.0001; * p< 0.05. *(Padhye et al JCI insight, 2021, in press).*

EVTs were also cultured in a matrix containing MG and collagen I, and as previously noted collagen promotes a mesenchymal phenotype in tumor cells[115,205], which made it ideal to test the efficacy of CDK4 inhibitor on this specific subpopulation. MEK inhibitor remained ineffective on the GFP^+ mesenchymal tumor cells, however, there was a significant reduction in the viability of EVTs with CDK4 treatment (Figure 55). Combination treatment proved to be significantly better over the individual treatments in both Matrigel and collagen matrices in terms of suppression of viability of tumor cells. In summary, these results demonstrate the efficacy of CDK4 and MEK inhibitors in combination for effective therapeutic targeting of the lung cancer subpopulations.

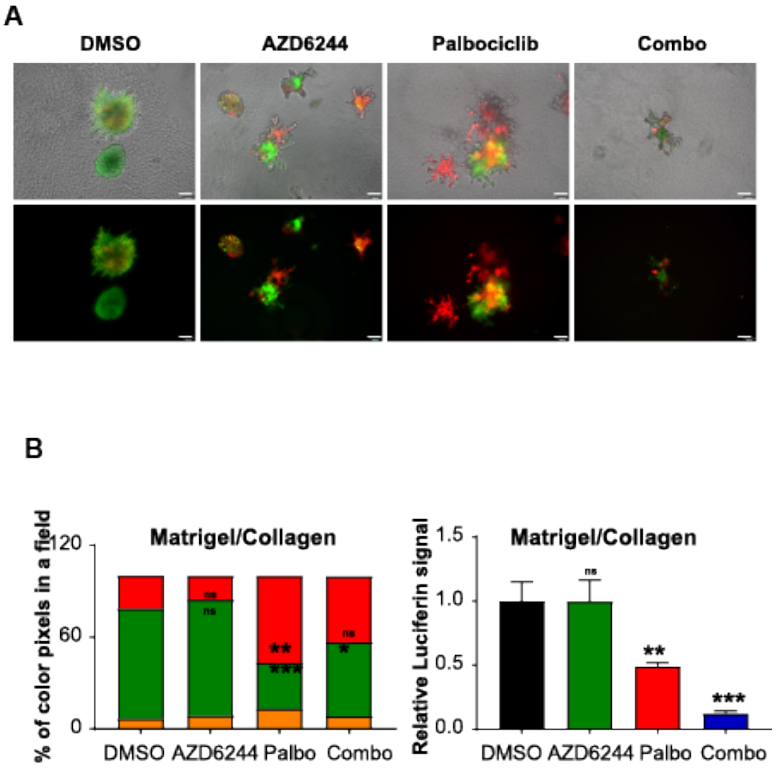

Figure 55. Co-targeting CDK4 and MAPK pathways in Z-cad EVTs in Matrigel/Collagen I. (A) EVTs were plated in a Collagen/Matrigel (Coll/MG) matrix. After 24 hours, EVTs were treated with AZD6244 (5 μM), palbociclib (5 μM) or the combination for 5 days. Representative images at the end of experiment shown (scale bar: 100 μM), (B) Quantification of percentage RFP and GFP color pixels in 4-6 FOVs (left panel) and relative luciferin signal using Cell Titer-Glo reagent (right panel). Treatment groups were compared to DMSO using one-way ANOVA in all the panels. **** p<0.0001; *** p<0.005; ** p<0.001; * p< 0.05; ns: not significant. *(Padhye et al JCI insight, 2021, in press).*

5.2.6 CDK4i and MEKi control tumor growth and prevent emergence of resistance

We next evaluated *in vivo* tumor response to the combination of CDK4 and MEK inhibitors. Mesenchymal (344SQ) or epithelial (393P) tumor cells were subcutaneously implanted in syngeneic wildtype mice. Tumor growth in response to either single agent (palbociclib or AZD6244) or both was monitored over a period of 6-14 weeks. Mice bearing 344SQ tumors remained unresponsive to AZD6244, but responded to palbociclib alone or in combination with AZD6244 (Figure 56 A). This treatment continued for ~6 weeks (short-term) and scored as additive using Bliss effect analysis[104] (Table 11). This promising tumor response in the short term led us to repeat the experiment to determine if there was a durable and sustained response to the combination treatment. Treatment of the cohorts for up to 10 weeks produced the emergence of resistance to palbociclib treatment alone (Figure 56 B). The tumors acquired resistance to single agent palbociclib over an extended period of time, which was prevented with combination treatment, and the group initially treated with only palbociclib was resensitized upon addition of AZD6244 at week 10, either as measured by tumor growth or fold change of tumor volume (Figure 56 B,D). We also observed an increase in E-cadherin and a decrease in nuclear ZEB1 with single-agent palbociclib treatment (Figure 56 C), demonstrating the selection for an epithelial phenotype. The combination treatment for a period of 14 weeks scored as an additive response (Table 11). The number of lung metastatic nodules were also significantly lower with palbociclib or combination (Figure 56 E).

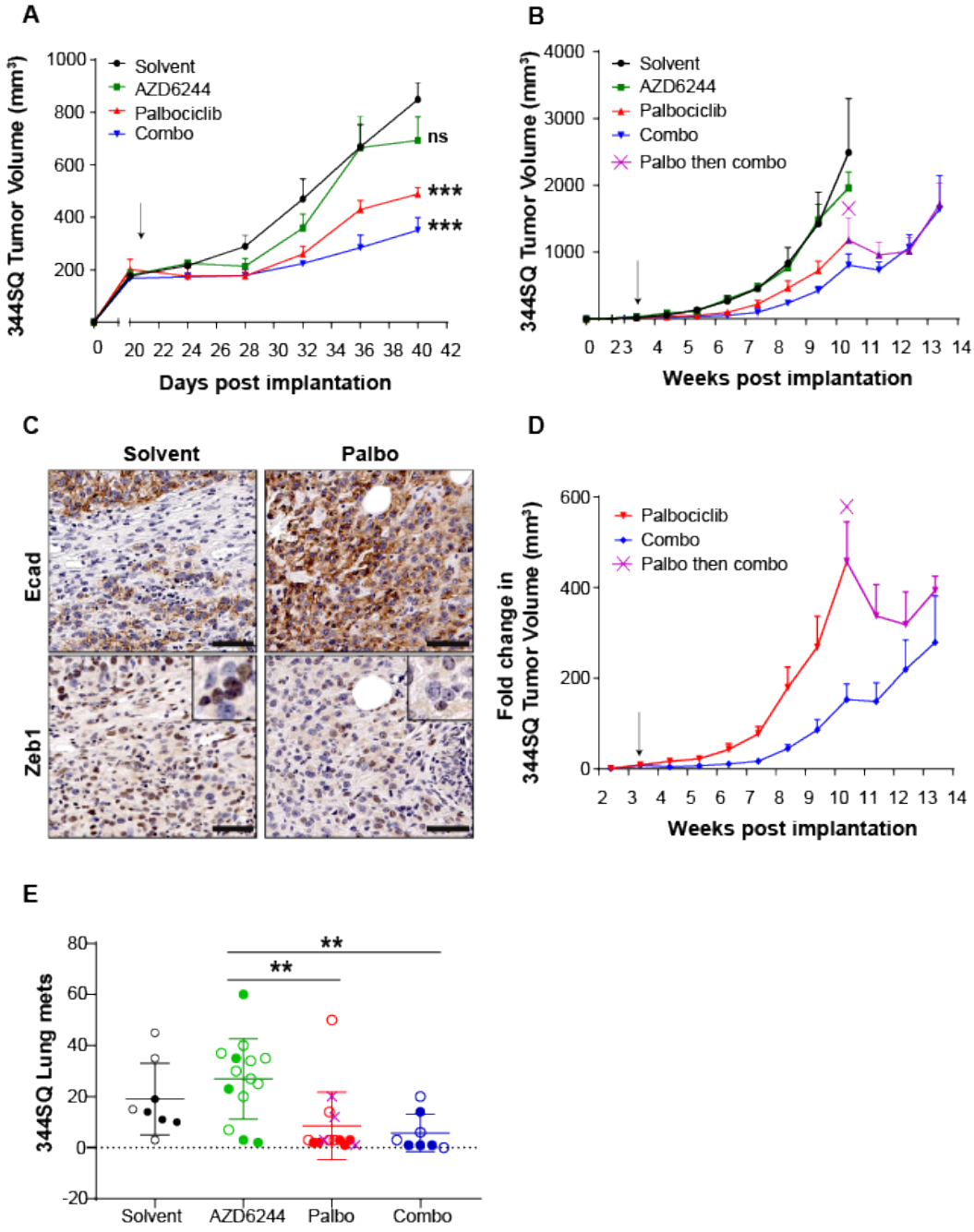

Figure 56. Combination of MEK and CDK4 inhibitors controls 344SQ tumor growth.
(A) Tumor measurements at the indicated time points in syngeneic WT mice (n=5 per group) after daily treatment with solvent, AZD6244 (25 mg/kg), palbociclib (50 mg/kg) or combination. Arrow indicates start of the treatment. (B) Mice were treated with solvent (n=5), AZD6244 (25 mg/kg) (n=10), palbociclib (50 mg/kg) (n=10) or combination (n=5) for 7 weeks at which point resistance to palbociclib emerged. 5 mice from palbociclib treatment alone arm were converted to combination arm and treatment was continued for another 3 weeks (marked by purple X). (C) Immunohistochemical analysis on tumors treated with solvent or palbociclib for 7 weeks. Scale bar: 50 μM. (D) Fold change in tumors in the palbociclib and combo arms over 13 weeks. (E) Mouse lungs were analyzed for macroscopic metastatic lung nodules in each treatment group. Black solid circles: short-term solvent, black open circles: long term solvent. Green solid circles: short term AZD6244, green open circles: long term palbociclib, purple crosses: palbo then combo. Blue solid circles: short-term combo, blue open circles: long term combo.*(Padhye et al JCI insight, 2021, in press).*

We further tested the response of this therapeutic regimen in 393P tumors. Epithelial tumors that initially respond to AZD644 will develop resistance to treatment by undergoing EMT. When treated with single agents, 393P tumors were resistant to palbociclib alone and responded to AZD6244 for about 7 weeks (Figure 57 A). However, the combination of both the drugs suppressed tumor growth with a durable response for ~10 weeks. In the 393P tumor model, combination of CDK4 and MEK inhibitor scored as synergistic using the Bliss effect analysis (Table 11). Since 393P is a non-metastatic model, there were no significant differences in lung metastases (Figure 57 B).

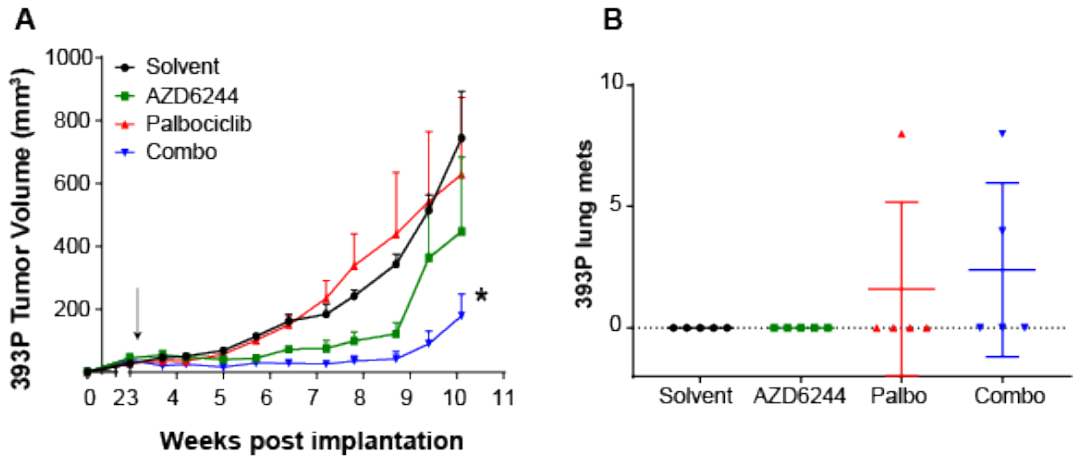

Figure 57. Combination of MEK and CDK4 inhibitors delays resistance in 393P tumors.
(A) Tumor measurements at the indicated time points in syngeneic WT mice (n=5 per group) after daily treatment with solvent, AZD6244 (25 mg/kg), palbociclib (50 mg/kg) or combination. Arrow indicates start of the treatment. (B) Metastatic lung nodules in mice with 393P tumors.
(Padhye et al JCI insight, 2021, in press).

Previously described 393P-vehicle and 393P-AZD^R cells were also implanted subcutaneously in syngeneic wildtype mice to assess the sensitivity to CDK4 and MEK inhibitors. 393P-vehicle tumors retained their sensitivity to AZD6244 and resistance to palbociclib (Figure 58), whereas the tumors derived from 393P-AZD^R cells were unresponsive to AZD6244, and responsive to palbociclib, with one mouse showing complete tumor regression (Figure 58).

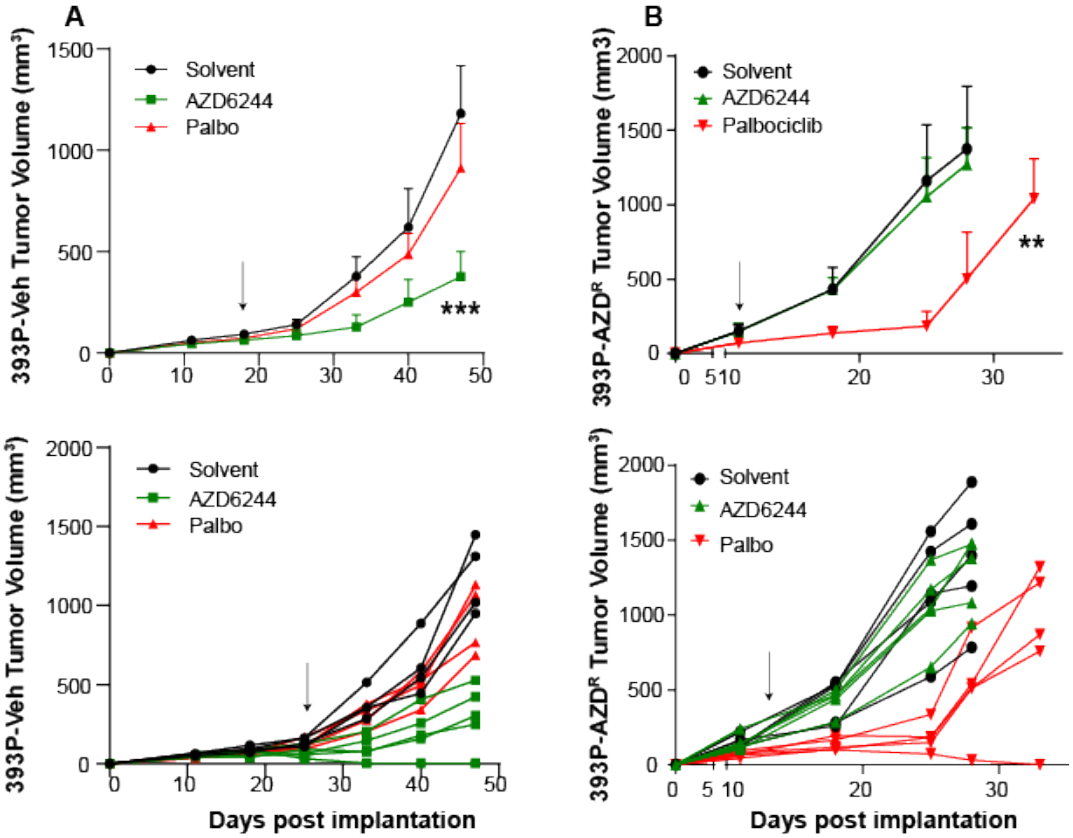

Figure 58. Palbociclib treatment controls tumor growth in 393P_AZD^R tumors.
(A) Tumor measurements of 393P-vehicle subcutaneous tumors in syngeneic WT mice (n=5 per group) after daily treatment with AZD6244 (25 mg/kg) or palbociclib (50 mg/kg). Arrow indicates start of treatment at day 20. Individual growth curves of 393P-vehicle tumors (bottom). (B) Tumor measurements of 393P-AZD^R subcutaneous tumors in syngeneic WT mice (n=5 per group) after daily treatment with AZD6244 (25 mg/kg) or palbociclib (50 mg/kg). Arrow indicates start of treatment at day 14. Individual growth curves of 393P-AZD^R tumors (bottom).
(Padhye et al JCI insight, 2021, in press).

Table 11. Summary of Bliss effect analysis of the *in vivo* studies

Model	Combo EAR	Combo actual	Bliss effect
344SQ_short term	383.4	350.9	Additive
344SQ_long term	342.8	237.4	Additive
393P	378.0	178.4	Synergistic

The mean of expected additive tumor volumes with combination (combo EAR) treatment were calculated by Bliss independent method. The actual tumor volumes with combination (combo actual) treatment lower than the expected additive tumor volumes are considered as synergistic.

Primary tumor tissues were collected at the end of the mouse experiments and stained for the CDK4 and MAPK signaling pathway markers. Untreated 344SQ tumors showed higher phospho-CDK4 and phospho-RB compared to untreated 393P tumors, which had higher phospho-Erk (Figure 59, Figure 60). In 344SQ tumors, treatment with palbociclib led to suppression of phospho-CDK4 and phospho-RB staining, with an increased phospho-Erk; AZD6244 treatment lead to an increase in phospho-CDK4, and the combination drug treatment suppressed both CDK4 and MAPK signaling. 393P tumors, on the other hand, showed suppression of phospho-Erk when treated with AZD6244, accompanied with an increased expression of phospho-Cdk4. Palbociclib caused an increase in phospho-Erk in 393P tumors as well. Combination drug treatment in both models suppressed both pathways significantly compared to either single agent (Figure 59, Figure 60).

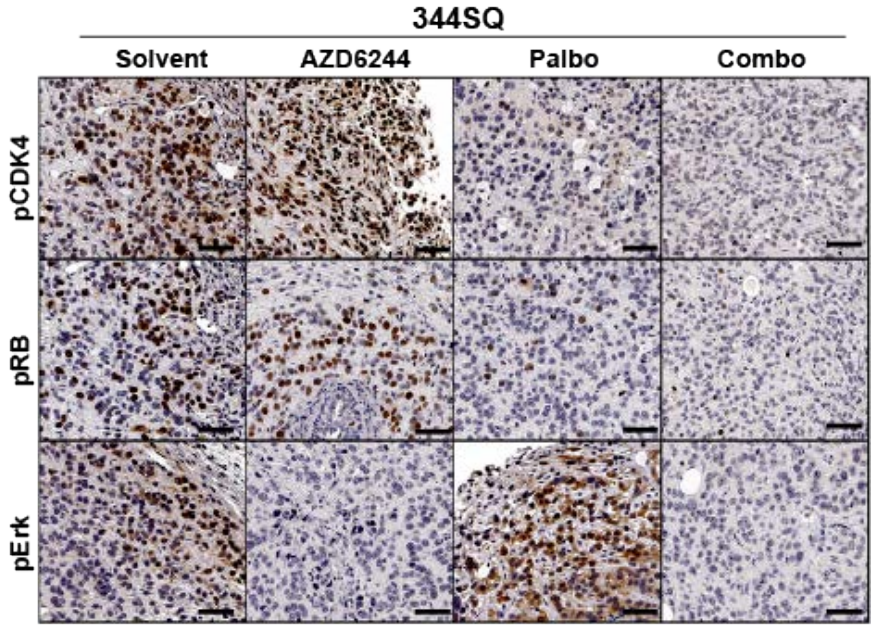

Figure 59. IHC analysis on 344SQ tumors.
Tumors harvested from Figure 56 were stained with indicated markers. Scale bar: 50 μM. *(Padhye et al JCI insight, 2021, in press).*

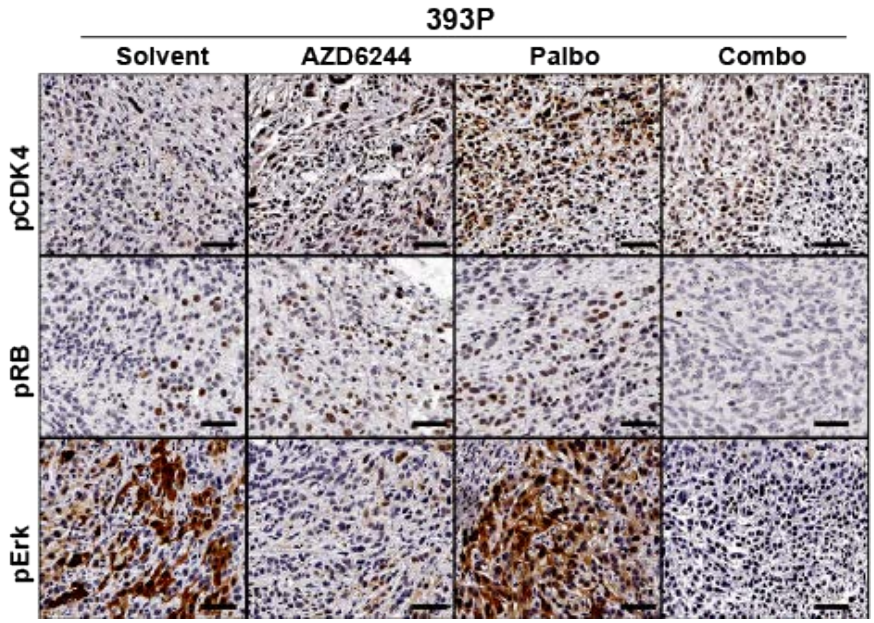

Figure 60. IHC analysis on 393P tumors.
Tumors harvested from Figure 57 were stained with indicated markers. Scale bar: 50 μM. *(Padhye et al JCI insight, 2021, in press).*

To determine the effect of single and combination agent treatments on cell proliferation and cell death, we performed Ki67 staining and TUNEL assay on the tumor tissues. 344SQ tumors treated with palbociclib for 6 weeks had fewer proliferating and more apoptotic cells (Figure 61).

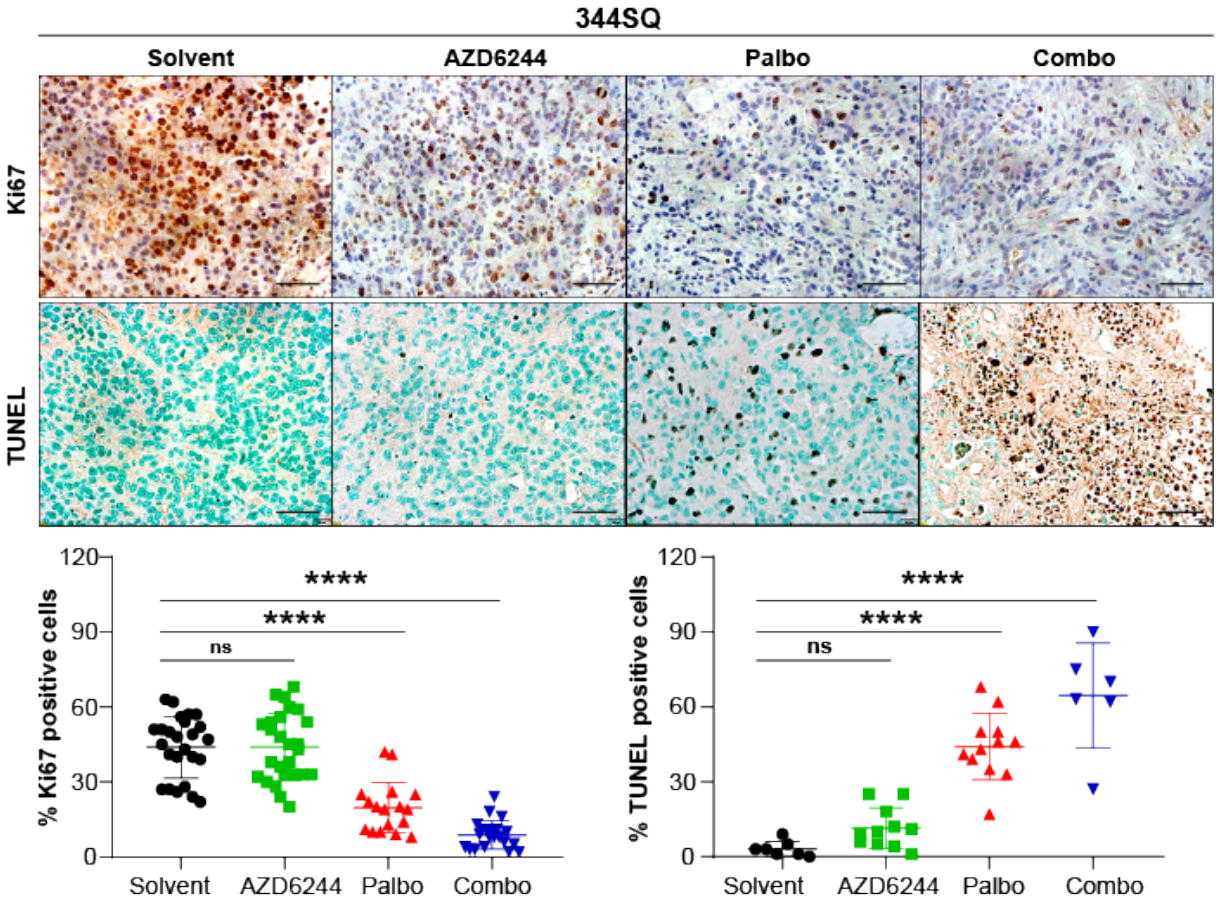

Figure 61. Ki67 and TUNEL staining in 344SQ tumors-short term treatment.
344SQ tumors were stained with Ki67 and TUNEL assay to measure cell proliferation and cell death respectively. Representative IHC images are shown. Scale bar: 50 μM. Images were quantified for Ki67 and TUNEL staining in each treatment group. n=2-3 per group with 3-6 FOV per mouse. Statistical significance was determined by one-way ANOVA. **** p<0.0001; *** p<0.005; ** p<0.001; * p< 0.05; ns: not significant. *(Padhye et al JCI insight, 2021, in press).*

393P tumors treated with AZD6244 had fewer proliferating cells and higher apoptotic cells (Figure 62). However, combination inhibitor treatment in both models significantly suppressed cell proliferation and produced apoptosis in >60% of the tumor cells.

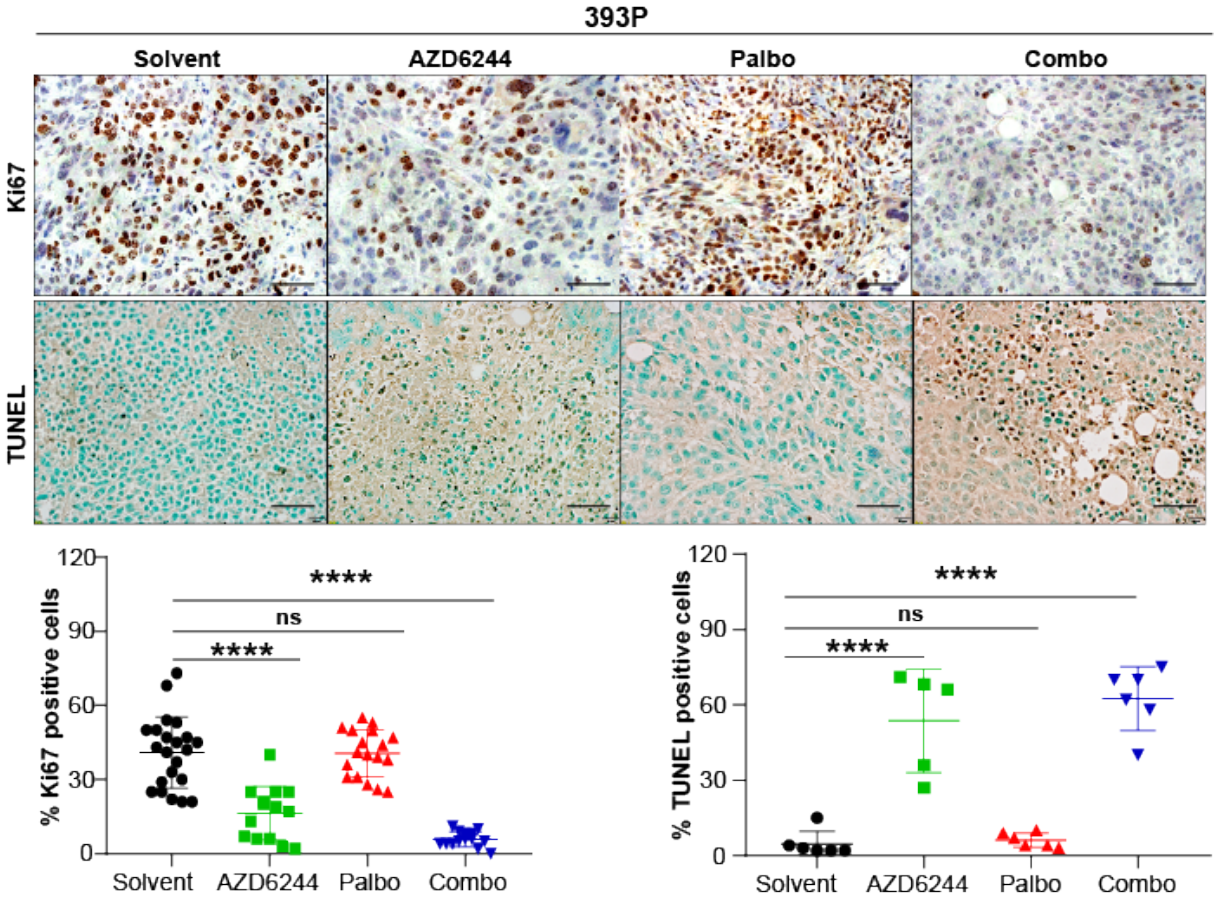

Figure 62. Ki67 and TUNEL staining in 393P tumors.
393P tumors were stained with Ki67 and TUNEL assay to measure cell proliferation and cell death respectively. Representative IHC images are shown. Scale bar: 50 μM. Images were quantified for Ki67 and TUNEL staining in each treatment group. n=2-3 per group with 3-6 FOV per mouse. Statistical significance was determined by one-way ANOVA. **** p<0.0001; *** p<0.005; ** p<0.001; * p< 0.05; ns: not significant. *(Padhye et al JCI insight, 2021, in press).*

We also compared the cell proliferation and death in the 344SQ tumors treated long term (10 weeks) with the single agents and combination. 344SQ tumors acquired resistance to palbociclib alone after 10 weeks. This was reflected in the Ki67 and TUNEL staining, which were similar to 344SQ tumors treated with AZD6244, which were unresponsive (Figure 63). With co-administration of AZD6244 after 10 weeks of single agent palbociclib, tumors underwent apoptosis with limited cell proliferation, similar to the tumors treated with combination from the start of the experiment (Figure 63). Tumor growth and histological staining collectively demonstrate the efficacy of utilizing a combinatorial approach for treatment of heterogeneous tumors with different tumor subpopulations.

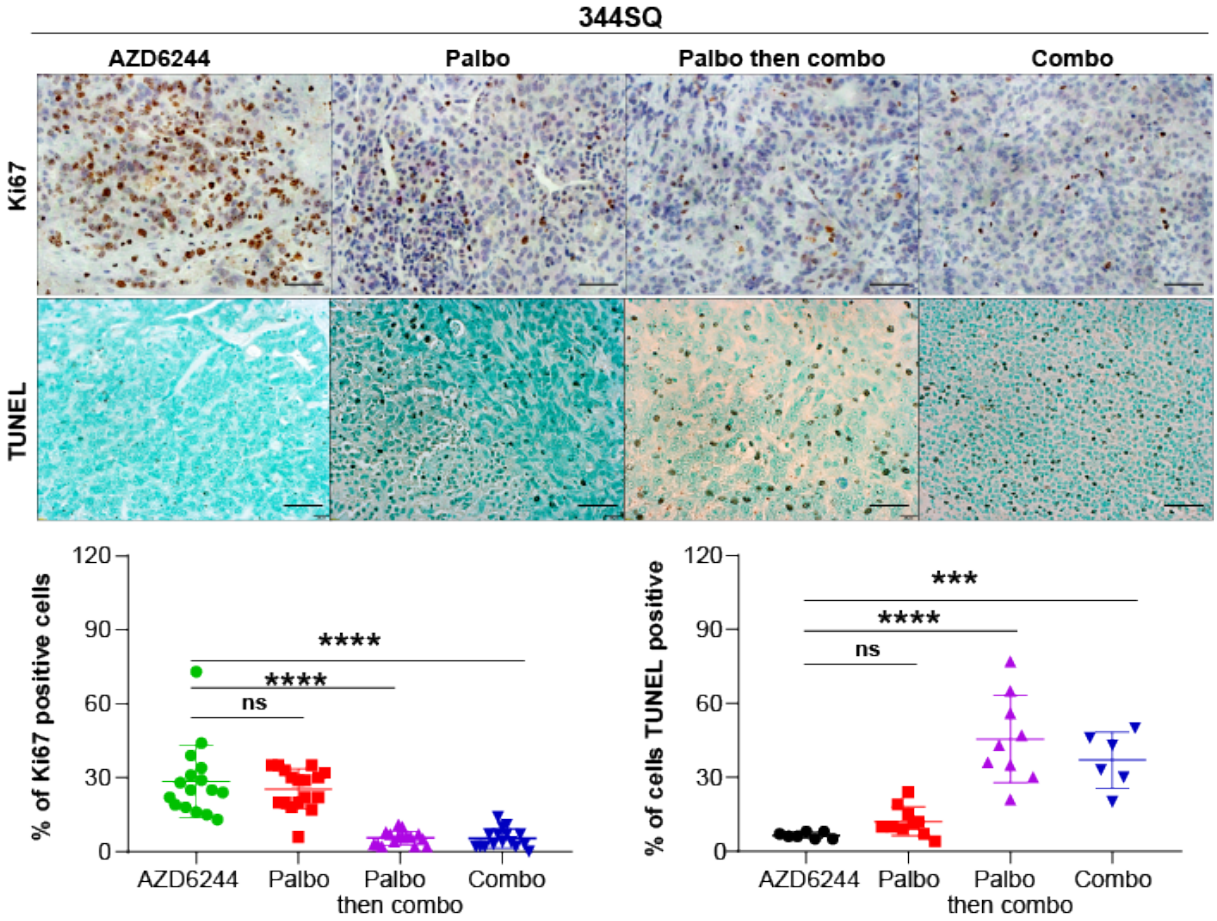

Figure 63. Ki67 and TUNEL staining in 344SQ tumors-long term.
344SQ tumors were stained with Ki67 and TUNEL assay to measure cell proliferation and cell death respectively. Representative IHC images are shown. Scale bar: 50 μM. Images were quantified for Ki67 and TUNEL staining in each treatment group. n=2-3 per group with 3-6 FOV per mouse. Statistical significance was determined by one-way ANOVA. **** p<0.0001; *** p<0.005; ** p<0.001; * p< 0.05; ns: not significant. *(Padhye et al JCI insight, 2021, in press).*

5.2.7 Concomitant CDK4 and MAPK targeting augments response in lung tumors

Autochthonous lung tumor models represent powerful and accurate preclinical models for recapitulating human cancer and exploration of treatment efficacy. Alterations in the tumor suppressor p53 is one of the most commonly occurring comutation in Kras driven lung cancer and cell cycle progression is controlled by p53 through direct transcriptional regulation of p21. Given that tumor cells with identical mutational profile can differ in phenotype and response to therapeutic agents, we investigated the effect on CDK4 and MEK inhibitors in different GEM models harboring either Kras point mutation G12D ($Kras^{LSL/+}$ (Kras)) alone or coupled with various p53 alterations such as: homozygous deletion ($Kras^{LSL/+}$;$p53^{flox/flox}$ ($KP^{flox/flox}$))[102,103], homozygous point mutant ($Kras^{LSL/+}$;$p53^{m/m}$($KP^{m/m}$))[206,207] or both ($Kras^{LSL/+}$;$p53^{m/flox}$($KP^{m/flox}$)) which mimics loss of heterozygosity frequently observed in patient tumors[208]. We also utilized a mouse models where Kras point mutation G12D ($Kras^{LSL/+}$ (Kras)) was coupled with homozygous deletion of miR-141/200c ($Kras^{LSL/+}$; $M^{-/-}$ (KM))[102,103]. Schematic representations of the different alterations are presented in Figure 64. These conditional autochthonous lung tumors were generated through intratracheal administration of adenovirus expressing Cre recombinase[102].

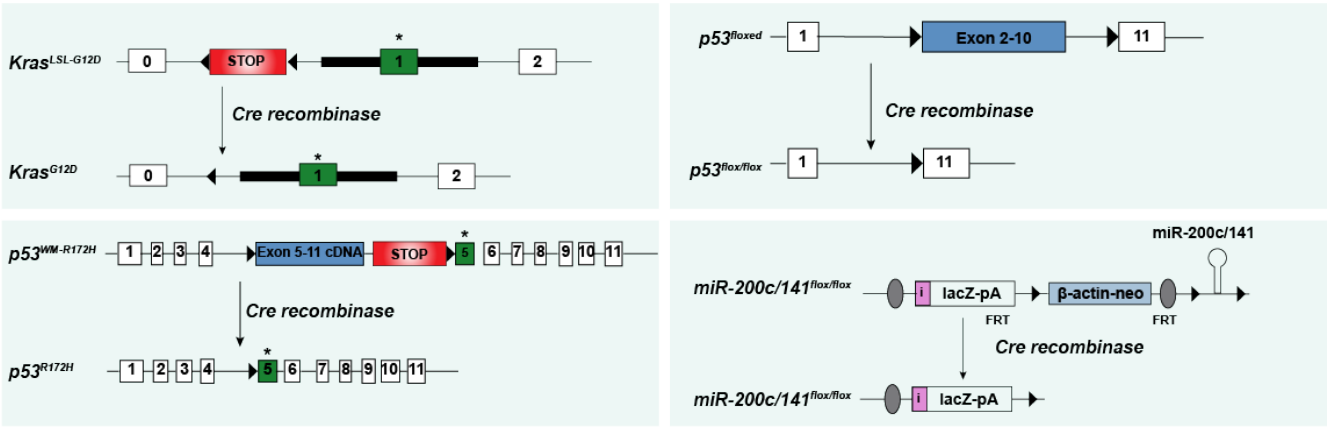

Figure 64. GEMM constructs before and after cre recombination.
(Padhye et al JCI insight, 2021, in press).

Previously published Kras, KP$^{flox/flox}$ and KM mouse models were initially utilized to investigate CDK4 and MAPK signaling pathways. Histological analyses on lung tumors displayed differences in signaling pathways across the different genetic backgrounds. Tumors with mutant Kras alone showed greater MAPK pathway activation compared to KP and KM tumors, which instead showed an activation of CDK4 pathway as demonstrated by phospho-CDK4 and phospho-RB staining (Figure 65).

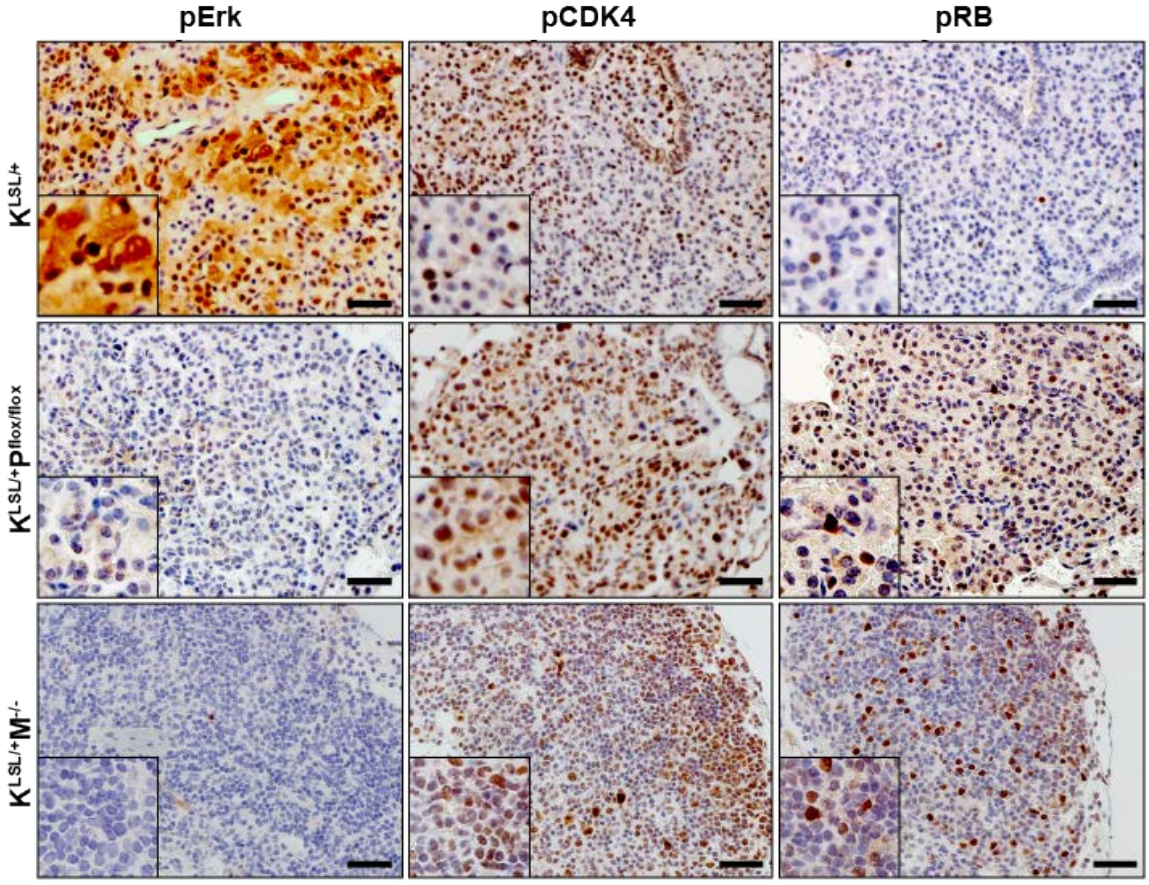

Figure 65. IHC analysis on autochthonous lung tumors for CDK4 and MAPK pathway.
Immunohistochemistry for indicated markers on Kras$^{LSL/+}$, Kras $^{LSL/+Pflox/flox}$ and Kras$^{LSL/+}$M$^{-/-}$ lung sections 18-20 weeks post Ad-Cre infection. Scale bar: 50 μM.
(Padhye et al JCI insight, 2021, in press).

We also utilized these models to interrogate if the ZEB1-p21 axis was altered within these tumors and could determine their sensitivity to palbociclib. Tumor regions with high nuclear ZEB1 corresponded to lower levels of nuclear p21 in KP and KM tumors as compared to Kras tumors alone (Figure 66).

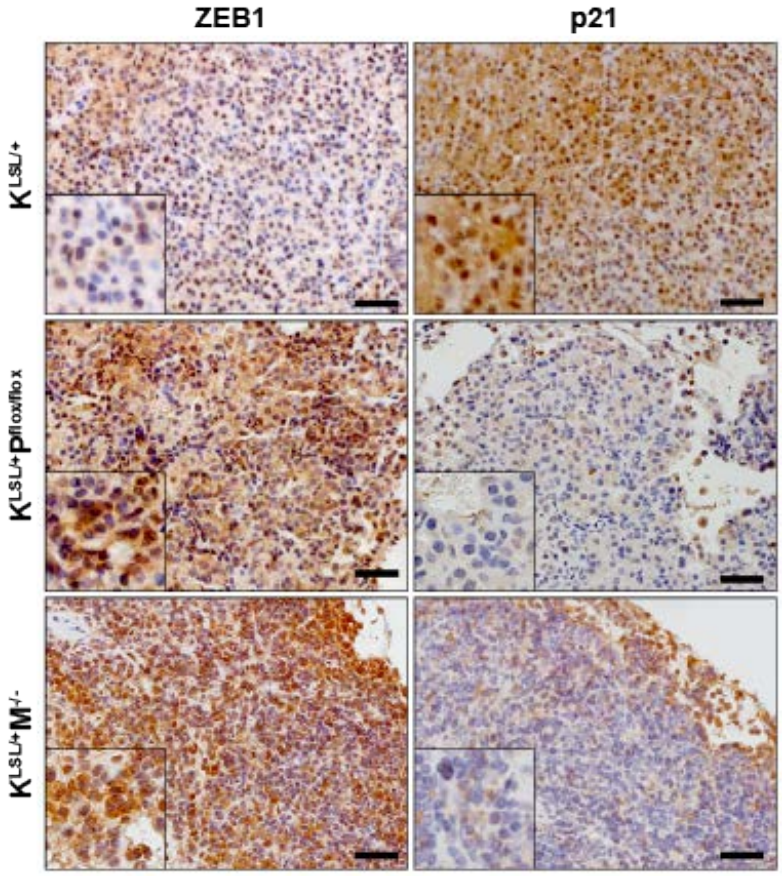

Figure 66. IHC analysis on autochthonous lung tumors for ZEB1 and p21.
Immunohistochemistry for indicated markers on $Kras^{LSL/+}$, $Kras^{LSL/+Pflox/flox}$ and $Kras^{LSL/+}M^{-/-}$ lung sections 18-20 weeks post Ad-Cre infection. Scale bar: 50 μM.
(Padhye et al JCI insight, 2021, in press).

Three months after induction, lung tumor formation was confirmed and monitored over 6-8 weeks by micro-CT scans for changes in overall lung tumor burden in response to pharmacological agents. Response to AZD6244 alone across all three genotypes was similar to our previous[103] results where K-ras tumors showed complete regression upon treatment and only partial response was achieved in KP and KM tumors. Palbociclib alone had more significant tumor growth control in KP and KM mice than AZD6244 alone with ~30% of tumors undergoing complete regression (Figure 67).

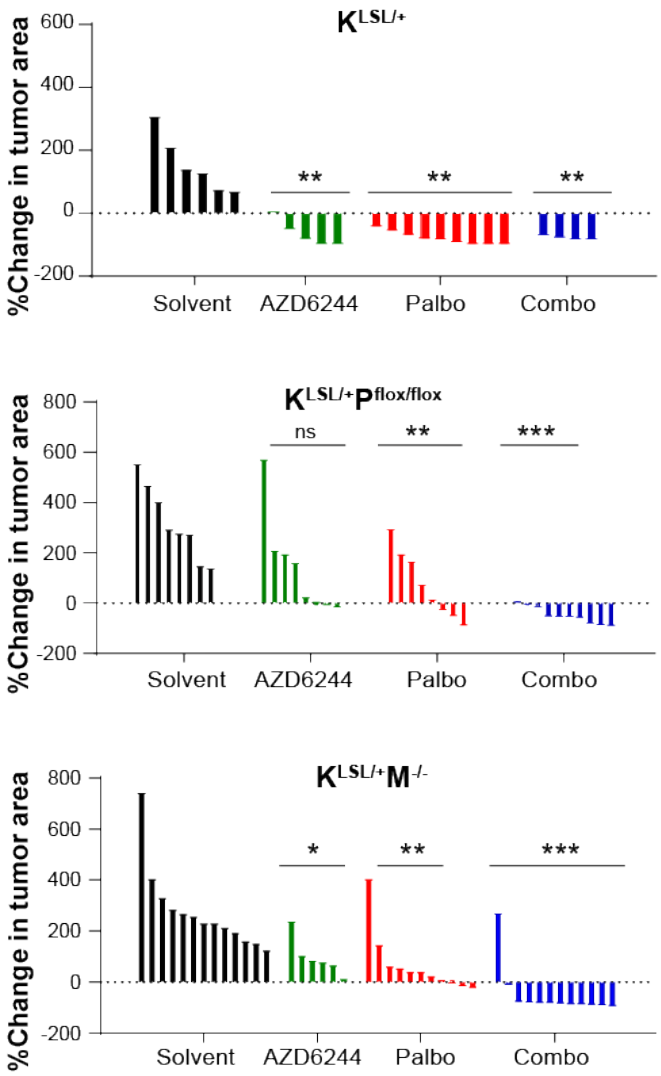

Figure 67. Concomitant CDK4 and MAPK targeting augments response in lung tumors. Percentage change in overall lung tumor area of $Kras^{LSL/+}$, $Kras^{LSL/+}P^{flox/flox}$ and $Kras^{LSL/+}M^{-/-}$ mice after 6-8 weeks of daily treatment with AZD6244 (25 mg/kg), palbociclib (50 mg/kg) or both as assessed by micro-CT imaging of mouse lungs. Significance was determined using Brown-Forsythe and Welch ANOVA tests. *(Padhye et al JCI insight, 2021, in press).*

Histological staining showed that treatment with each single agent led to an activation of reciprocal signaling pathway in KP and KM tumors (Figure 68). Palbociclib led to suppression of ZEB1 indicating a shift to an epithelial phenotype and AZD6244 led to an accumulation of ZEB1 indicating the presence of mesenchymal tumor cells (Figure 68). Combination of palbociclib and AZD6244 produced a more significant reduction of tumors over a period of 8 weeks with complete regression in ~80% mice across the three genotypes (Figure 67). Lack of sufficient tumor burden precluded us from staining the lung sections obtained from combination treatments.

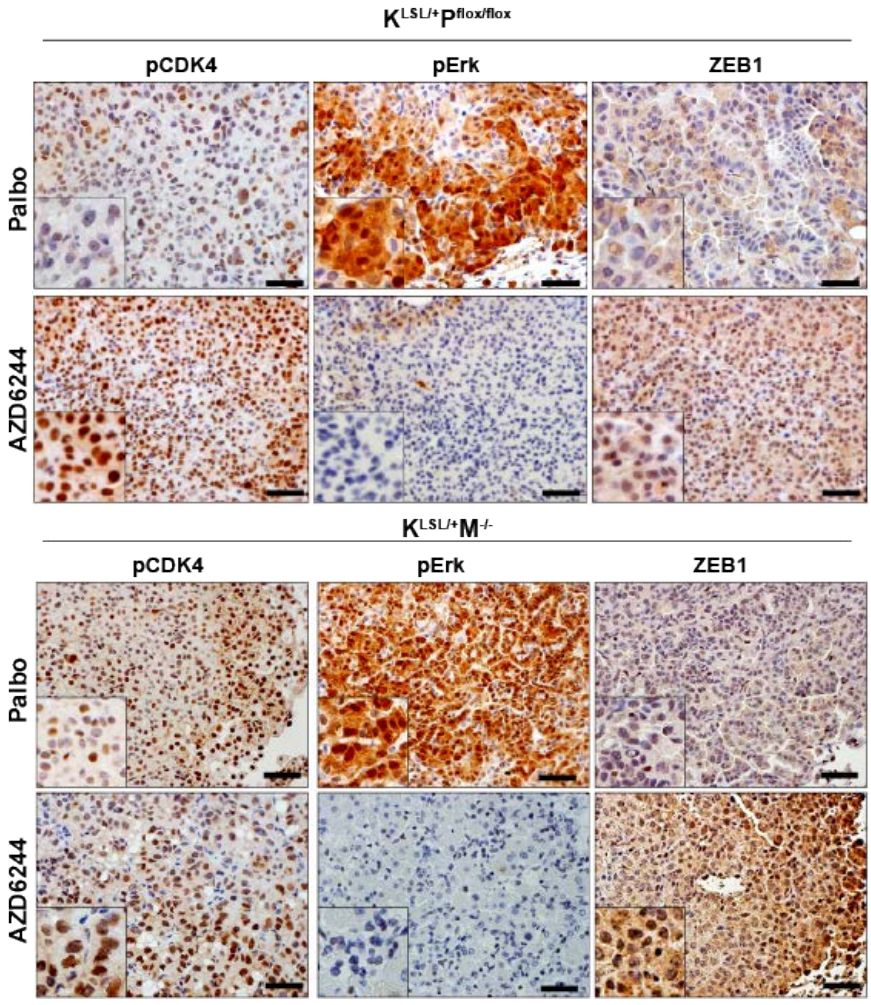

Figure 68. IHC analysis for indicated markers on lung sections after treatment.

Since p53 is more frequently mutated in human tumors than being null, we utilized a conditional point-mutant p53 (R172H) that allows for endogenous expression of mutant p53 upon Cre-mediated recombination (Figure 64). This allele was coupled with $Kras^{LSL/+}$ which generated lung tumors with $Kras^{LSL/+}$; $p53^{m/m}$ genotype. These tumors were expected to behave more similar to $Kras^{G12D/+}$ and $p53^{R172H\Delta g}$ from which our panel of murine NSCLC cell lines were derived. IHC on lung tissue revealed a higher activation of CDK4 pathway (Figure 69). H&E stained whole sections of lung showed larger lung tumors than $Kras^{LSL/+}$ or $Kras^{LSL/+}$; $p53^{flox/flox}$ and average percent fold change of tumor area as measured by mirco-CT scan: $Kras^{LSL/+}$; $p53^{m/m}$ (~500%) $Kras^{LSL/+}$; $p53^{flox/flox}$ (~300%); $Kras^{LSL/+}$ (~150%) (Figure 69). Three months after induction of lung tumors daily doses of the drugs were administered and micro-CT image analysis of changes in overall lung tumor area was monitored. Single drug treatment arms either slowed tumor growth (AZD6244) or caused partial regression in some mice (palbociclib), however, mice treated with the combination showed complete regression across the cohort (Figure 69). Patient tumors often demonstrate loss of heterozygosity (LOH) at one p53 allele with a missense mutation in the second allele which poses an important therapeutic issue. To mimic LOH, mice expressing $Kras^{LSL/+}$; $p53^{m/+}$ were crossed with $Kras^{LSL/+}$; $p53^{flox/+}$ to generate $Kras^{LSL/+}$; $p53^{flox/m}$ mice. The tumors appeared to be more heterogeneous than the other two KP tumors with both CDK4 and MAPK pathway activated within a region (Figure 69). H&E stains and micro-CT scans showed that lung tumor sizes were comparable to $Kras^{LSL/+}$; $p53^{m/m}$ with similar average fold change of tumor area in this genotype (Figure 69). Upon confirmation of lung tumors by micro-CT, we treated the mice daily with palbociclib, AZD6244 or both. Due to the heterogeneous nature of the tumors, either of the single agents could not effectively control tumor growth; however, combination yielded a net tumor regression across the cohort (Figure 69). We also utilized these models to interrogate if the Zeb1-p21 axis was altered within these tumors which could determine the sensitivity to palbociclib. Tumor regions with high nuclear Zeb1 corresponded to low levels or

lack of nuclear p21 in $Kras^{LSL/+;}$ $p53^{flox/flox}$ and $Kras^{LSL/+;}$ $p53^{m/m}$ mice (Figure 69). $Kras^{LSL/+}$; $p53^{flox/m}$ demonstrated more heterogeneity and complexity in terms of Zeb1 and p21 staining.

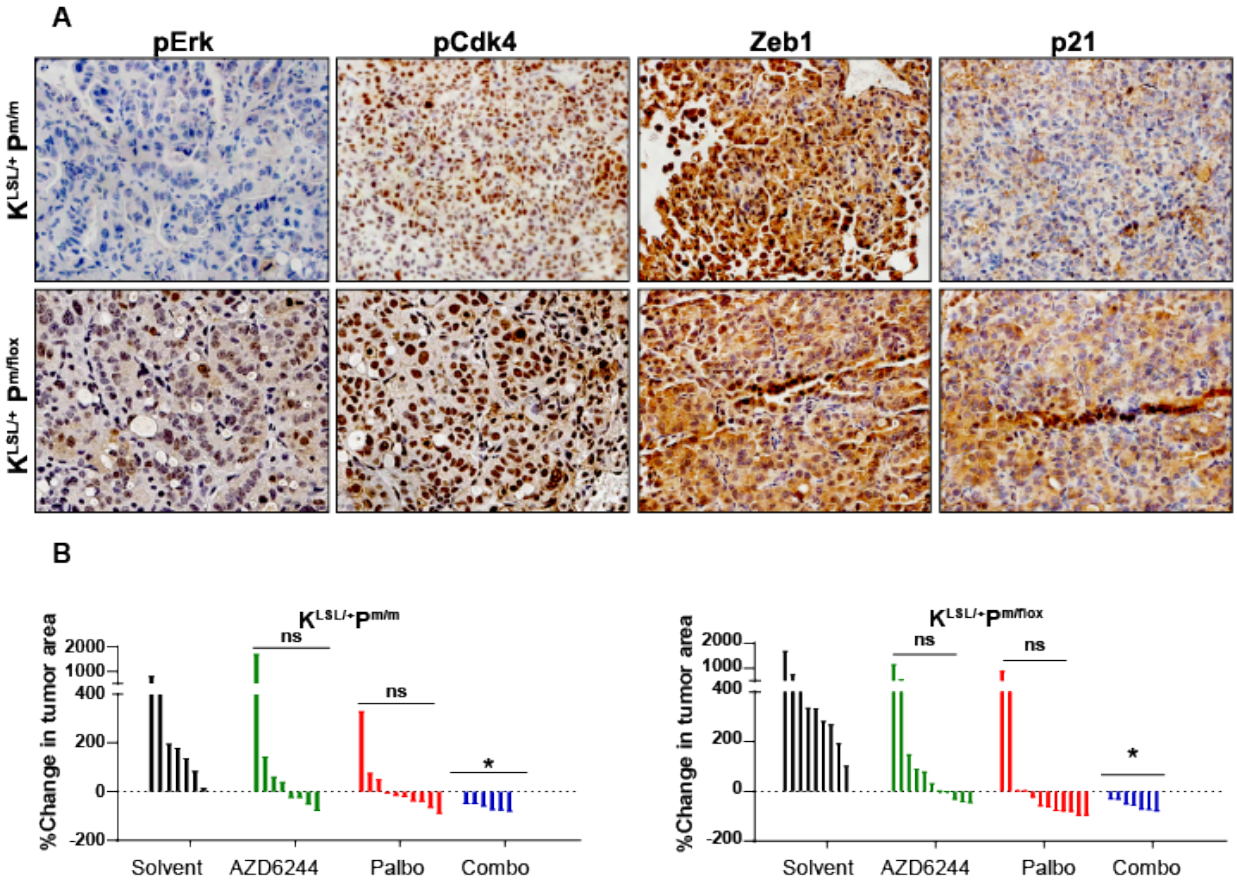

Figure 69. Response of Kras/p53 mutant and LOH tumors to CDK4 and MEK inhibitors.
(A) Immunohistochemistry for indicated markers on Kras $^{LSL/+m/m}$ and Kras $^{LSL/+m/flox}$ lung sections 18-20 weeks post Ad-Cre infection. Scale bar: 50 μM. (B) Percentage change in overall lung tumor area $Kras^{LSL/+}P^{m/m}$ and $Kras^{LSL/+}P^{m/flox}$ mice after 6-8 weeks of daily treatment with AZD6244 (25 mg/kg), palbociclib (50 mg/kg) or both as assessed by micro-CT imaging of mouse lungs. Significance was determined using Brown-Forsythe and Welch ANOVA tests.

Figure 70 shows the normal cells or epithelial cancer cells have an intact cell cycle regulation mediated by the intrinsic regulator p21. Increased binding of p21 to CDK4 prevents the kinase activity, limits RB phosphorylation and arrests cells in the G1 phase. However, this pathway is dysregulated in cancer cells undergoing EMT. ZEB1 is highly upregulated in mesenchymal cancer cells, which exerts transcriptional repression on p21. Lack of p21 leads to low or no binding of p21 to CDK4, allowing the kinase activity of CDK4 to occur unchecked. Such high dependency on CDK4 makes mesenchymal cells especially vulnerable to CDK4 inhibitors such as palbociclib. In heterogeneous tumors, with epithelial and mesenchymal cancer cells, net tumor killing requires drug combinations that preferentially target the vulnerabilities of each subpopulation (e.g., MEKi and CDK4i).

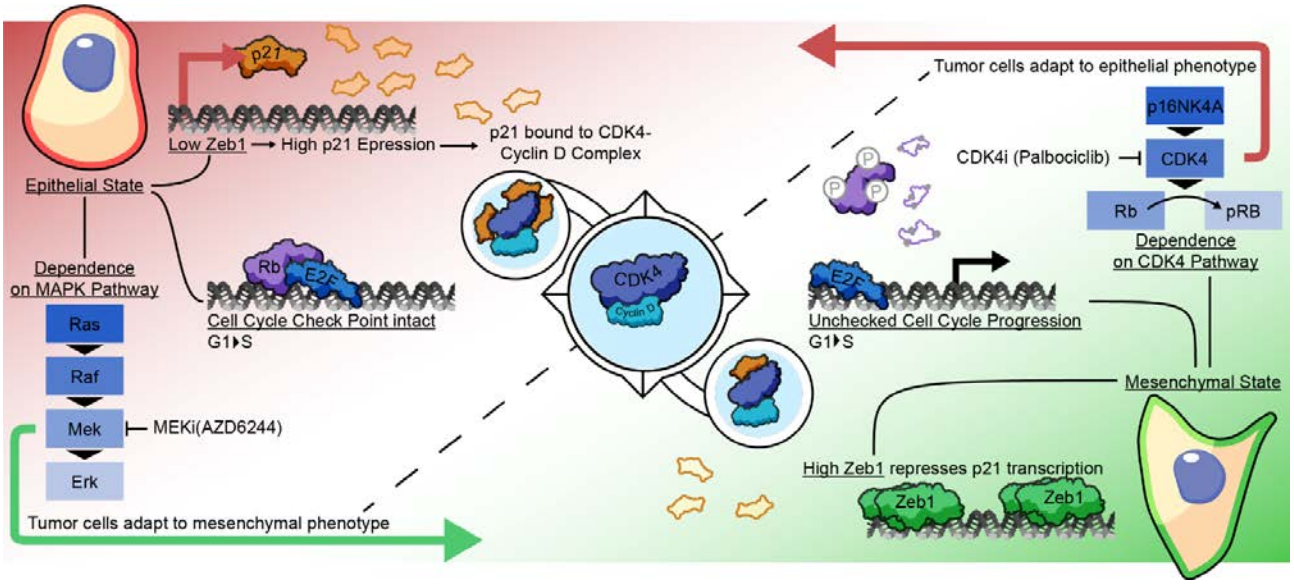

Figure 70. Proposed working model for differential therapeutic sensitivities in lung cancer.
(Padhye et al JCI insight, 2021, in press).

5.3 Discussion

Phenotypic switching and subsequent transcriptional rewiring in cancer cells in response to the tumor microenvironment or selective pressures of drug treatments allows the escape of cancer cells from cell death. An understanding of the mechanisms by which tumor cells alter their cellular state and molecular pathways can provide the basis for designing effective therapeutic strategies. Epithelial to mesenchymal transition is a dynamic phenomenon that contributes to tumor heterogeneity in cancer. We demonstrate that lung tumors with high ZEB1 that display mesenchymal phenotype have increased dependence on the CDK4 pathway for survival, which renders them especially vulnerable to CDK4-specific pharmacological inhibitors. Combined with the results previously published from our lab that showed higher sensitivity of epithelial cancer cells to MEK inhibitors[103], we investigated the combination of CDK4 and MEK inhibitors in multiple *in vitro* and *in vivo* models that recapitulate EMT-mediated tumor heterogeneity and demonstrated that the combination of CDK4 and MEK inhibition in Kras mutant lung adenocarcinoma is an effective strategy to combat EMT-mediated heterogeneity and therapeutic resistance.

CDK4 plays a key role in determining the progression of cells from G1 to S phase of the cell cycle. Disruption of the checkpoint leads to unregulated growth in cancer cells. Ordinarily, the cell cycle is regulated by extracellular mitogenic signals that are integrated by the MAPK pathway[196,209]. However, aberrant CDK4 activation in Kras mutant mesenchymal cancer cells can occur in a cell autonomous manner, without being coupled with extrinsic signals or the MAPK pathway. Thus, the independent activation of CDK4 serves as a survival mechanism activated in mesenchymal cancer cells allowing escape from MEK inhibitors. Interestingly, epithelial tumor cells are less dependent on CDK4 for survival, as shown by the stable knockdown of CDK4 and insensitivity to pharmacological inhibitors. Instead, CDK2-dependent RB phosphorylation seems to be the major cell cycle pathway in epithelial cancer cells. A previous study identified that MAPK mediated activation of CDK2 keeps a check on

RB activity and prevents progression of Kras mutant lung cancers[210]. This is in line with our observations in the epithelial cancer cells that have activated MAPK pathway and a proper cell cycle regulation. Although the results from Walter et al[210] were not studied in the context of EMT, our results show that the epithelial tumor cells are equally receptive to CDK2 and MEK inhibitors, whereas mesenchymal cancer cells are resistant. These findings reiterate the fact that CDK4 and MAPK pathways are closely linked in lung cancer and present an opportunity for therapeutic co-targeting.

Separate studies have presented contradictory findings for the correlation of EMT with CDK4 pathway signaling. CDK4 inhibition in triple negative breast cancer reversed the EMT status of cancer cells[211,212] as seen in the 344SQ mesenchymal tumors treated with palbociclib in the present study. Within Kras-mutant pancreatic cancer, one study showed that tumor cells underwent EMT with palbociclib monotherapy[213] and MET in another[214]. Another study in colorectal cancer noted no difference in EMT status of tumor cells in response to palbociclib[215]. These findings highlight the fact that there are cell-type or context-specific phenomena that warrant further investigation in different cancer types. In our studies, we found that modulation of the EMT status of cancer cells by perturbing the ZEB1/miR-200 axis lead to CDK4 pathway modulation and determined the sensitivity to CDK4 inhibitors both *in vitro* and *in vivo*.

Mechanistically, we identified that high ZEB1 in mesenchymal cancer cells was responsible for transcriptional repression of *CDKN1A* (gene encoding for p21) by direct binding to the promoter region. Conventionally, p21 is described as a suppressor of CDK4 kinase activity and a downregulation/loss in patients predicts poor survival[216,217]. Studies in the recent years have further explored the role of p21 and revealed a dual function of p21, acting in some cases as an activator for CDK4 activity[218]. Lower levels of p21 binding are generally required for the assembly and stability of the CDK4-cyclin D complex. p21 binding to CDK4 partially accounts for maintaining phosphorylation of CDK4, primes CDK4 for

catalysis by releasing the activation segment without affecting kinase function (e.g. phosphorylation of RB)[204]. On the other hand, a sustained presence of p21 at higher stoichiometric concentrations can render CDK4 ineffective[204]. We found that mesenchymal cancer cells had lower levels of p21 in the CDK4-p21 complex, which explains increased CDK4 activity. Continued presence of an activated CDK4 rendered the mesenchymal cells highly dependent on CDK4 for survival. Increased addiction to CDK4 translated to *de novo* vulnerability to CDK4 inhibitors. With p21 overexpression in mesenchymal cancer cells, we detected increased CDK4-p21 complex, reduced *in vitro* and *in vivo* growth of tumors. Interestingly, 344SQ cells demonstrated reduced sensitivity to palbociclib with p21 overexpression. A previous study had shown that p21 can interfere with the binding of small inhibitors to CDK4 complex, as we observe in wild type epithelial tumor cells and in p21 overexpressing mesenchymal cells[219]. Thus, p21 serves as a regulator of CDK4 activity and sensitivity to inhibitors in mesenchymal lung cancer cells.

CDK4 pathway activity can determined by other factors such cyclin activating kinase (CAK). This complex is responsible for the activating phosphorylation of CDK4 at T172[220]. Phosphorylation is the least studied level of CDK4 regulation. An inhibitory phosphorylation of CDK4 on Tyr17 has also been observed in UV irradiation-induced G1 arrest or during cell arrest in quiescence or in response to transforming growth factor β (TGF-β)[221]. The role of different phosphorylation sites on the activity of CDK4 and downstream signaling pathways has been debated over the years. A general consensus is that T172-phosphorylation of CDK4 bound to cyclin D is the central rate-limiting event in CDK4 activation and that CDK4 activation is not restricted by stoichiometric inhibitory phosphorylations[222]. Based on the T172-phosphorylation of CDK4 as critical to the kinase activation, an 11-gene classifier helps to segregate cancer subtypes and predict palbociclib sensitivity in breast cancer patients[222]. In addition to CDK4 phosphorylation, multisite RB phosphorylation also critically determines the effect on cell cycle progression and other biological processes. Depending on the phosphorylation events, RB protein can acquire unique conformations, each capable of

making different protein interactions and therefore exerting distinct tumor suppressor activities, opening avenues for independent targeting of upstream regulators[223]. CDK4-cyclin D complex is primarily responsible for S807/S811 phosphorylation, which act as priming site for further hyper-phosphorylation of RB by CDK2-cyclin E complex and progression through G1 to S phase. S807/S811 mutation results in loss of Rb phosphorylation levels beyond expected for mutation of only two sites, indicating an S807/S811 dependence for other phosphorylation events. It is still imperative to explore the role of other RB phosphorylation sites that are induced by different kinases. This will allow us to understand why certain cell types are more dependent on specific CDKs for survival which ultimately sensitized them to pharmacological inhibition.

ZEB1 mediated p21 regulation was demonstrated by utilizing isogenic pairs of cell lines expressing ZEB1 or miR-200 as well as by treatment by mocetinostat, an HDAC inhibitor. Mocetinostat induces miR-200 expression, which can relieve ZEB1 repression on the p21 promoter. Mocetinostat can also regulate the HDACs that are present in co-repressor complexes with ZEB1[182]. Evidence from past studies suggested that class I HDACs (HDAC1, 2 and 3) repress the p21 promoter as part of NuRD, Sin3A, NCoR-SMRT co-repressor complexes[224]. Recent work from our lab demonstrated that ZEB1 is present in such co-repressor complexes to regulate promoter activity of important genes altered in cancer progression[178]. There is also evidence that a trimeric complex of ZEB1, HDAC1/2 and p53 in stromal fibroblasts promotes breast cancer progression[225]. Independently, p53 is a well-established regulator of p21 expression which occurs in response to oncogenic stress to induce cell cycle arrest and/or apoptosis[226,227]. Loss of p53 in cancer can lead to the downregulation of p21 and unchecked cell growth[227], however we did not observe a direct effect of p53 on p21 expression to regulate the CDK4 pathway. Evidently, a complex network of transcriptional regulators determine p21 levels in the cells and further investigations are warranted to understand these intricacies. Our findings do highlight that correlation of EMT

status and p21 levels can serve a biomarker for response to CDK4 inhibitors in lung cancer patients.

With an understanding of how lung cancer cells adapt to therapeutic intervention, we interrogated the combination of CDK4 and MEK inhibitors. Normal cells possess intact cell cycle checkpoints and are spared by selective CDK4 inhibitors. CDK4 inhibition causes tumor cell senescence or apoptosis in addition to cell cycle arrest making these cancer cells particularly vulnerable to the inhibitors[228]. The remarkable success of CDK4 inhibitors in combination with endocrine therapy in breast cancer patients have encouraged investigations into the role of CDK4 inhibitors in other cancer types, including lung cancer[229-232]. K-Ras^{G12V} driven lung cancers were particularly susceptible to ablation of CDK4 with an induction of senescence and prevention of tumor progression[199]. A sustained tumor response was also achieved with concomitant CDK4 inactivation and RAF1 ablation in *Kras/p53* driven lung cancers[198]. A phase II trial in NSCLC patients with inactivated *CDKN2A* treated with palbociclib monotherapy showed modest response with stable disease in 50% of the patients[233]. Partial response to CDK4 inhibitor in a subset of lung cancer patients warranted an exploration of combination with other targeted therapies to achieve durable response. Zhou et al[234] demonstrated a synergistic growth inhibition in *KRAS* and *CDKN2A* mutant NSCLC xenografts with AZD6244 and palbociclib. Ongoing phase I/II clinical trials (NCT03170206 and NCT02022982) in advanced K-Ras driven NSCLC patients are investigating the combinatorial effect of MEK and CDK4 inhibitors. Additionally, the combination of CDK4 and MAPK pathway inhibitors have shown tumor regression in multiple other cancer types utilizing xenografts models, especially with *KRAS*, *NRAS* or *BRAF* mutations[104]. BRAF- and NRAS-mutant melanoma are particularly receptive to combinatorial therapy[235-238] and phase I clinical studies have shown promising activity in these tumor types as well[239]. Clinical trials are currently investigating BRAF and MEK inhibitors in combination with ribociclib in BRAF-mutant melanoma and other solid tumors with BRAFV600 mutations[240]. In K-Ras mutant colon cancer, monotherapy with either MEK or CDK4 inhibitors

has been disappointing[241,242]; however synergistic effects were observed in xenograft models of K-Ras mutant colorectal cancer upon treatment with a combination[215,243], which led to a phase II clinical trial in *KRAS*- or *NRAS*-mutant colorectal cancer patients testing binimetinib and palbociclib in combination[240]. Not only are the two therapies synergistic, but studies have also shown that CDK4 inhibitors are able to overcome MEK inhibitor resistance[244] and vice versa[245]. These findings are corroborated by our results in the present study demonstrating the efficacy of CDK4 and MEK inhibitors.

Results in our immunocompetent syngeneic models will allow us to further extend our investigation into effects on the immune microenvironment. Evidence from past studies indicated that CDK4 depletion reduced infiltration of CD4+ FoxP3+ Tregs[246] and CDK4 inhibitors increased tumour immunogenicity and cytotoxic T-cell mediated clearance of tumor cells[247]. CDK4 inhibitors also enhanced effector T-cell infiltration and activation[248]. Additionally, PD-L1 degradation stability was shown to be regulated by CDK4 through cullin 3–SPOP E3 ligase via proteasome-mediated degradation which primed the tumors for effective response to combination treatment with CDK4 inhibitor and PD-1-PD-L1 immune checkpoint blockade[249]. Other investigations revealed that PD-L1 expression was modulated RB-NF-κB axis which could be exploited to overcome cancer immune evasion triggered by conventional or targeted therapies[250]. Combination of CDK4 and MEK inhibitor induced a senescence-associated secretory phenotype (SASP) that provoked a natural killer cell surveillance program and resulted in tumor cell death[251].

The application of combinatorial treatments with MEK and CDK4 inhibitors in multiple pre-clinical *in vitro* (dual fluorescent sensor system, 3D assays) and *in vivo* models (syngeneic and autochthonous mouse models) effectively prevented outgrowth of resistant tumor subpopulations and was significantly better than either monotherapy. Such findings demonstrate that CDK4 and MAPK pathway are intertwined in lung cancer progression and durable response can be attained if these pathways are targeted judiciously. Fighting cancer

at two fronts: by interfering with two distinct regulatory networks and targeting tumor subpopulations should benefit patients and help to prevent resistance development. Additionally, timing of administration of drugs may be an important criteria to consider where a sequential regimen could provide improved targeting of tumor subpopulations that arise due to tumor plasticity.

Chapter 6: Conclusions and future directions

The overarching goal of the dissertation was to contribute to the understanding of tumor heterogeneity in lung cancer. We established a platform to model tumor microenvironment and tumor cell heterogeneity, and utilized different experimental approaches to identify a therapeutic strategy that allowed for a durable tumor growth control in lung cancer.

6.1 Tumor heterogeneity modeling

6.1.1 Major findings and significance

There are very limited organotypic models for studying lung cancer that effectively capture tumor heterogeneity when compared to other cancer types like colon, breast, and pancreatic[89,252]. Our primary aim was to establish such a platform for murine lung tumors that would be useful for interrogating cancer cell behavior in context of tumor microenvironment components. First, we demonstrated that the EVTs isolated from primary syngeneic tumors were indeed representative of the heterogeneity within lung cancer. With flow cytometry and immunofluorescence staining, we were able detected immune cells, CAFs, endothelial cells, ECM proteins like laminin and collagen I, and phenotypically distinct cancer cells. As a proof-of-principle, we investigated if EVTs retained biological responses to known stimuli, such as TGFβ treatment and alterations in the ECM composition. Characterization of EVT behavior was imperative before we used the platform investigated signaling pathways that can be targeted for therapeutic purposes. One such pathway was Src, which is known to mediate invasion and metastasis cancer. We found that Src pathway was activated downstream of collagen I-integrin β1 interaction and was necessary for initiation and maintenance of invasion in EVTs. Disrupting this signaling pathway, for e.g. in the absence of collagen I in the matrix, use of integrin β1 blocking antibody or pharmacological inhibitors of Src, led to loss of invasive potential in EVTs. These findings were then validated *in vivo* where dasatinib treatment prevented metastatic disease. Another significant finding was that EVTs were able to predict that FAK inhibitor was ineffective in lung cancer. Observations from 2D and 3D monocultures

would have indicated that FAK inhibitor was a potential therapeutic avenue for lung cancer, however, response of EVTs to FAK inhibitors was mirrored in tumor bearing mice. Therefore, our data suggests that EVTs can serve as a high throughput screening platform for pharmacological agents as well as identifying biomarker for drug sensitivity subverting the need to depend on time consuming animal models.

We also focused on EMT mediated tumor cell heterogeneity because there is a large body of evidence in lung cancer shows that EMT is associated with most aggressive form of the lung cancer including chemoresistance and metastasis[94,253-257]. The Z-cad EVT setup incorporates both a real-time readout for EMT mediated tumor cell heterogeneity, as well as tumor microenvironment components. As a proof-of-principal, we used Z-cad EVTs to demonstrate that external manipulation like TGFβ treatment and ECM manipulation can modify cellular phenotype. One of our big questions was to understand how the genetically identical and phenotypically distinct tumor subpopulations respond to drug treatments in order to identify specific therapeutic vulnerabilities that could allow us to find synergistic combinations. We identified two combinatorial approaches, MEK and AXL inhibitors as well as MEK and CDK4 inhibitors, which targeted of epithelial and mesenchymal tumor cell subpopulations within heterogeneous tumors thus yielding significant tumor growth control.

6.1.2 Future Directions

We fully characterized the EVTs derived from syngeneic primary tumors, but only began to scratch the surface with EVTs from autochthonous lung tumors. We have multiple GEMMs that are driven by Kras and p53 co-mutations and recapitulate human lung cancer very accurately. Upon further characterization of autochthonous EVTs, we will be able to utilize the platform to answer biological questions and circumvent the time constraints that usually accompany long term mouse experiments. In parallel to murine EVTs, the development of patient derived EVTs for lung cancer will be of enormous value. Patient derived xenografts are normally studied in either immunodeficient mouse models which lack accurate representation of the tumor microenvironment, or humanized mouse models which

can be expensive, time consuming and pose the problem of potential mouse- specific evolution of the human tumour[118,258,259]. Therefore, early attempts in different cancer types, including melanoma, colorectal cancer, renal carcinoma and even some instances of lung adenocarcinoma have been made for predicting therapeutic outcome by using a patient derived organoid platforms and have been successful to varying degrees[142,260-263]. With the advantages of preserving original tumor architecture, ability to cryopreserve for future use, expansion over long term and provide a high throughput screening of therapeutic agents, the murine and human EVTs will provide a powerful platform for pushing the frontiers of personalized medicine as well as developing a thorough understanding of the outstanding biological questions in lung cancer.

Using the models, we demonstrated the significance of collagen I-integrin β1 interaction in driving metastatic disease. The TME consists of a wide variety of ECM molecules in addition to collagen I that contribute to lung cancer progression. The unanswered questions include how ECM composition changes overtime from an early stage of preneoplastic disease to a more aggressive metastatic disease and what are the signaling cascades associated with such changes within tumor cells. The alteration is not only dynamic but also bi-directional with a co-operation between the aberrant tumor cells and the ECM proteins which allows for the emergence of the most aggressive cancer phenotype. We can start investigating these questions by using the autochthonous EVT model derived from lung tumors driven by Kras and Kras/p53 mutations and combining with synthetic-based matrices such as poly(ethylene glycol) (PEG) gels that are readily modifiable and tunable to the incorporation of desired ECM proteins and therefore can be fabricated for specific mechanistic interrogations [264]. The extracellular matrix composition is highly conserved across murine and human tissues and therefore our findings from the ex vivo model would be readily translatable. Prior mass spectrometry data from our non-metastatic and metastatic tumors have identified alterations in the ECM that could be associated with aggressive phenotype in lung cancer[265]. One such hit was fibronectin that is differentially expressed in

metastatic tumors. Fibronectin is also a part of the basement membrane alongwith laminin in lung tissue[266,267], which raises the question what changes are occurring in fibronectin expression, deposition, cross-linking and stiffness that are associated with highly metastatic disease. Interestingly, fibronectin has been associated with expression of mutant p53 as well as increased collagen I deposition[268]. With EVTs driven by different genetic alterations and cultured in highly controllable matrices, we can begin to dissect out the specific roles of different ECM components and interactions with genetically and phenotypically different cancer cells. An understanding of such changes will allow us to block these interactions and prevent disease progression.

In addition to ECM modeling, EVTs can be used to mimic other TME components such as immune cells and CAFs. We were already able to detect these heterotypic cells within the murine EVTs. Building upon what is known in the literature, we can start to layer in more complexities to investigate the heterotypic interactions with cancer cells. This is especially significant in context of phenotypically distinct tumor cells. We used the Z-cad sensor cells to detect changes in EMT state of cancer cells in response to therapeutic agents. There are many avenues that can be explored with the aid of Z-cad EVT tool. Interaction of distinct tumor cell subpopulations with the surrounding microenvironment (ECM, CAFs, immune cells etc) will aid in the understanding of how aggressive phenotypes emerge, what are the factors responsible for maintaining such cell types and if they contribute to therapeutic resistance. This will allow us to identify novel therapeutic approaches for better targeting of lung cancer cells.

Another potential area of investigation is tumor cell heterogeneity itself. Epithelial-to-mesenchymal transition is a dynamic phenomenon with cells acquiring intermediate cellular characteristics that lie between the two polar states, epithelial and mesenchymal. The markers associated with the polar states are very well-defined and for the longest time only these cellular states were investigated. Recent years have recognized the importance of the partial/hybrid EMT states where cancer cells express both epithelial and mesenchymal

features. Lack of defined markers associated with these subpopulations is a very open ended question. Z-cad sensor cells can serve as a starting point to assign a profile of markers that can define a particular cellular state which can then be applied to phenotypically different human lung cancer cells. Such an experimental approach can begin to dissect the partial/hybrid states of EMT.

Phenotypic heterogeneity should also be considered in the context of the genetic alterations driving tumorigenesis. Lung cancer mouse models driven by different genetic alterations such as $Kras^{G12D}$, $Kras^{G12D}/p53^{R172H}$ and $Kras^{G12D}/p53^{-/-}$ develop tumors that display distinct patterns of heterogeneity. Cancer cells derived from tumors with identical mutations, for e.g. 393P and 344P from primary lung tumors have $Kras^{G12D}/p53^{R172H}$ mutation, but exhibit very different EMT characteristics. There is evidence that mutant p53 can promote EMT by modulating micro-RNAs such as miR-200 and miR-130b that inhibit ZEB1 post-transcriptionally[269,270]. Exploring the role of selective pressures exerted by altered p53 (deleted vs mutated) to drive a specific lineage of cancer cells alongwith imparting phenotypic plasticity and the extent to which there is cooperation with other transcriptional programs to modulate cellular phenotype is important in determining tumor evolution as it has implications for therapeutic sensitivities and resistance.

6.2 Therapeutically targeting EMT mediated heterogeneity

6.2.1 Major findings and significance

Kras mutant lung adenocarcinoma continues to pose a therapeutic challenge in the clinic. MEK inhibitors which target activated MAPK pathway have failed to provide any sustained benefit due to intrinsic or acquired resistance in cancer cells. In this study, we utilized *in vivo* and *in vitro* short hairpin RNA dropout screens in Kras/p53 (KP) mutant murine models of epithelial and mesenchymal lung cancer to identify survival dependencies specific to each epithelial and mesenchymal subpopulations and highlighted their counter-dependencies on CDK4 and MAPK signaling. We identified CDK4 as an escape mechanism

for mesenchymal tumor cell subpopulations that are resistant to MEK inhibitors. Concomitant targeting of CDK4 and MAPK pathways with clinically approved pharmacological inhibitors yielded a durable tumor suppression by preventing emergence of resistance to either single agent. We demonstrated these findings in multiple syngeneic tumor models and autochthonous genetically-engineered mouse models of lung cancer. Analyses of multiple human cancer cell line and tumor tissue datasets confirm the signaling pathways critical to the findings.

We also demonstrated that the mechanism for enhanced dependency of mesenchymal cells on CDK4 signaling was due to the direct ZEB1-mediated regulation of p21. ZEB1 upregulation is critically linked to the mesenchymal phenotype in lung cancer cells. We found that there was a direct transcriptional suppression by ZEB1 of p21 which is an intrinsic regulator of CDK4 activity. At low levels p21 does not to exert an inhibitory effect on CDK4 activity, causing deregulation of cell cycle and unchecked proliferation of cancer cells. With an increased dependency on CDK4, these cancer cells become particularly vulnerable to CDK4 inhibitors. Thus, these data provide evidence for the incorporation of CDK4 inhibition into combination strategies to target phenotypic heterogeneity and EMT plasticity within lung cancer, with the ultimate goal of improving the anti-tumor efficacy of targeted agents.

6.2.2 Future Directions

As noted in many studies, resistance to targeted therapies eventually emerges which leads to recurrences and poor patient outcomes[271]. It is imperative stratify patients based on tumor characteristics to determine what subset of patients will respond to selected therapeutic regimen. Ongoing clinical trials assessing CDK4 and MEK inhibitor combination in lung cancer will provide critical information that will inform clinical decision making process based on the molecular profiling and histopathological analyses of tumors. ZEB1 and p21 can serve as biomarkers to determine sensitivity to CDK4 inhibitors. This needs to be further explored in lung cancer patient samples that were treated with prior chemotherapy or MEK inhibitors

or both. Establishing a more comprehensive biomarker profile will also be useful which can be done in both murine and patient tumors pre- and post-treatment. Our study also establishes a direct mechanistic regulation of ZEB1-p21-CDK4 axis. There are many other cyclin dependent kinases that regulate cell cycle and are altered during cancer progression. For e.g. CDK2 which is also regulated by p21. Our data indicates that CDK2 is differentially activated in epithelial cancer cells but exact mechanistic basis is unknown. Separately, we also observe that epithelial lung cancer cells require p21 for survival, as knockdown of p21 causes cell death. This indicates that mechanism of action of p21 is context dependent and can potentially regulate CDK2 activity by acting as an activator in this instance. Similarly, p27 is an intrinsic regulator of cyclin dependent kinases that should be further explored in context of EMT in cancer cells. These molecular studies will start to tease out additional mechanisms of resistance to CDK4 inhibitors. Recent findings indicate that compensatory upregulation of CDK6, or cyclin E and loss RB can mediate resistance to CDK4 inhibitors, especially in breast cancer[272]. Exploring these pathways in lung cancer will be important to combat resistance.

The advent of immune checkpoint blockade (ICB) in the field of oncology has been immensely successful in producing tumor remissions by limiting malignant progression as well as promoting tumor clearance. A large number of clinical trials are evaluating the efficacy of ICB with targeted therapies to attain an additive or synergistic effect, including lung cancer[273]. MEK inhibitor in combination with ICB are being evaluated in the clinical trials (NCT03225664). There have been only modest response to the combined therapy in different cancer types, including our syngeneic and autochthonous mouse models[274]. On the other hand, CDK4 inhibitors with ICB in lung cancer have only recently been tested in pre-clinical models[248]. An expected outcome from clinical trials with CDK4 inhibitors in combination with ICB is resistance to therapy, either upfront or acquired overtime. In fact, our preliminary findings in the syngeneic mouse models show that CDK4 inhibitor with PD-L1 blockade effectively control tumor growth in one-third of the tumors, but most tumors grow eventually develop resistance. We speculate that this resistance occurs because tumor cells are capable

of adapting and escaping death by activating alternative survival pathways, in this case MAPK. With this in mind, we co-administered CDK4 and MEK inhibitors with PD-L1 blockade which led to a sustained tumor suppression for about 8 weeks, which was in line with investigations in other cancer types[275-277]. The next steps include the evaluation of the immune landscape as well as the cancer cells in treated tumors to determine why the triple combination is significantly better than single or double agent treatment and will form the basis for future clinical investigations.

Lastly, there has been an increased focus on determining the best approach of administering drugs to patients[278]. A fundamental understanding of how cancer cells evolve in the face of treatments by either transcriptomic rewiring or interactions with the tumor microenvironment allows us to determine therapeutic vulnerabilities and optimal timing of drug administration for the enhancement of combination therapies. To achieve a greater benefit with CDK4i, MEKi and ICB, it will be worthwhile exploring the effects of upfront combination vs sequential drug treatments. It will help in the identification of drug-tolerant cells which usually remain dormant until drug withdrawal. These subpopulations can then be targeted with a different drug that has previously demonstrated benefit. This has specific clinical relevance due to the toxicities associated with the administration of multiple therapies at once. Using *ex vivo* as well as *in vivo* tumor models can help in establishing the optimal dosing schedule.

Chapter 7: References

1 Siegel, R. L., Miller, K. D. & Jemal, A. Cancer statistics, 2020. *CA: A Cancer Journal for Clinicians* **70**, 7-30, doi:10.3322/caac.21590 (2020).

2 Davidson, M. R., Gazdar, A. F. & Clarke, B. E. The pivotal role of pathology in the management of lung cancer. *Journal of thoracic disease* **5 Suppl 5**, S463-478, doi:10.3978/j.issn.2072-1439.2013.08.43 (2013).

3 Chen, Z., Fillmore, C. M., Hammerman, P. S., Kim, C. F. & Wong, K.-K. Non-small-cell lung cancers: a heterogeneous set of diseases. *Nature Reviews Cancer* **14**, 535, doi:10.1038/nrc3775 (2014).

4 Collisson, E. A., Campbell, J. D., Brooks, A. N., Berger, A. H., Lee, W., Chmielecki, J., Beer, D. G., Cope, L., Creighton, C. J., Danilova, L., Ding, L., Getz, G., Hammerman, P. S., Neil Hayes, D., Hernandez, B., Herman, J. G., Heymach, J. V., Jurisica, I., Kucherlapati, R., Kwiatkowski, D., Ladanyi, M., Robertson, G., Schultz, N., Shen, R., Sinha, R., Sougnez, C., Tsao, M.-S., Travis, W. D., Weinstein, J. N., Wigle, D. A., Wilkerson, M. D., Chu, A., Cherniack, A. D., Hadjipanayis, A., Rosenberg, M., Weisenberger, D. J., Laird, P. W., Radenbaugh, A., Ma, S., Stuart, J. M., Averett Byers, L., Baylin, S. B., Govindan, R., Meyerson, M., Rosenberg, M., Gabriel, S. B., Cibulskis, K., Sougnez, C., Kim, J., Stewart, C., Lichtenstein, L., Lander, E. S., Lawrence, M. S., Getz, G., Kandoth, C., Fulton, R., Fulton, L. L., McLellan, M. D., Wilson, R. K., Ye, K., Fronick, C. C., Maher, C. A., Miller, C. A., Wendl, M. C., Cabanski, C., Ding, L., Mardis, E., Govindan, R., Creighton, C. J., Wheeler, D., Balasundaram, M., Butterfield, Y. S. N., Carlsen, R., Chu, A., Chuah, E., Dhalla, N., Guin, R., Hirst, C., Lee, D., Li, H. I., Mayo, M., Moore, R. A., Mungall, A. J., Schein, J. E., Sipahimalani, P., Tam, A., Varhol, R., Gordon Robertson, A., Wye, N., Thiessen, N., Holt, R. A., Jones, S. J. M., Marra, M. A., Campbell, J. D., Brooks, A. N., Chmielecki, J., Imielinski, M., Onofrio, R. C., Hodis, E., Zack, T., Sougnez, C., Helman, E., Sekhar Pedamallu, C., Mesirov, J., Cherniack, A. D.,

Saksena, G., Schumacher, S. E., Carter, S. L., Hernandez, B., Garraway, L., Beroukhim, R., Gabriel, S. B., Getz, G., Meyerson, M., Hadjipanayis, A., Lee, S., Mahadeshwar, H. S., Pantazi, A., Protopopov, A., Ren, X., Seth, S., Song, X., Tang, J., Yang, L., Zhang, J., Chen, P.-C., Parfenov, M., Wei Xu, A., Santoso, N., Chin, L., Park, P. J., Kucherlapati, R., Hoadley, K. A., Todd Auman, J., Meng, S., Shi, Y., Buda, E., Waring, S., Veluvolu, U., Tan, D., Mieczkowski, P. A., Jones, C. D., Simons, J. V., Soloway, M. G., Bodenheimer, T., Jefferys, S. R., Roach, J., Hoyle, A. P., Wu, J., Balu, S., Singh, D., Prins, J. F., Marron, J. S., Parker, J. S., Neil Hayes, D., Perou, C. M., Liu, J., Cope, L., Danilova, L., Weisenberger, D. J., Maglinte, D. T., Lai, P. H., Bootwalla, M. S., Van Den Berg, D. J., Triche Jr, T., Baylin, S. B., Laird, P. W., Rosenberg, M., Chin, L., Zhang, J., Cho, J., DiCara, D., Heiman, D., Lin, P., Mallard, W., Voet, D., Zhang, H., Zou, L., Noble, M. S., Lawrence, M. S., Saksena, G., Gehlenborg, N., Thorvaldsdottir, H., Mesirov, J., Nazaire, M.-D., Robinson, J., Getz, G., Lee, W., Arman Aksoy, B., Ciriello, G., Taylor, B. S., Dresdner, G., Gao, J., Gross, B., Seshan, V. E., Ladanyi, M., Reva, B., Sinha, R., Onur Sumer, S., Weinhold, N., Schultz, N., Shen, R., Sander, C., Ng, S., Ma, S., Zhu, J., Radenbaugh, A., Stuart, J. M., Benz, C. C., Yau, C., Haussler, D., Spellman, P. T., Wilkerson, M. D., Parker, J. S., Hoadley, K. A., Kimes, P. K., Neil Hayes, D., Perou, C. M., Broom, B. M., Wang, J., Lu, Y., Kwok Shing Ng, P., Diao, L., Averett Byers, L., Liu, W., Heymach, J. V., Amos, C. I., Weinstein, J. N., Akbani, R., Mills, G. B., Curley, E., Paulauskis, J., Lau, K., Morris, S., Shelton, T., Mallery, D., Gardner, J., Penny, R., Saller, C., Tarvin, K., Richards, W. G., Cerfolio, R., Bryant, A., Raymond, D. P., Pennell, N. A., Farver, C., Czerwinski, C., Huelsenbeck-Dill, L., Iacocca, M., Petrelli, N., Rabeno, B., Brown, J., Bauer, T., Dolzhanskiy, O., Potapova, O., Rotin, D., Voronina, O., Nemirovich-Danchenko, E., Fedosenko, K. V., Gal, A., Behera, M., Ramalingam, S. S., Sica, G., Flieder, D., Boyd, J., Weaver, J., Kohl, B., Huy Quoc Thinh, D., Sandusky, G., Juhl, H., The Cancer Genome Atlas Research, N., Disease

analysis working, g., Genome sequencing centres: The, E., Edythe, L. B. I., Washington University in St, L., Baylor College of, M., Genome characterization centres: Canada's Michael Smith Genome Sciences Centre, B. C. C. A., The, E., Edythe, L. B. I., Harvard Medical, S. B., Women's Hospital, M. D. A. C. C., University of North Carolina, C. H., University of, K., The, U. S. C. J. H. U. E. C. C., Genome data analysis centres: The, E., Edythe, L. B. I., Memorial Sloan-Kettering Cancer, C., University of California, S. C. B. I., Oregon, H., Sciences, U., The University of Texas, M. D. A. C. C., Biospecimen core resource: International Genomics, C., Tissue source sites: Analytical Biological Service, I., Brigham, Women's, H., University of Alabama at, B., Cleveland, C., Christiana, C., Cureline, Emory, U., Fox Chase Cancer, C., Ilsbio, Indiana, U., Indivumed & John Flynn, H. Comprehensive molecular profiling of lung adenocarcinoma. *Nature* **511**, 543-550, doi:10.1038/nature13385 (2014).

5 West, L., Vidwans, S. J., Campbell, N. P., Shrager, J., Simon, G. R., Bueno, R., Dennis, P. A., Otterson, G. A. & Salgia, R. A novel classification of lung cancer into molecular subtypes. *PloS one* **7** (2012).

6 Schiller, J. H., Harrington, D., Belani, C. P., Langer, C., Sandler, A., Krook, J., Zhu, J. & Johnson, D. H. Comparison of four chemotherapy regimens for advanced non–small-cell lung cancer. *New England Journal of Medicine* **346**, 92-98 (2002).

7 Aisner, D. L. & Marshall, C. B. Molecular pathology of non–small cell lung cancer: a practical guide. *American journal of clinical pathology* **138**, 332-346 (2012).

8 Testa, U., Castelli, G. & Pelosi, E. Lung Cancers: Molecular Characterization, Clonal Heterogeneity and Evolution, and Cancer Stem Cells. *Cancers (Basel)* **10**, 248 (2018).

9 Schiller, J. H. A New Standard of Care for Advanced Lung Cancer. *New England Journal of Medicine* **378**, 2135-2137, doi:10.1056/NEJMe1804364 (2018).

10 Hellmann, M. D., Paz-Ares, L., Bernabe Caro, R., Zurawski, B., Kim, S.-W., Carcereny Costa, E., Park, K., Alexandru, A., Lupinacci, L., de la Mora Jimenez, E., Sakai, H., Albert, I., Vergnenegre, A., Peters, S., Syrigos, K., Barlesi, F., Reck, M., Borghaei, H., Brahmer, J. R., O'Byrne, K. J., Geese, W. J., Bhagavatheeswaran, P., Rabindran, S. K., Kasinathan, R. S., Nathan, F. E. & Ramalingam, S. S. Nivolumab plus Ipilimumab in Advanced Non–Small-Cell Lung Cancer. *New England Journal of Medicine* **381**, 2020-2031, doi:10.1056/NEJMoa1910231 (2019).

11 Ready, N., Hellmann, M. D., Awad, M. M., Otterson, G. A., Gutierrez, M., Gainor, J. F., Borghaei, H., Jolivet, J., Horn, L., Mates, M., Brahmer, J., Rabinowitz, I., Reddy, P. S., Chesney, J., Orcutt, J., Spigel, D. R., Reck, M., O'Byrne, K. J., Paz-Ares, L., Hu, W., Zerba, K., Li, X., Lestini, B., Geese, W. J., Szustakowski, J. D., Green, G., Chang, H. & Ramalingam, S. S. First-Line Nivolumab Plus Ipilimumab in Advanced Non–Small-Cell Lung Cancer (CheckMate 568): Outcomes by Programmed Death Ligand 1 and Tumor Mutational Burden as Biomarkers. *Journal of Clinical Oncology* **37**, 992-1000, doi:10.1200/jco.18.01042 (2019).

12 Skoulidis, F. & Heymach, J. V. Co-occurring genomic alterations in non-small-cell lung cancer biology and therapy. *Nat Rev Cancer* **19**, 495-509, doi:10.1038/s41568-019-0179-8 (2019).

13 Fischer, A. H., Young, K. A. & DeLellis, R. A. Incorporating pathologists' criteria of malignancy into the evolutionary model for cancer development. *Journal of cellular biochemistry* **93**, 28-36 (2004).

14 Gerlinger, M., Rowan, A. J., Horswell, S., Larkin, J., Endesfelder, D., Gronroos, E., Martinez, P., Matthews, N., Stewart, A. & Tarpey, P. Intratumor heterogeneity and branched evolution revealed by multiregion sequencing. *N Engl j Med* **366**, 883-892 (2012).

15 de Bruin, E. C., McGranahan, N., Mitter, R., Salm, M., Wedge, D. C., Yates, L., Jamal-Hanjani, M., Shafi, S., Murugaesu, N. & Rowan, A. J. Spatial and temporal

diversity in genomic instability processes defines lung cancer evolution. *Science* **346**, 251-256 (2014).

16 Zhang, J., Fujimoto, J., Zhang, J., Wedge, D. C., Song, X., Zhang, J., Seth, S., Chow, C.-W., Cao, Y. & Gumbs, C. Intratumor heterogeneity in localized lung adenocarcinomas delineated by multiregion sequencing. *Science* **346**, 256-259 (2014).

17 Carrera, P. M. & Ormond, M. Current practice in and considerations for personalized medicine in lung cancer: From the patient's molecular biology to patient values and preferences. *Maturitas* **82**, 94-99, doi:https://doi.org/10.1016/j.maturitas.2015.04.008 (2015).

18 Chen, Z., Fillmore, C. M., Hammerman, P. S., Kim, C. F. & Wong, K.-K. Non-small-cell lung cancers: a heterogeneous set of diseases. *Nature Reviews Cancer* **14**, 535-546 (2014).

19 Marusyk, A., Almendro, V. & Polyak, K. Intra-tumour heterogeneity: a looking glass for cancer? *Nature Reviews Cancer* **12**, 323-334 (2012).

20 Holliday, R. Epigenetics: a historical overview. *Epigenetics* **1**, 76-80 (2006).

21 Chung, C.-w. & Witherington, J. Progress in the discovery of small-molecule inhibitors of bromodomain–histone interactions. *Journal of biomolecular screening* **16**, 1170-1185 (2011).

22 Brzeziańska, E., Dutkowska, A. & Antczak, A. The significance of epigenetic alterations in lung carcinogenesis. *Molecular biology reports* **40**, 309-325 (2013).

23 Barlési, F., Giaccone, G., Gallegos-Ruiz, M. I., Loundou, A., Span, S. W., Lefesvre, P., Kruyt, F. & Rodriguez, J. A. Global histone modifications predict prognosis of resected non small-cell lung cancer. *J Clin Oncol* **25**, 4358-4364 (2007).

24 Rusek, A. M., Abba, M., Eljaszewicz, A., Moniuszko, M., Niklinski, J. & Allgayer, H. MicroRNA modulators of epigenetic regulation, the tumor microenvironment and the

immune system in lung cancer. *Mol Cancer* **14**, 34-34, doi:10.1186/s12943-015-0302-8 (2015).

25 Shackleton, M., Quintana, E., Fearon, E. R. & Morrison, S. J. Heterogeneity in cancer: cancer stem cells versus clonal evolution. *Cell* **138**, 822-829 (2009).

26 Reya, T. & Morrison, S. clarke, MF & Weissman, IL 2001. *Stem cells, cancer, and cancer stem cells. Nature* **414**, 105-111.

27 Dick, J. E. Stem cell concepts renew cancer research. *Blood, The Journal of the American Society of Hematology* **112**, 4793-4807 (2008).

28 Alamgeer, M., Peacock, C. D., Matsui, W., Ganju, V. & Watkins, D. N. Cancer stem cells in lung cancer: Evidence and controversies. *Respirology* **18**, 757-764 (2013).

29 Radisky, D. C. & Bissell, M. J. Matrix metalloproteinase-induced genomic instability. *Current opinion in genetics & development* **16**, 45-50 (2006).

30 Polyak, K. & Weinberg, R. A. Transitions between epithelial and mesenchymal states: acquisition of malignant and stem cell traits. *Nature Reviews Cancer* **9**, 265-273 (2009).

31 Hendrix, M. J., Seftor, E. A., Hess, A. R. & Seftor, R. E. Vasculogenic mimicry and tumour-cell plasticity: lessons from melanoma. *Nature reviews cancer* **3**, 411-421 (2003).

32 Bissell, M., Kenny, P. & Radisky, D. C. in *Cold Spring Harbor symposia on quantitative biology.* 343-356 (Cold Spring Harbor Laboratory Press).

33 Hynes, R. O. The extracellular matrix: not just pretty fibrils. *Science* **326**, 1216-1219 (2009).

34 Lu, P., Weaver, V. M. & Werb, Z. The extracellular matrix: a dynamic niche in cancer progression. *Journal of Cell Biology* **196**, 395-406 (2012).

35 Xu, R., Boudreau, A. & Bissell, M. J. Tissue architecture and function: dynamic reciprocity via extra-and intra-cellular matrices. *Cancer and metastasis reviews* **28**, 167-176 (2009).

36 Weaver, V. M., Petersen, O. W., Wang, F., Larabell, C., Briand, P., Damsky, C. & Bissell, M. J. Reversion of the malignant phenotype of human breast cells in three-dimensional culture and in vivo by integrin blocking antibodies. *The Journal of cell biology* **137**, 231-245 (1997).

37 Brassart-Pasco, S., Brézillon, S., Brassart, B., Ramont, L., Oudart, J.-B. & Monboisse, J. C. Tumor Microenvironment: Extracellular Matrix Alterations Influence Tumor Progression. *Frontiers in oncology* **10**, doi:10.3389/fonc.2020.00397 (2020).

38 Fisseler-Eckhoff, A., Prebeg, M., Voss, B. & Müller, K.-M. Extracellular matrix in preneoplastic lesions and early cancer of the lung. *Pathology-Research and Practice* **186**, 95-101 (1990).

39 Peng, D. H., Ungewiss, C., Tong, P., Byers, L. A., Wang, J., Canales, J. R., Villalobos, P. A., Uraoka, N., Mino, B., Behrens, C., Wistuba, I. I., Han, R. I., Wanna, C. A., Fahrenholtz, M., Grande-Allen, K. J., Creighton, C. J. & Gibbons, D. L. ZEB1 induces LOXL2-mediated collagen stabilization and deposition in the extracellular matrix to drive lung cancer invasion and metastasis. *Oncogene* **36**, 1925-1938, doi:10.1038/onc.2016.358 (2017).

40 Sethi, T., Rintoul, R. C., Moore, S. M., MacKinnon, A. C., Salter, D., Choo, C., Chilvers, E. R., Dransfield, I., Donnelly, S. C. & Strieter, R. Extracellular matrix proteins protect small cell lung cancer cells against apoptosis: a mechanism for small cell lung cancer growth and drug resistance in vivo. *Nature medicine* **5**, 662-668 (1999).

41 Thomas, P., Khokha, R., Shepherd, F. A., Feld, R. & Tsao, M. S. Differential expression of matrix metalloproteinases and their inhibitors in non-small cell lung cancer. *The Journal of Pathology: A Journal of the Pathological Society of Great Britain and Ireland* **190**, 150-156 (2000).

42 Koukourakis, M. I., Giatromanolaki, A., Brekken, R. A., Sivridis, E., Gatter, K. C., Harris, A. L. & Sage, E. H. Enhanced expression of SPARC/osteonectin in the

tumor-associated stroma of non-small cell lung cancer is correlated with markers of hypoxia/acidity and with poor prognosis of patients. *Cancer research* **63**, 5376-5380 (2003).

43 Caccavari, F., Valdembri, D., Sandri, C., Bussolino, F. & Serini, G. Integrin signaling and lung cancer. *Cell adhesion & migration* **4**, 124-129 (2010).

44 Ungewiss, C., Rizvi, Z. H., Roybal, J. D., Peng, D. H., Gold, K. A., Shin, D. H., Creighton, C. J. & Gibbons, D. L. The microRNA-200/Zeb1 axis regulates ECM-dependent beta1-integrin/FAK signaling, cancer cell invasion and metastasis through CRKL. *Sci Rep* **6**, 18652, doi:10.1038/srep18652 (2016).

45 Gibbons, D. L., Lin, W., Creighton, C. J., Rizvi, Z. H., Gregory, P. A., Goodall, G. J., Thilaganathan, N., Du, L., Zhang, Y. & Pertsemlidis, A. Contextual extracellular cues promote tumor cell EMT and metastasis by regulating miR-200 family expression. *Genes & development* **23**, 2140-2151 (2009).

46 Kalluri, R. & Zeisberg, M. Fibroblasts in cancer. *Nature Reviews Cancer* **6**, 392-401 (2006).

47 Yoshida, G. J., Azuma, A., Miura, Y. & Orimo, A. Activated Fibroblast Program Orchestrates Tumor Initiation and Progression; Molecular Mechanisms and the Associated Therapeutic Strategies. *Int J Mol Sci* **20**, 2256, doi:10.3390/ijms20092256 (2019).

48 Li, Y.-Y., Lam, S.-K., Zheng, C.-Y. & Ho, J. C.-M. The effect of tumor microenvironment on autophagy and sensitivity to targeted therapy in EGFR-mutated lung adenocarcinoma. *Journal of Cancer* **6**, 382 (2015).

49 Wang, W., Li, Q., Yamada, T., Matsumoto, K., Matsumoto, I., Oda, M., Watanabe, G., Kayano, Y., Nishioka, Y. & Sone, S. Crosstalk to stromal fibroblasts induces resistance of lung cancer to epidermal growth factor receptor tyrosine kinase inhibitors. *Clinical Cancer Research* **15**, 6630-6638 (2009).

50 Bremnes, R. M., Dønnem, T., Al-Saad, S., Al-Shibli, K., Andersen, S., Sirera, R., Camps, C., Marinez, I. & Busund, L.-T. The role of tumor stroma in cancer progression and prognosis: emphasis on carcinoma-associated fibroblasts and non-small cell lung cancer. *Journal of thoracic oncology* **6**, 209-217 (2011).

51 Kim, S.-H., Choe, C., Shin, Y.-S., Jeon, M.-J., Choi, S.-J., Lee, J., Bae, G.-Y., Cha, H.-J. & Kim, J. Human lung cancer-associated fibroblasts enhance motility of non-small cell lung cancer cells in co-culture. *Anticancer research* **33**, 2001-2009 (2013).

52 Chen, W.-J., Ho, C.-C., Chang, Y.-L., Chen, H.-Y., Lin, C.-A., Ling, T.-Y., Yu, S.-L., Yuan, S.-S., Chen, Y.-J. L. & Lin, C.-Y. Cancer-associated fibroblasts regulate the plasticity of lung cancer stemness via paracrine signalling. *Nature communications* **5**, 1-17 (2014).

53 Bota-Rabassedas, N., Banerjee, P., Niu, Y., Cao, W., Luo, J., Xi, Y., Tan, X., Sheng, K., Ahn, Y.-H., Lee, S., Parra, E. R., Rodriguez-Canales, J., Albritton, J., Weiger, M., Liu, X., Guo, H.-F., Yu, J., Rodriguez, B. L., Firestone, J. J. A., Mino, B., Creighton, C. J., Solis, L. M., Villalobos, P., Raso, M. G., Sazer, D. W., Gibbons, D. L., Russell, W. K., Longmore, G. D., Wistuba, I. I., Wang, J., Chapman, H. A., Miller, J. S., Zong, C. & Kurie, J. M. Contextual cues from cancer cells govern cancer-associated fibroblast heterogeneity. *Cell Reports* **35**, 109009, doi:https://doi.org/10.1016/j.celrep.2021.109009 (2021).

54 Sugiyama, Y., Kato, M., Chen, F.-A., Williams, S. S., Kawaguchi, Y., Miya, K., Jong, Y. S., Mathiowitz, E., Egilmez, N. K. & Bankert, R. B. Human inflammatory cells within the tumor microenvironment of lung tumor xenografts mediate tumor growth suppression in situ that depends on and is augmented by interleukin-12. *Journal of Immunotherapy* **24**, 37-45 (2001).

55 Welsh, T. J., Green, R. H., Richardson, D., Waller, D. A., O'Byrne, K. J. & Bradding, P. Macrophage and mast-cell invasion of tumor cell islets confers a marked survival

advantage in non–small-cell lung cancer. *Journal of clinical oncology* **23**, 8959-8967 (2005).

56 Dieu-Nosjean, M.-C., Antoine, M., Danel, C., Heudes, D., Wislez, M., Poulot, V., Rabbe, N., Laurans, L., Tartour, E. & de Chaisemartin, L. Long-term survival for patients with non–small-cell lung cancer with intratumoral lymphoid structures. *Journal of Clinical Oncology* **26**, 4410-4417 (2008).

57 Al-Shibli, K. I., Donnem, T., Al-Saad, S., Persson, M., Bremnes, R. M. & Busund, L.-T. Prognostic effect of epithelial and stromal lymphocyte infiltration in non–small cell lung cancer. *Clinical cancer research* **14**, 5220-5227 (2008).

58 Alifano, M., Mansuet-Lupo, A., Lococo, F., Roche, N., Bobbio, A., Canny, E., Schussler, O., Dermine, H., Régnard, J.-F. & Burroni, B. Systemic inflammation, nutritional status and tumor immune microenvironment determine outcome of resected non-small cell lung cancer. *PloS one* **9** (2014).

59 Stearman, R. S., Dwyer-Nield, L., Grady, M. C., Malkinson, A. M. & Geraci, M. W. A macrophage gene expression signature defines a field effect in the lung tumor microenvironment. *Cancer Research* **68**, 34-43 (2008).

60 Müller, P., Rothschild, S. I., Arnold, W., Hirschmann, P., Horvath, L., Bubendorf, L., Savic, S. & Zippelius, A. Metastatic spread in patients with non-small cell lung cancer is associated with a reduced density of tumor-infiltrating T cells. *Cancer Immunology, Immunotherapy* **65**, 1-11 (2016).

61 Phillips, R. J., Burdick, M. D., Lutz, M., Belperio, J. A., Keane, M. P. & Strieter, R. M. The stromal derived factor–1/CXCL12–CXC chemokine receptor 4 biological axis in non–small cell lung cancer metastases. *American journal of respiratory and critical care medicine* **167**, 1676-1686 (2003).

62 Shimizu, K., Okita, R. & Nakata, M. Clinical significance of the tumor microenvironment in non-small cell lung cancer. *Annals of translational medicine* **1** (2013).

63 Kwon, M.-c., Proost, N., Song, J.-Y., Sutherland, K. D., Zevenhoven, J. & Berns, A. Paracrine signaling between tumor subclones of mouse SCLC: a critical role of ETS transcription factor Pea3 in facilitating metastasis. *Genes & development* **29**, 1587-1592 (2015).

64 Zhong, L., Roybal, J., Chaerkady, R., Zhang, W., Choi, K., Alvarez, C. A., Tran, H., Creighton, C. J., Yan, S. & Strieter, R. M. Identification of secreted proteins that mediate cell-cell interactions in an in vitro model of the lung cancer microenvironment. *Cancer research* **68**, 7237-7245 (2008).

65 Foster, J. G., Wong, S. C. & Sharp, T. V. The hypoxic tumor microenvironment: driving the tumorigenesis of non-small-cell lung cancer. *Future Oncology* **10**, 2659-2674 (2014).

66 Cui, Y.-L., Wang, X. & Li, X.-F. 18F-fluoromisonidazole PET reveals spatial and temporal heterogeneity of hypoxia in mouse models of human non-small-cell lung cancer. *Future Oncology* **11**, 2841-2849 (2015).

67 Oxnard, G. R., Arcila, M. E., Sima, C. S., Riely, G. J., Chmielecki, J., Kris, M. G., Pao, W., Ladanyi, M. & Miller, V. A. Acquired resistance to EGFR tyrosine kinase inhibitors in EGFR-mutant lung cancer: distinct natural history of patients with tumors harboring the T790M mutation. *Clin Cancer Res* **17**, 1616-1622, doi:10.1158/1078-0432.Ccr-10-2692 (2011).

68 Yu, H. A., Arcila, M. E., Rekhtman, N., Sima, C. S., Zakowski, M. F., Pao, W., Kris, M. G., Miller, V. A., Ladanyi, M. & Riely, G. J. Analysis of tumor specimens at the time of acquired resistance to EGFR-TKI therapy in 155 patients with EGFR-mutant lung cancers. *Clin Cancer Res* **19**, 2240-2247, doi:10.1158/1078-0432.Ccr-12-2246 (2013).

69 Ramalingam, S. S., Vansteenkiste, J., Planchard, D., Cho, B. C., Gray, J. E., Ohe, Y., Zhou, C., Reungwetwattana, T., Cheng, Y., Chewaskulyong, B., Shah, R., Cobo, M., Lee, K. H., Cheema, P., Tiseo, M., John, T., Lin, M.-C., Imamura, F., Kurata, T.,

Todd, A., Hodge, R., Saggese, M., Rukazenkov, Y. & Soria, J.-C. Overall Survival with Osimertinib in Untreated, EGFR-Mutated Advanced NSCLC. *New England Journal of Medicine* **382**, 41-50, doi:10.1056/NEJMoa1913662 (2019).

70 Ortiz-Cuaran, S., Scheffler, M., Plenker, D., Dahmen, L., Scheel, A. H., Fernandez-Cuesta, L., Meder, L., Lovly, C. M., Persigehl, T., Merkelbach-Bruse, S., Bos, M., Michels, S., Fischer, R., Albus, K., König, K., Schildhaus, H. U., Fassunke, J., Ihle, M. A., Pasternack, H., Heydt, C., Becker, C., Altmüller, J., Ji, H., Müller, C., Florin, A., Heuckmann, J. M., Nuernberg, P., Ansén, S., Heukamp, L. C., Berg, J., Pao, W., Peifer, M., Buettner, R., Wolf, J., Thomas, R. K. & Sos, M. L. Heterogeneous Mechanisms of Primary and Acquired Resistance to Third-Generation EGFR Inhibitors. *Clin Cancer Res* **22**, 4837-4847, doi:10.1158/1078-0432.Ccr-15-1915 (2016).

71 Rosenbaum, J. N., Bloom, R., Forys, J. T., Hiken, J., Armstrong, J. R., Branson, J., McNulty, S., Velu, P. D., Pepin, K., Abel, H., Cottrell, C. E., Pfeifer, J. D., Kulkarni, S., Govindan, R., Konnick, E. Q., Lockwood, C. M. & Duncavage, E. J. Genomic heterogeneity of ALK fusion breakpoints in non-small-cell lung cancer. *Modern Pathology* **31**, 791-808, doi:10.1038/modpathol.2017.181 (2018).

72 Bedard, P. L., Hansen, A. R., Ratain, M. J. & Siu, L. L. Tumour heterogeneity in the clinic. *Nature* **501**, 355-364, doi:10.1038/nature12627 (2013).

73 Naidoo, J. & Drilon, A. KRAS-Mutant Lung Cancers in the Era of Targeted Therapy. *Advances in experimental medicine and biology* **893**, 155-178, doi:10.1007/978-3-319-24223-1_8 (2016).

74 Blumenschein, G. R., Jr., Smit, E. F., Planchard, D., Kim, D. W., Cadranel, J., De Pas, T., Dunphy, F., Udud, K., Ahn, M. J., Hanna, N. H., Kim, J. H., Mazieres, J., Kim, S. W., Baas, P., Rappold, E., Redhu, S., Puski, A., Wu, F. S. & Jänne, P. A. A randomized phase II study of the MEK1/MEK2 inhibitor trametinib (GSK1120212) compared with docetaxel in KRAS-mutant advanced non-small-cell lung cancer

(NSCLC)†. *Annals of oncology : official journal of the European Society for Medical Oncology* **26**, 894-901, doi:10.1093/annonc/mdv072 (2015).

75 Jänne, P. A., van den Heuvel, M. M., Barlesi, F., Cobo, M., Mazieres, J., Crinò, L., Orlov, S., Blackhall, F., Wolf, J., Garrido, P., Poltoratskiy, A., Mariani, G., Ghiorghiu, D., Kilgour, E., Smith, P., Kohlmann, A., Carlile, D. J., Lawrence, D., Bowen, K. & Vansteenkiste, J. Selumetinib Plus Docetaxel Compared With Docetaxel Alone and Progression-Free Survival in Patients With KRAS-Mutant Advanced Non–Small Cell Lung Cancer: The SELECT-1 Randomized Clinical Trial. *JAMA* **317**, 1844-1853, doi:10.1001/jama.2017.3438 (2017).

76 Dagogo-Jack, I. & Shaw, A. T. Tumour heterogeneity and resistance to cancer therapies. *Nature Reviews Clinical Oncology* **15**, 81-94, doi:10.1038/nrclinonc.2017.166 (2018).

77 Junttila, M. R. & de Sauvage, F. J. Influence of tumour micro-environment heterogeneity on therapeutic response. *Nature* **501**, 346 (2013).

78 Scagliotti, G. V., Bironzo, P. & Vansteenkiste, J. F. Addressing the unmet need in lung cancer: The potential of immuno-oncology. *Cancer treatment reviews* **41**, 465-475, doi:10.1016/j.ctrv.2015.04.001 (2015).

79 Phan, G. Q., Yang, J. C., Sherry, R. M., Hwu, P., Topalian, S. L., Schwartzentruber, D. J., Restifo, N. P., Haworth, L. R., Seipp, C. A., Freezer, L. J., Morton, K. E., Mavroukakis, S. A., Duray, P. H., Steinberg, S. M., Allison, J. P., Davis, T. A. & Rosenberg, S. A. Cancer regression and autoimmunity induced by cytotoxic T lymphocyte-associated antigen 4 blockade in patients with metastatic melanoma. *Proceedings of the National Academy of Sciences of the United States of America* **100**, 8372-8377, doi:10.1073/pnas.1533209100 (2003).

80 Chae, Y. K., Arya, A., Iams, W., Cruz, M. R., Chandra, S., Choi, J. & Giles, F. Current landscape and future of dual anti-CTLA4 and PD-1/PD-L1 blockade immunotherapy in cancer; lessons learned from clinical trials with melanoma and

non-small cell lung cancer (NSCLC). *Journal for ImmunoTherapy of Cancer* **6**, 39, doi:10.1186/s40425-018-0349-3 (2018).

81 Borghaei, H., Paz-Ares, L., Horn, L., Spigel, D. R., Steins, M., Ready, N. E., Chow, L. Q., Vokes, E. E., Felip, E., Holgado, E., Barlesi, F., Kohlhäufl, M., Arrieta, O., Burgio, M. A., Fayette, J., Lena, H., Poddubskaya, E., Gerber, D. E., Gettinger, S. N., Rudin, C. M., Rizvi, N., Crinò, L., Blumenschein, G. R., Jr., Antonia, S. J., Dorange, C., Harbison, C. T., Graf Finckenstein, F. & Brahmer, J. R. Nivolumab versus Docetaxel in Advanced Nonsquamous Non-Small-Cell Lung Cancer. *The New England journal of medicine* **373**, 1627-1639, doi:10.1056/NEJMoa1507643 (2015).

82 Rohaan, M. W., Wilgenhof, S. & Haanen, J. B. A. G. Adoptive cellular therapies: the current landscape. *Virchows Arch* **474**, 449-461, doi:10.1007/s00428-018-2484-0 (2019).

83 Walsh, R. J. & Soo, R. A. Resistance to immune checkpoint inhibitors in non-small cell lung cancer: biomarkers and therapeutic strategies. *Therapeutic advances in medical oncology* **12**, 1758835920937902, doi:10.1177/1758835920937902 (2020).

84 Sandler, A., Gray, R., Perry, M. C., Brahmer, J., Schiller, J. H., Dowlati, A., Lilenbaum, R. & Johnson, D. H. Paclitaxel–Carboplatin Alone or with Bevacizumab for Non–Small-Cell Lung Cancer. *New England Journal of Medicine* **355**, 2542-2550, doi:10.1056/NEJMoa061884 (2006).

85 Robertson-Tessi, M., Gillies, R. J., Gatenby, R. A. & Anderson, A. R. A. Impact of Metabolic Heterogeneity on Tumor Growth, Invasion, and Treatment Outcomes. *Cancer Research* **75**, 1567-1579, doi:10.1158/0008-5472.Can-14-1428 (2015).

86 Malakpour-Permlid, A., Buzzi, I., Hegardt, C., Johansson, F. & Oredsson, S. Identification of extracellular matrix proteins secreted by human dermal fibroblasts cultured in 3D electrospun scaffolds. *Scientific Reports* **11**, 6655, doi:10.1038/s41598-021-85742-0 (2021).

87 Rijal, G. & Li, W. A versatile 3D tissue matrix scaffold system for tumor modeling and drug screening. *Science Advances* **3**, e1700764, doi:10.1126/sciadv.1700764 (2017).

88 Fessart, D., Begueret, H. & Delom, F. Three-dimensional culture model to distinguish normal from malignant human bronchial epithelial cells. *The European respiratory journal* **42**, 1345-1356, doi:10.1183/09031936.00118812 (2013).

89 Clevers, H. & Tuveson, D. A. Organoid Models for Cancer Research. *Annual Review of Cancer Biology* **3**, 223-234, doi:10.1146/annurev-cancerbio-030518-055702 (2019).

90 Tammela, T. & Sage, J. Investigating Tumor Heterogeneity in Mouse Models. *Annual Review of Cancer Biology* **4**, 99-119, doi:10.1146/annurev-cancerbio-030419-033413 (2020).

91 Marusyk, A., Janiszewska, M. & Polyak, K. Intratumor Heterogeneity: The Rosetta Stone of Therapy Resistance. *Cancer cell* **37**, 471-484, doi:https://doi.org/10.1016/j.ccell.2020.03.007 (2020).

92 Kersten, K., de Visser, K. E., van Miltenburg, M. H. & Jonkers, J. Genetically engineered mouse models in oncology research and cancer medicine. *EMBO Mol Med* **9**, 137-153, doi:https://doi.org/10.15252/emmm.201606857 (2017).

93 Gibbons, D. L., Lin, W., Creighton, C. J., Rizvi, Z. H., Gregory, P. A., Goodall, G. J., Thilaganathan, N., Du, L., Zhang, Y., Pertsemlidis, A. & Kurie, J. M. Contextual extracellular cues promote tumor cell EMT and metastasis by regulating miR-200 family expression. *Genes Dev* **23**, 2140-2151, doi:10.1101/gad.1820209 (2009).

94 Mittal, V. Epithelial Mesenchymal Transition in Aggressive Lung Cancers. *Advances in experimental medicine and biology* **890**, 37-56, doi:10.1007/978-3-319-24932-2_3 (2016).

95 TSOUKALAS, N., ARAVANTINOU-FATOROU, E., TOLIA, M., GIAGINIS, C., GALANOPOULOS, M., KIAKOU, M., KOSTAKIS, I. D., DANA, E., VAMVAKARIS, I.,

KOROGIANNOS, A., TSIAMBAS, E., SALEMIS, N., KYRGIAS, G., KARAMERIS, A. & THEOCHARIS, S. Epithelial–Mesenchymal Transition in Non Small-cell Lung Cancer. *Anticancer Research* **37**, 1773-1778 (2017).

96 Tsai, J. H. & Yang, J. Epithelial-mesenchymal plasticity in carcinoma metastasis. *Genes & development* **27**, 2192-2206, doi:10.1101/gad.225334.113 (2013).

97 Fischer, K. R., Durrans, A., Lee, S., Sheng, J., Li, F., Wong, S. T. C., Choi, H., El Rayes, T., Ryu, S., Troeger, J., Schwabe, R. F., Vahdat, L. T., Altorki, N. K., Mittal, V. & Gao, D. Epithelial-to-mesenchymal transition is not required for lung metastasis but contributes to chemoresistance. *Nature* **527**, 472-476, doi:10.1038/nature15748 (2015).

98 Shibue, T. & Weinberg, R. A. EMT, CSCs, and drug resistance: the mechanistic link and clinical implications. *Nature reviews. Clinical oncology* **14**, 611-629, doi:10.1038/nrclinonc.2017.44 (2017).

99 Zhang, P., Wei, Y., Wang, L., Debeb, B. G., Yuan, Y., Zhang, J., Yuan, J., Wang, M., Chen, D., Sun, Y., Woodward, W. A., Liu, Y., Dean, D. C., Liang, H., Hu, Y., Ang, K. K., Hung, M.-C., Chen, J. & Ma, L. ATM-mediated stabilization of ZEB1 promotes DNA damage response and radioresistance through CHK1. *Nature Cell Biology* **16**, 864-875, doi:10.1038/ncb3013 (2014).

100 Zheng, X., Carstens, J. L., Kim, J., Scheible, M., Kaye, J., Sugimoto, H., Wu, C. C., LeBleu, V. S. & Kalluri, R. Epithelial-to-mesenchymal transition is dispensable for metastasis but induces chemoresistance in pancreatic cancer. *Nature* **527**, 525-530, doi:10.1038/nature16064 (2015).

101 Ferrarotto, R., Goonatilake, R., Young Yoo, S., Tong, P., Giri, U., Peng, S., Minna, J., Girard, L., Wang, Y., Wang, L., Li, L., Diao, L., Peng, D. H., Gibbons, D. L., Glisson, B. S., Heymach, J. V., Wang, J., Byers, L. A. & Johnson, F. M. Epithelial–Mesenchymal Transition Predicts Polo-Like Kinase 1 Inhibitor–Mediated Apoptosis

in Non–Small Cell Lung Cancer. *Clinical Cancer Research* **22**, 1674-1686, doi:10.1158/1078-0432.Ccr-14-2890 (2016).

102 DuPage, M., Dooley, A. L. & Jacks, T. Conditional mouse lung cancer models using adenoviral or lentiviral delivery of Cre recombinase. *Nature Protocols* **4**, 1064-1072, doi:10.1038/nprot.2009.95 (2009).

103 Peng, D. H., Kundu, S. T., Fradette, J. J., Diao, L., Tong, P., Byers, L. A., Wang, J., Canales, J. R., Villalobos, P. A., Mino, B., Yang, Y., Minelli, R., Peoples, M. D., Bristow, C. A., Heffernan, T. P., Carugo, A., Wistuba, II & Gibbons, D. L. ZEB1 suppression sensitizes KRAS mutant cancers to MEK inhibition by an IL17RD-dependent mechanism. *Sci Transl Med* **11**, doi:10.1126/scitranslmed.aaq1238 (2019).

104 Chen, S. H., Gong, X., Zhang, Y., Van Horn, R. D., Yin, T., Huber, L., Burke, T. F., Manro, J., Iversen, P. W., Wu, W., Bhagwat, S. V., Beckmann, R. P., Tiu, R. V., Buchanan, S. G. & Peng, S. B. RAF inhibitor LY3009120 sensitizes RAS or BRAF mutant cancer to CDK4/6 inhibition by abemaciclib via superior inhibition of phospho-RB and suppression of cyclin D1. *Oncogene* **37**, 821-832, doi:10.1038/onc.2017.384 (2018).

105 Albritton, J. L., Roybal, J. D., Paulsen, S. J., Calafat, N., Flores-Zaher, J. A., Farach-Carson, M. C., Gibbons, D. L. & Miller, J. S. Ultrahigh-throughput Generation and Characterization of Cellular Aggregates in Laser-ablated Microwells of Poly(dimethylsiloxane). *RSC advances* **6**, 8980-8991, doi:10.1039/c5ra26022a (2016).

106 Toneff, M. J., Sreekumar, A., Tinnirello, A., Hollander, P. D., Habib, S., Li, S., Ellis, M. J., Xin, L., Mani, S. A. & Rosen, J. M. The Z-cad dual fluorescent sensor detects dynamic changes between the epithelial and mesenchymal cellular states. *BMC Biology* **14**, 47, doi:10.1186/s12915-016-0269-y (2016).

107 Wiederschain, D., Wee, S., Chen, L., Loo, A., Yang, G., Huang, A., Chen, Y., Caponigro, G., Yao, Y. M., Lengauer, C., Sellers, W. R. & Benson, J. D. Single-vector inducible lentiviral RNAi system for oncology target validation. *Cell Cycle* **8**, 498-504, doi:10.4161/cc.8.3.7701 (2009).

108 Chou, T.-C. Theoretical Basis, Experimental Design, and Computerized Simulation of Synergism and Antagonism in Drug Combination Studies. *Pharmacological Reviews* **58**, 621-681, doi:10.1124/pr.58.3.10 (2006).

109 Carugo, A., Genovese, G., Seth, S., Nezi, L., Rose, J. L., Bossi, D., Cicalese, A., Shah, P. K., Viale, A., Pettazzoni, P. F., Akdemir, K. C., Bristow, C. A., Robinson, F. S., Tepper, J., Sanchez, N., Gupta, S., Estecio, M. R., Giuliani, V., Dellino, G. I., Riva, L., Yao, W., Di Francesco, M. E., Green, T., D'Alesio, C., Corti, D., Kang, Y. a., Jones, P., Wang, H., Fleming, J. B., Maitra, A., Pelicci, P. G., Chin, L., DePinho, R. A., Lanfrancone, L., Heffernan, T. P. & Draetta, G. F. In Vivo Functional Platform Targeting Patient-Derived Xenografts Identifies WDR5-Myc Association as a Critical Determinant of Pancreatic Cancer. *Cell Reports* **16**, 133-147, doi:https://doi.org/10.1016/j.celrep.2016.05.063 (2016).

110 Aisner, D. L. & Marshall, C. B. Molecular Pathology of Non–Small Cell Lung CancerA Practical Guide. *American Journal of Clinical Pathology* **138**, 332-346, doi:10.1309/AJCPFR12WJKCEEZZ (2012).

111 Joyce, J. A. & Pollard, J. W. Microenvironmental regulation of metastasis. *Nat Rev Cancer* **9**, 239-252, doi:10.1038/nrc2618 (2009).

112 Weigelt, B., Ghajar, C. M. & Bissell, M. J. The need for complex 3D culture models to unravel novel pathways and identify accurate biomarkers in breast cancer. *Advanced drug delivery reviews* **0**, 42-51, doi:10.1016/j.addr.2014.01.001 (2014).

113 Fong, E. L. S., Harrington, D. A., Farach-Carson, M. C. & Yu, H. Heralding a new paradigm in 3D tumor modeling. *Biomaterials* **108**, 197-213, doi:https://doi.org/10.1016/j.biomaterials.2016.08.052 (2016).

114 Bracken, C. P., Gregory, P. A., Kolesnikoff, N., Bert, A. G., Wang, J., Shannon, M. F. & Goodall, G. J. A Double-Negative Feedback Loop between ZEB1-SIP1 and the microRNA-200 Family Regulates Epithelial-Mesenchymal Transition. *Cancer Research* **68**, 7846-7854, doi:10.1158/0008-5472.Can-08-1942 (2008).

115 Ungewiss, C., Rizvi, Z. H., Roybal, J. D., Peng, D. H., Gold, K. A., Shin, D.-H., Creighton, C. J. & Gibbons, D. L. The microRNA-200/Zeb1 axis regulates ECM-dependent β1-integrin/FAK signaling, cancer cell invasion and metastasis through CRKL. *Scientific reports* **6**, 18652 (2016).

116 Yeatman, T. J. A renaissance for SRC. *Nature Reviews Cancer* **4**, 470, doi:10.1038/nrc1366 (2004).

117 Thomas, S. M. & Brugge, J. S. CELLULAR FUNCTIONS REGULATED BY SRC FAMILY KINASES. *Annual Review of Cell and Developmental Biology* **13**, 513-609, doi:10.1146/annurev.cellbio.13.1.513 (1997).

118 Altorki, N. K., Markowitz, G. J., Gao, D., Port, J. L., Saxena, A., Stiles, B., McGraw, T. & Mittal, V. The lung microenvironment: an important regulator of tumour growth and metastasis. *Nature Reviews Cancer* **19**, 9-31, doi:10.1038/s41568-018-0081-9 (2019).

119 Schliekelman, M. J., Creighton, C. J., Baird, B. N., Chen, Y., Banerjee, P., Bota-Rabassedas, N., Ahn, Y. H., Roybal, J. D., Chen, F., Zhang, Y., Mishra, D. K., Kim, M. P., Liu, X., Mino, B., Villalobos, P., Rodriguez-Canales, J., Behrens, C., Wistuba, II, Hanash, S. M. & Kurie, J. M. Thy-1(+) Cancer-associated Fibroblasts Adversely Impact Lung Cancer Prognosis. *Sci Rep* **7**, 6478, doi:10.1038/s41598-017-06922-5 (2017).

120 Dawson, J. C., Serrels, A., Stupack, D. G., Schlaepfer, D. D. & Frame, M. C. Targeting FAK in anticancer combination therapies. *Nature Reviews Cancer* **21**, 313-324, doi:10.1038/s41568-021-00340-6 (2021).

121 Chapman, A., Fernandez del Ama, L., Ferguson, J., Kamarashev, J., Wellbrock, C. & Hurlstone, A. Heterogeneous Tumor Subpopulations Cooperate to Drive Invasion. *Cell Reports* **8**, 688-695, doi:10.1016/j.celrep.2014.06.045 (2014).

122 Shintani, Y., Maeda, M., Chaika, N., Johnson, K. R. & Wheelock, M. J. Collagen I Promotes Epithelial-to-Mesenchymal Transition in Lung Cancer Cells via Transforming Growth Factor–β Signaling. *American Journal of Respiratory Cell and Molecular Biology* **38**, 95-104, doi:10.1165/rcmb.2007-0071OC (2008).

123 Pickup, M. W., Mouw, J. K. & Weaver, V. M. The extracellular matrix modulates the hallmarks of cancer. *EMBO Reports* **15**, 1243-1253, doi:10.15252/embr.201439246 (2014).

124 Nguyen-Ngoc, K.-V., Cheung, K. J., Brenot, A., Shamir, E. R., Gray, R. S., Hines, W. C., Yaswen, P., Werb, Z. & Ewald, A. J. ECM microenvironment regulates collective migration and local dissemination in normal and malignant mammary epithelium. *Proceedings of the National Academy of Sciences* **109**, E2595 (2012).

125 Byers, L. A., Sen, B., Saigal, B., Diao, L., Wang, J., Nanjundan, M., Cascone, T., Mills, G. B., Heymach, J. V. & Johnson, F. M. Reciprocal regulation of c-Src and STAT3 in non-small cell lung cancer. *Clin Cancer Res* **15**, 6852-6861, doi:10.1158/1078-0432.Ccr-09-0767 (2009).

126 Johnson, F. M., Saigal, B., Talpaz, M. & Donato, N. J. Dasatinib (BMS-354825) tyrosine kinase inhibitor suppresses invasion and induces cell cycle arrest and apoptosis of head and neck squamous cell carcinoma and non-small cell lung cancer cells. *Clin Cancer Res* **11**, 6924-6932, doi:10.1158/1078-0432.Ccr-05-0757 (2005).

127 Redin, E., Garmendia, I., Lozano, T., Serrano, D., Senent, Y., Redrado, M., Villalba, M., De Andrea, C. E., Exposito, F., Ajona, D., Ortiz-Espinosa, S., Remirez, A., Bertolo, C., Sainz, C., Garcia-Pedrero, J., Pio, R., Lasarte, J., Agorreta, J., Montuenga, L. M. & Calvo, A. SRC family kinase (SFK) inhibitor dasatinib improves

the antitumor activity of anti-PD-1 in NSCLC models by inhibiting Treg cell conversion and proliferation. *Journal for ImmunoTherapy of Cancer* **9**, e001496, doi:10.1136/jitc-2020-001496 (2021).

128 Chan, D., Tyner, J. W., Chng, W. J., Bi, C., Okamoto, R., Said, J., Ngan, B. D., Braunstein, G. D. & Koeffler, H. P. Effect of dasatinib against thyroid cancer cell lines in vitro and a xenograft model in vivo. *Oncology letters* **3**, 807-815, doi:10.3892/ol.2012.579 (2012).

129 Hu, M., Che, P., Han, X., Cai, G.-Q., Liu, G., Antony, V., Luckhardt, T., Siegal, G. P., Zhou, Y., Liu, R.-m., Desai, L. P., O'Reilly, P. J., Thannickal, V. J. & Ding, Q. Therapeutic Targeting of Src Kinase in Myofibroblast Differentiation and Pulmonary Fibrosis. *Journal of Pharmacology and Experimental Therapeutics* **351**, 87 (2014).

130 Abdalla, M., Thompson, L., Gurley, E., Burke, S., Ujjin, J., Newsome, R. & Somanath, P. R. Dasatinib inhibits TGFβ-induced myofibroblast differentiation through Src-SRF Pathway. *European Journal of Pharmacology* **769**, 134-142, doi:https://doi.org/10.1016/j.ejphar.2015.11.008 (2015).

131 Wang, F., Weaver, V. M., Petersen, O. W., Larabell, C. A., Dedhar, S., Briand, P., Lupu, R. & Bissell, M. J. Reciprocal interactions between β1-integrin and epidermal growth factor receptor in three-dimensional basement membrane breast cultures: A different perspective in epithelial biology. *Proceedings of the National Academy of Sciences* **95**, 14821-14826 (1998).

132 Weaver, V. M., Petersen, O. W., Wang, F., Larabell, C. A., Briand, P., Damsky, C. & Bissell, M. J. Reversion of the malignant phenotype of human breast cells in three-dimensional culture and in vivo by integrin blocking antibodies. *The Journal of cell biology* **137**, 231-245 (1997).

133 Muthuswamy, S. K., Li, D., Lelievre, S., Bissell, M. J. & Brugge, J. S. ErbB2, but not ErbB1, reinitiates proliferation and induces luminal repopulation in epithelial acini. *Nature cell biology* **3**, 785-792 (2001).

134 Streuli, C. H., Bailey, N. & Bissell, M. J. Control of mammary epithelial differentiation: basement membrane induces tissue-specific gene expression in the absence of cell-cell interaction and morphological polarity. *The Journal of Cell Biology* **115**, 1383-1395, doi:10.1083/jcb.115.5.1383 (1991).

135 Rebecca, V. W., Somasundaram, R. & Herlyn, M. Pre-clinical modeling of cutaneous melanoma. *Nature Communications* **11**, 2858, doi:10.1038/s41467-020-15546-9 (2020).

136 Smalley, K. S. M., Lioni, M. & Herlyn, M. Life ins't flat: Taking cancer biology to the next dimension. *In Vitro Cellular & Developmental Biology - Animal* **42**, 242-247, doi:10.1290/0604027.1 (2006).

137 Chatterjee, K., Lin-Gibson, S., Wallace, W. E., Parekh, S. H., Lee, Y. J., Cicerone, M. T., Young, M. F. & Simon, C. G., Jr. The effect of 3D hydrogel scaffold modulus on osteoblast differentiation and mineralization revealed by combinatorial screening. *Biomaterials* **31**, 5051-5062, doi:10.1016/j.biomaterials.2010.03.024 (2010).

138 De Luca, A., Raimondi, L., Salamanna, F., Carina, V., Costa, V., Bellavia, D., Alessandro, R., Fini, M. & Giavaresi, G. Relevance of 3d culture systems to study osteosarcoma environment. *J Exp Clin Cancer Res* **37**, 2-2, doi:10.1186/s13046-017-0663-5 (2018).

139 Gomez-Roman, N., Stevenson, K., Gilmour, L., Hamilton, G. & Chalmers, A. J. A novel 3D human glioblastoma cell culture system for modeling drug and radiation responses. *Neuro-oncology* **19**, 229-241, doi:10.1093/neuonc/now164 (2017).

140 Hostiuc, S., Rusu, M. C., Negoi, I., Perlea, P., Dorobanţu, B. & Drima, E. The moral status of cerebral organoids. *Regenerative Therapy* **10**, 118-122, doi:https://doi.org/10.1016/j.reth.2019.02.003 (2019).

141 Huang, L., Holtzinger, A., Jagan, I., BeGora, M., Lohse, I., Ngai, N., Nostro, C., Wang, R., Muthuswamy, L. B., Crawford, H. C., Arrowsmith, C., Kalloger, S. E., Renouf, D. J., Connor, A. A., Cleary, S., Schaeffer, D. F., Roehrl, M., Tsao, M.-S.,

Gallinger, S., Keller, G. & Muthuswamy, S. K. Ductal pancreatic cancer modeling and drug screening using human pluripotent stem cell– and patient-derived tumor organoids. *Nature Medicine* **21**, 1364, doi:10.1038/nm.3973 https://www.nature.com/articles/nm.3973#supplementary-information (2015).

142 Tomás-Bort, E., Kieler, M., Sharma, S., Candido, J. B. & Loessner, D. 3D approaches to model the tumor microenvironment of pancreatic cancer. *Theranostics* **10**, 5074-5089, doi:10.7150/thno.42441 (2020).

143 Li, X., Larsson, P., Ljuslinder, I., Öhlund, D., Myte, R., Löfgren-Burström, A., Zingmark, C., Ling, A., Edin, S. & Palmqvist, R. Ex Vivo Organoid Cultures Reveal the Importance of the Tumor Microenvironment for Maintenance of Colorectal Cancer Stem Cells. *Cancers (Basel)* **12**, 923 (2020).

144 Xu, X., Gurski, L. A., Zhang, C., Harrington, D. A., Farach-Carson, M. C. & Jia, X. Recreating the tumor microenvironment in a bilayer, hyaluronic acid hydrogel construct for the growth of prostate cancer spheroids. *Biomaterials* **33**, 9049-9060, doi:10.1016/j.biomaterials.2012.08.061 (2012).

145 Van Hemelryk, A. & van Weerden, W. M. Novel patient-derived 3D culture models to guide clinical decision-making in prostate cancer. *Current Opinion in Endocrine and Metabolic Research* **10**, 7-15, doi:https://doi.org/10.1016/j.coemr.2020.02.005 (2020).

146 Corrò, C., Novellasdemunt, L. & Li, V. S. W. A brief history of organoids. *American journal of physiology. Cell physiology* **319**, C151-c165, doi:10.1152/ajpcell.00120.2020 (2020).

147 Phan-Lai, V., Florczyk, S. J., Kievit, F. M., Wang, K., Gad, E., Disis, M. L. & Zhang, M. Three-dimensional scaffolds to evaluate tumor associated fibroblast-mediated suppression of breast tumor specific T cells. *Biomacromolecules* **14**, 1330-1337, doi:10.1021/bm301928u (2013).

148 Rodrigues, J., Heinrich, M. A., Teixeira, L. M. & Prakash, J. 3D In Vitro Model (R)evolution: Unveiling Tumor–Stroma Interactions. *Trends in Cancer* **7**, 249-264, doi:https://doi.org/10.1016/j.trecan.2020.10.009 (2021).

149 Yamada, K. M. & Cukierman, E. Modeling tissue morphogenesis and cancer in 3D. *Cell* **130**, 601-610, doi:10.1016/j.cell.2007.08.006 (2007).

150 Chen, L., Diao, L., Yang, Y., Yi, X., Rodriguez, B. L., Li, Y., Villalobos, P. A., Cascone, T., Liu, X., Tan, L., Lorenzi, P. L., Huang, A., Zhao, Q., Peng, D., Fradette, J. J., Peng, D. H., Ungewiss, C., Roybal, J., Tong, P., Oba, J., Skoulidis, F., Peng, W., Carter, B. W., Gay, C. M., Fan, Y., Class, C. A., Zhu, J., Rodriguez-Canales, J., Kawakami, M., Byers, L. A., Woodman, S. E., Papadimitrakopoulou, V. A., Dmitrovsky, E., Wang, J., Ullrich, S. E., Wistuba, I. I., Heymach, J. V., Qin, F. X.-F. & Gibbons, D. L. CD38-Mediated Immunosuppression as a Mechanism of Tumor Cell Escape from PD-1/PD-L1 Blockade. *Cancer Discovery*, doi:10.1158/2159-8290.Cd-17-1033 (2018).

151 Chen, L., Gibbons, D. L., Goswami, S., Cortez, M. A., Ahn, Y.-H., Byers, L. A., Zhang, X., Yi, X., Dwyer, D., Lin, W., Diao, L., Wang, J., Roybal, J. D., Patel, M., Ungewiss, C., Peng, D., Antonia, S., Mediavilla-Varela, M., Robertson, G., Jones, S., Suraokar, M., Welsh, J. W., Erez, B., Wistuba, I. I., Chen, L., Peng, D., Wang, S., Ullrich, S. E., Heymach, J. V., Kurie, J. M. & Qin, F. X.-F. Metastasis is regulated via microRNA-200/ZEB1 axis control of tumour cell PD-L1 expression and intratumoral immunosuppression. *Nature Communications* **5**, 5241, doi:10.1038/ncomms6241 https://www.nature.com/articles/ncomms6241#supplementary-information (2014).

152 Cukierman, E., Pankov, R., Stevens, D. R. & Yamada, K. M. Taking Cell-Matrix Adhesions to the Third Dimension. *Science* **294**, 1708-1712, doi:10.1126/science.1064829 (2001).

153 Cukierman, E., Pankov, R. & Yamada, K. M. Cell interactions with three-dimensional matrices. *Current Opinion in Cell Biology* **14**, 633-640, doi:https://doi.org/10.1016/S0955-0674(02)00364-2 (2002).

154 Grinnell, F. Fibroblast biology in three-dimensional collagen matrices. *Trends in Cell Biology* **13**, 264-269, doi:https://doi.org/10.1016/S0962-8924(03)00057-6 (2003).

155 Walpita, D. & Hay, E. Studying actin-dependent processes in tissue culture. *Nature Reviews Molecular Cell Biology* **3**, 137, doi:10.1038/nrm727 (2002).

156 Birgersdotter, A., Sandberg, R. & Ernberg, I. Gene expression perturbation in vitro—A growing case for three-dimensional (3D) culture systems. *Seminars in Cancer Biology* **15**, 405-412, doi:https://doi.org/10.1016/j.semcancer.2005.06.009 (2005).

157 Li, C., Kato, M., Shiue, L., Shively, J. E., Ares, M. & Lin, R.-J. Cell Type and Culture Condition–Dependent Alternative Splicing in Human Breast Cancer Cells Revealed by Splicing-Sensitive Microarrays. *Cancer Research* **66**, 1990-1999, doi:10.1158/0008-5472.can-05-2593 (2006).

158 Luca, A. C., Mersch, S., Deenen, R., Schmidt, S., Messner, I., Schäfer, K.-L., Baldus, S. E., Huckenbeck, W., Piekorz, R. P., Knoefel, W. T., Krieg, A. & Stoecklein, N. H. Impact of the 3D microenvironment on phenotype, gene expression, and EGFR inhibition of colorectal cancer cell lines. *PloS one* **8**, e59689-e59689, doi:10.1371/journal.pone.0059689 (2013).

159 Vinci, M., Gowan, S., Boxall, F., Patterson, L., Zimmermann, M., Court, W., Lomas, C., Mendiola, M., Hardisson, D. & Eccles, S. A. Advances in establishment and analysis of three-dimensional tumor spheroid-based functional assays for target validation and drug evaluation. *BMC Biology* **10**, 29, doi:10.1186/1741-7007-10-29 (2012).

160 Weaver, V. M., Lelièvre, S., Lakins, J. N., Chrenek, M. A., Jones, J. C. R., Giancotti, F., Werb, Z. & Bissell, M. J. beta4 integrin-dependent formation of polarized three-

dimensional architecture confers resistance to apoptosis in normal and malignant mammary epithelium. *Cancer cell* **2**, 205-216 (2002).

161 Blehm, B. H., Jiang, N., Kotobuki, Y. & Tanner, K. Deconstructing the role of the ECM microenvironment on drug efficacy targeting MAPK signaling in a pre-clinical platform for cutaneous melanoma. *Biomaterials* **56**, 129-139, doi:10.1016/j.biomaterials.2015.03.041 (2015).

162 Burrell, R. A. & Swanton, C. Tumour heterogeneity and the evolution of polyclonal drug resistance. *Molecular oncology* **8**, 1095-1111, doi:10.1016/j.molonc.2014.06.005 (2014).

163 Kaylan, K. B., Gentile, S. D., Milling, L. E., Bhinge, K. N., Kosari, F. & Underhill, G. H. Mapping lung tumor cell drug responses as a function of matrix context and genotype using cell microarrays. *Integrative biology : quantitative biosciences from nano to macro* **8**, 1221-1231, doi:10.1039/c6ib00179c (2016).

164 Mertens, J. C., Fingas, C. D., Christensen, J. D., Smoot, R. L., Bronk, S. F., Werneburg, N. W., Gustafson, M. P., Dietz, A. B., Roberts, L. R., Sirica, A. E. & Gores, G. J. Therapeutic effects of deleting cancer-associated fibroblasts in cholangiocarcinoma. *Cancer Res* **73**, 897-907, doi:10.1158/0008-5472.Can-12-2130 (2013).

165 Saunders, N. A., Simpson, F., Thompson, E. W., Hill, M. M., Endo-Munoz, L., Leggatt, G., Minchin, R. F. & Guminski, A. Role of intratumoural heterogeneity in cancer drug resistance: molecular and clinical perspectives. *EMBO Mol Med* **4**, 675-684, doi:10.1002/emmm.201101131 (2012).

166 Reticker-Flynn, N. E., Malta, D. F., Winslow, M. M., Lamar, J. M., Xu, M. J., Underhill, G. H., Hynes, R. O., Jacks, T. E. & Bhatia, S. N. A combinatorial extracellular matrix platform identifies cell-extracellular matrix interactions that correlate with metastasis. *Nat Commun* **3**, 1122, doi:10.1038/ncomms2128 (2012).

167 Jenkins, R. W., Aref, A. R., Lizotte, P. H., Ivanova, E., Stinson, S., Zhou, C. W., Bowden, M., Deng, J., Liu, H., Miao, D., He, M. X., Walker, W., Zhang, G., Tian, T., Cheng, C., Wei, Z., Palakurthi, S., Bittinger, M., Vitzthum, H., Kim, J. W., Merlino, A., Quinn, M., Venkataramani, C., Kaplan, J. A., Portell, A., Gokhale, P. C., Phillips, B., Smart, A., Rotem, A., Jones, R. E., Keogh, L., Anguiano, M., Stapleton, L., Jia, Z., Barzily-Rokni, M., Cañadas, I., Thai, T. C., Hammond, M. R., Vlahos, R., Wang, E. S., Zhang, H., Li, S., Hanna, G. J., Huang, W., Hoang, M. P., Piris, A., Eliane, J.-P., Stemmer-Rachamimov, A. O., Cameron, L., Su, M.-J., Shah, P., Izar, B., Thakuria, M., LeBoeuf, N. R., Rabinowits, G., Gunda, V., Parangi, S., Cleary, J. M., Miller, B. C., Kitajima, S., Thummalapalli, R., Miao, B., Barbie, T. U., Sivathanu, V., Wong, J., Richards, W. G., Bueno, R., Yoon, C. H., Miret, J., Herlyn, M., Garraway, L. A., Van Allen, E. M., Freeman, G. J., Kirschmeier, P. T., Lorch, J. H., Ott, P. A., Hodi, F. S., Flaherty, K. T., Kamm, R. D., Boland, G. M., Wong, K.-K., Dornan, D., Paweletz, C. P. & Barbie, D. A. Ex Vivo Profiling of PD-1 Blockade Using Organotypic Tumor Spheroids. *Cancer Discovery* **8**, 196-215, doi:10.1158/2159-8290.Cd-17-0833 (2018).

168 Neal, J. T., Li, X., Zhu, J., Giangarra, V., Grzeskowiak, C. L., Ju, J., Liu, I. H., Chiou, S.-H., Salahudeen, A. A., Smith, A. R., Deutsch, B. C., Liao, L., Zemek, A. J., Zhao, F., Karlsson, K., Schultz, L. M., Metzner, T. J., Nadauld, L. D., Tseng, Y.-Y., Alkhairy, S., Oh, C., Keskula, P., Mendoza-Villanueva, D., De La Vega, F. M., Kunz, P. L., Liao, J. C., Leppert, J. T., Sunwoo, J. B., Sabatti, C., Boehm, J. S., Hahn, W. C., Zheng, G. X. Y., Davis, M. M. & Kuo, C. J. Organoid Modeling of the Tumor Immune Microenvironment. *Cell* **175**, 1972-1988.e1916, doi:https://doi.org/10.1016/j.cell.2018.11.021 (2018).

169 Tam, W. L. & Weinberg, R. A. The epigenetics of epithelial-mesenchymal plasticity in cancer. *Nat Med* **19**, 1438-1449, doi:10.1038/nm.3336 (2013).

170 Thiery, J. P., Acloque, H., Huang, R. Y. & Nieto, M. A. Epithelial-mesenchymal transitions in development and disease. *Cell* **139**, 871-890, doi:10.1016/j.cell.2009.11.007 (2009).

171 Aktas, B., Tewes, M., Fehm, T., Hauch, S., Kimmig, R. & Kasimir-Bauer, S. Stem cell and epithelial-mesenchymal transition markers are frequently overexpressed in circulating tumor cells of metastatic breast cancer patients. *Breast cancer research : BCR* **11**, R46, doi:10.1186/bcr2333 (2009).

172 Gravdal, K., Halvorsen, O. J., Haukaas, S. A. & Akslen, L. A. A switch from E-cadherin to N-cadherin expression indicates epithelial to mesenchymal transition and is of strong and independent importance for the progress of prostate cancer. *Clin Cancer Res* **13**, 7003-7011, doi:10.1158/1078-0432.Ccr-07-1263 (2007).

173 Loboda, A., Nebozhyn, M. V., Watters, J. W., Buser, C. A., Shaw, P. M., Huang, P. S., Van't Veer, L., Tollenaar, R. A., Jackson, D. B., Agrawal, D., Dai, H. & Yeatman, T. J. EMT is the dominant program in human colon cancer. *BMC medical genomics* **4**, 9, doi:10.1186/1755-8794-4-9 (2011).

174 Teschendorff, A. E., Journée, M., Absil, P. A., Sepulchre, R. & Caldas, C. Elucidating the Altered Transcriptional Programs in Breast Cancer using Independent Component Analysis. *PLOS Computational Biology* **3**, e161, doi:10.1371/journal.pcbi.0030161 (2007).

175 Wellner, U., Schubert, J., Burk, U. C., Schmalhofer, O., Zhu, F., Sonntag, A., Waldvogel, B., Vannier, C., Darling, D., zur Hausen, A., Brunton, V. G., Morton, J., Sansom, O., Schüler, J., Stemmler, M. P., Herzberger, C., Hopt, U., Keck, T., Brabletz, S. & Brabletz, T. The EMT-activator ZEB1 promotes tumorigenicity by repressing stemness-inhibiting microRNAs. *Nat Cell Biol* **11**, 1487-1495, doi:10.1038/ncb1998 (2009).

176 Korpal, M., Lee, E. S., Hu, G. & Kang, Y. The miR-200 family inhibits epithelial-mesenchymal transition and cancer cell migration by direct targeting of E-cadherin

transcriptional repressors ZEB1 and ZEB2. *The Journal of biological chemistry* **283**, 14910-14914, doi:10.1074/jbc.C800074200 (2008).

177 Burk, U., Schubert, J., Wellner, U., Schmalhofer, O., Vincan, E., Spaderna, S. & Brabletz, T. A reciprocal repression between ZEB1 and members of the miR-200 family promotes EMT and invasion in cancer cells. *EMBO Rep* **9**, 582-589, doi:10.1038/embor.2008.74 (2008).

178 Manshouri, R., Coyaud, E., Kundu, S. T., Peng, D. H., Stratton, S. A., Alton, K., Bajaj, R., Fradette, J. J., Minelli, R., Peoples, M. D., Carugo, A., Chen, F., Bristow, C., Kovacs, J. J., Barton, M. C., Heffernan, T., Creighton, C. J., Raught, B. & Gibbons, D. L. ZEB1/NuRD complex suppresses TBC1D2b to stimulate E-cadherin internalization and promote metastasis in lung cancer. *Nature Communications* **10**, 5125, doi:10.1038/s41467-019-12832-z (2019).

179 Gregory, P. A., Bert, A. G., Paterson, E. L., Barry, S. C., Tsykin, A., Farshid, G., Vadas, M. A., Khew-Goodall, Y. & Goodall, G. J. The miR-200 family and miR-205 regulate epithelial to mesenchymal transition by targeting ZEB1 and SIP1. *Nat Cell Biol* **10**, 593-601, doi:10.1038/ncb1722 (2008).

180 Williams, E. D., Gao, D., Redfern, A. & Thompson, E. W. Controversies around epithelial–mesenchymal plasticity in cancer metastasis. *Nature Reviews Cancer* **19**, 716-732, doi:10.1038/s41568-019-0213-x (2019).

181 Konen, J. M., Rodriguez, B. L., Padhye, A., Ochieng, J. K., Gibson, L., Diao, L., Fowlkes, N. W., Fradette, J. J., Peng, D. H., Cardnell, R. J., Kovacs, J. J., Wang, J., Byers, L. A. & Gibbons, D. L. Dual inhibition of MEK and AXL targets tumor cell heterogeneity and prevents resistant outgrowth mediated by the epithelial-to-mesenchymal transition in NSCLC. *Cancer Res*, doi:10.1158/0008-5472.Can-20-1895 (2021).

182 Meidhof, S., Brabletz, S., Lehmann, W., Preca, B.-T., Mock, K., Ruh, M., Schüler, J., Berthold, M., Weber, A., Burk, U., Lübbert, M., Puhr, M., Culig, Z., Wellner, U., Keck,

T., Bronsert, P., Küsters, S., Hopt, U. T., Stemmler, M. P. & Brabletz, T. ZEB1-associated drug resistance in cancer cells is reversed by the class I HDAC inhibitor mocetinostat. *EMBO Mol Med* **7**, 831-847, doi:10.15252/emmm.201404396 (2015).

183 Pastushenko, I., Brisebarre, A., Sifrim, A., Fioramonti, M., Revenco, T., Boumahdi, S., Van Keymeulen, A., Brown, D., Moers, V., Lemaire, S., De Clercq, S., Minguijón, E., Balsat, C., Sokolow, Y., Dubois, C., De Cock, F., Scozzaro, S., Sopena, F., Lanas, A., D'Haene, N., Salmon, I., Marine, J.-C., Voet, T., Sotiropoulou, P. A. & Blanpain, C. Identification of the tumour transition states occurring during EMT. *Nature* **556**, 463-468, doi:10.1038/s41586-018-0040-3 (2018).

184 Gupta, P. B., Pastushenko, I., Skibinski, A., Blanpain, C. & Kuperwasser, C. Phenotypic Plasticity: Driver of Cancer Initiation, Progression, and Therapy Resistance. *Cell stem cell* **24**, 65-78, doi:10.1016/j.stem.2018.11.011 (2019).

185 Jolly, M. K., Tripathi, S. C., Jia, D., Mooney, S. M., Celiktas, M., Hanash, S. M., Mani, S. A., Pienta, K. J., Ben-Jacob, E. & Levine, H. Stability of the hybrid epithelial/mesenchymal phenotype. *Oncotarget* **7**, 27067-27084, doi:10.18632/oncotarget.8166 (2016).

186 Jolly, M. K., Boareto, M., Huang, B., Jia, D., Lu, M., Ben-Jacob, E., Onuchic, J. N. & Levine, H. Implications of the Hybrid Epithelial/Mesenchymal Phenotype in Metastasis. *Frontiers in oncology* **5**, 155, doi:10.3389/fonc.2015.00155 (2015).

187 Sharma, S. V., Haber, D. A. & Settleman, J. Cell line-based platforms to evaluate the therapeutic efficacy of candidate anticancer agents. *Nature reviews cancer* **10**, 241-253 (2010).

188 Herbst, R. S., Heymach, J. V. & Lippman, S. M. Lung cancer. *The New England journal of medicine* **359**, 1367-1380, doi:10.1056/NEJMra0802714 (2008).

189 Mascaux, C., Iannino, N., Martin, B., Paesmans, M., Berghmans, T., Dusart, M., Haller, A., Lothaire, P., Meert, A. P., Noel, S., Lafitte, J. J. & Sculier, J. P. The role of RAS oncogene in survival of patients with lung cancer: a systematic review of the

literature with meta-analysis. *British journal of cancer* **92**, 131-139, doi:10.1038/sj.bjc.6602258 (2005).

190 Cox, A. D., Fesik, S. W., Kimmelman, A. C., Luo, J. & Der, C. J. Drugging the undruggable RAS: Mission possible? *Nature reviews. Drug discovery* **13**, 828-851, doi:10.1038/nrd4389 (2014).

191 Hong, D. S., Fakih, M. G., Strickler, J. H., Desai, J., Durm, G. A., Shapiro, G. I., Falchook, G. S., Price, T. J., Sacher, A. & Denlinger, C. S. KRASG12C inhibition with sotorasib in advanced solid tumors. *New England Journal of Medicine* **383**, 1207-1217 (2020).

192 Jänne, P. A., Van Den Heuvel, M. M., Barlesi, F., Cobo, M., Mazieres, J., Crinò, L., Orlov, S., Blackhall, F., Wolf, J. & Garrido, P. Selumetinib plus docetaxel compared with docetaxel alone and progression-free survival in patients with kras-mutant advanced non–small cell lung cancer: the select-1 randomized clinical trial. *Jama* **317**, 1844-1853 (2017).

193 Singh, A., Greninger, P., Rhodes, D., Koopman, L., Violette, S., Bardeesy, N. & Settleman, J. A gene expression signature associated with "K-Ras addiction" reveals regulators of EMT and tumor cell survival. *Cancer cell* **15**, 489-500, doi:10.1016/j.ccr.2009.03.022 (2009).

194 Konen, J. M., Rodriguez, B. L., Padhye, A., Ochieng, J. K., Gibson, L., Diao, L., Fowlkes, N. W., Fradette, J. J., Peng, D. H., Cardnell, R. J., Kovacs, J. J., Wang, J., Byers, L. A. & Gibbons, D. L. Dual inhibition of MEK and AXL targets tumor cell heterogeneity and prevents resistant outgrowth mediated by the epithelial-to-mesenchymal transition in NSCLC. *Cancer Research*, canres.1895.2020, doi:10.1158/0008-5472.Can-20-1895 (2021).

195 Rubin, S. M., Sage, J. & Skotheim, J. M. Integrating Old and New Paradigms of G1/S Control. *Mol Cell* **80**, 183-192, doi:10.1016/j.molcel.2020.08.020 (2020).

196 Otto, T. & Sicinski, P. Cell cycle proteins as promising targets in cancer therapy. *Nature Reviews Cancer* **17**, 93-115, doi:10.1038/nrc.2016.138 (2017).

197 Bouclier, C., Simon, M., Laconde, G., Pellerano, M., Diot, S., Lantuejoul, S., Busser, B., Vanwonterghem, L., Vollaire, J., Josserand, V., Legrand, B., Coll, J.-L., Amblard, M., Hurbin, A. & Morris, M. C. Stapled peptide targeting the CDK4/Cyclin D interface combined with Abemaciclib inhibits KRAS mutant lung cancer growth. *Theranostics* **10**, 2008-2028, doi:10.7150/thno.40971 (2020).

198 Esteban-Burgos, L., Wang, H., Nieto, P., Zheng, J., Blanco-Aparicio, C., Varela, C., Gómez-López, G., Fernández-García, F., Sanclemente, M., Guerra, C., Drosten, M., Galán, J., Caleiras, E., Martínez-Torrecuadrada, J., Fajas, L., Peng, S.-B., Santamaría, D., Musteanu, M. & Barbacid, M. Tumor regression and resistance mechanisms upon CDK4 and RAF1 inactivation in KRAS/P53 mutant lung adenocarcinomas. *Proceedings of the National Academy of Sciences* **117**, 24415-24426, doi:10.1073/pnas.2002520117 (2020).

199 Puyol, M., Martín, A., Dubus, P., Mulero, F., Pizcueta, P., Khan, G., Guerra, C., Santamaría, D. & Barbacid, M. A synthetic lethal interaction between K-Ras oncogenes and Cdk4 unveils a therapeutic strategy for non-small cell lung carcinoma. *Cancer cell* **18**, 63-73, doi:10.1016/j.ccr.2010.05.025 (2010).

200 Nilsson, M. B., Sun, H., Robichaux, J., Pfeifer, M., McDermott, U., Travers, J., Diao, L., Xi, Y., Tong, P., Shen, L., Hofstad, M., Kawakami, M., Le, X., Liu, X., Fan, Y., Poteete, A., Hu, L., Negrao, M. V., Tran, H., Dmitrovsky, E., Peng, D., Gibbons, D. L., Wang, J. & Heymach, J. V. A YAP/FOXM1 axis mediates EMT-associated EGFR inhibitor resistance and increased expression of spindle assembly checkpoint components. *Sci Transl Med* **12**, doi:10.1126/scitranslmed.aaz4589 (2020).

201 Byers, L. A., Diao, L., Wang, J., Saintigny, P., Girard, L., Peyton, M., Shen, L., Fan, Y., Giri, U., Tumula, P. K., Nilsson, M. B., Gudikote, J., Tran, H., Cardnell, R. J., Bearss, D. J., Warner, S. L., Foulks, J. M., Kanner, S. B., Gandhi, V., Krett, N.,

Rosen, S. T., Kim, E. S., Herbst, R. S., Blumenschein, G. R., Lee, J. J., Lippman, S. M., Ang, K. K., Mills, G. B., Hong, W. K., Weinstein, J. N., Wistuba, II, Coombes, K. R., Minna, J. D. & Heymach, J. V. An epithelial-mesenchymal transition gene signature predicts resistance to EGFR and PI3K inhibitors and identifies Axl as a therapeutic target for overcoming EGFR inhibitor resistance. *Clin Cancer Res* **19**, 279-290, doi:10.1158/1078-0432.CCR-12-1558 (2013).

202 Chen, Y., Terajima, M., Yang, Y., Sun, L., Ahn, Y.-H., Pankova, D., Puperi, D. S., Watanabe, T., Kim, M. P. & Blackmon, S. H. Lysyl hydroxylase 2 induces a collagen cross-link switch in tumor stroma. *The Journal of clinical investigation* **125**, 1147-1162 (2015).

203 Chen, Y., Lu, X., Montoya-Durango, D. E., Liu, Y.-H., Dean, K. C., Darling, D. S., Kaplan, H. J., Dean, D. C., Gao, L. & Liu, Y. ZEB1 regulates multiple oncogenic components involved in uveal melanoma progression. *Scientific reports* **7**, 1-14 (2017).

204 Bisteau, X., Paternot, S., Colleoni, B., Ecker, K., Coulonval, K., De Groote, P., Declercq, W., Hengst, L. & Roger, P. P. CDK4 T172 phosphorylation is central in a CDK7-dependent bidirectional CDK4/CDK2 interplay mediated by p21 phosphorylation at the restriction point. *PLoS genetics* **9** (2013).

205 Padhye, A., Ungewiss, C., Fradette, J. J., Rodriguez, B. L., Albritton, J. L., Miller, J. S. & Gibbons, D. L. A novel ex vivo tumor system identifies Src-mediated invasion and metastasis in mesenchymal tumor cells in non-small cell lung cancer. *Scientific reports* **9**, 1-13 (2019).

206 Lang, G. A., Iwakuma, T., Suh, Y.-A., Liu, G., Rao, V. A., Parant, J. M., Valentin-Vega, Y. A., Terzian, T., Caldwell, L. C. & Strong, L. C. Gain of function of a p53 hot spot mutation in a mouse model of Li-Fraumeni syndrome. *Cell* **119**, 861-872 (2004).

207 Zhang, Y., Xiong, S., Liu, B., Pant, V., Celii, F., Chau, G., Elizondo-Fraire, A. C., Yang, P., You, M. J., El-Naggar, A. K., Navin, N. E. & Lozano, G. Somatic Trp53 mutations differentially drive breast cancer and evolution of metastases. *Nature Communications* **9**, 3953, doi:10.1038/s41467-018-06146-9 (2018).

208 Lozano, G. Mouse models of p53 functions. *Cold Spring Harb Perspect Biol* **2**, a001115-a001115, doi:10.1101/cshperspect.a001115 (2010).

209 Sherr, C. J. & Roberts, J. M. CDK inhibitors: positive and negative regulators of G1-phase progression. *Genes & development* **13**, 1501-1512 (1999).

210 Walter, D. M., Yates, T. J., Ruiz-Torres, M., Kim-Kiselak, C., Gudiel, A. A., Deshpande, C., Wang, W. Z., Cicchini, M., Stokes, K. L., Tobias, J. W., Buza, E. & Feldser, D. M. RB constrains lineage fidelity and multiple stages of tumour progression and metastasis. *Nature* **569**, 423-427, doi:10.1038/s41586-019-1172-9 (2019).

211 Tarasewicz, E., Hamdan, R., Straehla, J., Hardy, A., Nunez, O., Zelivianski, S., Dokic, D. & Jeruss, J. S. CDK4 inhibition and doxorubicin mediate breast cancer cell apoptosis through Smad3 and survivin. *Cancer biology & therapy* **15**, 1301-1311, doi:10.4161/cbt.29693 (2014).

212 Zelivianski, S., Cooley, A., Kall, R. & Jeruss, J. S. Cyclin-dependent kinase 4-mediated phosphorylation inhibits Smad3 activity in cyclin D-overexpressing breast cancer cells. *Mol Cancer Res* **8**, 1375-1387, doi:10.1158/1541-7786.Mcr-09-0537 (2010).

213 Liu, F. & Korc, M. Cdk4/6 inhibition induces epithelial-mesenchymal transition and enhances invasiveness in pancreatic cancer cells. *Mol Cancer Ther* **11**, 2138-2148, doi:10.1158/1535-7163.Mct-12-0562 (2012).

214 Rencuzogulları, O., Yerlikaya, P. O., Gürkan, A., Arısan, E. D. & Telci, D. Palbociclib, a selective CDK4/6 inhibitor, restricts cell survival and epithelial-

mesenchymal transition in Panc-1 and MiaPaCa-2 pancreatic cancer cells. *Journal of cellular biochemistry* **121**, 508-523, doi:10.1002/jcb.29249 (2020).

215 Lee, M. S., Helms, T. L., Feng, N., Gay, J., Chang, Q. E., Tian, F., Wu, J. Y., Toniatti, C., Heffernan, T. P., Powis, G., Kwong, L. N. & Kopetz, S. Efficacy of the combination of MEK and CDK4/6 inhibitors in vitro and in vivo in KRAS mutant colorectal cancer models. *Oncotarget* **7**, 39595-39608, doi:10.18632/oncotarget.9153 (2016).

216 Al Bitar, S. & Gali-Muhtasib, H. The Role of the Cyclin Dependent Kinase Inhibitor p21(cip1/waf1) in Targeting Cancer: Molecular Mechanisms and Novel Therapeutics. *Cancers (Basel)* **11**, 1475, doi:10.3390/cancers11101475 (2019).

217 Xiong, Y., Hannon, G. J., Zhang, H., Casso, D., Kobayashi, R. & Beach, D. p21 is a universal inhibitor of cyclin kinases. *Nature* **366**, 701-704, doi:10.1038/366701a0 (1993).

218 Kreis, N. N., Louwen, F. & Yuan, J. The Multifaceted p21 (Cip1/Waf1/CDKN1A) in Cell Differentiation, Migration and Cancer Therapy. *Cancers (Basel)* **11**, doi:10.3390/cancers11091220 (2019).

219 Guiley, K. Z., Stevenson, J. W., Lou, K., Barkovich, K. J., Kumarasamy, V., Wijeratne, T. U., Bunch, K. L., Tripathi, S., Knudsen, E. S. & Witkiewicz, A. K. p27 allosterically activates cyclin-dependent kinase 4 and antagonizes palbociclib inhibition. *Science* **366** (2019).

220 Lolli, G. & Johnson, L. N. CAK-Cyclin-dependent Activating Kinase: a key kinase in cell cycle control and a target for drugs? *Cell Cycle* **4**, 572-577 (2005).

221 Bockstaele, L., Kooken, H., Libert, F., Paternot, S., Dumont, J. E., de Launoit, Y., Roger, P. P. & Coulonval, K. Regulated activating Thr172 phosphorylation of cyclin-dependent kinase 4(CDK4): its relationship with cyclins and CDK "inhibitors". *Mol Cell Biol* **26**, 5070-5085, doi:10.1128/MCB.02006-05 (2006).

222 Raspé, E., Coulonval, K., Pita, J. M., Paternot, S., Rothé, F., Twyffels, L., Brohée, S., Craciun, L., Larsimont, D., Kruys, V., Sandras, F., Salmon, I., Van Laere, S., Piccart, M., Ignatiadis, M., Sotiriou, C. & Roger, P. P. CDK4 phosphorylation status and a linked gene expression profile predict sensitivity to palbociclib. *EMBO Mol Med* **9**, 1052-1066, doi:https://doi.org/10.15252/emmm.201607084 (2017).

223 Rubin, S. M. Deciphering the retinoblastoma protein phosphorylation code. *Trends Biochem Sci* **38**, 12-19, doi:10.1016/j.tibs.2012.10.007 (2013).

224 Wilson, A. J., Byun, D. S., Popova, N., Murray, L. B., L'Italien, K., Sowa, Y., Arango, D., Velcich, A., Augenlicht, L. H. & Mariadason, J. M. Histone deacetylase 3 (HDAC3) and other class I HDACs regulate colon cell maturation and p21 expression and are deregulated in human colon cancer. *The Journal of biological chemistry* **281**, 13548-13558, doi:10.1074/jbc.M510023200 (2006).

225 Fu, R., Han, C. F., Ni, T., Di, L., Liu, L. J., Lv, W. C., Bi, Y. R., Jiang, N., He, Y., Li, H. M., Wang, S., Xie, H., Chen, B. A., Wang, X. S., Weiss, S. J., Lu, T., Guo, Q. L. & Wu, Z. Q. A ZEB1/p53 signaling axis in stromal fibroblasts promotes mammary epithelial tumours. *Nat Commun* **10**, 3210, doi:10.1038/s41467-019-11278-7 (2019).

226 Macleod, K. F., Sherry, N., Hannon, G., Beach, D., Tokino, T., Kinzler, K., Vogelstein, B. & Jacks, T. p53-dependent and independent expression of p21 during cell growth, differentiation, and DNA damage. *Genes Dev* **9**, 935-944, doi:10.1101/gad.9.8.935 (1995).

227 Sherr, C. J. & McCormick, F. The RB and p53 pathways in cancer. *Cancer cell* **2**, 103-112, doi:10.1016/s1535-6108(02)00102-2 (2002).

228 Otto, T. & Sicinski, P. Cell cycle proteins as promising targets in cancer therapy. *Nat Rev Cancer* **17**, 93-115, doi:10.1038/nrc.2016.138 (2017).

229 Cadoo, K. A., Gucalp, A. & Traina, T. A. Palbociclib: an evidence-based review of its potential in the treatment of breast cancer. *Breast Cancer (Dove Med Press)* **6**, 123-133, doi:10.2147/BCTT.S46725 (2014).

230 Garrido-Castro, A. C. & Goel, S. CDK4/6 Inhibition in Breast Cancer: Mechanisms of Response and Treatment Failure. *Current breast cancer reports* **9**, 26-33, doi:10.1007/s12609-017-0232-0 (2017).

231 Patnaik, A., Rosen, L. S., Tolaney, S. M., Tolcher, A. W., Goldman, J. W., Gandhi, L., Papadopoulos, K. P., Beeram, M., Rasco, D. W., Hilton, J. F., Nasir, A., Beckmann, R. P., Schade, A. E., Fulford, A. D., Nguyen, T. S., Martinez, R., Kulanthaivel, P., Li, L. Q., Frenzel, M., Cronier, D. M., Chan, E. M., Flaherty, K. T., Wen, P. Y. & Shapiro, G. I. Efficacy and Safety of Abemaciclib, an Inhibitor of CDK4 and CDK6, for Patients with Breast Cancer, Non–Small Cell Lung Cancer, and Other Solid Tumors. *Cancer Discovery* **6**, 740-753, doi:10.1158/2159-8290.Cd-16-0095 (2016).

232 Johnston, S. R. D., Harbeck, N., Hegg, R., Toi, M., Martin, M., Shao, Z. M., Zhang, Q. Y., Rodriguez, J. L. M., Campone, M., Hamilton, E., Sohn, J., Guarneri, V., Okada, M., Boyle, F., Neven, P., Cortés, J., Huober, J., Wardley, A., Tolaney, S. M., Cicin, I., Smith, I. C., Frenzel, M., Headley, D., Wei, R., Antonio, B. S., Hulstijn, M., Cox, J., O'Shaughnessy, J., Rastogi, P., Members, o. b. o. t. m. C. & Investigators. Abemaciclib Combined With Endocrine Therapy for the Adjuvant Treatment of HR+, HER2−, Node-Positive, High-Risk, Early Breast Cancer (monarchE). *Journal of Clinical Oncology* **38**, 3987-3998, doi:10.1200/jco.20.02514 (2020).

233 Gopalan, P. K., Pinder, M. C., Chiappori, A., Ivey, A. M., Villegas, A. G. & Kaye, F. J. A phase II clinical trial of the CDK 4/6 inhibitor palbociclib (PD 0332991) in previously treated, advanced non-small cell lung cancer (NSCLC) patients with inactivated CDKN2A. *Journal of Clinical Oncology* **32**, 8077-8077, doi:10.1200/jco.2014.32.15_suppl.8077 (2014).

234 Zhou, J., Zhang, S., Chen, X., Zheng, X., Yao, Y., Lu, G. & Zhou, J. Palbociclib, a selective CDK4/6 inhibitor, enhances the effect of selumetinib in RAS-driven non-

small cell lung cancer. *Cancer Letters* **408**, 130-137, doi:https://doi.org/10.1016/j.canlet.2017.08.031 (2017).

235 Kim, H. S., Jung, M., Kang, H. N., Kim, H., Park, C. W., Kim, S. M., Shin, S. J., Kim, S. H., Kim, S. G., Kim, E. K., Yun, M. R., Zheng, Z., Chung, K. Y., Greenbowe, J., Ali, S. M., Kim, T. M. & Cho, B. C. Oncogenic BRAF fusions in mucosal melanomas activate the MAPK pathway and are sensitive to MEK/PI3K inhibition or MEK/CDK4/6 inhibition. *Oncogene* **36**, 3334-3345, doi:10.1038/onc.2016.486 (2017).

236 Kwong, L. N., Costello, J. C., Liu, H., Jiang, S., Helms, T. L., Langsdorf, A. E., Jakubosky, D., Genovese, G., Muller, F. L., Jeong, J. H., Bender, R. P., Chu, G. C., Flaherty, K. T., Wargo, J. A., Collins, J. J. & Chin, L. Oncogenic NRAS signaling differentially regulates survival and proliferation in melanoma. *Nature Medicine* **18**, 1503-1510, doi:10.1038/nm.2941 (2012).

237 Li, Z., Wang, B., Gu, S., Jiang, P., Sahu, A., Chen, C.-H., Han, T., Shi, S., Wang, X., Traugh, N., Liu, H., Liu, Y., Wu, Q., Brown, M., Xiao, T., Boland, G. M. & Shirley Liu, X. CRISPR Screens Identify Essential Cell Growth Mediators in BRAF Inhibitor-resistant Melanoma. *Genomics, Proteomics & Bioinformatics* **18**, 26-40, doi:https://doi.org/10.1016/j.gpb.2020.02.002 (2020).

238 Ramsdale, R., Jorissen, R. N., Li, F. Z., Al-Obaidi, S., Ward, T., Sheppard, K. E., Bukczynska, P. E., Young, R. J., Boyle, S. E., Shackleton, M., Bollag, G., Long, G. V., Tulchinsky, E., Rizos, H., Pearson, R. B., McArthur, G. A., Dhillon, A. S. & Ferrao, P. T. The transcription cofactor c-JUN mediates phenotype switching and BRAF inhibitor resistance in melanoma. *Science Signaling* **8**, ra82-ra82, doi:10.1126/scisignal.aab1111 (2015).

239 Sosman, J. A., Kittaneh, M., Lolkema, M. P. J. K., Postow, M. A., Schwartz, G., Franklin, C., Matano, A., Bhansali, S., Parasuraman, S. & Kim, K. A phase 1b/2 study of LEE011 in combination with binimetinib (MEK162) in patients with NRAS-

mutant melanoma: Early encouraging clinical activity. *Journal of Clinical Oncology* **32**, 9009-9009, doi:10.1200/jco.2014.32.15_suppl.9009 (2014).

240 Scheiblecker, L., Kollmann, K. & Sexl, V. CDK4/6 and MAPK-Crosstalk as Opportunity for Cancer Treatment. *Pharmaceuticals (Basel, Switzerland)* **13**, doi:10.3390/ph13120418 (2020).

241 Infante, J. R., Fecher, L. A., Falchook, G. S., Nallapareddy, S., Gordon, M. S., Becerra, C., DeMarini, D. J., Cox, D. S., Xu, Y. & Morris, S. R. Safety, pharmacokinetic, pharmacodynamic, and efficacy data for the oral MEK inhibitor trametinib: a phase 1 dose-escalation trial. *The lancet oncology* **13**, 773-781 (2012).

242 O'Hara, M. H., Edmonds, C., Farwell, M., Perini, R. F., Pryma, D. A., Teitelbaum, U. R., Giantonio, B. J., Damjanov, N., Lal, P. & Feldman, M. D. (American Society of Clinical Oncology, 2015).

243 Ziemke, E. K., Dosch, J. S., Maust, J. D., Shettigar, A., Sen, A., Welling, T. H., Hardiman, K. M. & Sebolt-Leopold, J. S. Sensitivity of KRAS-mutant colorectal cancers to combination therapy that cotargets MEK and CDK4/6. *Clinical Cancer Research* **22**, 405-414 (2016).

244 Yadav, V., Burke, T. F., Huber, L., Van Horn, R. D., Zhang, Y., Buchanan, S. G., Chan, E. M., Starling, J. J., Beckmann, R. P. & Peng, S.-B. The CDK4/6 Inhibitor LY2835219 Overcomes Vemurafenib Resistance Resulting from MAPK Reactivation and Cyclin D1 Upregulation. *Molecular Cancer Therapeutics* **13**, 2253-2263, doi:10.1158/1535-7163.Mct-14-0257 (2014).

245 de Leeuw, R., McNair, C., Schiewer, M. J., Neupane, N. P., Brand, L. J., Augello, M. A., Li, Z., Cheng, L. C., Yoshida, A., Courtney, S. M., Hazard, E. S., Hardiman, G., Hussain, M. H., Diehl, J. A., Drake, J. M., Kelly, W. K. & Knudsen, K. E. MAPK Reliance via Acquired CDK4/6 Inhibitor Resistance in Cancer. *Clin Cancer Res* **24**, 4201-4214, doi:10.1158/1078-0432.Ccr-18-0410 (2018).

246 Chow, Y. H., Zhu, X. D., Liu, L., Schwartz, B. R., Huang, X. Z., Harlan, J. M. & Schnapp, L. M. Role of Cdk4 in lymphocyte function and allergen response. *Cell Cycle* **9**, 4922-4930 (2010).

247 Goel, S., DeCristo, M. J., Watt, A. C., BrinJones, H., Sceneay, J., Li, B. B., Khan, N., Ubellacker, J. M., Xie, S., Metzger-Filho, O., Hoog, J., Ellis, M. J., Ma, C. X., Ramm, S., Krop, I. E., Winer, E. P., Roberts, T. M., Kim, H.-J., McAllister, S. S. & Zhao, J. J. CDK4/6 inhibition triggers anti-tumour immunity. *Nature* **548**, 471-475, doi:10.1038/nature23465 (2017).

248 Deng, J., Wang, E. S., Jenkins, R. W., Li, S., Dries, R., Yates, K., Chhabra, S., Huang, W., Liu, H., Aref, A. R., Ivanova, E., Paweletz, C. P., Bowden, M., Zhou, C. W., Herter-Sprie, G. S., Sorrentino, J. A., Bisi, J. E., Lizotte, P. H., Merlino, A. A., Quinn, M. M., Bufe, L. E., Yang, A., Zhang, Y., Zhang, H., Gao, P., Chen, T., Cavanaugh, M. E., Rode, A. J., Haines, E., Roberts, P. J., Strum, J. C., Richards, W. G., Lorch, J. H., Parangi, S., Gunda, V., Boland, G. M., Bueno, R., Palakurthi, S., Freeman, G. J., Ritz, J., Haining, W. N., Sharpless, N. E., Arthanari, H., Shapiro, G. I., Barbie, D. A., Gray, N. S. & Wong, K.-K. CDK4/6 Inhibition Augments Antitumor Immunity by Enhancing T-cell Activation. *Cancer Discovery* **8**, 216-233, doi:10.1158/2159-8290.Cd-17-0915 (2018).

249 Zhang, J., Bu, X., Wang, H., Zhu, Y., Geng, Y., Nihira, N. T., Tan, Y., Ci, Y., Wu, F., Dai, X., Guo, J., Huang, Y.-H., Fan, C., Ren, S., Sun, Y., Freeman, G. J., Sicinski, P. & Wei, W. Cyclin D–CDK4 kinase destabilizes PD-L1 via cullin 3–SPOP to control cancer immune surveillance. *Nature* **553**, 91-95, doi:10.1038/nature25015 (2018).

250 Jin, X., Ding, D., Yan, Y., Li, H., Wang, B., Ma, L., Ye, Z., Ma, T., Wu, Q., Rodrigues, D. N., Kohli, M., Jimenez, R., Wang, L., Goodrich, D. W., de Bono, J., Dong, H., Wu, H., Zhu, R. & Huang, H. Phosphorylated RB Promotes Cancer Immunity by Inhibiting NF-κB Activation and PD-L1 Expression. *Molecular Cell* **73**, 22-35.e26, doi:https://doi.org/10.1016/j.molcel.2018.10.034 (2019).

251 Ruscetti, M., Leibold, J., Bott, M. J., Fennell, M., Kulick, A., Salgado, N. R., Chen, C.-C., Ho, Y.-J., Sanchez-Rivera, F. J., Feucht, J., Baslan, T., Tian, S., Chen, H.-A., Romesser, P. B., Poirier, J. T., Rudin, C. M., de Stanchina, E., Manchado, E., Sherr, C. J. & Lowe, S. W. NK cell-mediated cytotoxicity contributes to tumor control by a cytostatic drug combination. *Science (New York, N.Y.)* **362**, 1416-1422, doi:10.1126/science.aas9090 (2018).

252 Corrò, C., Novellasdemunt, L. & Li, V. S. W. A brief history of organoids. *American Journal of Physiology-Cell Physiology* **319**, C151-C165, doi:10.1152/ajpcell.00120.2020 (2020).

253 Zhang, T., Guo, L., Creighton, C. J., Lu, Q., Gibbons, D. L., Yi, E. S., Deng, B., Molina, J. R., Sun, Z., Yang, P. & Yang, Y. A genetic cell context-dependent role for ZEB1 in lung cancer. *Nature Communications* **7**, 12231, doi:10.1038/ncomms12231 (2016).

254 Larsen, J. E., Nathan, V., Osborne, J. K., Farrow, R. K., Deb, D., Sullivan, J. P., Dospoy, P. D., Augustyn, A., Hight, S. K., Sato, M., Girard, L., Behrens, C., Wistuba, I. I., Gazdar, A. F., Hayward, N. K. & Minna, J. D. ZEB1 drives epithelial-to-mesenchymal transition in lung cancer. *The Journal of clinical investigation* **126**, 3219-3235, doi:10.1172/JCI76725 (2016).

255 Zhang, Y., Xu, L., Li, A. & Han, X. The roles of ZEB1 in tumorigenic progression and epigenetic modifications. *Biomedicine & Pharmacotherapy* **110**, 400-408, doi:https://doi.org/10.1016/j.biopha.2018.11.112 (2019).

256 Xiao, D. & He, J. Epithelial mesenchymal transition and lung cancer. *Journal of thoracic disease* **2**, 154-159, doi:10.3978/j.issn.2072-1439.2010.02.03.7 (2010).

257 Karacosta, L. G., Anchang, B., Ignatiadis, N., Kimmey, S. C., Benson, J. A., Shrager, J. B., Tibshirani, R., Bendall, S. C. & Plevritis, S. K. Mapping lung cancer epithelial-mesenchymal transition states and trajectories with single-cell resolution. *Nature Communications* **10**, 5587, doi:10.1038/s41467-019-13441-6 (2019).

258 Ben-David, U., Ha, G., Tseng, Y. Y., Greenwald, N. F., Oh, C., Shih, J., McFarland, J. M., Wong, B., Boehm, J. S., Beroukhim, R. & Golub, T. R. Patient-derived xenografts undergo mouse-specific tumor evolution. *Nature genetics* **49**, 1567-1575, doi:10.1038/ng.3967 (2017).

259 Walsh, N. C., Kenney, L. L., Jangalwe, S., Aryee, K.-E., Greiner, D. L., Brehm, M. A. & Shultz, L. D. Humanized Mouse Models of Clinical Disease. *Annu Rev Pathol* **12**, 187-215, doi:10.1146/annurev-pathol-052016-100332 (2017).

260 Morgan, K. M., Riedlinger, G. M., Rosenfeld, J., Ganesan, S. & Pine, S. R. Patient-Derived Xenograft Models of Non-Small Cell Lung Cancer and Their Potential Utility in Personalized Medicine. *Frontiers in oncology* **7**, doi:10.3389/fonc.2017.00002 (2017).

261 Bleijs, M., van de Wetering, M., Clevers, H. & Drost, J. Xenograft and organoid model systems in cancer research. *The EMBO Journal* **38**, e101654, doi:https://doi.org/10.15252/embj.2019101654 (2019).

262 Neal, J. T., Li, X., Zhu, J., Giangarra, V., Grzeskowiak, C. L., Ju, J., Liu, I. H., Chiou, S. H., Salahudeen, A. A., Smith, A. R., Deutsch, B. C., Liao, L., Zemek, A. J., Zhao, F., Karlsson, K., Schultz, L. M., Metzner, T. J., Nadauld, L. D., Tseng, Y. Y., Alkhairy, S., Oh, C., Keskula, P., Mendoza-Villanueva, D., De La Vega, F. M., Kunz, P. L., Liao, J. C., Leppert, J. T., Sunwoo, J. B., Sabatti, C., Boehm, J. S., Hahn, W. C., Zheng, G. X. Y., Davis, M. M. & Kuo, C. J. Organoid Modeling of the Tumor Immune Microenvironment. *Cell* **175**, 1972-1988.e1916, doi:10.1016/j.cell.2018.11.021 (2018).

263 Granat, L. M., Kambhampati, O., Klosek, S., Niedzwecki, B., Parsa, K. & Zhang, D. The promises and challenges of patient-derived tumor organoids in drug development and precision oncology. *Animal models and experimental medicine* **2**, 150-161, doi:10.1002/ame2.12077 (2019).

264 Gill, B. J., Gibbons, D. L., Roudsari, L. C., Saik, J. E., Rizvi, Z. H., Roybal, J. D., Kurie, J. M. & West, J. L. A synthetic matrix with independently tunable biochemistry and mechanical properties to study epithelial morphogenesis and EMT in a lung adenocarcinoma model. *Cancer Res* **72**, 6013-6023, doi:10.1158/0008-5472.Can-12-0895 (2012).

265 Schliekelman, M. J., Gibbons, D. L., Faca, V. M., Creighton, C. J., Rizvi, Z. H., Zhang, Q., Wong, C. H., Wang, H., Ungewiss, C., Ahn, Y. H., Shin, D. H., Kurie, J. M. & Hanash, S. M. Targets of the tumor suppressor miR-200 in regulation of the epithelial-mesenchymal transition in cancer. *Cancer Res* **71**, 7670-7682, doi:10.1158/0008-5472.Can-11-0964 (2011).

266 Wang, J. P. & Hielscher, A. Fibronectin: How Its Aberrant Expression in Tumors May Improve Therapeutic Targeting. *J Cancer* **8**, 674-682, doi:10.7150/jca.16901 (2017).

267 Efthymiou, G., Saint, A., Ruff, M., Rekad, Z., Ciais, D. & Van Obberghen-Schilling, E. Shaping Up the Tumor Microenvironment With Cellular Fibronectin. *Frontiers in oncology* **10**, doi:10.3389/fonc.2020.00641 (2020).

268 Parker, A. L. & Cox, T. R. The Role of the ECM in Lung Cancer Dormancy and Outgrowth. *Frontiers in oncology* **10**, doi:10.3389/fonc.2020.01766 (2020).

269 Chang, C.-J., Chao, C.-H., Xia, W., Yang, J.-Y., Xiong, Y., Li, C.-W., Yu, W.-H., Rehman, S. K., Hsu, J. L., Lee, H.-H., Liu, M., Chen, C.-T., Yu, D. & Hung, M.-C. p53 regulates epithelial-mesenchymal transition and stem cell properties through modulating miRNAs. *Nature cell biology* **13**, 317-323, doi:10.1038/ncb2173 (2011).

270 Dong, P., Karaayvaz, M., Jia, N., Kaneuchi, M., Hamada, J., Watari, H., Sudo, S., Ju, J. & Sakuragi, N. Mutant p53 gain-of-function induces epithelial–mesenchymal transition through modulation of the miR-130b–ZEB1 axis. *Oncogene* **32**, 3286-3295, doi:10.1038/onc.2012.334 (2013).

271 Peters, S., Mok, T., Passaro, A. & Jänne, P. A. The Promising Evolution of Targeted Therapeutic Strategies in Cancer. *Cancer Discovery* **11**, 810-814, doi:10.1158/2159-8290.Cd-21-0124 (2021).

272 Álvarez-Fernández, M. & Malumbres, M. Mechanisms of Sensitivity and Resistance to CDK4/6 Inhibition. *Cancer cell* **37**, 514-529, doi:https://doi.org/10.1016/j.ccell.2020.03.010 (2020).

273 Kubli, S. P., Berger, T., Araujo, D. V., Siu, L. L. & Mak, T. W. Beyond immune checkpoint blockade: emerging immunological strategies. *Nature reviews. Drug discovery*, doi:10.1038/s41573-021-00155-y (2021).

274 Peng, D. H., Rodriguez, B. L., Diao, L., Gaudreau, P.-O., Padhye, A., Konen, J. M., Ochieng, J. K., Class, C. A., Fradette, J. J., Gibson, L., Chen, L., Wang, J., Byers, L. A. & Gibbons, D. L. Th17 cells contribute to combination MEK inhibitor and anti-PD-L1 therapy resistance in KRAS/p53 mutant lung cancers. *Nature Communications* **12**, 2606, doi:10.1038/s41467-021-22875-w (2021).

275 Knudsen, E. S., Kumarasamy, V., Chung, S., Ruiz, A., Vail, P., Tzetzo, S., Wu, J., Nambiar, R., Sivinski, J., Chauhan, S. S., Seshadri, M., Abrams, S. I., Wang, J. & Witkiewicz, A. K. Targeting dual signalling pathways in concert with immune checkpoints for the treatment of pancreatic cancer. *Gut* **70**, 127-138, doi:10.1136/gutjnl-2020-321000 (2021).

276 Teh, J. L. F., Erkes, D. A., Cheng, P. F., Tiago, M., Wilski, N. A., Field, C. O., Chervoneva, I., Levesque, M. P., Xu, X., Dummer, R. & Aplin, A. E. Activation of CD8⁺ T Cells Contributes to Antitumor Effects of CDK4/6 Inhibitors plus MEK Inhibitors. *Cancer Immunology Research* **8**, 1114-1121, doi:10.1158/2326-6066.Cir-19-0743 (2020).

277 Lelliott, E. J., Mangiola, S., Ramsbottom, K. M., Zethoven, M., Lim, L., Lau, P. K. H., Oliver, A. J., Martelotto, L. G., Kirby, L., Martin, C., Patel, R. P., Slater, A., Cullinane, C., Papenfuss, A. T., Haynes, N. M., McArthur, G. A., Oliaro, J. & Sheppard, K. E.

Combined BRAF, MEK, and CDK4/6 Inhibition Depletes Intratumoral Immune-Potentiating Myeloid Populations in Melanoma. *Cancer Immunology Research* **9**, 136-146, doi:10.1158/2326-6066.Cir-20-0401 (2021).

278 Settleman, J., Neto, J. M. F. & Bernards, R. Thinking Differently about Cancer Treatment Regimens. *Cancer Discovery* **11**, 1016-1023, doi:10.1158/2159-8290.Cd-20-1187 (2021).

VITA

Aparna Padhye was born in Lucknow, Uttar Pradesh, India on October 22, 1990, the daughter of Shripad Padhye and Sandhya Padhye. After completing her high school at Seth M.R. Jaipuria School, Lucknow, India in 2008, she entered G.S.V.M. Medical College, Kanpur. She received Bachelor of Medicine and Bachelor of Surgery (MBBS) degree in 2014. She then entered The University of Texas MD Anderson Cancer Center UTHealth Graduate School of Biomedical Sciences in Fall 2014 to pursue Ph.D. in Experimental Therapeutics.

Appendices

Table 12. Quality control metrics for the Kinome shRNA screens

	393P					344P				
	in-vivo			in-vitro		in-vivo			in-vitro	
reagent	1	2	3	1	2	1	2	3	1	2
LUC_10041	1.38	0.39	-0.02	3.72	2.88	0.31	1.16	4.12	0.24	0.74
LUC_10042	-0.28	2.36	3.94	-1.22	2.9	-0.61	-6.96	0.67	0.88	0.41
LUC_10043	-0.02	0.09	-0.99	1.86	3.15	0.71	1.05	0.8	0.41	0.17
LUC_10044	2.85	0.71	1.06	1.09	4.05	-0.32	-0.01	1.59	0.84	1.51
LUC_10045	0.42	0.07	0.49	1.03	1.27	1.4	4.17	0	0.55	0.49
LUC_10046	-0.57	-1.06	-0.2	-1.01	-4.08	0.16	3.94	5.75	-0.38	1.14
LUC_10047	-0.34	0.06	0.21	-1.19	-2.85	0.45	1.81	2.79	3.95	3.98
LUC_10048	2.32	2.82	0.34	3.24	2.22	-0.12	3.86	1.17	1.13	0.68
LUC_10049	0.58	0.97	1.98	0.9	2.21	1.72	1.99	0.18	0.67	0.49
LUC_10050	-1.72	-0.38	-1.06	-1.63	1.06	-11.82	-0.14	-5.76	0.4	0.08
LUC_10051	0.73	4.01	1.21	3.5	2.2	-0.06	0.55	-0.66	-0.11	0.5
LUC_10052	3.63	-1.99	0.52	3.37	1.95	-0.58	1.84	-1.68	0.97	0.87
LUC_10053	0.36	0.7	2.6	3.35	3.99	0.59	-0.62	-9.14	0.95	0.16
LUC_10054	-1.47	0.69	-0.44	-1.81	3.4	-1.25	0.53	-12.03	0.11	0.23
LUC_10055	-1.3	-0.68	-0.49	-0.44	-0.99	0.16	0.59	0.24	1.81	1.67
LUC_10056	-2.53	-3.06	-0.09	-0.69	-1.69	-11.55	-11.55	-11.55	-1.36	-2.68
LUC_10057	1.28	0.7	-1.12	0.07	0.75	0.36	0.42	-0.87	0.34	0.39
LUC_10058	-0.74	-10.09	-2.44	-4.1	-0.78	0.43	0.29	-10.58	-6.65	-10.58
LUC_10059	-0.02	-1.96	-1.36	-4.1	-4.93	0.72	-12.24	-0.3	-3.95	-4.25
LUC_10060	-1.89	-5.64	-2.07	-4.09	-4.19	-10.99	-10.99	-10.99	-10.99	-10.99
Rpl30_10001	-0.99	1.45	-2.72	-4.68	-4.75	1.67	-1.7	-0.04	-1.73	-0.26
Rpl30_10002	-2.81	-6.85	-2.84	-4.59	-5.92	-0.94	-11.57	-8.5	-1.04	-11.57
Rpl30_10003	2.72	-0.86	-2.75	-1.42	0.24	-1.28	0.33	-2.12	-4.64	-2.6
Rpl30_10004	-3.98	-1	-1.36	-0.69	-0.05	-8.09	-12.99	-12.99	-4.6	-5.72
Rpl30_10005	-4.59	-4.45	-4.55	-3.42	-4.88	-1.08	-13.05	-13.05	-13.05	-13.05
Rpl30_10006	0.14	-1.62	-2.69	-3.05	-1.94	-12.41	1.24	-12.41	-1.98	-5.41
Rpl30_10007	-1.39	-1.88	-3.38	-2.45	-1.91	-1.46	-1.44	-14.32	-0.93	-3.42
Rpl30_10008	-4.03	-4.86	-2.98	-3.95	-2.52	-1.42	-1.73	-2.76	-12.6	-5.04
Rpl30_10009	-2.2	-2	-1.2	-2.46	2.67	-1.75	-1.17	-1.15	-2.98	-2.59
Rpl30_10010	1.11	-3.03	-1.45	-4.62	-1.4	-11.93	-11.93	-7.51	-2.85	-7.36
Rpl30_10011	-3.37	-0.88	-0.81	-1.58	-1.24	-3.91	-0.71	-2.21	-2.07	-3.95
Rpl30_10012	-0.79	-10.23	-6.2	-4.48	-5.47	-0.37	-10.03	0.74	-10.03	-10.03
Rpl30_10013	-2.1	-2.79	-7.91	-4.82	-4.16	-11.51	-11.51	-11.51	-2.57	1.55
Rpl30_10014	-6.31	-1.31	-1.56	-6.23	-6.16	-1.26	-11.57	0.13	-4.59	-2.36
Rpl30_10015	-4.73	-2.52	-5.41	-3.72	-4.28	-11.85	-11.85	-11.85	-0.82	-2.19
Rpl30_10016	-2.42	-6.94	0.17	-4.55	-5.7	-12.57	-8.97	-0.58	-4.23	-5.01

Rpl30_10017	-2.78	-2.13	-3.33	1.11	-0.56	-1.21	-8.07	0.48	-2.9	-5.83
Rpl30_10018	-2.01	1.65	-6.21	-0.57	-0.82	-4.46	0.22	-10.87	-0.7	-7.47
Rpl30_10019	-3.65	-6.19	-4.08	-4.56	-3.87	-1.21	-8.41	0.06	-2.81	-2.21
Rpl30_10020	-4.31	-7.71	-2.93	0.3	-4.64	-10.75	-3.9	-10.75	-0.25	-10.75
Psma1_10021	0.48	1.8	0.46	-3.37	-2.48	0.97	2.85	3.32	0.9	1.26
Psma1_10022	0.05	0.54	0.16	-0.9	-3.02	1.72	5.68	1.73	1.07	0.74
Psma1_10023	0.67	1.09	0.55	-1.03	0.68	-1.27	0.63	0.97	1.45	1.84
Psma1_10024	-0.14	0.52	0.63	-1.45	-0.04	3.48	1.4	2.77	0.76	0.9
Psma1_10025	0.32	1.67	0.62	-0.46	-0.08	0.89	0.06	3.09	0.83	0.35
Psma1_10026	-2.71	0.77	-2.09	-5.09	-5.23	-2.62	-11.47	-11.47	-6.42	-6.66
Psma1_10027	-1.38	-1.87	-3.7	-4.41	-3.91	-0.26	1.44	-0.82	-2.51	-3.41
Psma1_10028	-1.6	-2.28	-3.82	-4.57	-2.51	-0.53	-1.47	-11.63	-11.63	-11.63
Psma1_10029	-2.94	-2.64	-1.95	-4.7	-1.94	-0.96	-0.17	-0.02	-4.07	-2.93
Psma1_10030	-5.53	-2.56	-5.78	-4.23	-4.39	-10.91	-10.91	-10.91	-10.91	-10.91
Psma1_10031	-4.04	2.34	-3.58	-2.61	-4.77	-1.23	-1.5	-13.16	-3.76	-3.89
Psma1_10032	-5.03	-3.91	-2.96	-4.66	-4.11	-1.4	-3.85	-1.65	-2.82	-2.18
Psma1_10033	-3.83	-3.54	-2.49	-2.58	-0.56	-3.57	6.82	-1.08	-3.53	-6.22
Psma1_10034	-1.81	-1.99	-7.37	-4.93	-4.59	-7.15	-11.13	0.94	-11.13	-11.13
Psma1_10035	-0.32	5.82	-0.4	0.36	-0.75	-2.96	-0.14	-1.94	-3.48	-4.76
Psma1_10036	-10.25	-10.25	-1.74	-3.73	-4.29	-11.08	-11.08	-11.08	-11.08	-11.08
Psma1_10037	-8.81	-8.81	-8.81	-4.43	-5.23	-11.15	-11.15	-11.15	-1.96	-11.15
Psma1_10038	-6.37	-6.37	-6.37	-3.65	-6.37	-10.44	-10.44	-10.44	-10.44	-10.44
Psma1_10039	-6.23	-5.79	-6.48	-4.16	-3.97	0.23	-10.7	-10.7	-10.7	-10.7
Psma1_10040	-1.85	-5.17	-3.4	-4.68	-4.3	-10.76	-10.76	-10.76	-10.76	-10.76

Table 13. Gene level dropout scores for each of the Kinome screens

model	393P				344P			
condition	nude		in-vitro.2		nude		in-vitro.2	
metric	logP	rank	logP	rank	logP	rank	logP	rank
Adrbk2	-5.86	4	-5.11	5	-5.29	1	-5.06	6
Cdk4	-4.98	7	-0.33	432	-5.04	2	-7.40	2
Csnk2a2	-1.71	101	-1.90	78	-4.36	3	-2.36	56
Dapk3	-3.43	21	-0.12	490	-4.29	4	-1.84	108
Wnk1	-2.80	40	-1.16	189	-4.23	5	-1.16	207
Rps6kc1	-1.57	117	-1.47	129	-4.07	6	-4.67	9
Btk	-0.54	368	-2.91	23	-3.90	7	-1.64	134
Rps6ka5	-1.64	106	-2.21	54	-3.90	8	-1.22	194
Kalrn	-2.86	37	-0.89	250	-3.87	9	-2.48	48
Aurka	-2.41	46	-2.72	33	-3.78	10	-5.49	4
Plk1	-5.44	6	-5.98	2	-3.68	11	-4.72	8
Hipk4	-0.18	474	-0.46	392	-3.64	12	-0.43	396
Bmpr1b	-0.70	322	-2.59	37	-3.57	13	-0.85	266
Akt1	-2.74	43	-1.44	134	-3.47	14	-1.49	156
Smg1	-2.09	70	-1.32	151	-3.46	15	-3.86	11
Stk16	-0.72	309	-0.43	403	-3.44	16	-3.28	19
Wnk2	-1.20	178	-1.04	216	-3.43	17	-3.16	21
Erbb3	-5.92	2	-4.34	6	-3.41	18	-2.64	40
Map2k5	-3.58	18	-2.47	43	-3.28	19	-5.97	3
Raf1	-5.50	5	-4.30	7	-3.28	20	-1.66	132
Flt4	-1.27	163	-2.10	62	-3.22	21	-3.69	14
Fes	-4.09	12	-2.86	27	-3.13	22	-1.64	136
Nek7	-4.06	13	-3.21	18	-3.07	23	-1.64	135
Akt3	-2.30	53	-1.67	110	-3.01	24	-0.79	286
Wnk3	-0.32	438	-0.61	335	-2.99	25	-0.97	242
Rps6ka6	-2.41	45	-3.46	14	-2.95	26	-2.17	70
Pomk	-0.48	383	-1.30	155	-2.87	27	-1.25	183
Mtor	-3.79	16	-5.49	4	-2.87	28	-2.52	45
Bub1b	-2.90	35	-3.56	12	-2.84	29	-3.62	15
Pik3cg	-0.16	482	-0.05	505	-2.74	30	-0.90	255
Stk35	-0.79	275	-1.38	143	-2.68	31	-0.77	291
Mark3	-2.31	52	-0.66	315	-2.68	32	-1.71	122

Csnk1e	-2.38	48	-2.11	59	-2.63	33	-1.61	139
Jak1	-1.65	105	-2.42	45	-2.59	34	-0.84	268
Nrbp1	-3.29	25	-1.79	92	-2.58	35	-1.67	130
Ttk	-1.32	153	-3.17	19	-2.54	36	-2.73	36
Tnik	-1.55	124	-1.85	82	-2.54	37	-0.49	378
Prkdc	-0.91	242	-0.86	257	-2.53	38	-2.02	86
Map3k7	-0.39	414	-0.04	509	-2.47	39	-0.10	488
Akt2	-1.57	121	-6.37	1	-2.46	40	-2.13	75
Cdkl4	-0.66	336	-0.59	342	-2.46	41	-0.38	417
Pik3ca	-3.82	15	-1.06	211	-2.45	42	-4.31	10
Pkn2	-1.87	85	-1.93	75	-2.43	43	-2.88	30
Bckdk	-0.97	230	-1.70	105	-2.35	44	-2.31	57
Adck4	-1.08	202	-1.78	94	-2.30	45	-2.30	58
Eif2ak3	-1.28	162	-1.29	159	-2.30	46	-3.17	20
Pi4ka	-0.77	289	-0.44	400	-2.29	47	-2.05	83
Atr	-5.98	1	-3.94	9	-2.27	48	-7.69	1
Stk38	-2.06	74	-1.01	223	-2.25	49	-0.92	249
Snrk	-2.09	69	-1.88	79	-2.24	50	-1.96	93
Pask	-1.58	115	-2.56	40	-2.23	51	-0.52	365
Sik3	-2.14	64	-1.42	140	-2.23	52	-1.55	145
Cask	-2.00	78	-1.99	69	-2.22	53	-1.54	148
Mapk12	-0.46	390	-0.41	414	-2.19	54	-1.73	120
Lats1	-0.70	321	-0.70	304	-2.19	55	-1.06	228
Gsg2	-1.58	114	-1.98	72	-2.17	56	-1.14	211
Mark1	-1.29	159	-2.03	67	-2.17	57	-2.44	51
Pak2	-1.19	181	-3.85	10	-2.16	58	-1.89	101
Mapk7	-0.59	360	-0.90	246	-2.16	59	-1.48	158
Prkg1	-2.86	38	-0.70	302	-2.14	60	-1.00	236
Ryk	-3.74	17	-1.05	214	-2.14	61	-3.84	12
Map3k6	-2.27	56	-0.35	427	-2.13	62	-2.44	52
Mastl	-1.19	183	-0.96	234	-2.13	63	-1.55	146
Stk3	-1.79	93	-1.25	170	-2.13	64	-1.98	90
Rps6kl1	-1.46	137	-0.32	434	-2.12	65	-2.10	80
Prkcg	-1.90	82	-1.30	156	-2.11	66	-0.54	360
Cdk10	-1.30	157	-0.58	349	-2.10	67	-1.80	111
Ntrk1	-0.04	513	-0.48	382	-2.10	68	-0.02	515
Ripk4	-0.63	346	-0.82	269	-2.10	69	-1.99	88

Mapk6	-0.85	256	-1.43	136	-2.10	70	-1.52	150
Pxk	-1.74	99	-2.07	64	-2.09	71	-1.75	118
Camk1d	-0.80	271	-0.48	384	-2.09	72	-0.86	263
Yes1	-3.37	23	-0.90	245	-2.05	73	-1.78	113
Prkab2	-1.08	198	-0.63	326	-2.04	74	-3.82	13
Nek3	-2.74	42	-0.96	233	-2.04	75	-2.52	44
Musk	-0.73	304	-0.43	402	-2.03	76	-3.10	23
Riok2	-0.80	272	-0.64	322	-2.03	77	-1.63	137
Vrk1	-1.21	170	-0.48	383	-2.02	78	-0.05	506
Pink1	-0.78	283	-3.26	16	-2.02	79	-3.07	24
Cdk6	-1.49	134	-0.87	255	-2.01	80	-2.18	67
LUC	-0.78	278	-1.24	173	-2.00	81	-1.61	140
Mapkapk5	-0.30	443	-1.70	106	-1.98	82	-1.92	95
Mapk9	-2.07	71	-1.98	73	-1.96	83	-1.92	97
Bmp2k	-1.46	138	-0.89	251	-1.96	84	-2.52	47
Epha5	-2.24	58	-1.83	86	-1.95	85	-1.77	114
Prkd3	-1.87	84	-0.22	466	-1.94	86	-0.63	332
Ern1	-1.19	180	-3.62	11	-1.93	87	-0.51	372
Sik1	-0.30	445	-0.42	404	-1.93	88	-0.65	326
Prkcd	-4.60	9	-2.87	26	-1.89	89	-2.54	43
Nek1	-1.75	96	-4.30	8	-1.88	90	-1.97	92
Trrap	-3.31	24	-3.26	17	-1.88	91	-2.03	84
Cnksr1	-0.25	456	-0.60	341	-1.88	92	-1.53	149
Mylk	-1.58	116	-0.27	449	-1.84	93	-1.25	184
Map2k6	-0.31	440	-0.66	316	-1.84	94	-1.38	167
Mast1	-3.50	19	-0.52	366	-1.84	95	-0.83	270
Map2k2	-1.19	182	-1.43	138	-1.83	96	-0.56	352
Map3k13	-0.14	491	-2.73	32	-1.82	97	-0.23	456
Epha1	-1.05	213	-0.83	266	-1.81	98	-0.64	327
Nek9	-1.36	148	-2.43	44	-1.81	99	-2.79	32
Epha4	-0.71	315	-1.03	219	-1.80	100	-0.40	408
Egfr	-1.86	87	-1.07	207	-1.79	101	-3.12	22
Dstyk	-1.06	205	-0.28	441	-1.79	102	-1.23	191
Ddr1	-0.85	257	-1.19	183	-1.78	103	-2.14	72
Fgfr4	-2.41	47	-2.78	29	-1.77	104	-2.66	38
Trib1	-1.57	120	-1.25	169	-1.76	105	-1.22	193
Chek1	-0.94	235	-1.10	199	-1.76	106	-1.45	161

Camk2a	-1.82	88	-1.27	161	-1.76	107	-0.87	259
Prkci	-0.24	460	-1.06	209	-1.75	108	-0.80	278
Map3k5	-0.55	367	-0.59	344	-1.75	109	-1.50	153
Met	-0.70	323	-0.37	424	-1.75	110	-0.13	479
Cdk7	-0.39	415	-0.05	504	-1.74	111	-0.45	389
Ptk2	-1.33	151	-1.29	158	-1.71	112	-3.02	27
Camkk1	-0.74	301	-0.96	235	-1.71	113	-0.59	343
Ulk1	-2.22	61	-0.63	330	-1.70	114	-0.42	403
Zap70	-1.07	203	-0.80	277	-1.68	115	-0.68	318
Srpk3	-1.06	204	-1.04	217	-1.68	116	-0.44	395
Map3k14	-1.21	175	-0.73	297	-1.67	117	-1.01	235
Crkl	-0.50	379	-0.82	268	-1.67	118	-1.26	181
Aatk	-1.63	108	-1.04	215	-1.66	119	-1.27	179
Pik3r3	-0.37	423	-0.02	514	-1.66	120	-0.57	350
Cdk8	-1.24	166	-2.08	63	-1.66	121	-2.13	74
Axl	-0.96	231	-0.67	313	-1.65	122	-0.62	335
Ddr2	-0.49	381	-1.05	212	-1.65	123	-1.11	219
Sgk2	-1.00	218	-0.24	462	-1.64	124	-0.63	331
Mok	-4.38	10	-1.84	83	-1.63	125	-1.83	110
Epha6	-0.77	291	-1.16	193	-1.62	126	-2.19	64
Stk32c	-2.80	41	-1.29	160	-1.62	127	-0.88	258
Rps6ka4	-0.93	238	-2.50	41	-1.61	128	-1.43	163
Sik2	-0.91	244	-1.07	208	-1.60	129	-1.15	209
Csk	-0.19	467	-0.66	317	-1.58	130	-0.86	265
Mknk1	-1.12	191	-0.59	346	-1.55	131	-0.60	339
Adck5	-3.48	20	-2.57	39	-1.54	132	-1.16	206
Rock2	-0.76	295	-0.91	241	-1.52	133	-0.45	388
Frk	-1.21	172	-2.18	55	-1.51	134	-0.89	256
Map4k1	-0.71	313	-1.02	222	-1.49	135	-1.12	217
Ret	-0.10	496	-0.35	428	-1.48	136	-0.37	418
Map3k2	-2.35	51	-1.56	120	-1.48	137	-0.25	449
Gm711	-1.10	193	-1.90	76	-1.47	138	-1.18	200
Camk4	-0.52	373	-0.21	472	-1.47	139	-1.27	177
Alpk3	-2.02	77	-0.51	372	-1.46	140	-0.18	469
Araf	-1.51	130	-0.53	363	-1.45	141	-0.99	239
Bmpr2	-0.77	290	-2.33	49	-1.45	142	-2.71	37
Npr2	-0.68	329	-0.48	381	-1.44	143	-0.91	253

Kdr	-0.28	449	-0.58	350	-1.44	144	-2.96	29
Mst1r	-1.28	161	-0.31	436	-1.44	145	-0.92	251
Txk	-0.50	378	-0.48	385	-1.43	146	-2.18	68
Stk17b	-0.70	324	-0.28	442	-1.42	147	-0.16	474
Cdk16	-0.96	232	-1.19	184	-1.42	148	-2.29	60
Pkn1	-0.91	241	-1.38	144	-1.41	149	-2.19	65
Csnk1d	-0.38	421	-0.54	361	-1.41	150	-0.55	354
Hipk3	-0.99	224	-1.56	119	-1.41	151	-0.79	280
Stk33	-1.68	104	-0.90	243	-1.41	152	-0.78	288
Ripk3	-0.10	500	-1.21	178	-1.40	153	-1.52	151
Bub1	-1.62	109	-2.12	57	-1.37	154	-1.19	198
Plk4	-0.83	264	-1.45	132	-1.37	155	-2.07	81
Mos	-0.60	357	-1.79	93	-1.37	156	-1.57	143
Pdpk1	-2.84	39	-2.70	34	-1.37	157	-2.37	55
Cdk11b	-1.41	145	-1.76	97	-1.36	158	-1.83	109
Mark4	-1.52	128	-0.80	274	-1.35	159	-3.00	28
Pak7	-0.92	239	-0.63	331	-1.35	160	-1.25	182
Mapk8	-1.50	133	-0.65	319	-1.35	161	-1.13	215
Aurkb	-4.96	8	-1.45	133	-1.35	162	-5.47	5
Dapk1	-1.76	95	-0.26	451	-1.34	163	-1.31	173
Styk1	-1.73	100	-0.37	421	-1.34	164	-2.28	61
Stk40	-1.57	118	-0.51	373	-1.33	165	-1.49	154
Map3k9	-0.40	412	-0.48	380	-1.33	166	-0.10	487
Prkch	-0.69	328	-0.77	285	-1.32	167	-0.31	436
Csnk1g1	-0.08	504	-1.16	191	-1.32	168	-0.75	302
Blk	-1.43	142	-1.26	167	-1.31	169	-1.35	170
Pim3	-1.29	160	-0.62	332	-1.31	170	-2.14	73
Fgr	-0.88	251	-0.72	299	-1.31	171	-0.76	297
Pdgfrb	-1.49	135	-0.83	265	-1.30	172	-0.31	438
Nek11	-1.87	83	-0.21	471	-1.30	173	-2.39	53
Trib2	-1.45	140	-1.15	194	-1.30	174	-0.53	363
Tbk1	-1.55	125	-2.33	50	-1.30	175	-2.02	85
Limk1	-0.45	393	-0.30	439	-1.30	176	-0.09	491
Sbk1	-1.44	141	-1.23	174	-1.29	177	-0.51	373
Ikbkb	-0.80	274	-0.51	375	-1.29	178	-1.75	117
Tex14	-4.20	11	-1.34	148	-1.28	179	-1.14	210
Jak2	-3.25	26	-2.26	52	-1.28	180	-1.94	94

Prkd2	-0.93	237	-0.99	228	-1.28	181	-2.45	50
Mapk14	-2.38	49	-1.57	117	-1.27	182	-0.77	289
Stk32b	-1.57	122	-1.32	153	-1.27	183	-1.37	168
Nim1k	-1.24	167	-1.36	145	-1.26	184	-1.17	202
Lrrk2	-1.51	129	-2.61	36	-1.25	185	-0.81	274
Map4k3	-3.08	29	-1.43	137	-1.24	186	-0.62	333
Mapk1	-0.83	263	-2.88	24	-1.21	187	-0.26	445
Pik3c3	-0.59	361	-0.64	321	-1.21	188	-0.54	361
Cdk9	-2.22	60	-1.11	196	-1.21	189	-0.47	385
Phkg2	-0.21	465	-0.13	488	-1.20	190	-2.10	77
Lmtk2	-0.47	388	-0.24	463	-1.20	191	-1.03	230
Mapk15	-3.08	30	-1.30	157	-1.19	192	-0.93	247
Eif2ak4	-0.97	228	-1.10	198	-1.18	193	-0.48	381
Cdkl5	-0.72	308	-0.25	459	-1.18	194	-1.22	196
Mapk4	-5.86	3	-0.64	324	-1.17	195	-0.48	382
Fastk	-0.83	262	-1.16	190	-1.17	196	-1.74	119
Riok1	-3.02	32	-2.88	25	-1.17	197	-3.39	18
Irak2	-1.61	110	-0.90	247	-1.15	198	-1.88	103
Fgfr1	-0.64	340	-0.39	417	-1.14	199	-0.68	320
Fert2	-1.09	195	-0.77	281	-1.13	200	-0.20	462
Ulk4	-0.66	337	-0.54	362	-1.13	201	-0.33	428
Erbb2	-3.02	31	-1.27	163	-1.12	202	-1.20	197
Mast4	-0.57	366	-0.26	452	-1.12	203	-0.77	290
Nek8	-0.13	493	-2.73	31	-1.12	204	-1.75	116
Trib3	-2.11	68	-1.27	162	-1.11	205	-0.79	281
Map3k11	-0.32	434	-1.04	218	-1.11	206	-1.18	201
Epha10	-1.18	184	-0.91	242	-1.11	207	-1.42	164
Scyl2	-1.08	197	-2.11	60	-1.11	208	-0.80	277
Insr	-2.13	65	-0.52	368	-1.11	209	-0.87	262
Ttbk1	-0.33	433	-0.81	271	-1.09	210	-0.76	298
Sgk3	-1.13	189	-0.59	347	-1.09	211	-0.33	431
Tec	-1.50	132	-0.86	258	-1.08	212	-2.19	66
Nrk	-0.78	281	-0.30	438	-1.08	213	-0.50	375
Stk19	-2.07	72	-0.41	413	-1.07	214	-2.25	63
Epha3	-0.41	409	-2.59	38	-1.06	215	-2.29	59
Riok3	-0.74	298	-1.03	220	-1.06	216	-1.98	89
Ror2	-0.99	222	-1.75	98	-1.05	217	-2.10	78

Map3k19	-0.86	254	-1.09	204	-1.05	218	-1.54	147
Pim1	-0.64	342	-1.42	139	-1.05	219	-1.51	152
Strada	-0.72	310	-0.63	329	-1.05	220	-0.05	505
Ttbk2	-1.48	136	-0.77	283	-1.05	221	-1.26	180
Pskh1	-1.80	90	-2.29	51	-1.03	222	-1.69	125
Tssk6	-1.74	98	-1.34	149	-1.03	223	-2.00	87
Ulk2	-1.34	149	-2.84	28	-1.03	224	-0.88	257
Hunk	-0.53	372	-1.16	188	-1.03	225	-1.69	126
Wee1	-3.17	27	-5.74	3	-1.02	226	-1.91	98
Mknk2	-0.70	319	-0.10	498	-1.02	227	-0.79	284
Aak1	-1.11	192	-1.32	152	-1.02	228	-1.13	213
Chek2	-0.88	252	-0.23	465	-1.02	229	-1.88	102
Pbk	-0.40	410	-0.37	425	-1.02	230	-0.76	295
Dclk3	-1.03	215	-0.42	406	-1.01	231	-1.00	238
Braf	-0.73	307	-1.96	74	-1.01	232	-0.18	466
Mylk4	-0.78	277	-0.58	352	-1.00	233	-0.74	304
Cdkl2	-0.26	453	-0.95	236	-1.00	234	-1.24	186
Ilk	-2.94	33	-1.36	146	-1.00	235	-1.68	128
Prkca	-0.58	362	-0.54	358	-1.00	236	-0.57	351
Mapk13	-0.75	296	-3.51	13	-0.98	237	-1.03	232
Myo3b	-0.45	391	-1.78	95	-0.98	238	-1.22	195
Ern2	-1.80	89	-1.81	89	-0.98	239	-3.05	25
Taf1	-2.35	50	-2.11	58	-0.97	240	-0.80	275
Nek10	-0.71	318	-1.05	213	-0.97	241	-0.55	355
Hipk2	-1.06	208	-1.74	100	-0.97	242	-1.11	218
Cdk14	-0.42	401	-0.07	502	-0.96	243	-0.74	303
Ripk1	-0.52	374	-0.24	461	-0.96	244	-1.23	189
Dclk2	-0.18	476	-0.75	293	-0.96	245	-0.08	500
Tnni3k	-1.77	94	-2.37	47	-0.96	246	-0.72	308
Matk	-0.90	247	-0.34	429	-0.96	247	-1.09	223
Trpm6	-1.21	174	-0.87	254	-0.95	248	-0.21	458
Tesk2	-1.64	107	-0.52	367	-0.95	249	-0.48	380
Stk24	-0.97	229	-0.78	279	-0.95	250	-0.06	502
Acvr1c	-0.96	233	-0.77	282	-0.95	251	-2.83	31
Tssk4	-0.41	406	-0.49	379	-0.94	252	-1.06	227
Acvr2a	-0.74	299	-0.51	371	-0.94	253	-0.61	338
Alk	-1.32	155	-1.74	101	-0.94	254	-1.23	190

Irak4	-2.51	44	-0.76	287	-0.93	255	-1.62	138
Fgfr2	-0.59	359	-0.79	278	-0.93	256	-2.18	69
Stk11	-1.71	102	-0.42	409	-0.93	257	-0.33	430
Amhr2	-0.38	420	-1.40	141	-0.93	258	-0.34	424
Cdk20	-1.08	201	-1.87	80	-0.92	259	-2.78	33
Itk	-0.34	427	-1.09	203	-0.91	260	-1.07	226
Map3k10	-2.89	36	-1.31	154	-0.90	261	-2.05	82
Dyrk2	-0.39	418	-0.67	310	-0.90	262	-0.39	409
Map2k3	-1.33	152	-0.31	437	-0.90	263	-0.54	356
Ptk2b	-0.71	312	-1.01	224	-0.90	264	-0.59	344
Mast3	-0.67	332	-0.47	387	-0.89	265	-0.58	347
Cdc42bpb	-0.35	426	-0.38	420	-0.89	266	-0.93	246
Cdk12	-0.65	338	-0.15	484	-0.89	267	-0.37	419
Nek2	-1.06	206	-0.93	239	-0.88	268	-0.72	307
Srms	-0.14	488	-0.11	493	-0.88	269	-0.35	422
Sbk2	-0.62	350	-0.81	272	-0.87	270	-1.91	99
Nuak1	-2.24	59	-0.47	388	-0.87	271	-0.33	426
Twf1	-1.60	111	-0.28	445	-0.86	272	-0.87	261
Ikbke	-0.69	325	-1.27	165	-0.85	273	-2.65	39
Scyl1	-1.54	126	-0.67	311	-0.85	274	-1.60	141
Wnk4	-1.79	91	-1.00	227	-0.83	275	-0.22	457
BC021891	-0.39	419	-0.44	398	-0.83	276	-1.41	165
Gucy2f	-1.26	164	-1.82	88	-0.83	277	-2.54	42
Tlk2	-1.56	123	-1.47	128	-0.83	278	-2.11	76
Grk6	-0.38	422	-0.12	492	-0.83	279	-0.08	497
Ankk1	-0.84	258	-1.09	205	-0.82	280	-0.69	316
Stk36	-2.06	73	-1.54	125	-0.80	281	-1.24	187
Pdk1	-1.20	179	-2.10	61	-0.80	282	-0.91	252
Hipk1	-1.94	80	-0.64	323	-0.79	283	-2.63	41
Ulk3	-2.28	55	-1.19	180	-0.78	284	-1.79	112
Eif2ak1	-0.28	452	-0.14	486	-0.78	285	-0.09	494
Mapk11	-0.31	442	-0.49	378	-0.78	286	-0.64	330
D8Ertd82e	-0.37	424	-0.18	479	-0.77	287	-0.17	472
Tesk1	-0.74	303	-0.23	464	-0.77	288	-0.15	475
Lats2	-0.30	444	-0.89	249	-0.77	289	-1.48	157
Obscn	-0.68	331	-0.71	301	-0.77	290	-0.21	460
Pkn3	-0.41	404	-0.40	416	-0.77	291	-0.28	443

Rps6kb2	-2.18	63	-2.92	22	-0.77	292	-2.10	79
Lmtk3	-1.57	119	-1.63	115	-0.76	293	-0.46	386
Mink1	-0.86	253	-0.80	276	-0.76	294	-0.75	301
Plk3	-2.25	57	-0.45	397	-0.76	295	-2.46	49
Tek	-1.01	217	-0.45	395	-0.76	296	-1.76	115
Pkdcc	-0.85	255	-1.18	185	-0.74	297	-2.77	34
Trio	-0.59	358	-0.21	470	-0.74	298	-2.26	62
Trp53rk	-0.78	282	-0.77	284	-0.74	299	-2.16	71
Pdk4	-3.42	22	-1.54	124	-0.74	300	-0.51	369
Kit	-0.12	494	-0.75	291	-0.73	301	-0.71	310
Fgfr3	-0.58	365	-0.81	270	-0.73	302	-0.80	276
Limk2	-0.91	245	-0.13	489	-0.73	303	-0.96	244
Adck2	-0.83	265	-0.98	229	-0.73	304	-0.50	376
Epha7	-1.45	139	-0.75	292	-0.72	305	-0.10	489
Grk5	-0.62	354	-0.25	460	-0.72	306	-0.44	394
Melk	-0.33	431	-0.83	267	-0.72	307	-0.79	279
Prkaa1	-0.32	436	-0.97	231	-0.71	308	-1.89	100
Ksr2	-0.84	260	-0.55	357	-0.70	309	-0.62	336
Vrk2	-1.25	165	-0.63	328	-0.70	310	-4.95	7
Pi4k2a	-0.39	417	-1.71	102	-0.69	311	-3.48	16
Rps6kb1	-0.58	363	-0.92	240	-0.69	312	-1.55	144
Camk2g	-1.43	143	-0.10	496	-0.69	313	-0.26	447
Map3k15	-3.17	28	-2.35	48	-0.68	314	-1.67	131
Pik3c2a	-0.98	227	-1.75	99	-0.68	315	-0.73	305
Jak3	-1.03	214	-1.06	210	-0.68	316	-0.56	353
Cit	-1.00	221	-0.10	500	-0.68	317	-0.24	455
Mark2	-0.88	250	-1.47	131	-0.67	318	-1.40	166
Cdk17	-0.77	288	-0.46	390	-0.67	319	-0.37	420
Rnasel	-0.23	461	-0.08	501	-0.67	320	-0.08	498
Trpm7	-1.92	81	-0.90	244	-0.66	321	-1.72	121
Myo3a	-0.44	394	-1.98	70	-0.66	322	-0.45	390
Lck	-0.90	246	-1.08	206	-0.66	323	-0.24	454
Erbb4	-0.32	437	-0.19	477	-0.65	324	-0.70	314
BC030499	-0.34	428	-1.57	118	-0.65	325	-0.42	400
Tie1	-1.42	144	-1.82	87	-0.65	326	-0.51	370
Pak6	-0.69	327	-0.26	454	-0.65	327	-0.12	482
Eif2ak2	-0.74	300	-0.71	300	-0.65	328	-1.05	229

Cdk13	-0.76	292	-0.76	286	-0.65	329	-0.02	512
Taok2	-0.90	248	-1.65	113	-0.65	330	-1.27	178
Camkk2	-0.15	485	-0.25	455	-0.65	331	-0.09	496
Ripk2	-0.70	320	-1.47	130	-0.64	332	-2.52	46
Stk31	-1.74	97	-1.35	147	-0.64	333	-1.30	175
Nrbp2	-1.21	171	-3.05	20	-0.64	334	-0.73	306
Flt1	-1.05	212	-1.67	109	-0.64	335	-0.52	366
Cdkl1	-2.05	75	-2.67	35	-0.63	336	-0.67	322
Vrk3	-1.20	176	-0.75	294	-0.63	337	-0.79	285
Pak1	-0.02	515	-0.47	389	-0.63	338	-0.33	427
Nuak2	-0.18	475	-0.37	423	-0.63	339	-1.68	129
Adck1	-0.47	386	-0.10	499	-0.62	340	-0.54	357
Ntrk3	-1.24	168	-1.51	127	-0.62	341	-0.38	415
Mertk	-0.78	279	-1.84	84	-0.62	342	-1.17	203
Ptk6	-0.75	297	-1.52	126	-0.62	343	-0.62	334
Bmpr1a	-0.33	432	-2.00	68	-0.61	344	-0.35	421
Pik3r2	-1.05	209	-1.90	77	-0.61	345	-1.00	237
Grk1	-1.21	173	-0.89	248	-0.60	346	-0.54	359
Prpf4b	-3.86	14	-2.78	30	-0.59	347	-3.03	26
Abl2	-0.01	516	-0.51	374	-0.59	348	-0.41	405
Ptk7	-2.92	34	-0.51	369	-0.59	349	-2.39	54
Dmpk	-0.63	347	-1.70	104	-0.59	350	-0.28	441
Dapk2	-0.29	447	-0.84	262	-0.58	351	-1.08	225
Aurkc	-0.26	454	-1.86	81	-0.58	352	-0.71	311
Lrrk1	-0.63	348	-1.27	166	-0.58	353	-1.13	216
Phkg1	-0.74	302	-0.42	410	-0.58	354	-1.17	205
Csnk2a1	-1.86	86	-1.55	122	-0.58	355	-1.69	127
Acvrl1	-0.71	316	-0.41	411	-0.57	356	-0.13	481
Cdk1	-2.12	66	-1.09	201	-0.57	357	-1.47	160
Eef2k	-0.62	351	-0.21	468	-0.57	358	-1.33	171
Irak3	-0.19	468	-1.02	221	-0.57	359	-0.26	448
Pdik1l	-1.12	190	-0.52	365	-0.56	360	-0.18	468
Dyrk4	-0.83	267	-1.84	85	-0.56	361	-1.13	214
Cdk18	-0.78	284	-0.28	443	-0.56	362	-1.03	231
Bmx	-0.61	355	-0.85	260	-0.56	363	-0.77	294
Tgfbr2	-0.41	407	-0.87	256	-0.56	364	-0.70	315
Bcr	-0.43	396	-0.67	314	-0.55	365	-0.75	300

Pik3c2g	-1.58	113	-0.60	339	-0.55	366	-0.54	358
Camk1g	-1.59	112	-1.27	164	-0.55	367	-1.01	233
Mylk2	-1.30	156	-0.61	337	-0.55	368	-1.98	91
Srpk2	-0.25	455	-0.12	491	-0.54	369	-0.41	406
Dyrk3	-0.28	451	-0.88	252	-0.54	370	-0.20	461
Srpk1	-0.05	510	-0.83	263	-0.54	371	-0.17	471
Tbck	-0.53	370	-0.18	481	-0.53	372	-0.08	499
Ephb3	-0.68	330	-0.68	308	-0.53	373	-0.38	416
Prkab1	-1.37	146	-0.62	334	-0.53	374	-0.67	321
Stk38l	-1.34	150	-0.81	273	-0.53	375	-1.65	133
Pik3cb	-0.65	339	-0.10	497	-0.52	376	-0.03	511
Brsk2	-1.08	199	-0.44	401	-0.52	377	-0.39	413
Rps6ka1	-0.20	466	-2.07	65	-0.52	378	-0.19	464
Map2k7	-0.42	403	-0.44	399	-0.52	379	-0.27	444
Stk10	-1.20	177	-0.69	305	-0.51	380	-0.39	412
Pik3cd	-0.10	497	-0.27	448	-0.51	381	-0.18	470
Map4k2	-0.99	225	-1.67	111	-0.51	382	-1.19	199
Ntrk2	-0.32	435	-1.22	176	-0.51	383	-1.10	221
Zak	-1.09	196	-0.21	469	-0.50	384	-1.87	105
Igf1r	-0.72	311	-0.54	359	-0.49	385	-0.42	399
Ephb2	-0.42	402	-0.27	446	-0.49	386	-0.54	362
Fyn	-0.71	317	-0.18	478	-0.49	387	-1.15	208
Pdgfra	-1.23	169	-0.18	480	-0.48	388	-0.76	296
Csf1r	-0.77	286	-1.24	172	-0.47	389	-0.43	397
Cdk19	-0.53	369	-0.04	511	-0.47	390	-0.29	439
Mak	-0.51	377	-0.59	343	-0.47	391	-0.04	509
Scyl3	-0.18	471	-0.45	396	-0.47	392	-0.64	328
Csnk1g3	-1.36	147	-2.15	56	-0.46	393	-0.44	393
Nlk	-0.48	384	-1.00	225	-0.45	394	-0.41	407
Ick	-0.31	439	-0.33	431	-0.45	395	-0.71	309
Map3k8	-0.15	483	-0.39	418	-0.45	396	-0.76	299
Prkacb	-1.00	220	-0.58	351	-0.45	397	-0.87	260
Map3k1	-0.62	353	-0.01	515	-0.45	398	-0.09	493
Alpk1	-0.29	448	-0.51	376	-0.45	399	-0.19	465
Camk2b	-0.19	470	-0.69	307	-0.45	400	-0.70	313
Ephb1	-0.71	314	-0.76	290	-0.45	401	-0.83	271
Cdc7	-0.18	473	-0.59	348	-0.44	402	-0.86	264

Acvr2b	-1.09	194	-0.97	232	-0.43	403	-0.49	379
Insrr	-2.20	62	-0.72	298	-0.43	404	-0.92	250
Map3k4	-0.82	270	-0.56	353	-0.43	405	-0.19	463
Hck	-0.82	269	-1.26	168	-0.43	406	-0.15	476
Cdkl3	-0.91	243	-0.22	467	-0.42	407	-0.11	483
Prkcb	-0.73	305	-0.06	503	-0.41	408	-0.70	312
Dclk1	-0.29	446	-0.46	393	-0.41	409	-0.39	411
Lyn	-1.32	154	-1.12	195	-0.41	410	-0.50	377
Adrbk1	-0.04	512	-0.20	476	-0.40	411	0.00	516
Irak1	-0.92	240	-0.69	306	-0.40	412	-0.58	346
2610018G03Rik	-1.95	79	-1.80	91	-0.40	413	-0.79	282
Ttn	-1.71	103	-1.66	112	-0.40	414	-0.66	324
Prkaa2	-0.40	411	-0.49	377	-0.39	415	-0.42	404
Tyro3	-0.24	458	-0.46	391	-0.39	416	-0.42	401
Ephb6	-0.14	489	-0.11	494	-0.39	417	-1.30	174
Pnck	-0.04	511	-0.25	458	-0.39	418	-1.69	124
Pdk2	-0.07	506	-0.39	419	-0.38	419	-0.43	398
Pak3	-1.52	127	-1.61	116	-0.37	420	-1.71	123
Tlk1	-0.64	344	0.00	517	-0.37	421	-0.35	423
Taok3	-0.43	398	-0.34	430	-0.37	422	-0.52	368
Epha8	-0.78	280	-0.88	253	-0.37	423	-0.57	349
Cdk2	-0.07	507	-0.14	485	-0.37	424	-1.85	106
Brsk1	-0.17	477	-0.26	453	-0.37	425	-0.57	348
Tssk1	-1.08	200	-0.80	275	-0.37	426	-0.09	495
Tyk2	-0.33	430	-1.19	179	-0.36	427	-1.36	169
Pi4kb	-1.02	216	-0.03	513	-0.36	428	-0.77	292
Camk1	-1.50	131	-1.11	197	-0.36	429	-0.48	384
Sgk1	-0.44	395	-0.51	370	-0.36	430	-1.49	155
Mapkapk3	-0.41	408	-0.37	422	-0.36	431	-0.33	429
Map4k4	-0.13	492	-0.55	355	-0.36	432	-0.68	319
Adck3	-0.14	490	-0.53	364	-0.36	433	-0.39	414
Cdk15	-0.21	464	-0.83	264	-0.35	434	-1.87	104
Rps6ka3	-0.52	375	-0.66	318	-0.35	435	-0.32	432
Src	-0.89	249	-1.18	186	-0.35	436	-0.60	341
Pik3c2b	-0.18	472	-0.73	296	-0.34	437	-0.25	451
Tnk1	-1.17	185	-0.56	354	-0.34	438	-0.66	325
Gsk3a	-0.94	236	-0.13	487	-0.34	439	-0.60	342

Epha2	-0.69	326	-0.17	482	-0.33	440	-0.28	442
Pim2	-0.83	266	-1.77	96	-0.33	441	-0.32	434
Csnk1g2	-0.84	259	-1.18	187	-0.32	442	-0.50	374
Prkd1	-1.79	92	-1.22	177	-0.32	443	-1.17	204
Ros1	-0.14	487	-0.61	338	-0.32	444	-1.11	220
Acvr1b	-0.67	334	-1.70	103	-0.32	445	-1.09	224
Gsk3b	-1.06	207	-0.41	412	-0.31	446	-0.53	364
Taok1	-0.08	505	-0.30	440	-0.31	447	-0.09	490
Prkaca	-1.30	158	-0.20	474	-0.30	448	-1.27	176
Stk32a	-0.73	306	-1.19	182	-0.30	449	-2.77	35
Gak	-0.83	261	-1.22	175	-0.29	450	-0.32	435
Pdk3	-0.79	276	-1.68	107	-0.29	451	-1.25	185
Map3k12	-0.36	425	-0.05	508	-0.29	452	-0.24	453
Pik3r5	-1.17	186	-0.76	288	-0.29	453	-0.77	293
Map2k1	-0.39	416	-1.40	142	-0.28	454	-0.52	367
Mylk3	-0.22	463	-1.68	108	-0.27	455	-0.83	272
Chuk	-0.64	343	-0.54	360	-0.27	456	-0.29	440
Peak1	-0.31	441	-0.33	433	-0.27	457	-0.02	514
Mapk10	-0.46	389	-1.81	90	-0.27	458	-1.23	192
Plk2	-0.47	387	-0.63	325	-0.27	459	-0.64	329
Mast2	-0.28	450	-0.42	407	-0.26	460	-0.15	477
Syk	-0.15	486	-1.54	123	-0.26	461	-1.01	234
Stk25	-0.24	459	-0.62	333	-0.25	462	-0.79	283
Ephb4	-0.76	294	-0.64	320	-0.24	463	-0.78	287
Clk2	-0.63	349	-0.21	473	-0.24	464	-0.48	383
Prkce	-2.12	67	-1.98	71	-0.24	465	-3.45	17
Prkg2	-0.76	293	-0.74	295	-0.24	466	-0.85	267
Clk4	-0.67	335	-0.03	512	-0.23	467	-0.06	501
Nek6	-0.99	223	-0.35	426	-0.23	468	-0.66	323
Clk1	-0.67	333	-0.59	345	-0.23	469	-1.32	172
Tssk2	-0.98	226	-1.09	202	-0.23	470	-0.92	248
Acvr1	-0.58	364	-0.63	327	-0.22	471	-0.99	240
Hspb8	-1.00	219	-2.23	53	-0.22	472	-1.84	107
Ror1	-0.41	405	-0.47	386	-0.21	473	-0.09	492
Abl1	-0.77	287	-1.09	200	-0.21	474	-1.44	162
Stk39	-0.47	385	-1.16	192	-0.21	475	-0.61	337
Mapk3	-0.17	479	0.00	516	-0.21	476	-0.32	433

Cdk5	0.00	517	-0.40	415	-0.20	477	-0.34	425
Camkv	-0.40	413	-0.76	289	-0.20	478	-0.05	504
Csnk1a1	-2.30	54	-1.43	135	-0.20	479	-0.11	485
Prkcq	-0.10	499	-1.24	171	-0.20	480	-0.05	503
Dyrk1a	-0.06	509	-3.43	15	-0.20	481	0.00	517
Pik3r4	-0.64	345	-2.38	46	-0.20	482	-0.69	317
Gucy2c	-0.95	234	-0.98	230	-0.20	483	-0.14	478
Clk3	-0.09	502	-0.93	237	-0.20	484	-0.90	254
Tgfbr1	-0.51	376	-0.93	238	-0.19	485	-0.11	484
Nek4	-0.80	273	-0.32	435	-0.19	486	-1.58	142
Camk2d	-0.42	400	-0.42	408	-0.19	487	-0.60	340
Pak4	-0.77	285	-0.67	309	-0.18	488	-1.92	96
Magi1	-1.05	210	-2.47	42	-0.18	489	-0.13	480
Twf2	-0.49	380	-1.00	226	-0.18	490	-0.21	459
Flt3	-0.17	478	-0.25	457	-0.17	491	-0.02	513
Map3k3	-1.05	211	-1.56	121	-0.17	492	-0.51	371
Map2k4	-0.09	501	-0.05	506	-0.17	493	-0.45	391
Map4k5	-0.08	503	-0.85	259	-0.16	494	-0.39	410
Alpk2	-0.62	352	-0.25	456	-0.15	495	-0.24	452
Tssk3	-0.22	462	-0.60	340	-0.15	496	-0.25	450
Tnk2	-0.64	341	-2.03	66	-0.14	497	-0.59	345
Mapkapk2	-0.53	371	-0.27	447	-0.14	498	-0.97	243
Prkx	-1.14	188	-0.85	261	-0.14	499	-0.99	241
Stk4	-2.04	76	-1.63	114	-0.14	500	-1.09	222
Slk	-0.15	484	-1.19	181	-0.13	501	-0.84	269
Nek5	-0.02	514	-0.05	507	-0.13	502	-0.03	510
Pkmyt1	-0.25	457	-0.61	336	-0.13	503	-0.11	486
Atm	-0.42	399	-0.42	405	-0.12	504	-1.13	212
Rps6ka2	-0.16	481	-0.55	356	-0.12	505	-1.48	159
Ltk	-0.10	498	-0.70	303	-0.11	506	-0.94	245
Oxsr1	-0.43	397	-0.28	444	-0.11	507	-0.45	392
Mlkl	-0.83	268	-1.33	150	-0.10	508	-0.04	508
Rock1	-0.49	382	-0.11	495	-0.10	509	-0.42	402
Npr1	-0.33	429	-0.04	510	-0.08	510	-1.23	188
Grk4	-0.45	392	-0.78	280	-0.07	511	-0.26	446
Dyrk1b	-0.07	508	-0.20	475	-0.06	512	-0.04	507
Prkcz	-1.14	187	-0.67	312	-0.05	513	-0.82	273

Gucy2e	-0.19	469	-2.96	21	-0.05	514	-0.46	387
Uhmk1	-0.12	495	-0.27	450	-0.05	515	-0.18	467
Pik3r1	-0.60	356	-0.46	394	-0.03	516	-0.16	473
Cdc42bpa	-0.16	480	-0.16	483	-0.01	517	-0.31	437

Table 14. Quality control metrics for the FDAome shRNA screens

	393P			344P		
	in-vivo (sv129)			in-vivo (sv129)		
reagent	1	2	3	1	2	3
LUC_CONTROL_199590	-0.44	-0.99	0.24	-0.15	1.02	0.93
LUC_CONTROL_199591	0.58	1.24	0.95	2.21	0.42	0.68
LUC_CONTROL_199592	3.67	1.45	1.3	0.98	1.36	1.57
LUC_CONTROL_199593	0.63	0.24	1.16	1.86	0.96	0.91
LUC_CONTROL_199594	0.56	1.03	-0.32	0.53	1.6	0.02
LUC_CONTROL_199595	1	0.52	-0.3	3.2	0.36	1.44
LUC_CONTROL_199596	1.7	-0.11	1.08	1.34	2.09	1.42
LUC_CONTROL_199597	0.42	0.38	0.29	1.5	1.36	1.5
LUC_CONTROL_199598	0.97	1.68	0.11	1.37	-0.45	1.82
LUC_CONTROL_199599	0.63	0.86	1.44	0.98	0.56	0.68
LUC_CONTROL_199600	0.03	0.03	-0.39	0.43	0.16	0.3
LUC_CONTROL_199601	0.5	0.6	0.46	0.35	-0.07	-0.07
LUC_CONTROL_199602	-0.35	0.5	0.39	0.28	0.84	0.19
LUC_CONTROL_199603	0.08	0.1	0.61	1.55	0.47	0.87
LUC_CONTROL_199604	1.03	0.19	0.46	1.94	1.41	1.36
LUC_CONTROL_199605	-0.46	-1.33	0.1	-0.56	-0.42	0.53
LUC_CONTROL_199606	-0.9	-0.08	-0.29	-2.49	-0.73	-0.57
LUC_CONTROL_199607	-1.48	-1.77	-0.53	-3.62	-1.35	-1.95
LUC_CONTROL_199608	2.21	-0.97	2.33	-1.41	-2.23	-1.17
LUC_CONTROL_199609	1.51	-1.22	-0.81	0.83	0.56	-0.12
Rpl30_CONTROL_199550	-3.66	-2.43	-6.01	-2.15	-5.47	-3.24
Rpl30_CONTROL_199551	-2.5	-2.2	-2.32	-2.16	-1.2	-2.24
Rpl30_CONTROL_199552	-2.81	-1.29	-1.84	-3.33	-2.66	-2.27
Rpl30_CONTROL_199553	-3.06	-2.16	-0.55	-1.52	-4.67	-4.42
Rpl30_CONTROL_199554	-4.35	-1.56	-7.23	-0.75	-3.11	-2.37
Rpl30_CONTROL_199555	-3.06	0.62	-2.12	-2.08	-1.62	3.62
Rpl30_CONTROL_199556	0.65	-2.41	-2.32	-3.85	-4.82	-1.05
Rpl30_CONTROL_199557	-1.19	-2.45	-1.86	-3.07	-2.75	4.05
Rpl30_CONTROL_199558	-1.83	-3.17	-5.23	-1.66	-5.34	-5.74
Rpl30_CONTROL_199559	-2.83	-2.35	-1.37	-2.67	-1.37	-1.43
Rpl30_CONTROL_199560	-1.45	-2.73	-0.46	-1.24	-0.96	-2.42
Rpl30_CONTROL_199561	-2.74	-0.93	-1.62	-1.71	-1.22	0.67

Rpl30_CONTROL_199562	-1.94	-2.15	-6.81	-4.87	-3.79	-5.3
Rpl30_CONTROL_199563	0.23	-1.86	-0.83	-2.45	0.16	-4.01
Rpl30_CONTROL_199564	-3.53	-3.75	2.1	2.08	3.35	3.3
Rpl30_CONTROL_199565	-2.34	-1.22	-1.02	-0.08	1.23	-0.08
Rpl30_CONTROL_199566	-1.35	-0.7	-2.25	-0.83	-2.53	0.91
Rpl30_CONTROL_199567	-2.4	-1.98	-1.94	-4.46	-0.8	-4.82
Rpl30_CONTROL_199568	-0.31	-0.07	-1.1	-1.2	-1.66	-0.3
Rpl30_CONTROL_199569	-1.82	-2.41	-0.65	-1.66	-0.59	0.17
Psma1_CONTROL_199570	-0.4	0.14	-0.21	0.07	-0.15	0.87
Psma1_CONTROL_199571	-0.48	0.12	-0.08	0.14	-0.8	0.57
Psma1_CONTROL_199572	-0.17	0.69	1.12	0.68	-0.82	1.08
Psma1_CONTROL_199573	-0.4	-0.13	0.39	0.32	-0.91	0.45
Psma1_CONTROL_199574	-0.64	1.2	-0.55	0.14	-0.77	0.69
Psma1_CONTROL_199575	-1.87	-1.15	-2.89	-3.15	-4.68	-2.21
Psma1_CONTROL_199576	-0.79	-2.69	-2.16	-3.74	-3.26	-2.09
Psma1_CONTROL_199577	-2.09	-1.83	-2.47	-1.06	-4.2	-0.41
Psma1_CONTROL_199578	-1.21	-1.04	-1.45	-3.77	-3.23	0.28
Psma1_CONTROL_199579	-0.13	-3.03	-1.85	-3.59	-0.89	-0.42
Psma1_CONTROL_199580	-5.79	-1.62	-2.03	-1.25	-1.41	-1.49
Psma1_CONTROL_199581	-2.39	-0.92	-3.94	2.18	1.05	-1.39
Psma1_CONTROL_199582	-3.55	-1.32	-1.94	-1.8	-2.79	-1.31
Psma1_CONTROL_199583	0.38	-2.77	-2.26	-0.4	0.05	-1.54
Psma1_CONTROL_199584	3.07	-2.07	-0.04	-0.66	-0.29	-1.57
Psma1_CONTROL_199585	-2.24	-2.29	-2.23	0.19	-1.96	-2.18
Psma1_CONTROL_199586	-1.99	-3.39	-5.29	-2.93	-0.8	-0.4
Psma1_CONTROL_199587	-0.88	-3.44	-3.52	-1.28	-2.67	-0.79
Psma1_CONTROL_199588	-3.08	-1.86	-1.86	1.67	-1.34	0.48
Psma1_CONTROL_199589	-1.98	-2.77	-4.74	-0.5	1.74	-0.22

Table 15. Gene level dropout scores for each of the FDAome screens

	393P	**393P**	**344P**	**344P**
	sv129	**sv129**	**sv129**	**sv129**
gene	**logP**	**rank**	**logP**	**rank**
Pik3ca	-5.5	4	-8.4	1
Cdk4	-3.2	16	-7.8	2
Myc	-4.1	11	-7.7	3
Bcl2	-2.9	18	-6.3	4
Prkcd	-4.4	8	-5.8	5
Cdk7	-0.7	110	-5.4	6
Ctnnb1	-0.8	102	-5.1	7
Plk1	-2.9	19	-4.7	8
Mtor	-2.9	17	-4.3	9

Cdk6	-2.0	32	-4.2	10
Psmd1	-4.4	9	-4.1	11
Top2b	-0.2	164	-4.0	12
Psmb1	-10.1	1	-3.9	13
Rarb	-0.8	96	-3.9	14
Erbb2	-5.4	5	-3.7	15
Mcl1	-1.4	56	-3.3	16
Esr1	-4.5	7	-3.2	17
Birc5	-0.9	88	-3.1	18
Insr	-1.8	39	-2.9	19
Rac1	-6.5	3	-2.8	20
Fgfr4	-1.3	61	-2.8	21
Tec	-1.1	69	-2.7	22
Top1	-1.4	54	-2.5	23
Epha2	-1.7	42	-2.5	24
Notch1	-1.7	41	-2.5	25
Itk	-0.8	100	-2.5	26
Rarg	-1.1	73	-2.5	27
Ptpn6	-1.1	68	-2.4	28
Raf1	-8.7	2	-2.4	29
Stat3	-4.8	6	-2.4	30
Axl	-0.7	114	-2.2	31
Gsk3a	-2.7	20	-2.2	32
Akt2	-0.2	162	-2.2	33
Pim1	-1.2	64	-2.2	34
Wee1	-2.6	23	-2.1	35
Top2a	-4.2	10	-2.1	36
Mapk3	-0.3	160	-2.1	37
Parp3	-1.2	65	-2.1	38
Prkcg	-1.0	81	-2.0	39
Chek2	-0.1	175	-2.0	40
Trim24	-1.6	48	-2.0	41
Whsc1	-1.2	63	-2.0	42
Cd274	-0.4	152	-1.9	43
Tnfsf13b	-0.2	167	-1.9	44
Prkci	-0.2	166	-1.9	45
Atr	-1.8	36	-1.9	46
Jak1	-0.7	112	-1.9	47
Aurkb	-2.2	28	-1.9	48
Cdk9	-1.3	60	-1.8	49
Mapk1	-3.6	13	-1.8	50
Aurka	-1.7	43	-1.8	51
Fgr	-0.1	170	-1.8	52
Pak4	-2.0	30	-1.8	53

Abl2	-0.1	172	-1.8	54
Mapk7	-1.9	35	-1.7	55
Mapk12	-0.7	104	-1.7	56
Flt4	-1.1	74	-1.7	57
Pik3cg	-1.2	66	-1.6	58
Rps6kb1	-0.7	107	-1.6	59
Hdac1	-0.6	123	-1.6	60
Tyms	-0.1	180	-1.6	61
Jak2	-2.6	22	-1.5	62
Met	-2.3	25	-1.5	63
Tyro3	-1.1	76	-1.5	64
Fgfr1	-0.9	91	-1.5	65
Ptgs2	-1.1	70	-1.5	66
Rrm1	-2.0	31	-1.5	67
Xpo1	-1.6	50	-1.5	68
Ntrk1	-1.4	55	-1.5	69
Egfr	-1.5	51	-1.4	70
Chek1	-0.2	163	-1.4	71
Cdk2	-1.8	37	-1.4	72
Gls	-0.4	144	-1.4	73
Parp1	-0.7	113	-1.4	74
Esr2	-1.1	77	-1.4	75
Mapk9	-0.5	135	-1.4	76
Dot1l	-1.1	72	-1.3	77
Il1b	-0.7	116	-1.3	78
Ptk2	-1.7	40	-1.3	79
Hdac3	-0.5	141	-1.3	80
Eif4e	-3.8	12	-1.3	81
Map3k14	-0.6	130	-1.3	82
Ehmt2	-1.9	34	-1.2	83
P4hb	-0.8	103	-1.2	84
Mapk11	-1.7	45	-1.2	85
Kdm1a	-1.0	86	-1.2	86
Brd4	-1.0	80	-1.2	87
Ppm1d	-0.7	111	-1.2	88
Mapk8	-1.3	59	-1.1	89
Abl1	0.0	187	-1.1	90
Mapk14	-0.4	153	-1.1	91
Nr2c2	-0.5	139	-1.0	92
Pigf	-0.4	146	-1.0	93
Lyn	-0.6	128	-1.0	94
Rxrb	-1.8	38	-1.0	95
Flt1	-1.2	67	-1.0	96
Ikbke	-2.2	27	-0.9	97

Cdk1	-1.0	83	-0.9	98
Prkdc	-3.4	14	-0.9	99
Alk	-0.7	106	-0.9	100
Irak4	-0.4	149	-0.9	101
Hsp90aa1	-1.4	53	-0.9	102
Smo	-0.8	97	-0.8	103
Casp3	-0.5	143	-0.8	104
Prkca	-0.9	93	-0.8	105
Syk	0.0	188	-0.8	106
Pdgfra	-0.5	134	-0.8	107
Src	-0.8	99	-0.8	108
Vegfa	-1.0	85	-0.8	109
Pgd	-1.3	57	-0.8	110
Bcr	-0.6	126	-0.8	111
Ezh2	-0.9	89	-0.8	112
Map4	-2.5	24	-0.8	113
Tubb4a	-1.0	87	-0.7	114
Parp2	-0.7	105	-0.7	115
Pdgfrb	-0.6	118	-0.7	116
Map2k1	-1.1	71	-0.7	117
Prkce	-0.8	95	-0.7	118
Txn1	-0.5	131	-0.7	119
Btk	-1.7	46	-0.7	120
Il6	-0.4	155	-0.7	121
Ccr5	-1.0	79	-0.7	122
Frk	-0.9	90	-0.7	123
Idh2	-0.1	186	-0.7	124
Mapk13	-0.4	148	-0.7	125
Tnfrsf8	-0.3	159	-0.7	126
Prkch	-0.7	108	-0.7	127
Ptch1	-0.6	127	-0.7	128
Rock2	-1.5	52	-0.6	129
Nfkb1	-2.7	21	-0.6	130
Fyn	-2.1	29	-0.6	131
Pdk1	-0.2	165	-0.5	132
Gsk3b	-1.7	44	-0.5	133
Fgfr2	-1.0	78	-0.5	134
Map3k8	-0.3	161	-0.5	135
Crebbp	-0.1	179	-0.5	136
Kit	-0.1	176	-0.5	137
Ar	-0.4	147	-0.4	138
Hdac6	-0.6	117	-0.4	139
Mapt	-0.7	109	-0.4	140
Xiap	-0.6	121	-0.4	141

Atm	-1.1	75	-0.4	142
Prkaa1	-0.4	154	-0.4	143
Tnf	-0.6	119	-0.4	144
Ret	-0.1	177	-0.4	145
Idh1	-0.5	132	-0.4	146
Hdac2	-0.6	129	-0.4	147
Dhfr	-3.4	15	-0.4	148
Drd2	-1.6	49	-0.4	149
Il6ra	-0.9	94	-0.4	150
Jak3	-0.1	173	-0.3	151
Blk	-0.8	101	-0.3	152
Pik3cd	-1.3	58	-0.3	153
Map2	-0.2	168	-0.3	154
Mknk1	-0.3	156	-0.3	155
Nampt	-0.6	125	-0.3	156
Lap3	-1.0	82	-0.3	157
Lck	0.0	191	-0.3	158
Rxra	-0.2	169	-0.3	159
Fgfr3	-0.6	120	-0.3	160
Akt1	-0.8	98	-0.2	161
Aurkc	-0.5	133	-0.2	162
Prkcq	-0.9	92	-0.2	163
Mdm2	-0.5	138	-0.2	164
Tek	-0.1	174	-0.2	165
Prkcb	-0.7	115	-0.2	166
Braf	-0.6	124	-0.2	167
Hdac8	-0.5	136	-0.2	168
Ldha	-1.6	47	-0.2	169
Prkcsh	-1.9	33	-0.2	170
Rara	-0.1	171	-0.2	171
Pim3	-0.4	150	-0.2	172
Prkcz	-0.1	182	-0.2	173
Akt3	-0.5	137	-0.1	174
Tnfsf11	-1.2	62	-0.1	175
Ms4a1	-0.4	151	-0.1	176
Trpv1	-0.5	140	-0.1	177
Ptpn11	-2.3	26	-0.1	178
Nudt1	-0.1	183	-0.1	179
Pik3cb	-1.0	84	-0.1	180
Flt3	-0.4	145	-0.1	181
Cd52	-0.1	185	-0.1	182
Bmx	0.0	192	-0.1	183
Kdr	-0.3	157	-0.1	184
Tbk1	-0.1	178	-0.1	185

Rock1	-0.1	184	-0.1	186
Igf1r	0.0	189	0.0	187
Map2k2	-0.6	122	0.0	188
Pak1	-0.5	142	0.0	189
Sgk3	-0.1	181	0.0	190
Porcn	-0.3	158	0.0	191
Pim2	0.0	190	0.0	192